Thèse Présentée pour obtention le grade de
Docteur de l'Université de Strasbourg
Discipline: Chimie-Physique

Par
Zhiqiang ZHENG

Spray-Assembly of Polyelectrolyte and Polyelectrolyte/Nanoparticle Films: Structural Characterization and Improvement of Mechanical Properties

Soutenue publiquement le 26 Octobre 2009
à l'Institut Charles Sadron

Membres du Jury:

Directeur de Thèse:	M. Gero Decher, Professeur, Strasbourg, France
Président du jury:	M. Pierre Schaaf, Professeur, Strasbourg, France
Rapporteur Externe:	M. Nicholas Kotov, Professeur, Michigan, USA
Rapporteur Externe:	M. Lars Wagberg, Professeur, Stockholm, Sweden
Membre Invité:	M. Olivier Félix, CR1, Strasbourg, France

He that seeks finds

Thomas Heywood

British playwright

学而不思则罔

思而不学则殆

论语第 2 篇

孔子

Learn without thinking begets ignorance

Think without learning is dangerous

The Confucian Analects, Chapter 2

Confucius

Acknowledgement

First of all, I would like to express my sincere gratitude to my advisor Professor Gero Decher for the continuous support during my doctoral studies and research and his patience, enthusiasm, and immense passion in science. He gave me the opportunity to get familiar with the amazing technique: LbL and supported me in becoming a scientific researcher.

I am grateful for the abundant and invaluable help from Dr. Olivier Félix, without whose extraordinary support my research project would not have been possible.

I would like to thank Shahid QUERESHI, from Quaid-i-Azam University, Pakistan. He was a visiting Ph. D student twice in our team, we worked together in Amine based LbL films construction and the LbL films mechanical resistance improvement. I highly appreciate the support from Dr. Martin Brinkmann, ICS, for his help in LbL films mechanical resistance tests by rubbing machine.

Special thanks to all my colleges, Tam, Rohama, Seb, Nicolas, FIX, Guillaume, Jean-Louis and Eric, and also my office mates Emek and Gabi, for all the joyful moments that we have shared in the past three years, for your fruitful scientific discussions and inspiring ideas during my research program.

I would like to thank all the researchers, technicians and administrative staff at l'Institut Charles Sadron for offering me such a wonderful and friendly working environment. I express my gratitude especially to Dr. Fabrice Cousin in CEA, Saclay for his collaboration within our Neutron reflectometry project., to Dr. Robert Wengeler and Dr. Sabrina Pancera as well as BASF in Ludwigshafen, Germany for the collaborative project "RoboSpray". Special thanks to Dr. Karine Mougin at UHA, Mulhouse for enlightening me the first glance of research.

I would like to express my gratitude to Professors Kotov, Wågberg and Schaaf for having accepted to act as referees for my thesis work.

Thanks to French ministry of Higher Education and Research (Ministère de l'enseignement supérieur et de la recherche), Centre Natioanal de la Recherche Scientifique (CNRS) and BASF, Ludwigshafen, Germany for providing me with financial support.

I dedicate my thesis to my family, my parents, and my wife nuan nuan. Without your support and encouragement, the road could not have led so far. To my beloved grandparents as well, I miss you and I love you all.

Last but not least, I would like to thank every scientist working in the field of layer-by-layer assembly. Had it not been for your effort, I would never have the opportunity to enter this amazing world.

Table of Contents

List of Abbreviation

Techniques and Instruments:

Langmuir-Blodgett films:	LB films
Self-Assembled Monolayers:	SAMs
Layer-by-layer:	LbL
Atomic Force Microscopy:	AFM
UV-Visible Spectroscopy:	UV-Visible
Quartz Crystal Microbalance:	QCM
scattering length density:	SLD
Transmission Electronic Microscope:	TEM
root mean square:	RMS

Chemical compounds and polymers

Nanoparticle:	NP
Gold Nanoparticle:	Au NP
tetrachloroauric acid:	$HAuCl_4 \bullet 3H_2O$
poly(sodium 4-styrenesulfonate):	PSS or PSS-h7
perdeuterated poly(sodium 4-styrenesulfonate):	PSS-d7
poly(allylamine hydrochloride):	PAH
branched poly(ethylenimin):	PEI
poly(acrylic acid):	PAA
poly-(L-glutamic acid):	PGA
poly-(L-lysine):	PLL
hyaluronic acid:	HA
Poly((o-cresyl glycidyl ether)-co-formaldehyde):	CNER
poly(ethylene terephthalate):	PET
Poly(carbonate):	PC

poly(tetrafluoro ethylene):	PTFE
single-walled carbon nanotubes:	SWNT
poly(diallydimethylammonium chloride):	PDDA

Introduction

➢ Self-Assembly, a general concept of surface functionalization

The use of materials can be traced to thousands of years ago, even some periods in history are named after materials, such as the Stone Age, the Bronze Age and the Steel Age[1]. At that time, materials are used in their raw form. With the advance of science and technology, man can analyze and characterize, control and modify materials properties, create and synthesize new complex materials. This progress is directly linked to man's knowledge in material science.

Why is surface science as important as materials science? Materials are not isolated, they interact with their environment via their surface. Therefore, if the surface properties can be controlled, materials properties can be controlled as well. That is exactly the reason why surface functionalization causes many interests in scientific research since the last two decades. Surface functionalization is the easiest and the most efficient way to artificially control surface properties. When the surface of a material is covered by another material, certain properties will change, for example, steel covered with Tin or Zinc thin film can efficiently resist corrosion.

In surface functionalization, self-assembly is the most employed method. In a self-assembly process, molecules grafted on the surface have an oriented structure and have different collective properties than individual molecule, liquid crystals are a good example where collective properties differ from those of individual molecular properties. However, self-assembly in bulk and at interface must be better distinguished.

The research of self-assembly at interface was carried out many decades ago. For example, in the 30s, the Langmuir-Blodgett films[2], based on the transfer of non aqueous soluble organic molecules from water/air interface to solid/air interface, and in the 80s, the adsorption of fatty acids or organosilanes on the gold or hydrophilic surface by forming a uniform self-assembled monolayers[3] (SAMs).

In the 90s, a new self-assembly method, called layer-by-layer (LbL) assembly was introduced by Decher et al.[4]. This method is based on the alternative adsorption of oppositely charged polyelectrolyte on a charged surface by forming a multilayer thin film. The film construction is based on the charge overcompensation process. When a charged polymer chain is approaching the charged surfaces, some polymer charge sites interact

with those of substrate surface. But some other charge sites interact with small counterions, such as salt, presented in the solution. After the film formation, those counterions associated charge sites can interact with new approaching oppositely charged polymer chains to continue the film growth. A rinse step is introduced after each deposition step in order to remove weakly adsorbed materials and ensure the homogeneity of the formed surface. The principle of this method is demonstrated in Figure 1.

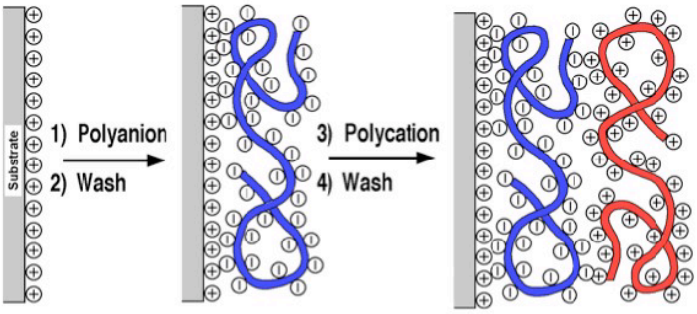

Figure 1: Principle of Layer-by-Layer assembly of polyelectrolyte multilayer

LbL assembly gains rapidly the popularity in scientific research because of its versatility. Not only polymers, but also other components, such as inorganic nanoparticle, micelles, protein, DNA, and virus can be incorporated into film construction. Moreover, interactions employed in LbL assembly are not limited in electrostatic interactions or other weak interactions, such as Van der Waals, hydrogen bonding or strong interactions like covalent bonding can be involved in films build-up process as well.

➢ LbL film growth mechanism, preparation method and structure study

LbL assembled multilayer have three different growth mechanisms, stagnation, linear and super-linear. In stagnation growth mechanism, the film growth stops after certain layer pairs. In most research, continuous film growth is more interested. In linear growth regime, some film properties, like thickness and adsorbed quantity increase linearly as a function of number of deposited polymer layer pairs. So-called super-linear growth regime is based on the fact that some “free” polymer chains are capable to diffuse in and out of the film. Details of these two growth mechanisms will be reviewed later, but in this work, only linearly grown films properties study were carried out.

Similar to LB films and SAMs preparation, the firstly used LbL preparation method, called dipping, consists of alternative introduction of substrate into polymer solution, presented in Figure 2, left. A substrate is dipped into, for example, polyanion solution (blue). After a certain adsorption time, in the order of 15-30minutes (where we try to approach the plateau of adsorption), and rinse step, the substrate is dipped into polycation solution (red) followed by a rinsing. By repeating this procedure, a multilayer can be formed. In 2000, Schlenoff[5] introduced the spraying method, Figure 2, right, where polyanion, and polycation solutions are sprayed onto a vertically set up substrate surface, followed by a rinsing after each polymer deposition. This spray preparation method can accelerate polymers adsorption time from 25 to 150 times depending on the chemical nature of the compounds and the experimental parameters. The typical adsorption time can be as small as a few seconds per layer. A detailed review of these two preparation methods will be discussed later.

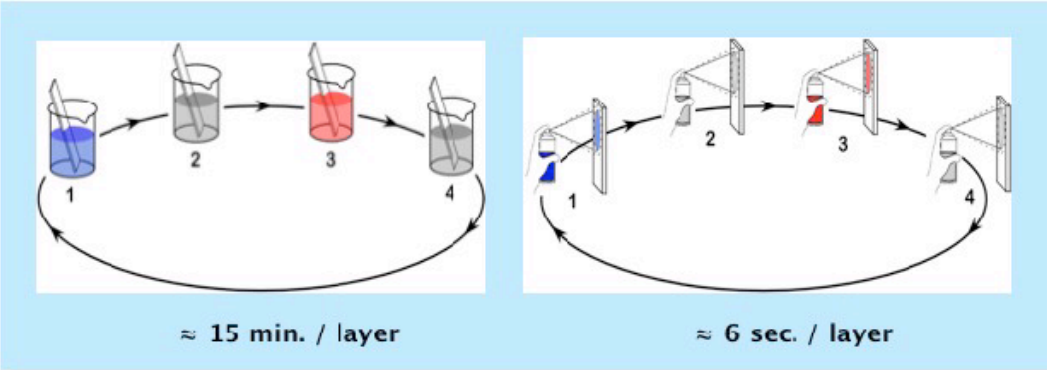

Figure 2: Schematic presentation of LbL dipping (left) and spraying (right) methods

The internal structure of dipped LbL films or functional LbL films were thoroughly studied[6], especially by neutron reflectometry[6,7,8]. The use of neutron, instead of X-ray, ensure a good penetration of investigation beams in the film. And moreover, interactions between neutrons and nucleus instead of those of X-rays and electrons improve the signal contrast. Neutron reflectometry provides enough information on films internal structure. For example, in a LBL films layer structure study by neutron reflectometry, not only Kiessig fringes, same in X-ray reflectometry, but also Bragg peaks, which corresponds to a well organized layer structure will be observed.

In LbL films, every component were layer by layer assembled, but they have a gradual boundary instead of a sharp one between two adjacent layer pairs. In another word, LbL assemble multilayers have a stratified internal structure. However, no similar studies

were carried out in sprayed films, which means that the stratified internal structure was not confirmed in such films.

➢ Introduction of the present research work

There are two major parts in the present work, preparation and characterization of pure polymer films and gold nanoparticle incorporated hybrid films. The first part concerns studies of internal layer structure in sprayed LbL films, precisely poly(styrene sulfonate) (PSS)/ poly(allylamine hydrochloride) (PAH) films by neutron reflectometry, with the collaboration of F. Cousin from laboratoire Léon Brillouin, Saclay, France.

Previous studies in dipped and sprayed $(PSS/PAH)_n$ films by X-ray reflectometry and AFM revealed that dipped films are thicker and rougher than sprayed films[9]. But these techniques did not provide enough information in sprayed film internal structure. In the present work, four samples were prepared and analyzed by neutron reflectometry in order to find if the stratified structure will be observed in sprayed $(PSS/PAH)_n$ films Figure 3. Two reference samples, (Figure 3A and B) composed by PAH layers, in red, hydronated PSS layers, in blue (Figure 3A) and deuterated PSS layers, in yellow (Figure 3B) were analyzed firstly in order to obtain some reference information, such as film increment thickness, surface roughness and a theoretical model. Then, this information was applied to two complicated samples (Figure 3C and D) with different architectures in order to check if they have a stratified structure.

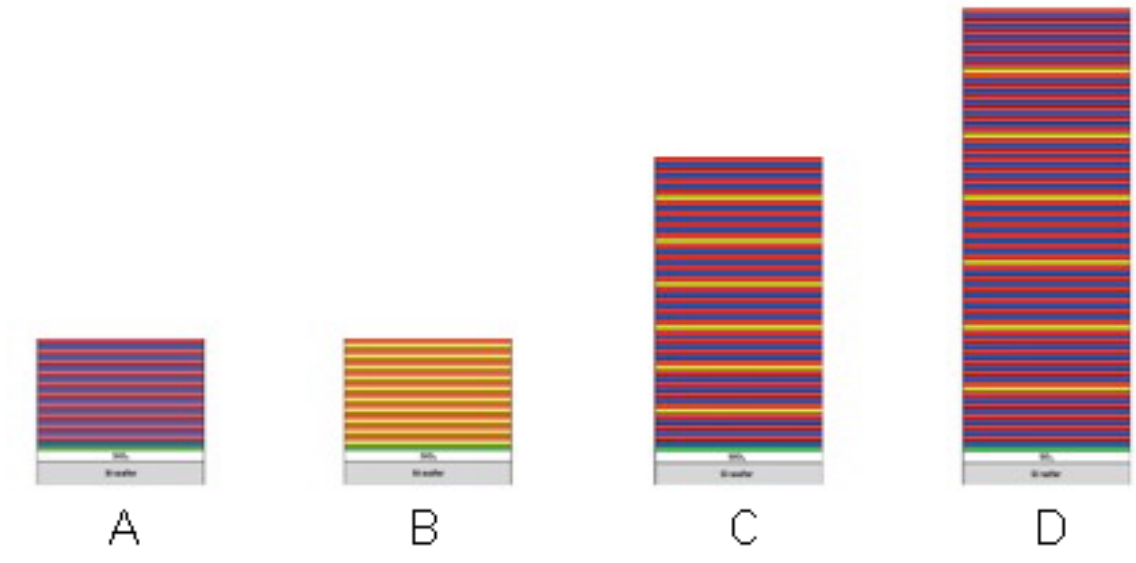

Figure 3: Schematic representation of simplified structure of samples measured by neutrons reflectometry

After sprayed film internal structure studies, a simultaneous spray system was elaborated with the collaboration of BASF (Ludwigshafen, Germany). In this study, optimum conditions for films construction of BASF polymers poly(vinylamine) and poly(acrylic acid, sodium salt) were studied. Film thickness and surface roughness of the best formed film were tested in comparison to those of LbL sprayed (poly(vinylamine)/poly(acrylic acid, sodium salt))$_n$ films. The aim of this study is to speed up film deposition even more by using a simple "simultaneous" spraying approach.

The second part of this thesis is based on the study of functional LbL films based on polyelectrolyte and gold nanoparticle. Construction behavior of this functional films as well as their wear properties improvement were studied.

One interesting property of metallic nanoparticles is their strong surface plasmon band. This surface plasmon band is coming from the electron density fluctuation at metallic nanoparticle surface[10a,10b]. It is well known that nanoparticle have a great surface/volume ration and metallic materials have a great number of "free" electrons (electron clouds) on the surface. In metallic nanoparticle, this exposed electron clouds can be easily influenced by the slightly change of their environment. For example, the excitation of electron density by photon can cause an energy absorption, normally in UV-Visible range. These characteristics mean that the surface plasmon band is extremely sensitive with environment changes. As one of most stable noble metallic nanoparticle, gold nanoparticle have a surface plasmon band at about 520nm to 550nm, according to gold nanoparticle size distribution and polydispersity. Surface plasmon properties of Au NP incorporated thin film are fully investigated, including in LbL assembled films.

Dipped polyelectrolyte/Au NP films were successfully prepared. Film growth mechanism and the plasmon interactions between two adjacent Au NP layers were studied as well[11]. However, in such dipped system, the Au NP surface adsorption needs around 6 hours, which makes its application difficult. Inspired by sprayed (PSS/PAH)$_n$ films, sprayed polyelectrolyte/Au NP films, associated with only electrostatic interactions, were prepared as well. Au NP surface adsorption time can be reduced from several hours to several minutes. Sprayed films construction behavior and surface morphology properties were investigated. Meanwhile, same as dipped films, the plasmon interactions between two adjacent Au NP layers can be successively reduced by increasing the spacing distance between them.

Not only the enormous reduction of Au NP adsorption time, but also the approach to the construction of metal-like films[12] in sprayed films preparation allow potential industrial applications. A study of functional LbL film with Au NP was carried out. Sprayed $(PAH/Au\ NP)_n$ films with at least 40 Au NP layers were prepared and characterized. Since every Au NP layer was separated by one PAH layer, whose thickness is less than 1.5nm, the plasmon interactions influence in such films morphology and Au NP surface distribution were characterized by AFM. During sprayed $(PAH/Au\ NP)_n$ film construction, the substrate surface underwent a violet to a metallic golden coloration transformation after incorporation of 15 Au NP layers. After films preparation, all substrates had a very homogeneous metal-like appearance, Figure 4. The scratch on the right part of the photo is due to the mark of tweezers.

Figure 4: Sprayed $(PAH/Au\ NP)_{40}$ film, (left) and of a sprayed $(PAH/Au\ NP)_{50}$ film, (right)

Then, mechanical properties, most particularly the wear properties of sprayed $(PAH/Au\ NP)_n$ films were studied, with the help of a simple rubbing machine (Figure 5). The mechanical resistance of such films was characterized in term of films thickness and surface morphology variation after different rubbing cycles.

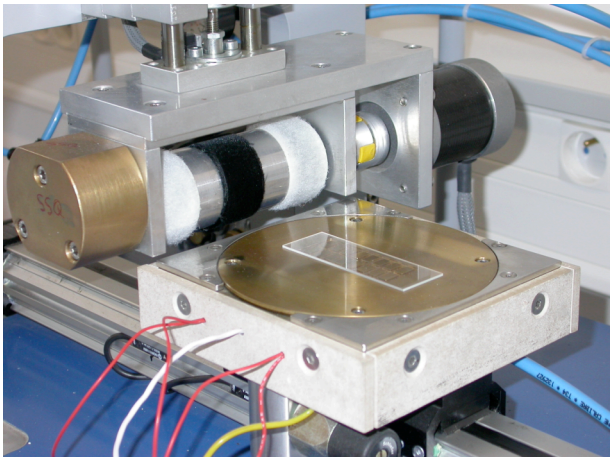

Figure 5: The rubbing machine

This rubbing machine (Figure 5) is a semi-quantitative instrument, there is no information about the exact value of applied shear force during each rubbing cycles. But in each rubbing cycle, every parameters, such as air pressure, the rotation speed of the testing roll, and samples moving speed are kept as constant. As a consequence, one only obtains information on either film stability or film abrasion is as a function of the number of rubbing cycles.

Some Au NP films were mechanically very weak and a covalently linked LbL assembled film was deposited on $(PAH/Au\ NP)_n$ films in order to study their mechanical resistance improvement. Experimental results revealed that this covalently linked LbL films could efficiently protect $(PAH/Au\ NP)_n$ films and moreover, this protection effect is a function of covalently linked LbL films thickness.

To sum up, present work provided an internal structure study of sprayed polyelectrolyte multilayer by neutrons reflectometry. A new surface deposition process, "simultaneous spray" was performed for potential industrial applications. Optimal conditions were obtained in BASF (sprayed $(poly(vinylamine)/poly(acrylic\ acid,\ sodium\ salt))_n$ films) film construction and these films were characterized by ellipsometry and AFM. Besides pure polymer films, polymer/Au NP hybrid films were prepared with spraying LbL technique as well. Films construction, plasmon interactions between Au NP layers and mechanical resistance of these films were characterized as well. Finally, a protection film based on covalent LbL assembly was obtained. This film had an excellent protection effect for polymer/Au NP hybrid films during rubbing tests and this protection effect varies with the thickness of the protection film.

Chapter I. State of the Art

I.1. A brief review of 2D Self-Assembly system: From LB films to LbL films

Some components are capable to form more complicated new objects with unique properties that are not observed in each individual component. Life is a very good example. Atoms form a new molecule, molecules form a new cell, and cells form life. For centuries, man has mastered only a little fraction of object formation on the length scale. Figure 6 presents the different forms of material organization at different length scale. In the last two decades, scientific community is very interested in nano-organization where the length scale varies from nanoscopic to microscopic. This length scale is life's minimum size and also the one that man doesn't fully understand either in bottom up chemical synthesis or top down miniaturization approaches[13].

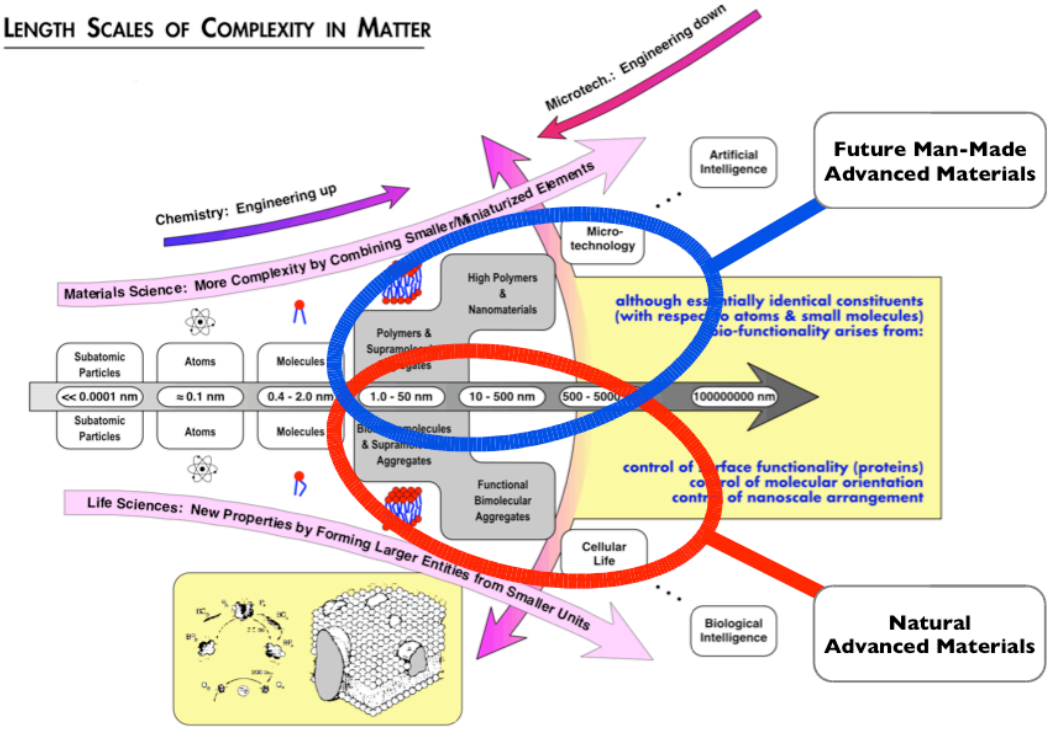

Figure 6: Complexity as a function of length scale. Image extracted from reference 13

Everything in the nature has a certain order and the understanding of the order or the arrangement of the nature and the attempt to fabricate artificially arranged objects started long time ago. Irving Langmuir was one of the founders in artificial molecule assembly system[2a]. Together with Katharine Blodgett[2], they had successfully transferred one or

more monolayers of an organic material deposited from liquid surface to a solid substrate by immersing or emerging it into or from the liquid[2], Figure 7.

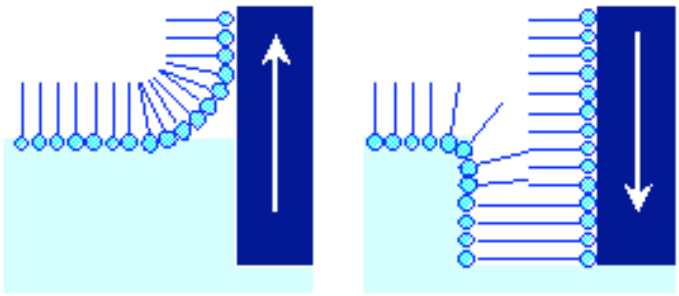

Figure 7: Formation of LB films by immersing the substrate into the solution. Image extracted from http://sci- tech.ksc.kwansei.ac.jp/~ozaki/e_lb.htm

In Lb films, each adsorbed monolayer is homogeneously distributed on substrate surface and the formed film has a very accurate thickness. The film they formed was named as the Langmuir-Blodgett (LB) film. Advantage of LB film is its capability to form a uniform film with variable surface composition. However, the LB film has an instable structure due to weak non-covalent bonding and can be easily contaminated during film preparation, meanwhile, only non aqueous soluble molecules can be used in LB assembly.

An important progress in film assembly was the work of Kuhn[14] during the 60s, by using donor and acceptor dyes in different layers of LB films. However, the LB technique has never been massively commercialized, due to the inaccessibility of experimental instrument and the instability of LB films. Molecules are often not firmly attached on the substrate surface and are rearranged after or even during film preparation.

In the 80s, thanks to the pioneer work of Allara and Nuzzo[3a-h], in which they successfully assembled organosulfur molecules, such as octadecanethiol, and other alkane thiols on gold surface by forming a stable and organized monolayer. They also demonstrated that this monolayer could be assembled on metal oxides surface. Sagiv presented as well the formation of a silane monolayer on silica surface in the 80s[3i]. In the beginning of the 90s, this monolayer was also intensively studied by Ulman et al.[15]. A simplified schema is presented in Figure 8, where organosilanes could be assembled on silicon oxide surface, fatty acids could be assembled on aluminum oxide surface and thiols could be assembled on metal surface.

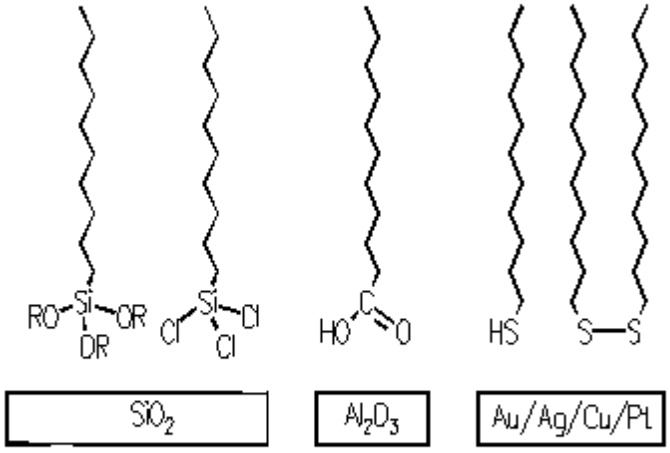

Figure 8: Simplified schema of self-assembled monolayer on silicon oxide surface (left), on aluminum oxide surface

(middle) and on metal surface (right). Image extracted from www.physics.uwo.ca/~smittler/surface.html

The formation of this compact monolayer on solid surface represents the notion of Self-Assembled Monolayers (SAMs). This notion refers to a process in which molecules are spontaneously formed with ordered structure. SAMs provides flexibility in both molecular and material design level and offers the possibility to create molecular complexity on the structure and stability of two-dimensional assemblies. Moreover SAMs are highly ordered and oriented films and their highly dense and stable structure ensures the potential applications. SAMs technique is a very convenient surface functionalization method and has been widely used since 1990s. Whitesides[16,17,18] pointed out some advantages of SAMs. First of all, it is very scientifically interesting as it is the simplest imitation to life form. SAMs provides the arrangement of molecules with regular structures. In a SAMs process, not only small molecules, but also larger components can be involved. SAMs is one of the most generating and promising strategies for obtaining nanostructure.

However, SAMs has a limited surface functionalization versatility, because its preparation is limited in thiols on gold substrate or silanes on hydroxylated surfaces. And the quality of formed films depends on substrate quality. During a SAMs formation, substrate defaults may deteriorate the films' quality. The formed layers have a limited stability, for example, they are unstable to oxidation. Despite these disadvantages, SAMs preparation is one of the most commonly used surface functionalization methods since the 90s and are widely used nowadays.

In 1997, Decher et al.[19,20,] introduced a new self-assembly method based on the alternating sequential adsorption of oppositely charged polymers, the so-called Layer-by-Layer (LbL) technique, where each adsorbed component interacts electrostatically with the other components. This technique was firstly used in the middle of 60s by Iler[21], in inorganic colloid particles self-assembly. Due to its simplicity and accessibility, LbL technique quickly attracted many research teams concern. This technique is very robust and environmentally friendly, while requiring inexpensive experimental instruments. Moreover, it provides an easy way to incorporate new combinations of molecules and other functionalities into a layered system, when the design of new materials with a greater complexity is a widely studied scientific subject. LbL technique can create multi-material composites in a very simple way while traditional synthesis is impractical by putting large functions together in the synthesis of multifunctional materials. In a word, LbL technique is a real versatile multifunctional coating method available for surfaces of almost any kind and any shape. Thanks to its advantages, during last ten years, reported publications in this filed have grown considerably.

I.2. An introduction of Polyelectrolyte Multilayer and Layer-by-Layer Self-Assembly technique

I.2.1. An overview of Layer-by-Layer Self-Assembly technique

Compared to traditional self-assembly techniques, LbL technique is a fast template assisted assembly technique. The assembly of several components in the same spatial arrangement can be achieved without any further chemical modification of these components' functionalities. Under weak interactions, basically electrostatic interactions, the assembly of multifunctional materials can be easily controlled and tailored. However, the involving interactions in LbL assembly are not limited in electrostatics, other interactions such as donor/acceptor[22], hydrogen bonding[23,24], even strong interaction like covalent bonding[25,26], are possible. Furthermore, not only polyelectrolye but also inorganic compounds[27,28,29], macromolecules[30,31], biomaterials[32,33,34,35], colloid[36,37,38,39] or even fibers and cellulose[40,41,42,43] can be incorporated in LbL assembled films. These characteristics make LbL very convenient for the design of even complicated structured multifunctional materials.

In LbL assembly process, each corresponding component is adsorbed in a single step, and after whole assembly construction, films have a defined sequence. Therefore, LbL assembly can be considered as a sort of multifunctional synthesis by using mostly weak interactions. In a traditional chemical synthesis, each reagent is used in each reaction

steps and a given structured molecule or other products are obtained. Similar to chemical synthesis, in LbL process, only one specie is involved in the single step of adsorption and finally, a multilayer with perhaps different participating species but with strictly defined sequence even structure can be obtained. LbL assembly can be applied to any solvent accessible surface and a surface coating even for objects with a surface of several square meters is possible.

Like in chemical synthesis, the structure and properties of LbL assembled films depends on many parameters, which will be discussed in following sections. During LbL films construction, many routine analytical instruments can monitor films build-up procedure. For example, UV-Visible spectroscopy can efficiently monitor multilayer build-up with at least one colorful participating material. Ellipsometry and reflectometry methods (X-ray and Neutrons) can provide enough information in film thickness and surface roughness variation. And quartz crystal microbalance (QCM) provides film growth mechanism, while surface plasmon spectroscopy provides interactions in LbL films[44,45].

A variation in ways of LbL films deposition is another example of its versatility. Dipping is the most common preparation method introduced by Decher in his early work[19,20] and it still is the mostly used method. In 2000, Schlenoff[5,46] introduced spraying as a new LbL deposition method and spin-coating[47,48,49] is used in LbL deposition as well. Compared to dipping deposition, both spraying and spin-coating depositions require only a small amount of liquid for the surface coating. The differences in preparation methods influence the structure and properties of LbL assembled films.

I.2.2. Polyelectrolyte multilayer formation, films construction and structure

I.2.2.1. Polyelectrolyte multilayer formation: Mechanism and the three-zone model

In early days of LbL assembly, questions like why a multilayer is stable were frequently asked. When the substrate with pre-adsorbed film is in contact with oppositely charged polymers solution, why these counterpart polymers will get adsorbed onto the substrate by forming a new layer instead of stripping off the pre-adsorbed layer? In LbL assembly, every component is "trapped" in multilayer by electrostatic interactions. Adsorbed polymers in one layer do not have enough time to achieve their equilibrium state before the adsorption on another layer on the surface, meaning that LbL assembly is an irreversible dynamic self-assembly process. The irreversibility of LbL multilayer leads to a considerable stability with time. This stability is only for strong polyelectrolyte and

certainly not for super linear growth systems, which will be discussed later. In general, smaller molecules are easier exchanged or displaced than large ones, the use of polymers in LbL self-assembly leads to films stability improvement comparing to LB films or SAMs.

Several theoretical treatments[50,51,52,53,54] predicted that the formation of LbL multilayer is thermodynamically favorable. The group of Jonas and Laschewsky[55] pointed out that entropy, instead of enthalpy or free energy in most cases, is one of the primary driving forces of LbL multilayer assembly. In solution, charged polyelectrolyte chains are surrounded by small counterions (salt). When the complexation between polication and polyanion takes place on a charged surface, most of these counterions are not capable to associate with polyion complex. The repulsion of these dissociated couterions increases the entropy of the system. Moreover, the liberation of solvent in polyions complex may lead to an additional entropy gain in LbL assembly.

However, the surface charge overcompensation during LbL assembly is the major driving force to ensure a successful film build-up. Presented in Figure 1, a positively charged substrate is in contact with polyanion solution and the long-range electrostatic force of the charged substrate will attract polyanion to get adsorbed on the surface, and the amount of adsorbed polyanion depends on the surface charge density. After a certain adsorption time, the substrate is rinsed in order to remove weakly associated polyanion on the surface and then the substrate is negatively charged. The substrate will again be in contact with polycation solution and the same procedure will happen. By repeating these polyanion and polycation adsorption steps as well as their corresponding rinse steps, a multilayer film can be built up.

If the surface charge has been overneutralized on each adsorption step, how such a multilyer structure can be constructed? The film build-up should have stopped after the first layer adsorption. The notion of intrinsic and extrinsic charges introduced by Schlenoff[56,57] provides an answer to this question. Considering a diluted polymer solution as presented by Barrat and Joanny[58], the conformation of polymer chains will be Gaussian if the charge is low and electrostatic interactions do not play a role. If the charge is high, polymer chains will be stretched by repulsive forces between monomers and polyelectrolytes in solution has such conformation. However, polyelectrolyte chains are not isolated in solution, some oppositely charged salt counterions are also presented in solution and associated with polyelectrolyte chains.

During the surface charge overcompensation or the polyions complexation in a LbL assembly, some counterion of both polyanion and polycation will be repulsed from the complex. Liberated charge sites of polyions will lead to the complexation and repulsive counterions will increase the entropy of the system, making LbL assembly thermodynamically possible. However, there are still some counterions associated with polyions and temporarily "frozen" in polyions complex. Charge sites compensated or overneutralized by oppositely charged polyelectrolyte are intrinsic charge sites while those compensated by couterions or other charged molecules are extrinsic charge sites. These extrinsic charge sites can be liberated again when a charged polyelectrolyte chain is approaching polyion complex. The extrinsic charge sites are responsible for charge overcompensation as the primary driving force in a polyelectrolyte multilayer build-up.

Suggested by Decher et al.[59,60], a three zone-model can describe the formation of polyelectrolyte multilayer (Figure 9). A well-formed polyelectrolyte multilayer is composed of three distinct zones. Zone I is composed of one or few polyelectrolyte layers close to the substrate. Zone III is composed of one or few polyelectrolyte layers close to the surface of the film. Zone II is the "bulk" film between Zone I and Zone III and the property of this zone is not influenced by either substrate or air.

In most cases, chemical composition and structure of these three zones are different. Zone II is globally neutral while zone I and III are normally charged by different numbers of extrinsic charge sites. Although zone II is neutral, some counterions can be founded. As a result, even polyelectrolyte with 1:1 stochiometric formation capability might not able to realize a 1:1 stochiometric charge overcompensation. Charge density in Zone III is more important than in Zone I because Zone III is responsible for further polyelectrolyte adsorption, charge overcompensation and film growth, meaning that counterions are ubiquitous in Zone III. The omnipresence of counterions indicates that the border between different zones is not sharp. Individual polymer layers are rather strongly intermingled with neighboring layers, even layers further away from the surface will contribute to the surface charge excess. This is the "fuzzy" notion introduced by Decher[4]. The structure of polyelectrolyte multilayer is not perfectly defined as a crystal, but it is not completely disordered either. There is positional order between molecules, but not between atoms.

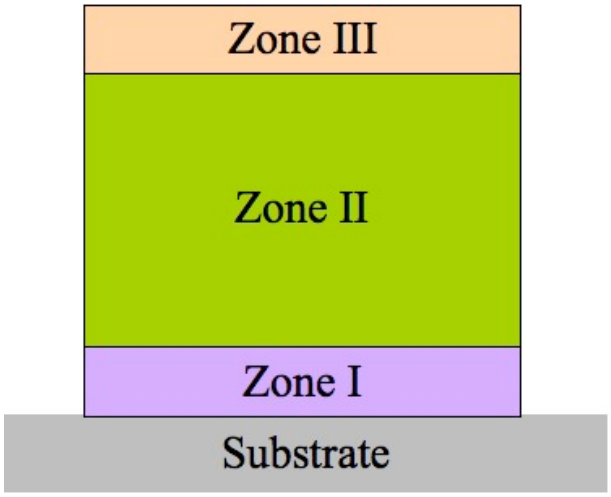

Figure 9: The three zones model for polyelectrolyte multilayer. Interfaces between different zones is diffuse rather that a sharp plane.

The number of layers belong to Zone I and III respectively should be a function of many parameters, such as substrate, chemical structures of polyions complex and deposition method and/or conditions, but the exact number remains unknown as of today. This three zone-model is only valid in polyelectrolyte multilayers with a sufficient number of layers deposited. Detailed film formation is presented in Figure 10.

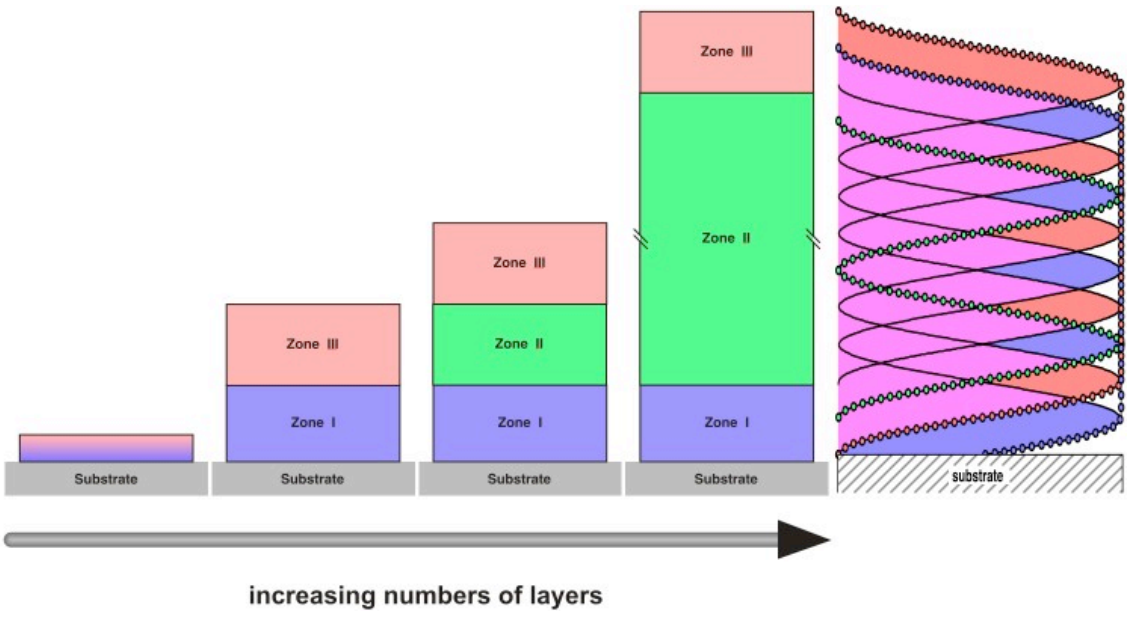

Figure 10: The zone model for polyelectrolyte multilayer. The part of the schematic above the arrow shows the development of zones during film deposition. The first layer pair is shown on the left and a film consisting of several layers is shown on the right. Once all three zones are established only Zone II grows with increasing number of layers[60]. On the very right is depicted how the three zones can be correlated with model consisting of individual but strongly overlapping layers. Image extracted from reference 12.

In the three zones model, zone II will only be formed when both Zone I and Zone III have reached their final chemical composition and thickness. More polyelectrolyte deposition and polyions formation will not change the thickness of Zone I and III, especially the latter, only thickness of Zone II will increase. As mentioned previously, the border of these three zones is not sharp but gradual and there is probably a chain diffusion between different zone interface. When more polyelectrolytes have been deposited on the surface, newly formed polyions complex will increase the distance between polymers at the interface of Zone II/III and the surface. Influences of these polymers at the interface to the outermost surface will be decreased as well. These polymers will now be considered more likely to be a part of Zone II instead of formerly interface situated polymers. These formerly interface situated polymers will successively embedded in zone II when more layers are added by keeping the thickness of Zone III as constant. Polyelectrolyte multilayers thickness increase corresponds in fact to the film growth of Zone II. This "transition" character during multilayers construction also defines the notion of "fuzzy" and makes borders between each zone gradual. Polymer chains interdiffusion at each zone interface level, presented on the very right part of Figure 10, is possible, diffusion in the whole film will be discussed later.

Even though the exact structure and composition of these three zones are not clear, the difference between charged Zone I/III and "neutral" Zone II influences the physiochemical behavior of the whole polyelectrolyte multilayer. Charged Zones I and III, especially Zone III, where film growth occurs only on the top of this zone, acts more like individual polyelectrolyte during a film build-up process while "neutral" Zone II is not so active in film construction. An attention should be paid here, the inactivity of zone II is only valid for linear growth film. In super linear growth film, polymers can diffuse into zone II, and in this case, zone II is a "reservoir" for these mobile polymer chains. The behavior of this "reservoir" of polyelectrolyte film will be discussed in the section of polyelectrolyte film growth regime

Even zone II is "neutral" and inactive in a global way, many different chemical compounds can diffuse "into" a film at high "outside" concentrations. The swell/deswell tendency of certain polyelectrolyte multilayer in the presence of salt in the solution, discovered by Decher[61] is a good example and will be discussed later.

I.2.3. Key parameters in polyelectrolyte multilayer formation

The polyelectrolyte multilayer formation and structure are controlled by many parameters such as ionic strength or salt concentrations[57, 62,63,64,65,66,67], pH[68,69,70,71], Deposition temperature[72,73], films properties like water distribution in multilayer[73,74,75,76] will be influenced by these parameters as well. Only influences of ionic strength and pH will be discussed here because these two parameters will directly control the charge density distribution of polyelectrolyte and the charge overcompensation process.

In the simplest case of a stoichiometric system, the entropy gained from releasing the counterions is the most important driving force of LbL film formation. And the charge overcompensation, caused by extrinsic charged sites, is responsible for continual film growth. The charge overcompenation process of a stoichiometric system in zone III will be discussed in the following.

The adsorption of polyelectrolyte onto an oppositely charged surface is like ion exchange phenomena[77] with salt ions presented both in solution and in film, especially in zone III. However, the difference between LbL films assembly and ion exchange is that in LbL films assembly, polyeletrolyte chains are not free to leave the assembled film matrix. The adsorption of polyelectrolytes on the surface and formation of multilayer can often be assumed to be an irreversible process.

The polyelectrolyte complex formation including the process of complex formation at interfaces can generally be explained by[63]:

$$Pol^+I^- + Pol^-I^+ \rightleftharpoons Pol^+Pol^- + I^+I^- \qquad \textbf{Equation 1}$$

in which I^- denotes an anionic and I^+ denotes a cationic counterion, Pol^+ and Pol^- are corresponding polycation and polyanion. Pol^+Pol^- are formed polyion complex and counterion pairs I^+I^- are typically highly solvated and only weakly associated.

Similar to a chemical reaction, the constant of association K for polyion complex formation can be presented by Equation 2:

$$K = \frac{\left[Pol^+Pol^-\right]\left[I^-I^+\right]}{\left[Pol^+I^-\right]\left[Pol^-I^+\right]} \qquad \textbf{Equation 2}$$

From Equation 2, we can clearly observe that the formation of polyelectrolyte multilayer as well as stability of formed film is strongly controlled by salt concentration $\left[I^{+}I^{-}\right]$ in the film. For example, a higher salt concentration corresponds to an large value of K, but this higher salt concentration leads the Equation 1 to the dissociation direction. In a LbL films formation, salt concentration plays an important role in the polyion complex association/dissociation competition. Salt concentration influence as well some properties of LbL films, such as thickness and surface roughness[62].

Besides ionic strength or salt concentration, pH value can influence LbL film formation as well. In a polyelectrolyte multilayer construction process, some polyelectrolyte are fully charged like poly(styrenesulfonate, sodium) so called PSS, characterized as strong polyelectrolyte. But there are also some polyelectrolytes are partially charged, such as poly(allylamine hydrochloride) so called PAH and poly(acrylic acid) so called PAA, characterized as weak polyelectrolyte. In the film construction by using at least one weak polyelectrolyte, the pH value will influence film formation because the pH adjustment controls the degree of ionization of weak polyelectrolyte in both solution and multilayer. For example, the presence of an abundant cationic groups will increase the degree of ionization of PAA[70]. On the contrary, fully charged strong electrolytes will not be influenced by pH value during film construction. As ionic strength, the pH adjustment will control polyelectrolyte behavior. Ideally, the pH is optimally adjusted when 50% of the polymer's functional groups have been ionized according to different pKa of individual polyelectrolyte[70].

In the example of PAA/PAH films[70] construction, the film thickness can be adjusted by changing pH value. At neutral pH, assembled polymer pairs have a thin film thickness indicating that PAA is acting as fully charged polyelectrolyte. While at a higher (>8.5) or lower pH value (< 5.5), assembled polymer pairs thickness is ten times thicker than at neutral pH value with a partially charged PAA. pH value adjustment can also cause the swelling/deswelling effect of polyelectrolyte multilayer, which corresponds to a thick films growth regime and eventually lead to films decomposition[71] or dissociation of the film[78].

I.2.4. Different polyelectrolyte multilayer growth regime: linear and super linear growth

During a polyelectrolyte multilayer build-up process, most polycation/polyanion combinations demonstrate a linear film growth regime, in term of film thickness measured by ellipsometry or adsorbed mass as measured by QCM. For example, in this growth regime, films thickness increases linearly as function of deposited layer pairs. The mechanism of this growth regime can be easily explained by using the LbL self-assembly scheme presented in Figure 1. After or during film construction, adsorbed layer pairs have been kinetically trapped by electrostatic interaction and they are fixed in film matrix although some polymers interdiffusion is expected at different zones interface. But a free diffusion of polymer chains in the whole film is impossible. Each adsorbed layer pair will contribute to the film thickness and quantity increase.

However, since 2002, this linear growth regime has not been observed in certain polyelectrolyte systems[79,80,81,82,83,84,85,86,]. After a few layer pairs deposition, the film has a super-linear growth behavior which has been frequently observed in weakly charged polyelectrolytes self-assemble such as poly(L-glutamic acid) so called PGA, poly(L-lysine) so called PLL, hyaluronic acid so called HA, PAA, polysaccharide etc. The mechanism of this super-linear growth regime can be interpreted by a diffuse "in" and "out" theory of "free" polyelectrolyte chains in the multilayer suggested by the group of Schaaf[84,85,86].

A theoretical model suggested by Lavalle et al[86] can explain mathematically this "in" and "out" diffusion phenomena. Laugel et al[87] suggested a semi-theoretical model for the prediction of which polyelectrolyte couples will have a linear or super-linear growth regime during the multilayer construction

The super-linear growth regime is frequently observed only after several layer pairs deposition, normally less than 10 layer pairs. If deposition cycles continue, a linear growth regime will be observed after certain layer pairs deposition cycles, normally over 15 or 20 layer pairs, or even more[88,89,90]. However the mechanism of this super-linear/linear transition is not clear yet.

In this manuscript, films with only linear growth were studied and characterized.

I.2.5. Structure of polyelectrolyte multilayer

The three-zone model of polyelectrolyte multilayer formation suggests that polyelectrolyte multilayer have a gradual border between different zones instead of a sharp border. Polylectrolyte chains at each borders interface are more or less interpenetrated. Have polyelectrolyte multilayer a real layered structure or does polyelectrolyte chain interpenetration cause perfectly homogeneous mixing? To answer this question, specular X-ray and neutron reflectivity measurements are employed in polyelectrolyte multilayer structure characterization. These two instruments are widely used in the structural characterization of films[7,91,92,93].

In X-ray reflectivity studies, electron density in the normal direction will be analyzed. Kiessig fringes, derived from the destructive interference between reflected beam from air/film interface and film/substrate interface, can be observed[94,95,96,97] for smooth films. However, X-ray reflectivity measurement can not reveal the internal layer structure of polyelectrolyte multilayer, represented by Bragg peaks. The absence of Bragg reflexes in X-ray reflectivity measurement can be explained in two ways. Either the stratification in multilayer is not sufficient enough for adjacent layers to interdigitate or the electron density contrast of individual layers is not large enough[98].

On the contrary, in neutron reflectometry studies, the scattering length density (SLD) profile perpendicular to the surface will be analyzed. This SLD profile can be interpreted by a "box" model with a specific value for thickness, roughness and density attributed to each box. Besides Kiessig fringes, Bragg peaks have been observed by several groups[99,100101,102,103] for films containing individual layers of deuterated polymers. These Bragg peaks indicate a well-defined stratified multilayer structure, corresponding to a super lattice structure in normal direction, with more or less interpenetration of adjacent layers not only in different zones border but also in the whole film.

I.2.6. Comparison of preparation methods: dipping, spraying and spin coating

Dipping, spraying and spin coating are the three major preparation methods used in LbL assembly. Since the use of spin coating is limited in both substrate's size and planarity, dipping and spraying are two most frequently used preparation methods.

Similar to the LB adsorption, dipping is the first preparation method used in polylectrolyte multilayer construction. The substrate is brought into contact with

polyelectrolyte solutions. After a certain adsorption time, polymer chains will diffuse from bulk solution to the surface and get adsorbed. The necessary adsorption time for a single layer pair varies from 20 minutes to 60 minutes in different systems.

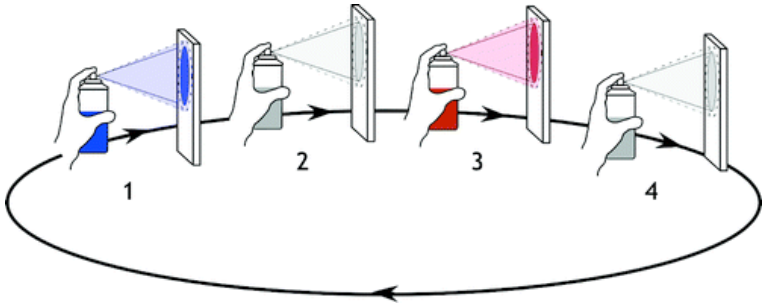

Figure 11: Simplified spray process

Schlenoff[5] and Winterton[104] introduced a new preparation method "spraying" respectively in 2000 and 2004. This method can accelerate the adsorption time with a factor of 25-150[9]. In fact, spraying is much more that a technology used for dispersing liquids in air or to point objects. One can consider spraying as a very powerful method to bring a surface into contact with a liquid producing a very homogeneous liquid film at the interface. It is thus extremely well suited for LbL-assembly, especially for the homogeneous wetting of large or uneven surface.

In the spraying process, substrate is vertically set up and liquid is horizontally sprayed onto the substrate. Once liquid reaches substrate surface, drainage caused by gravity will ensure the liquid coverage on the surface (Figure 11, step1). Because of the vertically installed substrate and the gravity-induced drainage, weakly adsorbed polymer chains are difficult to attach the surface. Nevertheless, a rinse step is necessary to remove weakly adsorbed polyelectrolyte on the surface. Rinse solution is sprayed onto the substrate and an additional waiting time is necessary for the drainage of rinse solution (Figure 11, step2). After the rinse step, oppositely charged polymer solution can be sprayed again onto the surface (Figure 11, step3), followed by another rinse step (Figure 11, step4).

Nowadays, many groups[9,105,106,107] work with sprayed LbL self-assembly and comparisons between dipping and spraying have been ascertained. Generally, confirmed by X-ray reflectometry and AFM analysis, sprayed polyelectrolyte multilayer is thinner but smoother than dipped ones[9]. But Kolasinska et al[105] found out that sprayed polyelectrolyte multilayer is thinner but rougher than dipped ones, even with the same polyelectrolyte couple (PSS/PAH). According to Izquierdo[9] and Kolasinska, it is because

the $(PSS/PAH)_n$ films are not prepared under the same conditions. As explained before, different physiochemical conditions will influence the structure and properties of polyelectrolyte multilayer.

A thinner film in spraying preparation is partially due to the reduced spraying contact time (typically several seconds)[9]. But reasons why sprayed film is thinner is still unknown. Some controllable and uncontrollable parameters in spraying LbL assembly[9] can also explain this phenomenon. Examples of controllable parameters include spray distance, spray volume, concentrations of polyelectrolyte while droplet size, droplet speed and speed distribution during spraying process, concentrations of polyelectrolyte in droplets are examples of parameters that are not easy to control.

As mentioned before, polyelectrolyte multilayer structure and properties can be influenced by many factors, and all structural analysis results demonstrated in previous sections are based on dipped prepared films. Does the difference in preparation method change the structure of polyelectrolyte multilayer? Does the shear force during spraying preparation remove not only weakly adsorbed polymer but also a part of well-adsorbed films? Is this removal the reason behind the thickness diminution in sprayed films? Does it induce a loss of stratified structure in sprayed polyelectrolyte multilayer? All these questions will be discussed in the section of sprayed LbL films layer structure analysis by neutron reflectometry.

I.2.7 Beyond consecutive assembly steps: simultaneous "one-step" spraying

Besides LB films, SAMs and LbL films, it could be desirable to simplify surface functionalization even more. Hubbell et al[108] reported a simultaneous spraying films formation composed of polyelectrolyte without details in films formation mechanism and films structure investigation. Hiorth et al[109] also reported a simultaneous spraying polyelectrolyte films formation on a rotating cylinder. But during such formation procedure, films are constantly dried and salt or other substance presented in aqueous solution can not be removed from the formed films. By applying spraying procedure of polycation and polyanion at the same time should be a promising method to perform a one step functionalization process. In 2005, Porcel et al[110] reported a new simultaneous spraying method, in which traditional spraying instrument set up was used, presented in Figure 12.

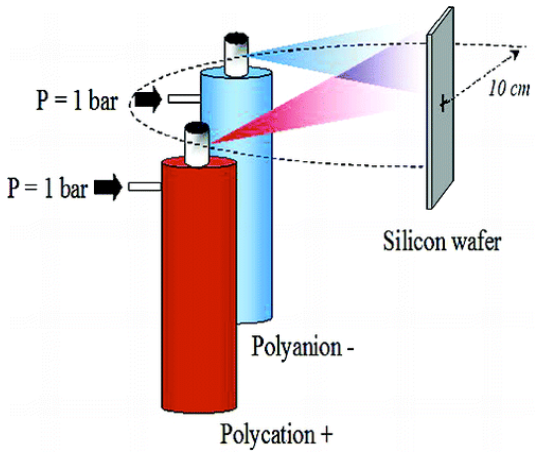

Figure 12: Experimental set up for simultaneous spraying films formation. Image extracted from reference 110.

Other than alternatively adsorption in LbL self-assembly, polycation and polyanion solutions were sprayed at the same time to the surface in a simultaneous spraying procedure. Reported by Porcel et al[110], a linearly grown (PGA/PAH) film was obtained with this simultaneous spraying process, although a typical super-linear growth regime for such film is observed in LbL self-assembly. In a simultaneous spraying process, important controlling parameters are polyelectrolyte concentrations, spraying rate, spraying time, adsorption time and rinse time.

Porcel et al[110] proposed a film formation mechanism for simultaneous spraying process. In a polyions complexation, there exists a characteristic time τ when all charged groups of a polyelectrolyte interact thoroughly with groups of oppositely charged polyelectrolyte. When a polycation is spayed onto a negatively charged surface, it will interact immediately with polyanion on the surface. After this characteristic time τ, polyions complexation can be considered as complete. But if during the time τ, another polyanion is sprayed again to the surface, it will also interact immediately with polycations already presented on the surface, even though the complexation between polycation and former adsorbed polyanion is not completely finished yet. If polyelectrolyte spraying time interval is within this characteristic time τ, the film formation process should be continuous and simultaneous.

They also explained that the unusual linear growth regime of (PGA/PAH) film is due to the steady-state conditions caused by constant spraying conditions and a further deposition of sprayed LbL film is totally possible on the top of such simultaneous sprayed film. However, difficulties in simultaneous spraying process are the lack of precisely parameters control in film formation and the possibility to apply this method to

other polyelectrolyte pairs. But simultaneous spraying is to be a promising method in a one step functionalization by combining different components.

I.3. Functional LbL films containing layers of inorganic nanoparticle

I.3.1. Inorganic nanoparticle (NP) and their assembly-assembly

The fabrication of nanodevice with variable properties and applications requires often multifunctional materials. The assembly of nanoparticle (NP) and polymer is one interesting case. Nanoparticle present some very interesting properties between those of individual atoms or molecules and those of bulk materials. By reducing the size of a material to microparticle, then to nanoparticle, some new properties that bulk materials do not have will show up. For example, semiconductor nanoparticle will have some new energy level[111]. Inorganic metallic nanoparticle will present some new properties in electronic[112] and optical[113] fields. Nanoparticle great surface area to volume ratio will lead to special interests in catalysis[114] etc.

The attempt of nanoparticle assembly, especially inorganic nanoparticle, started decades ago. LB technique can successfully assemble NP in a transferable monolayer. However, the application of LB assembled NP layers is limited due to their poor stability after preparation, and loss of long range order caused incompatible surface energies during the transfer of a large area layer to other substrate[115].

One advantage of LbL self-assembly process is its possibility to merge different functionalities of its component. Assembled layers properties can easily be controlled by the sequence of deposition layers and tailoring of individual component properties. The pioneer work of Iler[21] in LbL self-assembly lies alternatively in assembly of oppositely charged silica and alumina colloid particles and the estimation of film thickness according to interference color. After gaining popularity in 90s by Decher's work[4], LbL self-assembly has been considered as a convenient method for a variety of thin film device fabrication composed by NP and other related materials. Kotov[13] has pointed out several advantages in NP assembly by using LbL method. First of all, LbL technique is a universal deposition technique for nearly any aqueous dispersed NP steady film build-up assembly. LbL coating produces highly homogeneous and stable films with precise lateral NP packing control. The possibility to combine with other functional materials leads to a palette of multifunctional nanostructured materials[116].

Typically, inorganic nanoparticle refer to crystallites of inorganic materials with a diameter varying from 1 to 100nm. After synthesis, NP are normally dispersed in colloid solution and surrounded by organic molecules or polymers acting as stabilizer in order to avoid NP precipitation and aggregation. Therefore NP are not "naked" particles. NP assembly abilities mostly depend on this outmost layer's properties. According to this layer's chemical property, a matching polyelectrolyte can be found out. There are two assembly methods in NP/polymer films build-up. One is similar to traditional LbL assembly. After synthesis, NP will act as an individual component in LbL assembly process. This method is the mostly used routine assembly method in NP incorporated films fabrication. The other method is called "one-step assemble"[117,118,119]. For the desired NP, corresponding metal ion dispersed in colloid solution will be assembled with matching polyelectrolyte and the NP synthesis will be carried on in the film after assembly. This method has not been widely used because salt or other substances present in colloid solution cannot be removed after film construction.

NP is usually visibly colorful and the assembly process can easily be monitored by UV-Visible spectroscopy. NP corresponding absorption intensity should increase linearly with the number of deposition cycles. The distribution of NP in macroscale is quite homogeneous and after enough deposition cycles, the substrate will be homogeneously colored. Many groups work currently on NP/polyelectrolyte LbL assembly. Lvov et al [120] successful assembled ordered SiO_2, CeO_2, TiO_2 incorporated films. Salgueirino-Maceira et al[121] assembled silica coated Au or Ag NP with tailored optical properties. Lvov et al[122] assembled gold coated cobalt magnetic NP films. Farhat et al[123] fabricated a new type of thin-film electrode based on carbon colloid dispersion LbL assembly. Dotzauer et al[124] reported a catalytic membrane based on metallic NP assembly and even NP containing free standing film have been prepared as well[115,125,126,127]. The ultra strong films based on clay/polymer LbL assembly, was also reported by Kotov et al.[127,128]. This ultra strong film is comparable to natural nacre and lamellar bones.

Abu-Sharkh[129] reported the mechanism of NP/polyelectrolyte LbL self-assembly process based on molecular dynamics simulation. When a polycation is adsorbed on the negatively charged surface, the polymer chain has three different conformations: train, loop and tail, as presented in Figure 13. Train is the polycation chain part attached on the surface while tail and loop extend into the solution because of the electrostatic repulsion.

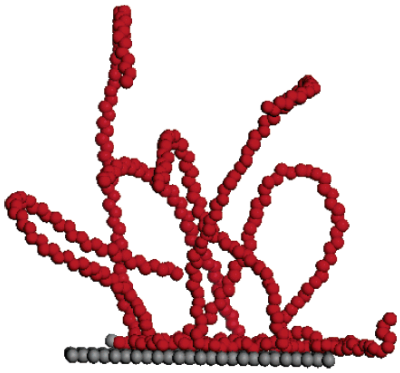

Figure 13: Structure of adsorbed polycation on surface with three conformations. Image extracted from reference 129.

In the next NP adsorption step, tails will firstly capture approaching NP and get adsorbed and folded on its surface (Figure 14a). Once NP are trapped by tails, either NP will pull polycation from the surface (Figure 14b) or polycation will pull NP toward the surface (Figure 14c), the dominant mechanism depends on the strength of anchor points between polycation's train parts and surface. Since NP adsorption is an irreversible process, NP should be pushed toward the surface. Strongly anchored polycation chain starts folding around NP and brings it gradually to the surface (Figure 14d). Some small NP aggregates can be found during this procedure but can be removed in rinse step. Briefly, the adsorption of NP consists of the capture of NP by polymer chain and gradual folding or approach to the surface. A second polycation layer's adsorption can be similarly preceded. One or both end of polymer chains will reach adsorbed NP surface or uncovered substrate surface, followed by gradual folding or approach to NP surface and so on, alternative NP/polyelectrolyte adsorption continues. In addition, NP is organized not only parallel but also perpendicular to the surface because some of them are bridged together by polyelectrolyte, both in solution and on the surface. After an equilibrium time of 100ns, a highly ordered NP/polyelectrolyte system in which NP are assembled in well-defined layer will be formed.

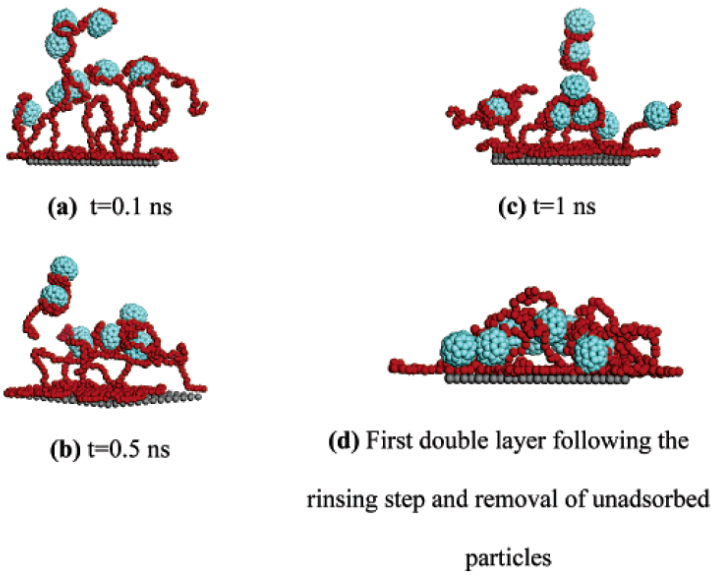

Figure 14: Mechanism of first NP layer deposition. Image extracted from reference 129.

I.3.2. Gold nanoparticle (Au NP) and their assembly

Since the pioneer work of Mie[10a], Maxwell-Garnett[10c,10d] and Debye[10e], Properties of metallic micro- or nanoparticle, especially noble metallic particles such as silver and gold, cause a great interest in scientific research. As one of stable metallic nanoparticle, the use of colorful aqueous solution of gold colloids can be traced back to Roman time[130]. The notion of gold nanoparticle was introduced by Faraday[131] in 1857 for the first time. At present time, the mostly used gold nanoparticle routine synthesis is the citrate reduction of $HAuCl_4$ precursor in aqueous solution, reported by Natan et al[132]. Synthesized gold nanoparticle are stabilized and surrounded by negatively charged citrate ions.

In many nanoparticle preparations, NP has insufficient dispersion stability while gold NP is enormously stable. Therefore, gold nanoparticle plays an important role in multifunctional materials fabrication[133,134]. Nowadays, gold nanoparticle are also highly involved in LbL self-assembly. Decher et al[135] reported a linearly grown Au NP/polyelectrolyte LbL assembled multilayer. They also found that the average Au NP surface coverage is around 30% although AFM analysis indicates a fully Au NP covered surface.

One distinguishing property of Au NP is its strong surface plasmon interactions, which the existence was discovered by R.H. Ritchie[10f] in 1957. A metal atom is surrounded by a large number of conduction electrons, these electrons are less linked to the positive

nucleus and can be considered as "free" electrons. These free electrons can be easily excited by a magnetic or an electric field, for example the light wave with a corresponding energy adsorption in ultra-violet or visible range. The notion of plasmon corresponds to this oscillation or the excitation of the free electron gas density against the fixed positive ions in a metal. The plasmon energy can be described by using the free electron model as:

$$E_p = \hbar\sqrt{\frac{ne^2}{m\varepsilon_0}} \qquad \textbf{Equation 3}$$

where $\hbar$ is the reduced plank constant, which equals to h/2π, n is the conduction electron density, e is the elementary charge, m is the electron mass and ε_0 is the permittivity of free space.

In the case where plasmons are confined to surface, they are called surface plasmons and the interaction between these surface plasmons and exciting light corresponds to a polarization of the material. Surface plasmon was extensively studied and the foremost work was that of H.Raether[10g] and E. Kretschmann[10h]. A brief description of surface plasmon will be discussed as following, based on the reference of http://en.wikipedia.org/wiki/Surface_Plasmon.

In the case where free electrons are excited by the light, which is a electromagnetic propagation. The electric field of this light can be expressed by:

$$E = E_0 e^{-i\omega t} \qquad \textbf{Equation 4}$$

When this wave is propagating on a interface separated by the free space and the material, the wave number is defined:

$$k = \frac{\omega}{c}\left(\frac{\varepsilon_0 \times \varepsilon_1}{\varepsilon_0 + \varepsilon_1}\right)^{\frac{1}{2}} \qquad \textbf{Equation 5}$$

where c is the light speed in the vacuum, ω and ε_0 are the same the Equation 3 and ε_1 is the permittivity of the material.

In the free electron model of an electron gas, excited by a light. We suppose that no magnetic field is applied and the attenuation is neglected as well. The metallic dielectric constant of the material is defined as:

$$\varepsilon(\omega) = 1 - \frac{\omega_P^2}{\omega^2} \qquad \textbf{Equation 6}$$

where ω_P is the bulk plasmon frequency defined by equation 7:

$$\omega_P = \sqrt{\frac{ne^2}{\varepsilon_0 m}} \qquad \textbf{Equation 7}$$

where n, e, ε_0 m are same in equation 3. And the surface plasmon frequency is given by:

$$\omega_{SP} = \frac{\omega_P}{\sqrt{1+\varepsilon_1}} \qquad \textbf{Equation 8}$$

In a metal, the dielectric constant ε_1 has a real part and an imaginary part and is expressed by:

$$\varepsilon_1 = \varepsilon_1^{'} + i\varepsilon_1^{''} \qquad \textbf{Equation 9}$$

and the wavenumber k can also be expressed in terms of its real and imaginary parts:

$$k = k^{'} + ik^{''} = \left(\frac{\omega}{c} \left(\frac{\varepsilon_1^{'} \varepsilon_0}{\varepsilon_1^{'} + \varepsilon_0} \right)^{\frac{1}{2}} \right) + i \left(\frac{\omega}{c} \left(\frac{\varepsilon_1^{'} \varepsilon_0}{\varepsilon_1^{'} + \varepsilon_0} \right)^{\frac{3}{2}} \frac{\varepsilon_1^{''}}{2\left(\varepsilon_1^{'}\right)^2} \right) \qquad \textbf{Equation 10}$$

In both equation 9 and 10, the imaginary part correspond to the light adsorption by metallic particles. And the energy of the surface plasmon is the same in equation 3, $E_{SP} = \hbar\omega_{SP}$.

The surface plasmon frequency ω_{SP} can be easily influenced by the change of the environment. For example, any dielectric constant changes caused by the environment will change the surface plasmon frequency. Decher et al[135] reported a strong surface plasmon interactions between two adjacent Au NP layers causes a 120 nm red shift of Au NP plasmon absorption band.

However, this strong surface plasmon interactions can be minimized either by increasing the spacing distance between two adjacent Au NP layers[135], by changing the environment of adsorbed Au NP[136], or by applying appropriate post-treatment, such as annealing[137]. For example, a spacing distance superior to 10nm will reduce sufficiently the surface plasmon interactions between two adjacent Au NP layers[135].

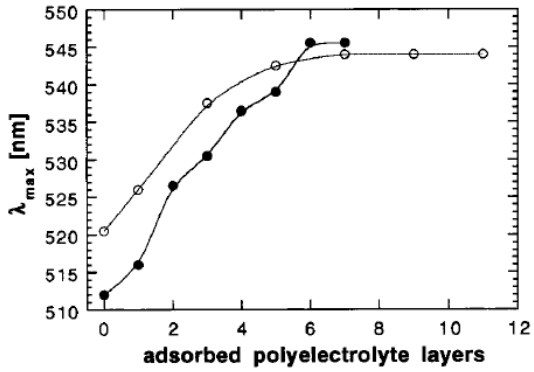

Figure 15: Maximum positions of Au NP layers on silane (full circles) and PEI (open circles) as a function of the number of adsorbed polyelectrolyte layers. Image extracted from the reference 136.

Figure 15 is an example of direct evidence that the surface plasmon band of Au NP can easily be influenced by the change of their environment[136]. In this experiment, a Au NP layer was assembled on silane or polyelectrolyte with different number of layers. By changing this number of layer, the surface plasmon band absorption of Au NP can be shifted for several dozens of nanometers.

Even in some cases, gold nanoparticle surface plasmon interactions are undesirable. These interactions favor the long range electron transport or communication in different Au NP layers, which is useful in Au NP embedded multilayer electric properties studies, especially in the field of conductivity. The group of Labbe[138] and the group of Natan[139] reported a successful fabrication of Au NP containing films with respectively redox behavior and conductive behavior. Resistivity (5×10^{-4} Ω cm) of films assembled by Natan is very close to that of pure gold (2.4×10^{-6} Ω cm).

All Au NP/polyelectrolyte multilayer reported above are assembled by dipping process, and the typical Au NP adsorption time is around 4-6 hours[135]. However, this adsorption time can be greatly reduced by applying spraying process. Fery[140] firstly reported the employment of spraying LbL technique in a Au NP based multilayer films construction. With spraying LbL technique, a single layer of Au NP will be prepared in a minute. But he used a cross-linker to bridge Au NP layers and corresponding polyelectrolyte layers, as a consequence, Au NP in such films is covalently linked with polyelectrolyte. At present time, the assembly of pure electrostatic interacted Au NP/polyelectrolyte multilayer by using spraying technique is not reported yet.

I.4. LbL assembly using strong interactions: covalently linked LbL films

Not as weakly interactions involved LB assembly, substances in LbL self-assembly can be linked not only by Van der Waals interactions or hydrogen bonding, but also by covalently bondings by forming a 3 dimensional network. Among those substance, epoxy is a very interesting family in covalently assembly process because of its unique properties.

Epoxy or polyepoxide is a thermosetting epoxide polymer that can be cured, either by polymerization or by cross-linking, when mixed with a catalyzing agent or "hardener". Most epoxy resin is derived from the chemical reactions between epichlorohydrin and bisphenol-A. Generally, the reputation of epoxy is based on its good adhesion, both chemical and thermal resistance and excellent mechanical properties. Moreover, these properties can be modified either by changing preparation conditions or by combining with other materials, such as carbon fibers in reinforcement applications. Epoxies can be cured by several types of cross-linkers during a film network formation and polyamines is a particularly interesting one. In such film formation, epoxy chains are normally very strongly linked with polyamine chains through numerous covalent bonding, and no gaseous by-products will be formed and emitted during the reaction.

The major application of epoxy is in coating and adhesives. For example, the group of Gleason[141] reported the formation of a new high-strength nano-adhesive film based on poly(glycidymethacrylate) and poly(allylamine). This film can be easily prepared on different substrates like silicon wafer, glass, quartz, poly(ethylene terephthalate) (PET), poly(carbonate) (PC), and even poly(tetrafluoro ethylene) (PTFE). Epoxy also has a very excellent mechanical property. It can be used in reinforcement combined with other components like carbon nanotube. The group of Grujicic[142] reported the excellent mechanical reinforcement behavior of a poly(vinyl-ester-epoxy)/multi-walled carbon nanotube materials. And even though epoxy is usually dissolved in organic solvents, the application of epoxy based materials in biological field has also been mentioned, such as in enzyme immobilization[143]. The presence of amino-epoxy film allows a rapid immobilization process to be carried on in a relatively low ion strength environment. Enzyme can be even immobilized on hydrophilic substrate surfaces.

Gurumurthy et al.[144] revealed that, during an epoxy and polyimide cross-linking reaction, the interpenetration of the epoxy into polyimide layer will increase the entanglement between polymer chains and probably increase the number of the number of primary

covalent bonds across the film interface. This may explains the origin of epoxy films excellent adhesive and mechanical properties. However, Tsukruk et al.[145] pointed out that, as a big family component, some epoxies especially some silane functional epoxies will form a disordered and chemically heterogeneous molecular layer due to the hydrolysis/interaction/adsorption/reactivity competition of the head-end epoxy groups with the hydroxyl-terminated silicon oxide surfaces. They performed a thorough investigation in epoxysilane monolayer formation at different concentrations and different adsorption time, as well as corresponding mechanical properties. They found out that a smooth uniform film with rare surface aggregates can be formed at relatively high concentration (1%, volume ratio), while at relatively low concentrations (0.1-0.5%, volume ratio), loosely packed film with many bi- or trilayers molecules aggregates will be formed. So, in an epoxy layers formation experiment, the optimum preparation conditions, like epoxy concentration, appropriate layer's adsorption time should be found at first in order to ensure a uniform layer formation with best corresponding properties.

Once a homogeneous film is formed, chemically attached epoxy layer reduces significantly shear strength and dissipation of mechanical energy during friction force measurement. The homogeneously formed epoxy film is extremely stable and well attached on the surface. It is almost impossible to mechanically remove the layer without damaging underlying silicon substrate.

I.5. LbL films mechanical behavior study

Both chemical and physical stabilities of a nano-structured device are key controlling parameters in its potential applications. More specifically, mechanical properties of LbL assembled films have been intensively investigated by several groups. The group of Vinogradova[146,147,148] investigated the Young's modulus of LbL assembled polymer films, and they found out that $(PSS/PAH)_n$ films Young's modulus is in order of 100~200MPa while E. Donath et al.[149] reported the Young's modulus of a LbL assembled $(PSS/PAH)_n$ capsules is around 700MPa. Vinogradova suggested that the Young's modulus of LbL assembled polymer films is in function of films thickness and she proposed the theory of ionic strength to explain the Young's modulus difference in different polymer couples. The Young's modulus of LbL assembled polymer films depend on the number of ionic cross-links of oppositely charged polyelectrolyte couples. Fully charged strong polyelectrolyte (PSS) mechanical property is better than partially charged weak polyelectrolyte (PAH) and the use of such weak polyelectrolyte in LbL assembled films construction will decrease films Young's modulus.

Besides the elastic property, tribology properties of LbL assembled polymer films have been investigated as well. The group of Gearing and Cohen[150,151] reported the friction and wear behavior of $(PAH/PAA)_n$ films, and they also found out that wear property of such films is also strongly linked with films thickness. In their nanoindentation experiment, a (PAH/PAA) film with 70nm thickness can protect efficiently the steel substrate.

Moreover, LbL assembled multilayer with incorporated nanometric metallic or inorganic compounds demonstrate a significant increase in mechanical properties. One of the leading works in this field has been performed by group of Kotov[127,152], and they pointed out that the LbL self-assembly technique can increase incorporated substance/polyelectrolyte connectivity in film matrix and prevent efficiently the phase segregation, which is responsible for mechanical failure in hybrid materials. A single-walled carbon nanotubes (SWNT)/polyelectrolyte films has an exceptionally strong tensile strength approaching that of hard ceramics .And for the free standing poly(diallydimethylammonium) chloride (PDDA)/montmorillonite clay films have a surprisingly Yong's modulus in order of 11GPa, closing or exceeding to those of plywood bones (6-16GPa)[127] and comparable to the tensile properties of natural nacre (64GPa)[127]. Fery et al.[140] studied the Young's modulus of sprayed LbL assemblies of gold nanoparticle and different polyelectrolyte, a chemical covalent cross-linking treatment has been performed after films assembly and they found out that the Young's modulus of such films vary from 0.4GPa to 2.3GPa. Thanks to excellent mechanical properties of LbL assembled films, fabrication of free-standing polymer or hybrid membrane becomes possible[127,153].

Schönhoff et al.[154] suggested a theoretical model based on residual water content in multilayer in films mechanical properties behavior. During a polyelectrolyte adsorption on surface, some water molecules can also be adsorbed as well. After oppositely charged polyelectrolyte adsorption, the film structure will be slightly compressed, meaning that a part of pre-adsorbed water has been expelled from the film while still a part of water has been immobilized in the film. In a freshly prepared $(PSS/PAH)_n$ films, this immobilized water volume fraction can be up to 56%[154]. A polyions complex can associate 6-8 water molecules[154,155,156], and multilayer are capable to swell and deswell after preparation. In a deswell and dehydraton process, the polymer network will be strengthened without rearrangement of the loop structures within the layers. During such process, water molecules are removed from polymer matrix by leaving some void places, however, these avoids are not completely recovered by polymer chains because of steric hindrance between them. This hydration water will partially control the local molecular interactions,

especially in the polyions complexation and influence films local properties. In mechanical properties tests, the hydration water acts probably as lubricant and the percentage of this hydration water will tailor films mechanical responding. A highly hydration water contained films are supposed to have weak mechanical properties. In hybrid LbL assembled materials, incorporated compounds will fill the void place in polyelectrolyte chains, resulting an expel of immobilized water and the decrease of hydration water percentage in films matrix, finally leading to an improved mechanical properties.

Till now, most mechanical properties of LbL assembled multilayer studies focus on films tensile strength, stretch or elastic properties research, only a few focuses on films wear properties study[140]. In films wear property study, nanoindentation is a powerful investigation technique, and has been widely used. However, this technique offers only local mechanical property information. At present time, no mechanical properties, especially wear behavior researches in macroscopic scale have been carried out. For the purpose of real applications, the homogeneity of the mechanical responding of a material should be investigated as well even sometimes, it has an excellent mechanical property in local nanometric scale,

I.6. Applications of LbL assembled films: toward commercial applications

The use of both LB films and SAMs has been limited by their lack of commercial applications possibility. But thanks to versatility of LbL self-assembly, a surface functionalization by combining any substance on any substrates regardless what their form and size offers the accessibility of this technique to real commercial applications. Derived from original "Bola" molecules[19,20] the LbL self-assembly technique has been used in many different fields. For example, catalytic membranes can be prepared by using LbL adsorption of polyelectrolyte/metal nanoparticle in porous supports[157]. LbL assembled polyelectrolyte multilayer with embedded liposomes can be used as immobilized submicronic reactors for mineralization[158]. Besides traditional planar substrate, polyelectrolyte multilayer can be assembled on spherical substrate by using nanoparticle template, which makes the fabrication of hollow capsule possible. This hollow capsule fabrication has already been reported by several groups[159,160]. These well-defined hollow polymeric capsules have direct applications in drug delivery, catalysis, and dye dispersion industries.

After several year of laboratory research activities, some commercial products based on

LbL self-assembly technique have appeared in the market. CIBA-Vision's Focus® ExcelensTM, a contact lens with a LbL based coating on the surface, was the first commercial product announced in 2002 (Figure 16). A food package film with LbL incorporated ethylene consuming enzyme has been invented and commercialized by Shiratori from Keio university. Other LbL based products, such as Metal Rubber™, developed by Nanosonic for its excellent electrical conductivity with low elasticity modulus, large operation temperature range and CBAS™ anticoagulation layers, developed by Carmeda for heparin-coated blood oxygenator applications are also good examples for LbL technique commercial applications.

Figure 16 : Photo of CIBA-Vision's Focus® contact lens based on LbL films

Looking back on the history of LbL technique, some disagreements like "pre-adsorbed layers should desorb upon deposition of the next one"; "LbL multilayer coating are not stable"; "LB technique did not work for applications so why should LbL?" were frequently heard in its early years. But the appearance of all these commercial products contradicts all initial counterarguments often associated with new technologies. Layer-by-Layer self-assembly technique has made so many progresses than most of people gave credit for 10 years ago and no one knows what this technique will look like tomorrow.

Bibliography*

*: All references cited in this thesis have their independent citation style in the corresponding journals

[1] http://en.wikipedia.org/wiki/Material_science

[2] (a) I Langmuir, *J. Am. Chem. Soc.*, **1917**, 39, 1848.
(b) K. B. Blodgett, *J. Am. Chem. Soc.*, **1935**, 57, 1007.
(c) K.B. Blodgett, *J. Am. Chem. Soc.,* **1934**, 56, 495.
(d) K.B. Blodgett, I. Langmuir, *Phys.Rev.,* **1937**, 51, 946.

[3] (a) R.G. Nuzzo, D.L. Allara, *J. Am. Chem. Soc.,* **1983**, 105, 365.
(b) R.G. Nuzzo, B.R. Zegarski, L.H. Dubois, *Journal of the American Chemical Society* **1987**, *109*, 733-740.
(c) E.B. Troughton, C.D. Bain, G.M. Whitesides, R.G. Nuzzo, D.L. Allara, M.D. Porter, *Langmuir* **1988**, *4*, 365-385.
(d) C.D. Bain, E.B. Troughton, Y.T. Tao, J. Evall, G.M. Whitesides, R.G. Nuzzo, *J. Am. Chem. Soc.,* **1989**, 111, 321.
(e) P.E. Laibinis, G.M. Whitesides, D.L. Allara, Y.T. Tao, A.N. Parikh, R.G. Nuzzo, *J. Am. Chem. Soc.,* **1991**, 113, 7152.
(f) L.H. Dubois, B.R. Zegarski, R.G. Nuzzo, *Journal of Chemical Physics* **1993**, *98*, 678-688.
(g) Atre, S. V.; Liedberg, B.; Allara, D. L. *Langmuir* **1995**, *11*, 3882-3893.
(h) Allara, D. L.; Parikh, A. N.; Rondelez, F. *Langmuir* **1995**, *11*, 2357-2360.
(i) J. Sagiv, *J. Am. Chem. Soc.*, **1980**, 102, 92.

[4] G. Decher, *Science,* **1997**, 277, 1232.

[5] J.B. Schlenoff, S.T. Dubas, T. Farhat, *Langmuir,* **2000**, 16, 9968.

[6] (a) J. Schmitt, T. Grünewald, G. Decher, P.S. Pershan, K. Kjaer, M. Lösche, *Macromolecules,* **1993**, 26, 7058.
(b) M. Kolasinska, T. Gutberlet, R. Krastev, *Langmuir,* **2009**, 25, 10292.

[7] T.P. Russell, *Mater. Sci. Rep.,***1990**, 5, 171.

[8] Y. Lvov, G. Decher, H. Möhwald, *Langmuir,* **1993**, 9, 481.

[9] A. Izquierdo, S. S. Ono, J.-C. Voegel, P. Schaaf, and G. Decher, *Langmuir,* **2005**, 21, 7558.

[10] (a) G. Mie, *Annalen der Physik*, **1908**, 25, 377.
(b) G. Oldfield, T. Ung, P. Mulvaney, *Advanced materials,* **2000**, 12, 1519.
(c) J.C. Maxwell-Garnett, *Philosophical Transactions of the Royal Society,* **1906**, 237,237.
(d) J.C. Maxwell-Garnett, *Philosophical Transactions of the Royal Society,* **1904**, 203,385.
(e) P. Debye, *Annalen der Physik*, **1909**, 30, 57.
(f) R.H. Ritchie, *Physical Review*, **1957**, 106, 874.
(g) H. Raether, Springer Tracts in Modern Physics 111. New York: Springer-Verlag, 1988, ISBN 0-387-17363-3.
(h) E. Kretschmann, *Optics Communications*, **1972**, 5 331.

[11] J. Schmitt, T. Gruenewald, G. Decher, P.S. Pershan, K. Kjaer, Mathias Loesche, *Macromolecules*, **1993**, 26, 7058.
[12] T. Yonezawa, S. Onoue, t. Kunitake, *Advanced materials,* **1998**, 10, 414.
[13] G. Decher, J.B. Schlenoff, Multilayer Thin Films: Sequential Assembly of Nanocomposite Materials, **2003**, Wiley-VCH: Weinheim.
[14] (a) H. Kuhn, D. Möbius, *Angew. Chem.*, **1971**, 83, 672.
(b) O. Inacker, H. Kuhn, D. Möbius, G. Debuch, *Phys. Chem.Neue Folge*, **1976**, 101, 337.
[15] (a) A. Ulman, *Chem. Rev.,* **1996**, 96, 1533.
(b) S.D. Evans, A. Ulman, K.E. Goppertberarducci, L.J. Gerenser, *J. Am. Chem. Soc.,* **1991**, *113*, 5866.
(c) S.D. Evans, E. Urankar, A. Ulman, N. Ferris, Ibid., 4121.
(d) Ulman, An Introduction to Ultrathin Organic Films: From Langmuir--Blodgett to Self—Assembly, **1991**, Academic Press.
[16] (a) G.M. Whitesides, B. Grzybowski. *Science,* **2002**, 295, 2418.
(b) G.M. Whitesides, M. Boncheva, *Proceedings of the National Academy of Sciences of the United States of America* **2002**, *99*, 4769.
[17] E.E. Simanek, J.P. Mathias, C.T. Seto, D. Chin, M. Mammen, D.M. Gordon, G.M. Whitesides, *Acc. Chem. Res.,* **1995**, 28, 37.
[18] G.M. Whitesides, J.P. Mathias, C.T. Seto, *Science,* **1991**, 254, 1312.
[19] G. Decher, J.D. Hong, J. Schmitt, *Thin Solid Films* **1992**, 210, 831.
[20] (a) G. Decher, J.D. Hong, *Makromolekulare Chemie-Macromolecular Symposia,* **1991**, 46, 321.
(b) G. Decher, J.D. Hong, *Berichte Der Bunsen-Gesellschaft-PHysical Chemistry Chemical Physics,* **1991**, 95, 1430.
[21] R.K. Iler, *J. Colloid Interf. Sci.,* **1966**, 21, 569.
[22] Y. Shimazaki, M. Mitsuishi, S. Ito, M. Yamamoto, *Langmuir*, **1997**, 13, 1385.
[23] E.C. Hao, T.Q. Lian, *Chem. Mater.,* **2000**, 12, 3392.
[24] W.B. Stockton, M.F. Rubner, *Macromolecules*, **1997**, 30, 2717.
[25] C. Pearson, J. Nagel, M.C. Petty, *J. PHys. D, Appl. Phys.*, **2001**, 34, 285.
[26] P. Kohli, G.J. Blanchard, *Langmuir*, **2000**, 16, 4655.
[27] K. Ariga, Y. Lvov, T. Kunitake, *J. Am. Chem. Soc.,* **1997**, 119, 2224.
[28] Tang Z.Y., Kotov N.A., Magonov S., Ozturk B., *Nature Materials*, **2003,** 2, 413.
[29] P. Podsiadlo, Z. Liu, D. Paterson, P.B. Messersmith, N.A. Kotov, *Advanced Materials,* **2007**, 19, 949.
[30] V.V. Tsukruk, F. Rinderspacher, V. N. Bliznyuk, *Langmuir*, **1997**, 13, 2171.
[31] A.J. Khopade, F. Caruso, *Nano letters*, **2002**, 2, 415.
[32] F. Caruso, K. Niikura, D.N. Furlong, Y. Okahata, *Langmuir*, **1997**, 13, 3427.
[33] M. Michel, D. Vautier, J.C. Voegel, P. Schaaf, V. Ball, *Langmuir*, **2004**, 20, 4835.
[34] M. Michel, A. Izquierdo, G. Decher, J.-C. Voegel, P. Schaaf, V. Ball, *Langmuir,* **2005**, 21, 7854.

[35] M. Michel, Y. Arntz, G. Fleith, J. Toquant, Y. Haikel, J.C. Voegel, P. Schaaf, V. Ball, *Langmuir,* **2006**, 22, 2358.
[36] J. W. Ostrander, A.A. Mamedov, N.A. Kotov, *J. Am. Chem. Soc.,* **2001,** 123, 1101.
[37] N. Malikova, I. Pastoriza-Santos, M. Schierhorn, N. A. Kotov, L.M. Liz-Marzán, *Langmuir,* **2002**, 18, 3694.
[38] J. Cho, F. Caruso, *Chem. Mater.,* **2005**, 17, 4547.
[39] D.M. Dotzauer, J. Dai, L. Sun, M.L. Bruening, N*ano Letters*, **2006**, 6, 2268.
[40] R. Lingström, L. Wågberg, P.T. Larsson, *J. Colloid and Interface Sci.,* **2006**, 296, 396.
[41] I. Wistrand, R. Lingström, L. Wågberg, *European Polym. J.,* **2007**, 43, 4075.
[42] L. Wågberg, G. Decher, M. Norgren, T. Lindström, M. Ankerfors, K. Axnäs, *Langmuir,* **2008**, 24, 784.
[43] C. Aulin, I. Varga, P.M. Claesson, L. Wågberg, T. Lindström, *Langmuir,* **2008**, 24, 2509.
[44] R. Advincula, E. Aust, W. Meyer, W. Knoll, *Langmuir,* **1996**, 12, 3536.
[45] D.G. Kurth, R. Osterhout, *Langmuir,* **1999**, 15, 4842.
[46] C.B. Bucur, K. Hart, J.B. Schlenoff, *Abstracts of Papers of the American Chemical Society* **2006**, *231*, 305.
[47] S.S. Lee, J.D. Hong. C.H. Kim, K. Kim, J. P. Koo, K.B. Lee, *Macromolecules*, **2001**, 34, 5358.
[48] J. Cho, K. Char, J.D. Hong, K.B. Lee, *Adv. Mater.*, **2001**, 13, 1076.
[49] P. A. Chiarelli, M. S. Johal, J. L. Casson, J. B. Roberts, J. M. Robinson, H.L. Wang, *Adv. Mater.*, **2001**, 13, 1167.
[50] H.G.M. Van de Steeg, M.A. Cohen Stuart, A. De Keizer, B.H. Bijsterbosch, *Langmuir,* **1992**, 8, 2538.
[51] N.G. Hoogeveen, M.A. Cohen Stuart, G.J. Fleer, M.R. Böhmer, *Langmuir,* **1996**, 12, 3675.
[52] M. Castelnovo, J.F. Joanny, *Langmuir,* **2000**, 16, 7524.
[53] K. Lowack, C. A. Helm, *Macromolecules*, **1998**, 31, 823.
[54] J.F. Joanny, *Eur. Phys. J.B.,* **1999**, 9,117.
[55] P. Bertrand, A. Jonas, A. Laschewsky, R. Legras, *Macromol. Rapid Commun.*, **2000**, 21, 319.
[56] T.R. Farhat, J.B. Schlenoff, *Langmuir,* **2001**, 17, 1184.
[57] J.B. Schlenoff, S.T. Dubas, *Macromolecules*, **2001**, 34, 592.
[58] J.L. Barrat, J.F. Joanny, *Adv. Chem. PHys.*, **1996**, 94, 1.
[59] G. Ladam, P. Schaad, J. C. Voegel, P. Schaaf, G. Decher, F. Cuisinier, *Langmuir,* **2000**, 16, 1249.
[60] D. Pointu, G. Decher, Actualites GFP, **2000**, *Bulletin* No 88, 3.

[61] G.B. Sukhorukov, J. Schmitt, G. Decher, *Berichte Der Bunsen-Gesellschaft-Physical Chemistry Chemical Physics* **1996**, 100, 948.
[62] S.T. Dubas, J.B. Schlenoff, *Macromolecules*, **1999**, 32, 8153.
[63] T.Farhat, J.B. Schlenoff, *Langmuir,* **2001**, 17, 1184.
[64] S.T. Dubas, J.B. Schlenoff, *Macromolecules*, **2001**, 34, 3736.
[65] R.A. McAloney, M. Sinyor, V. Dudnik, M.C. Goh, *Langmuir,* **2001**, 17, 6655.
[66] K. Büscher, K.Graf, H. Ahrens, C.A. Helm, *Langmuir,* **2002**, 18, 3585.
[67] R. Steitz, V. Leiner, R. Siebrecht, R.v. Klitzing, *Colloids and Surfaces A: Physicochem.Eng. Aspects***, 2000,** 163, 63.
[68] S. S. Shiratori, M. F. Rubner, *Macromolecules*, **2000**, 33, 4213.
[69] L. Zhai, A.J. Nolte, R.E. Cohen, M.F. Rubner, *Macromolecules*, **2004**, 37, 6113.
[70] J. Choi, M.F. Rubner, *Macromolecules*, **2005**, 38, 116.
[71] K. Itano, J. Choi, M.F. Rubner, *Macromolecules*, **2005**, 38, 3450.
[72] M. Gopinadhan, H. Ahrens, J.-U. Günther, R. Steitz, C.A. Helm, *Macromolecules*, **2005**, 38, 5228.
[73] M. Gopinadhan, O. Ivanova, H. Ahrens, J.U. Günther, R. Steitz, C.A. Helm, *J. Phys. Chem. B*, **2007**, 111, 8426.
[74] O.M. Tanchak, K.G. Yager, H. Fritzsche, T. Harroun, J. Katsaras, C.J. Barrett, *Langmuir,* **2006**, 22, 5137.
[75] R. Kügler, J. Schmitt, W. Knoll, *Macromol. Chem. PHys.,* **2002**, 203, 413.
[76] M. Schönhoff, V. Ball, A.R. Bausch, C. Dejugnat, N. Delorme, K. Glinel, R.v. Klitzing, R. Steitz, *Colloids and Surfaces A: PHysicochem.Eng. Aspects***, 2007,** 303, 14.
[77] F. Helfferich, *Ion Exchange*, McGraw-Hill, New York, **1962.**
[78] S.A. Sukhishvili, S. Granick, *J. Am. Chem. Soc.,* **1998,** 109, 9861.
[79] C. Picart, P. Lavalle, P. Hubert, F.J.G. Cusinier, G. Decher, P. Schaaf, J.C. Vogel, *Langmuir,* **2001**, 17, 7414.
[80] C. Picart, J. Mutterer, L. Richert, Y. Luo, G.D. Prestwich, P. Schaaf, J.C. Vogel, P. Lavalle, *Proc. Natl. Acad. Sci. U.S.A.,* **2002**, 99, 12531.
[81] L. Kolarik, D.N. Furlong, H. Joy, C. Struijk, R. Rowe, *Langmuir,* **1999**, 15, 8265.
[82]P. Lavalle, C. Gergely, F.J.G. Cuisinier, G. Decher, P. Schaaf, J.C. Voegel, C. Picart, *Macromolecules*, **2002**, 35, 4458.
[83] F. Boulmedais, V. Ball, P. Schwinte, B. Frisch, P. Schaaf, J.C. Voegel, *Langmuir,* **2003**, 19, 440.
[84] P. Lavalle, V. Vivet, N. Jessel, G. Decher, J.C. Voegel, P.J. Mesini, P. Schaaf, *Macromolecules*, **2004**, 37, 1159.
[85] L. Richert, P. Lavalle, E. Payan, X.Z. Shu, G.D. Prestwich, J.F. Stoltz, P. Schaaf, J.C. Voegel, C. Picart, *Langmuir,* **2004**, 20, 448.
[86] P. Lavalle, C. Picart, J. Mutterer, C. Gergely, H. Reiss, J.C. Voegel, B. Senger, P. Schaaf, *J. Phys.Chem. B*, **2004**, 108, 635.

[87] N. Laugel, C. Betscha, M. Winterhalter, J.C. Voegel, P. Schaaf, V. Ball, *J. Phys.Chem. B*, **2006**, 110, 19443.

[88] E. Hubsch, V. Ball, B. Senger, G. Decher, J.-C. Voegel, P. Schaaf, *Langmuir,* **2004**, 20, 1980.

[89] M. Michel, A. Izquierdo, G. Decher, J.-C. Voegel, P. Schaaf, V. Ball, *Langmuir,* **2005**, 21, 7854.

[90] M. Salomaki, I.A. Vinokurov, J. Kankare, *Langmuir,* **2005**, 21, 11232.

[91] S.H. Anastasiadis, T.P. Russell, *J. Chem. Phys.*, **1990**, 92, 5677.

[92] I. M. Tidswell, B. M. Ocko, P. S. Pershan, S. R. Wasserman, G. M. Whitesides, J. D. Axe, *Phys. Rev. B*, **1990**, 41, 1111.

[93] T. P. Russell, A. Karim, A. Mansour, G. P. Felcher, *Macromolecules*, **1988**, 21, 1890.

[94] H. Hong, R. Steitz, S. Kirstein, D. Davidov, *Adv. Mater.*, **1998**, 10, 1104.

[95] I. Benjamin, H. Hong, Y. Avny, D. Davidov, R. Neumann, *J. Mater. Chem.,* **1998**, 8, 919.

[96] Y. Lvov, F. Essler, G. Decher, *J. Chem. Phys.*, **1993**, 97, 13773.

[97] X. Arys, A. M. Jonas, B. Laguitton, A. Laschewsky, R. Legras, E. Wischerhoff, *Thin Solid Films*, **1998**, 327-329, 734.

[98] G. Decher, Y. Lvov, J. Schmitt, *Thin Solid Films*, **1994**, 244, 772.

[99] G. Decher, M. Eckle, J. Schmitt, B. Struth, *Curr. Opin. Colloid Interface Sci.*, **1998**, 3, 32.

[100] H. Hong, R. Steitz, S. Kirstein, D. Davidov, *Adv. Mater.,* **1998,** 10, 1104

[101] J. Schmitt, T. Gruenewald, G. Decher, P.S. Pershan, K. Kjaer, Mathias Loesche, *Macromolecules*, **1993**, 26, 7058.

[102] M. Tarabia, H. Hong, D. Davidov, S. Kirstein, R. Steitz, R. Neumann, Y. Avny, *J. Appl. Phys.*, **1998**, 83, 725.

[103] S. Kirstein, H. Hong, R. Steitz, D. Davidov, *Synthetic Metals*, **1999**, 102, 1067.

[104] A. Gilliard, L.C. Winterton, R.V. Andino, J. Lally, *US patent*, **2004,** No.6811805.

[105] M. Kolasinska, R. Krastev, T. Gutberlet, P. Warszynski, *Langmuir,* **2009**, 25, 1224.

[106] K. C. Krogman, N. S. Zacharia, S. Schroeder, P. T. Hammond, *Langmuir,* **2007**, 23, 3137.

[107] K. C. Krogman, K. F. Lyon, P. T. Hammond, *Journal of Physical Chemistry B*, **2008**, 112, 14453.

[108] J.A. Hubbell, D.L. Elbert, C.B. Herbert, US patent 6, 743, 521, 2004.

[109] M. Hiorth, I. Tho, S.A. Sande, *Eu. J.Pharm.Biopharm.*, **2003**, 56, 175.

[110] C. H. Porcel, A. Izquierdo, V. Ball, G. Decher, J.C. Voegel, P. Schaaf, *Langmuir,* **2005**, 21, 800.

[111] J.H. Fendler, *Chem. Mater.*, **1996**, 8, 1616.

[112] A. N. Shipway, A. N.; Lahav, M.; Willner, I. *Advanced Materials* **2000**, *12*, 993.

[113] S. F. Cheng, S. F.; Chau, L. K. *Analytical Chemistry* **2003**, *75*, 16.

[114] C. J. Zhong, C. J.; Maye, M. M. *Advanced Materials* **2001**, *13*, 1507.
[115] M. H. Lim, D. G. Ast, Ibid., 718.
[116] A.A. Mamedov, N.A. Kotov, *Langmuir,* **2000**, 16, 5530.
[117] X. Sun, S. Dong, E. Wang, *Materials Chemistry and Physics*, **2006**, 96, 29.
[118] J. Dai, M.L. Bruening, *Nano Letters*, **2002**, 2, 497.
[119] P. Schuetz, F. Caruso, *Chemistry of Materials,* **2004**, 16, 3066.
[120] Y. Lvov, K. Ariga, M. Onda, I. Ichinose, T. Kunitake, *Langmuir,* **1997**, 13, 6195.
[121] V. Salgueirino-Maceira, Caruso, L.M. Liz-Marzan, *Journal of Physical Chemistry B,* **2003**, 107, 10990.
[122] Z.H. Lu, M.D. Prouty, Z.H. Guo, V.O. Golub, C. Kumar, Y.M. Lvov, *Langmuir,***2005**, 21, 2042.
[123] T.R. Farhat, P.T. Hammond, *Advanced Functional Materials,* **2006**, 16, 433.
[124] D.A. Dotzauer, Bhattacharjee, Y. Wen, M.L. Bruening, *Langmuir,* **2009**, 25, 1865.
[125] C.Y. Jiang, S. Markutsya, V.V. Tsukruk, *Advanced Materials,* **2004**, 16, 157.
[126] C.Y. Jiang,; V.V. Tsukruk, *Soft Matte,r* **2005**, 1, 334.
[127] Z. Tang, N.A. Kotov, S. Magonov, B. Ozturk, *Nat. Mater.,* **2003**, 2,413.
[128] P. Podsiadlo, Z. Liu, D. Paterson, P. B. Messersmith, N. A. Kotov, *Advanced Materials,* **2007**, 19, 949.
[129] B. Abu-Sharkh, *Langmuir,* **2006**, 22, 3028.
[130] J.W. Mellor, A comprehensive Treatise on Inorganic and Theoritical Chemistry, **1923**, Longmans, Green and Co, London.
[131] M. Faraday, *Philos. Trans. R. Soc. London*, **1857**, 147, 145.
[132] K.C. Grabar, R.G. Freeman, M.B. Hommer, M.J. Natan, *Anal. Chem.,* **1995**, 67, 735.
[133] G. Schmid, Clusters and Colloids, **1994**, VCH, Weinheim.
[134] G. Schmid, A. Lehnert, *Angew. Chem., Int. Ed. Engl.,* **1989**, 28, 780.
[135] J. Schmitt, G. Decher, W.J. Dressick, S.L. Brandow, R.E. Geer, R. Shashidhar, J.M. Calvert, *Advanced Materials,* **1997**, 9, 61.
[136] J. Schmitt, P. Machtle, D. Eck, H. Möhwald, C.A. Helm, *Langmuir,* **1999**, 15, 3256.
[137] C. Lu, H. Möhwald, A. Fery, *J. PHys. Chem. C,* **2007**, 111, 10082.
[138] N. Ferreyra, L. Coche-Guérente, J. Fatisson, M.L. Teijelo, P.Labbé, *Chem. Commun.*, **2003**, 2056.
[139] M.D. Musick, C.D. Keating, M.H. Keefe, M.J. Natan, *Chem. Mater.,* **1997**, 9, 1499.
[140] C. Lu, I. Dönch, M. Nolte, A. Fery, *Chem. Mater.,* **2006**, 18, 6204.
[141] S.G. Im, K.W. Bong, C.H. Lee, P.S. Doyle, K.K. Gleason, *Lab on a Chip,* **2009**, 9, 411.
[142] M. Grujicic, D.C. Angstadt, Y.P. Sun, K.L. Koudela, *Journal of Materials Science,* **2007**, 42, 4609.
[143] C. Mateo, R. Torres, G. Fernandez-Lorente, C. Ortiz, M. Fuentes, A. Hidalgo, F. Lopez-Gallego, O. Abian, J.M. Palomo, L. Betancor, B.C.C. Pessela, J.M. Guisan, R. Fernandez-Lafuente, *Biomacromolecules,* **2003**, 4, 772.
[144] C. Gurumurthy, E.J. Kramer, C.Y. Hui, *Journal of Adhesion,* **2006**, 82, 239.

[145] I. Luzinov, D. Julthongpiput, A. Liebmann-Vinson, T. Cregger, M.D. Foster, V.V. Tsukruk, *Langmuir,* **2000**, 16, 504.
[146] B.S. Kim, O.V. Lebedeva, D.H. Kim, A.M. Caminade, J.P. Majoral, W. Knoll, O.I. Vinogradova, *Langmuir,* **2005**, 21, 7200.
[147] O.I. Vinogradova, *J. Phys.: Condens. Matter.,* **2004**, 16, R1105.
[148] O.I. Vinogradova, D. Andrienko, V.V. Lulevich, S. Nordschild, G.B. Sukhorukov, *Macromolecules*, **2004**, 37, 1113.
[149] C. Gao, E. Donath, S. Moya, V. Dudnik, H. Möhwald, *Eur. Phys. J. E.,* **2001**, 5, 21.
[150] P.V. Pavoor, B.P. Gearing, R.E. Gorga, A. Bellare, R.E. Cohen, *J. Appli. Poly. Sci.,* **2004**, 92, 439.
[151] P.V. Pavoor, B.P. Gearing, A. Bellare, R.E. Cohen, *Wear*, **2004**, 256, 1196.
[152] A.A. Mamedov, N.A. Kotov, M. Prato, D.M. Guldi, J.P. Wicksted, A. Hirsch, *Nat. Mater.,* **2002**, 1,190.
[153] S.S. Ono, G. Decher, *Nano Letters,* **2006**, 6, 592.
[154] M. Schönhoff, V. Ball, A.R. Bausch, C. Dejugnat, N. Delorme, K. Glinel, R.v. Klitzing, R. Steitz, *Colloids and Surfaces A: Physicochem.Eng. Aspects***, 2007,** 303, 14.
[155] T. Farhat, G. Yassin, S.T. Dubas, J.B. Schlenoff, *Langmuir,* **1999**, 15, 6621.
[156] J.A. Jaber, J.B. Schlenoff, *Langmuir,* **2007**, 23, 896.
[157] D.M. Dotzauer, J. Dai, L. Sun, M.L. Bruening, *Nano Letters,* **2006**, 6, 2268.
[158] M. Michel, Y. Arntz, G. Fleith, J. Toquant, Y. Haikel, J.C. Voegel, P. Schaaf, V. Ball, *Langmuir,* **2006**, 22, 2358.
[159] D.I. Gittins, F. Caruso, *Advanced Materials,* **2000**, 12, 1947.
[160] G. Schneider, G. Decher, *Nano Letters,* **2004**, 4, 1833.

Chapter II Materials and Methods

II.1. Materials

II.1.1. Polymer abbreviations and structures

- Poly(sodium 4-styrenesulfonate) → PSS or PSSh7, $\overline{M_w}$ = 70,000 g/mol
- Deuterated poly(sodium 4-styrenesulfonate) → PSSd7, $\overline{M_w}$ = 80,800 g/mol
- Poly(allylamine hydrochloride) → PAH, $\overline{M_w}$ = 70,000 g/mol
- Branched Poly(ethylenimin) → PEI, $\overline{M_w}$ = 25,000 g/mol
- Poly[(o-cresyl glycidyl ether)-co-formaldehyde] → CNER, $\overline{M_n}$ = 1270 g/mol
- Poly(vinylamine) → received as gift from BASF with the following molecular weights:
  - $\overline{M_w}$<10,000g/mol
  - $\overline{M_w}$=45,000g/mol
  - $\overline{M_w}$=340,000g/mol
- Poly(acrylic acid), Sodium Salt → received as gift from BASF with the following molecular weights:
  - $\overline{M_w}$=2,500g/mol
  - $\overline{M_w}$=70,000g/mol

All polymers except PSS_{d7} were purchased from Aldrich (Lyon, France) and PSS_{d7} was purchased from Polymer Standards Service GmbH (Mainz, Germany). Some specifications in PSS molecule weights has been introduced in chapter III, section of $(PSS/PAH)_n$ films construction, influence of polymers molecule weight. Polymers structure are presented in the following figure:

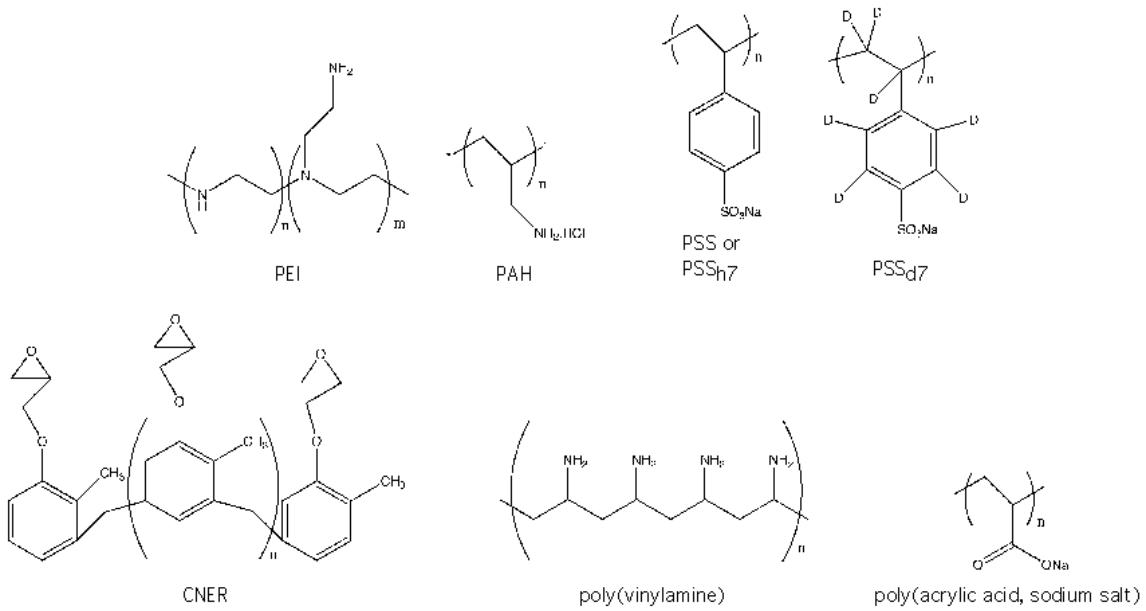

Figure 1: Chemical structures of the polymers used for this work

II.1.2. Synthesis of gold nanoparticle

Gold nanoparticle (Au NP) can be synthesized by reducing the tetrachloroauric acid ($HAuCl_4 \bullet 3H_2O$) in acqueous solution in the presence of different reducers like sodium citrate, sodium borohydrate or even some polymers with amine groups, like poly(ethylenimine) for example[1]. The experimental conditions (heating or not for example) of the Au NP synthesis is function of the nature of reducing agents. In this work, Au NP have been synthesized by reducing $HAuCl_4$ with citrate sodium at 90°C. The concentrations of $HAuCl_4$ and citrate sodium were respectively 1.0 mM and 38.8 mM. 1.5 L of $HAuCl_4$ solution was first heated to 90°C under vigorous agitation and then the sodium citrate solution (150 ml) was added very quickly. The average diameter of synthesized Au NP is around 13.6nm.

Figure 2 shows a simplified gold nanoparticle structure and a transmission electronic microscope photo of the gold nanoparticle.

The transmission electronic microscope photo demonstrates that the synthesized gold nanoparticle are mono-dispersed.

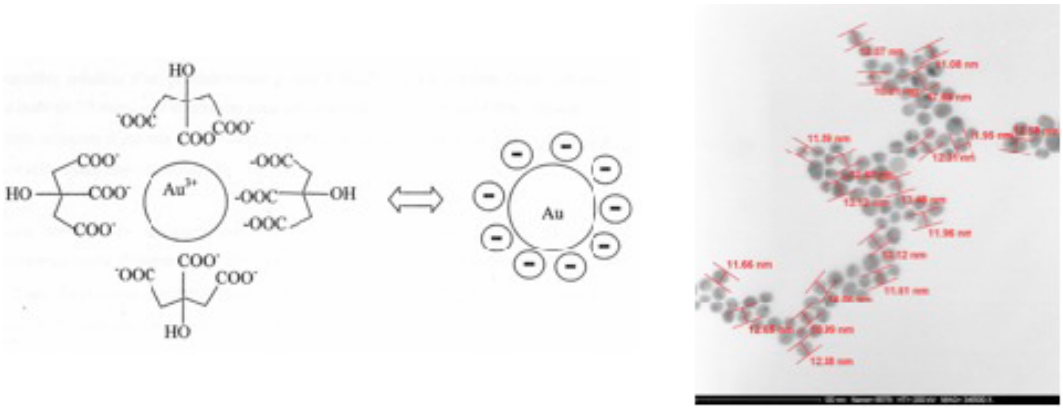

Figure 2: Schematic representation of a gold nanoparticle (left) and a transmission electronic photo of gold Nanoparticles with a diameter 13.6nm (right).

II.1.3. Substrate and cleaning methods

The silicon wafer was the major substrate for the deposition of thin films except for the UV-Visible analysis where a quartz slide was used. Silicon wafers with an orientation (100) were purchased from Wafernet Inc. UK. All wafers were cut to a size of about 12 mm × 45 mm for film construction or 25 mm × 75 mm for rubbing machine tests. Standard cut edges quartz slides were purchased from Hellma, Germany.

Before film deposition, Silicon wafers and quartz slides were pre-cleaned by immersing firstly in a mixed solution of methanol and hydrochloric acid (1:1, v/v) for 30 minutes and then stored in a concentrated sulfuric acid solution for at least overnight. Methanol (>99%, Grade: analytical reagent) was purchased from Prolabo. Hydrochloric acid (HCl 37%) and concentrated sulfuric acid (H_2SO_4 95-97%) were purchased from Sigma-Aldrich. Finally, wafers and quartz slides were extensively rinsed with Milli-Q water (Milli-Q Gradient system, Millipore, Molsheim, France) with a resistivity of 18.2 MΩ·cm. and dried under a stream of nitrogen before the deposition of multilayer films.

All chemical products mentioned above were used without purification.

II.1.4. Protocol for film preparation by spraying

Except some cases, all polyelectrolyte multilayer films or polymer/gold nanoparticle films were deposited on a PEI precursor layer. The PEI layer was obtained by dipping a pre-cleaned Si wafer for 5 minutes into a PEI solution, followed by an abundant Milli-

Q water rinse and a drying step under a nitrogen flux before the spray or dipping deposition.

II.1.4.1. Manually operated sprayer cans: “Air Boy”

In this manuscript, most of the films have been deposited onto the substrate by spray with a commercial manual sprayer called “Air Boy” purchased from Carl Roth (ref, 0110.1; size, height 217, diameter 55 mm; nozzle, 0.40 mm). This spray bottle is made of polypropylene and polyethylene. Each experiment requires four sprayers: one for polyanion, one for polycation, one for the rinsing solution of polycation and one for the rinsing solution of polyanion.

II.1.4.2. Automated simultaneous spraying

In collaboration with BASF (Ludwigshafen, Germany), we have developed a new simultaneous spray system (Figure 3).

Figure 3, A is the general set up of this automatic spray machine. This spray machine is composed of four HPLC Compact Pump, type Bischoff 2250 (Figure 3C), four corresponding nozzles (Figure 3D), four gas regulators units (Figure 3) and a central control unit (Figure 3D). In such apparatus, liquid and gas are mixed in each nozzle before sprayed onto the sample surface. The major advantages of such system compared to manual sprayer are the precise control of air pressure and liquid flow rate (size and number of droplets), the ability to spray simultaneously several liquids and the possibility to develop a computer driven system.

Figure 3: Simultaneous spray machine (A) General set up (B) Central control unit (C) HPLC pumps and gas controller and (D) zoomed spray nozzles

The liquid flow rate range of the Bischoff HPLC Compact Pump 2250 is from 0.1ml/min to 19.9ml/min and the air pressure range is from 0MPa to 15MPa respectively. This machine has only been employed in the study of BASF poly(vinylamine)/poly(acrylic acid, sodium salt) film deposition.

II.1.4.3. Control parameters for manual spraying

Most samples were prepared by manual spray using the "air boy" sprayer following the set up shown in Figure [2]. The distance between sprayer nozzle and the vertically fixed sample was typically 10-15cm. Fluorescent pictures demonstrate that the center of spray spot is quite homogeneous although the edge of the spot is more or less inhomogeneous.

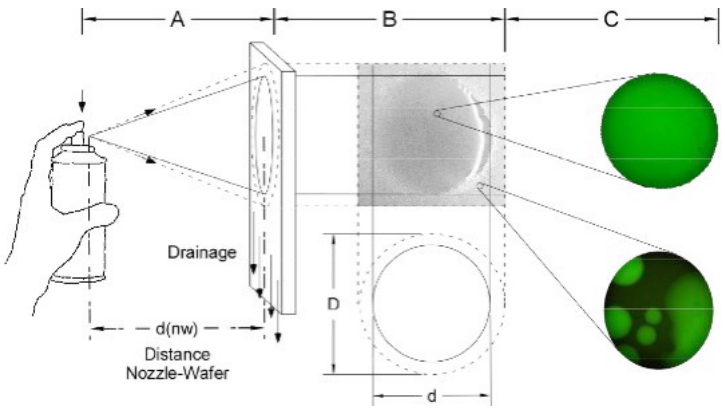

Figure 4: Experimental set up for manual spray[2].

A typical spray procedure consists on four steps, the spray of polycation or polyanion and the spray of rinse solution of polycation and polyanion respectively. Figure 5 shows a schematic representation of a spray cycle for a $(PSS/PAH)_n$ film deposition.

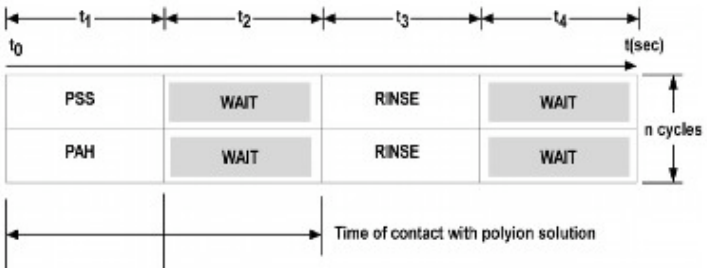

Figure 5: Schematic representation of a spray cycle for a $(PSS/PAH)_n$ film deposition

On a positively charge sample, the polyanion, PSS, is sprayed on the surface for t_1 time. After a t_2 waiting/adsorption time, the rinse solution is sprayed onto the surface for t_3 time. Finally, after a t_4 waiting/rinse time, the same protocol is repeated for the polycation, PAH. For a single layer pair, the total spray time is $(t_1+ t_2+ t_3+ t_4)\times 2$. During my research, typically, $t_1 = t_3 = 5$ seconds and $t_2 = t_4 = 15$ seconds, so the total spray time for a single layer pair is 80seconds.

II.2. Methods

II.2.1. Ellipsometry

The description of the principal of ellipsometry is adapted from the reference 3, reference 4.

Ellipsometry is an optical technique for the investigation of the thickness and the dielectric properties, such as refractive index or dielectric function, of thin film. Basically, it uses a polarized light as the investigation source; it measures the polarization changes of reflected or transmitted light beam. Typically, most of ellipsometers are used in reflection mode. The polarization changes is determined by the sample's properties like film thickness, refractive index etc, which makes ellipsometry a powerful instrument in the investigation of films with thicknesses that vary from several nanometers to several micrometers with an angstrom resolution. In addition, ellipsometry is a non-destructive and contactless characterization methods as all optical measurement technique. In terms of sample preparation, the sample should be covered by a optically homogeneous and

isotopic well-defined layers in order to get the best dielectric properties investigation of such layers.

II.2.1.1. Principal of ellipsometry measurement

II.2.1.1.1. Polarized light

Any light is an electromagnetic wave and can be represented by 2 vectors, the electric field $\vec{E}$ and the magnetic field $\vec{B}$. These two vectors are perpendicular to each other and also perpendicular to the propagation direction of the incident light wave. This propagation direction is defined by another vector $\vec{k}$ with the magnitude $\left|\vec{k}\right| = \frac{2\pi}{\lambda}$ where λ is the wavelength of investigated light wave. In an ellipsometry measurement, only the electric field vector $\vec{E}$ varies (magnetic field $\vec{B}$ is constant in ambient conditions).

The following image is extracted from wikipedia/elliptically polarization.

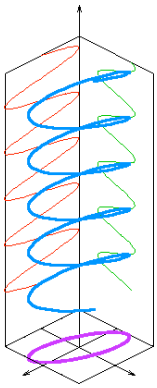

This image explains the elliptical polarization of the laser used in ellipsometry measurement. The laser from the light source is polarized by a polarizer. As a sinusoidal plan wave, polarized the laser can be divided into two linearly polarized waves in phase quadrature, with their polarization planes at right angles to each other. But the projection of this laser wave in its propagation direction is ellipse, where comes the notion of elliptically polarized laser.

The electrical filed vector $\vec{E}$ can also been divided into two components, one is parallel polarized to the plane of incidence or light wave propagation direction, called "*p-polarized*" electrical field vector $\vec{E}_p$, while another is perpendicular polarized, called "*s-polarized*" electrical field vector $\vec{E}_s$. The electrical field vector $\vec{E}$ and its parallel and

perpendicular components of incident light wave can been represented by a simplified coordinate system if the time dependence can been neglected (Equation 1).

$$\vec{E} = \begin{pmatrix} |E_p| e^{i\delta_p} \\ |E_s| e^{i\delta_s} \end{pmatrix} = \begin{pmatrix} E_p \\ E_s \end{pmatrix} \qquad \textbf{Equation 1}$$

The equation is the so called Jones vector equation, where $|E_p|$ and $|E_s|$ are the amplitudes of relative parallel and perpendicular electrical filed vector, δ_p and δ_s are the parallel and perpendicular phase of the electrical field vector.

The Jones vector defines the electrical properties of a polarized light, according to the difference between the parallel phase δ_p and the perpendicular phase δ_s. Thus, different polarization states can also be defined:

- A linear polarization, where $\delta_p - \delta_s = 0$ or $\delta_p - \delta_s = \pi$
- An elliptical polarization, where $\delta_p \neq \delta_s$ and $|E_p| \neq |E_s|$, where the electrical field oscillation forms an ellipse after one period.
- A circular polarization, where $\delta_p - \delta_s = \frac{\pi}{2}$ and $|E_p| = |E_s|$

II.2.1.1.2. Mathematical equations used in ellipsometry measurement

In a typical ellipsometry experiment, incident light with a well defined polarization state reaches the sample surface and after the surface reflection, the reflected light will change its polarization state. These changes are measured and calculated in order to find the desired sample information, such as film thickness or reflection index.

Both incident and reflected light beam can be described by their corresponding Jones vector (Equation 2).

$$\vec{E}_i = \begin{pmatrix} |E_p^i| e^{i\delta_p^i} \\ |E_s^i| e^{i\delta_s^i} \end{pmatrix} \quad \vec{E}_r = \begin{pmatrix} |E_p^r| e^{i\delta_p^r} \\ |E_s^r| e^{i\delta_s^r} \end{pmatrix} \qquad \textbf{Equation 2}$$

Where "*i*" and "*r*" represent the incident and reflected light beam.

In order to describe the changes in the state of polarization, two new equations Ψ (Equation 3) and Δ (Equation 4) are introduced:

$$\tan\Psi = \frac{\frac{\left|E_p^r\right|}{\left|E_p^i\right|}}{\frac{\left|E_s^r\right|}{\left|E_s^i\right|}} \qquad \textbf{Equation 3}$$

$$\Delta = \left(\delta_p^r - \delta_s^r\right) - \left(\delta_p^i - \delta_s^i\right) \qquad \textbf{Equation 4}$$

The tanΨ of the equation 3 describes the changes in the ratio of the reflected parallel electrical field vector and the incident parallel electrical field vector as well as the ratio of the reflected perpendicular electrical field vector and the incident perpendicular electrical field vector. The value of Ψ can be measured directly by ellipsometry. Δ corresponds to the phase difference of both incident and reflected light and can also be measured directly.

During an ellipsometry experiment, the reflectivity properties of a sample can be described by two reflection coefficients, r_p, the reflection coefficient in parallel direction and r_s, the reflection coefficient in perpendicular direction. These two coefficients represent the changes in both amplitude and phase of the reflected electric field E^r and the incident electric field E^i.

$$r_p = \frac{\left|E_p^r\right|}{\left|E_p^i\right|} e^{i(\delta_p^r - \delta_p^i)} \qquad r_s = \frac{\left|E_s^r\right|}{\left|E_s^i\right|} e^{i(\delta_s^r - \delta_s^i)} \qquad \textbf{Equation 5}$$

Using previous definitions, the following basic equation of ellipsometry can been obtained:

$$\frac{r_p}{r_s} = \tan\Psi \bullet e^{i\Delta} = \rho = \Re(\rho) + i\Im(\rho) \qquad \textbf{Equation 6}$$

This equation is composed two parts, a real part $\Re(\rho)$ and an imaginary part $\Im(\rho)$. During an ellipsometry experiment, the ellipsometer will measure directly the value of Ψ and Δ, then calculate the ratio of the reflection coefficient in parallel direction and the reflection coefficient in perpendicular direction.

II.2.1.2. Data acquisition

After the discussion about the reflected beam, we will now introduce the refraction in the presence of a film. If a sample is covered by a optically homogeneous and isotropic layer, the refraction of the incident light beam is determined by Descartes law:

$$N_0 Sin(\theta_0) = N_1 Sin(\theta_1) \qquad \textbf{Equation 7}$$

with: N_0, the refractive index of media 0
N_1, the refractive index of media 1
θ_0, the incident angle
θ_1, the refraction angle

As for light reflection, two transmission coefficients t_p and t_s can also been defined in the same way. They represent the ratio between transmitted electric filed vector and incident electric field vector in both parallel and perpendicular directions (Equation 8).

$$t_p = \frac{\left|E_p^t\right|}{\left|E_p^i\right|} e^{i(\delta_p^t - \delta_p^i)} \qquad t_s = \frac{\left|E_s^t\right|}{\left|E_s^i\right|} e^{i(\delta_s^t - \delta_s^i)} \qquad \textbf{Equation 8}$$

Taking into account the continuity of tangent component for electric field vector, both reflection coefficient (r_p, r_s) and transmission coefficient (t_p, t_s) can be represented as following:

$$r_p = \frac{N_1 \bullet Cos(\theta_0) - N_0 \bullet \cos(\theta_1)}{N_1 \bullet Cos(\theta_0) + N_0 \bullet \cos(\theta_1)} \qquad \textbf{Equation 9}$$

$$r_s = \frac{N_0 \bullet Cos(\theta_0) - N_1 \bullet \cos(\theta_1)}{N_0 \bullet Cos(\theta_0) + N_1 \bullet \cos(\theta_1)} \qquad \textbf{Equation 10}$$

$$t_p = \frac{2 \bullet N_0 \bullet \cos(\theta_0)}{N_1 \bullet Cos(\theta_0) + N_0 \bullet \cos(\theta_1)} \qquad \textbf{Equation 11}$$

$$t_s = \frac{2 \bullet N_0 \bullet \cos(\theta_0)}{N_0 \bullet Cos(\theta_0) + N_1 \bullet \cos(\theta_1)} \qquad \textbf{Equation 12}$$

These equations clearly demonstrate that both reflection coefficients (r_p, r_s) and transmission coefficients (t_p, t_s) depend only on the incident angle θ_0 and the refractive indexes of media 0 and media 1. In a typical ellipsometry experiment in air, the media 0 corresponds to air and the media 1 corresponds to the film present on the surface of the mirror.

During the measurement, the calculation of ρ leads to the identification of two parameters, Ψ and Δ, which are measured by the ellipsometer. If the incident angle is kept constant and only one wavelength of investigation light beam is employed. From these two measured parameters, the refractive index N and the thickness of a film can be calculated if the extinction coefficient of the substrate is known. During my research, this working mode has always been employed.

II.2.1.3. Basic experimental setup for constant-angle-of-incidence ellipsometry

Different ellipsometry instrument set up have been reviewed by Azzan and Bashara[5]. But only the experimental set up of ellipsometer with constant angle of incidence will be focused.

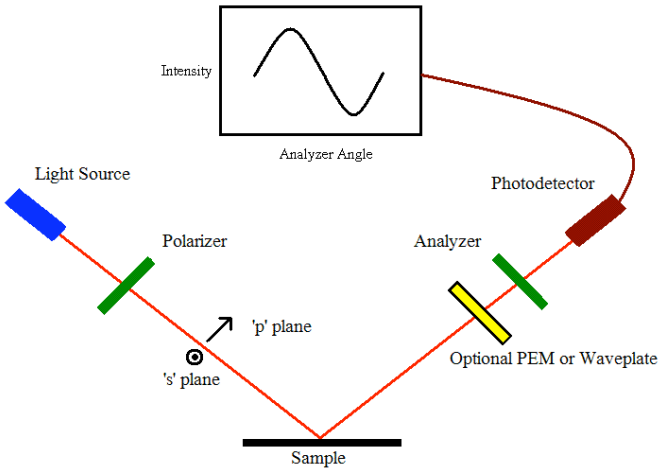

Figure 6: Schematic representation of an ellipsometer set up

Figure 6 shows a typical set up of an ellipsometer. A laser beam from the light source is polarized by a high-grade polarizer filter, into the "s" or "p" polarization plane compare to the sample. When the polarized laser beam hits the sample surface, an ellipticity, based on the dielectric properties of the sample surface, is created. The reflected light is filtered again by another polarizer, called analyzer. Behind the analyzer, a photodetector measures the variation of the sinusoidal change of the light intensity by rotating the analyzer. This variation is a function of the analyzer angle and can be used to determine

the components of the polarization in the "p" and "s" plane, r_p and r_s respectively. The ratio of r_p/r_s and the phase difference between r_p and r_s will determine the polarization ellipticity of the laser beam. These two quantities can be matched to the numeric predictions of the real and imaginary parts of Equation 6. Both real and imaginary parts in Equation 6 should satisfy the Kramers-Kronig relations, which will be discussed in the next section.

II.2.1.4. Limits of ellipsometric measurements

As mentioned above, the real and imaginary part should satisfy the Equation 6 and the so-called " Kramers-Kronig" relation which connects the real and imaginary parts of Equation 6.

For example, for a complex function $\chi(\omega) = \chi_1(\omega) + i\chi_2(\omega)$ of the complex variable ω, the Kramers-Kronig relations are given by:

$$\chi_1(\omega) = \frac{1}{\pi} \mathrm{P} \int_{-\infty}^{\infty} \frac{\chi_2(\omega')}{\omega' - \omega} d\omega' \text{ and } \chi_2(\omega) = -\frac{1}{\pi} \mathrm{P} \int_{-\infty}^{\infty} \frac{\chi_1(\omega')}{\omega' - \omega} d\omega' \qquad \textbf{Equation 13}$$

where P is the Cauchy principal value. From these two equations, we can clearly see that the real and imaginary parts of such a complex function are not independent and the full function can be reconstructed by giving just one of its parts.

By considering the integral $\oint \frac{\chi(\omega')}{\omega' - \omega} d\omega' = 0$, the complex function can be presented by:

$$\mathrm{P} \int_{-\infty}^{\infty} \frac{\chi(\omega')}{\omega' - \omega} d\omega' - i\pi\chi(\omega) = 0 \qquad \textbf{Equation 14}$$

By taking the theory of residues, the Equation 13 can be rearranged as a compact form of the Kramers-Kronig relations:

$$\chi(\omega) = \frac{1}{i\pi} \mathrm{P} \int_{-\infty}^{\infty} \frac{\chi(\omega')}{\omega' - \omega} d\omega' \qquad \textbf{Equation 15}$$

In an optical reflectivity analysis, the need of Kramers-Kronig relation is based on the fact that an refractive index of N a material and its dielectric constant ε have both a real and imaginary part, presenting as following:

$$N = n + ik = \sqrt{\varepsilon} \qquad \textbf{Equation 16}$$

Taking account into the reflectivity r and the electric field E in both "p" and "s" plane, the reflectivity of investigated light on sample's surface can be represented as:

$$r = \frac{\left|E^r\right|^2}{\left|E^i\right|^2} = \frac{\left|1-N\right|^2}{\left|1+N\right|^2} = \frac{(1-n)^2+k^2}{(1+n)^2+k^2} \qquad \textbf{Equation 17}$$

where E^r is the reflected electric field and E^i is the incident electric field.

Since the real and imaginary part of a complex function are not independent, the Kramers-Kronig relation will eliminate the free variable and permit to calculate the refractive index of components "n" and "k" by using the reflectivity "r". Beside a mathematical relation, the Kramers-Kronig relations have also a physical interpretation in a real optical reflectometry measurement. The real part of the function describes the light dispersion during the measurement while the imaginary part of the function describes how a system dissipates energy, which means the light absorption of the sample at the wavelength of the incident light.

II.2.1.5. Ellipsometers used in current research: PLASMOS SD2300 and Multiskop

During my research, two ellipsometers have been used: a PLASMOS SD2300 ellipsometer (Horiba Jobin Yvon, Chilly Mazarin, France) and a Multiskop ellipsometer (Optrel GbR, Kleinmachnow, Germany).

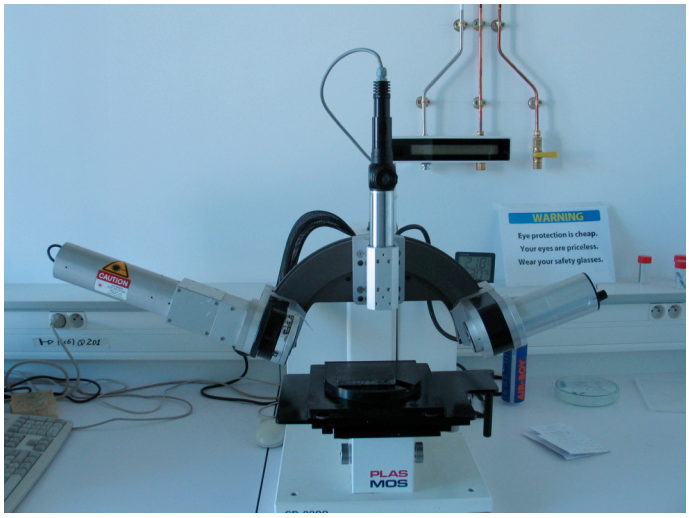

Figure 7: The PLASMOS SD2300 ellipsometer

The PLASMOS SD2300 ellipsometer (Figure 7), is used for routine measurements, operates with a He/Ne laser source at the single wavelength of 632.8 nm and at a constant incident angle of 70°. The refractive index of all polymer films was assumed to be constant at n = 1.465. While this procedure will lead to slightly incorrect values with respect to the absolute film thickness, it allows a quick determination of the relative film thickness. All film thickness values mentioned in this manuscript were obtained using this assumption. In order to determine the thickness of each layer pair, ten points were measured to obtain the average values for the film thickness and to determine the film homogeneity.

The Multiskop ellipsometer from Optrel GbR (Figure 8), operating at a laser wavelength of 632.8 nm and a constant angle of 70°, was used for the film thickness measurements with high precision, especially for samples prepared for Neutron reflectometry experiments (see Section Results and Discussions). The measurement was operated under a Multi70 software environment (version 8.0) and the film thickness was obtained by simulation under a Elli software environment (version 5.2). In order to obtain film thicknesses and refractive indexes of the samples. A model with pre-set film thickness and refractive index was applied. The real thickness and refractive index was calculated by combining the measured data and this model. Compared to the PLASMOS SD2300 ellipsometer, the Multiskop will offer a more precise film thickness value as well as the film refractive index, but the measurement operating of the Multiskop takes more time than the PLASMOS SD2300. Typically 30 minutes or more for a single spot are needed for a Multiskop measurement compared to 1 minute/sample for a PLASMOS SD2300 measurement for 10 spots.

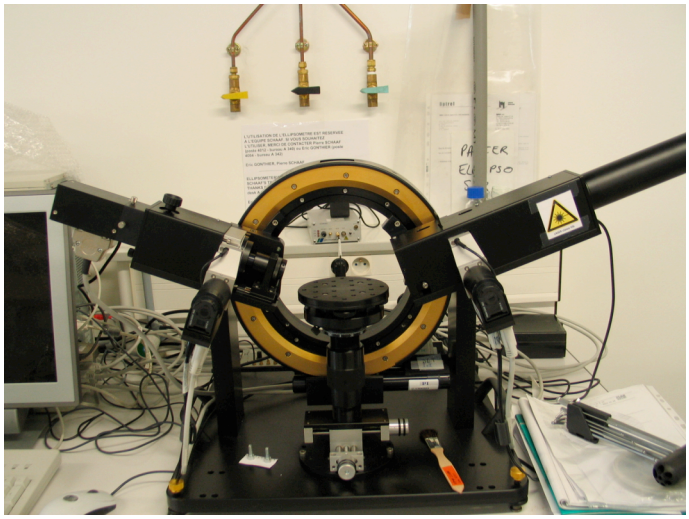

Figure 8: The Multiskop ellipsometer

For a polymer, the imaginary part of the refractive index is negligible because most polymers have no measurable absorbance in the range of the operation laser wavelength, which is around 632.8nm. As consequence, there's no Kramers-Kronig restriction for most polymer film measurement. However, attention should be paid for the polymer/nanoparticle films, especially polymer/gold nanoparticle films. Due to the strong plasmon absorption of gold nanoparticle from 550-600nm, which is close to operating laser wavelength of our ellipsometers. During such a measurement, there is a measurable light absorption by the gold nanoparticle present within the films, As consequence, the imaginary part of the refractive index should not be negligible any more, corresponding to a Kramers-Kronig restriction.

However, qualitative interpretation of the film thickness is possible even when neglecting the absorbance of the film. For both PLASMOS SD2300 and Multiskop ellipsometers, there is no imaginary part in the refractive index settings, the thickness of polymer/gold Nanopaticles film measured by these ellipsometers will be an indicative value other than a true value in the case of pure polymer film. However, these values will give us a rapid estimation for the film growth mechanism. The growth of such polymer/gold nanoparticle film was also monitored by Ultraviolet-Visible Spectroscopy.

II.2.2. Ultraviolet-Visible Spectroscopy

Ultraviolet-Visible (UV-Visible) Spectroscopy refers to the spectroscopy of photons in the UV-Visible region. The source provides light wavelengths in the visible, near ultraviolet and near infrared zones. This method is quantitative for determining the concentration of an absorbing species in solution.

II.2.2.1. Beer-Lambert Law

The use of UV-Visible spectroscopy is based on the Beer-Lambert Law (Equation 18):

$$A = -\log_{10}(I/I_0) = \varepsilon \times c \times L \qquad \textbf{Equation 18}$$

where A is the measured absorbance, I_0 is the intensity of incident light at a given wavelength, I is the transmitted intensity, L is the length of cell containing the sample and c is the concentration of the absorbing species in the solution. For each species at a specific wavelength, ε is a constant known as the molar absorptivity or extinction coefficient. This constant is a fundamental molecular property in a given solvent, at a particular temperature and pressure.

The Beer-Lambert law is very useful for characterizing UV-Vis absorbing compounds. However, it is not a universal relationship for the concentration and absorption of all substance. Sometime, a second order polynomial relationship between absorption and concentration is required for some very large, complex molecules such as organic dyes.

II.2.2.2. Experimental setup of an UV-Visible spectrophotometer

The instrument used in UV-Visible spectroscopy is called a UV-Visible spectrophotometer. It measures the intensity of light passing through a sample (I), and compares this intensity to its original intensity (I_0). The ratio I/I_0 is called transmittance, usually expressed as a percentage (%T). The absorbance, A, is based on the transmittance as well:

$$A = -\log_{10}(\%T/100\%)$$

The basic set up for a spectrophotometer is a light source, a sample holder, a diffraction grating or monochromator to separate the different wavelengths of light and a detector.

II.2.2.3. Applications of UV-Visible

UV-Visible spectroscopy is routinely used in the determination of materials containing metal ions and highly conjugated organic compounds. The d electrons of the metal ions or organic compounds, especially those with a high degree of conjugation can be excited by the investigated light from one electronic state to another, resulting an absorption peak in the spectrum. Every specific substance has its unique absorption peak at a certain wavelength, which makes the UV-Visible spectroscopy a quantitative and qualitative technique to characterize the presence of absorbing substances.

During my graduate research, a Varian CARY 500 Scan UV-Vis-NIR spectrometer with a wavelength range of 190-800nm was used for UV-Visible analysis (Figure 9).

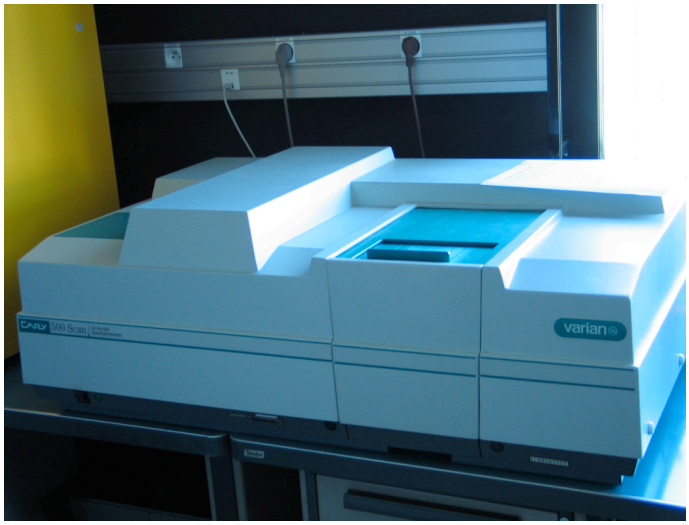

Figure 9: The Varian CARY 500 Scan UV-Vis-NIR spectrometer

II.2.3. Atomic force microscopy (AFM)

The description of the principal of ellipsometry is adapted from the reference 6.

The atomic force microscopy (AFM) is similar to the high-resolution scanning tunneling microscope (STM), developed by Binning, Quate and Gerber in 1986[7]. The atomic force microscope does not really visualize the sample surface as scanning electronic microscope but it feels the surface with a mechanical probe by measuring the interaction variations between the scanning probe and the sample surface. The use of piezoelectric elements facilitates the movements of the scanning probe on the surface, which makes AFM one of the best analytical instruments for imaging, measuring and manipulating small objects on the surface with a nanometric resolution.

II.2.3.1. Principle and Basic set up of AFM

The AFM is typically composed of a cantilever with a sharp tip at its end as scanning unit; a piezoelectric element as mechanical movement unit; a laser source and a photodiode detector as analytical unit. A schematic representation of the basic set up of an AFM is depicted in Figure 10.

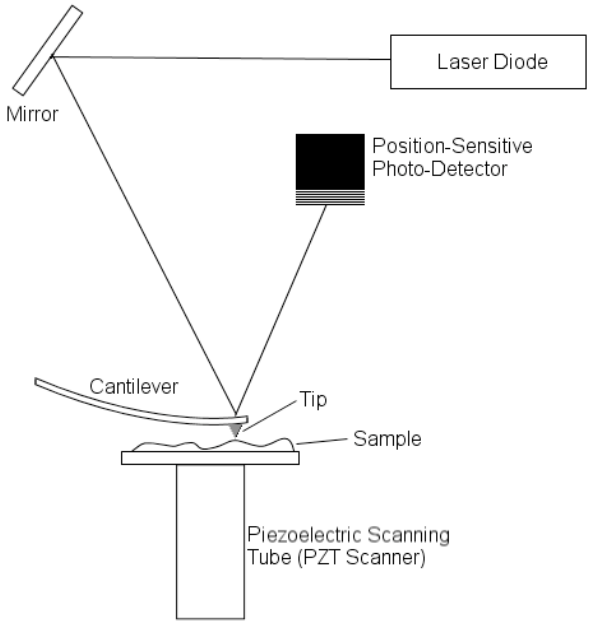

Figure 10: Schematic representation of the AFM set up

The cantilever and the tip are normally made of silicon or silicon nitride. The curvature radius of the tip is on the order of nanometers and the tip is ideally terminated by a single atom in order to ensure the best resolution.

When the tip is brought into proximity of a sample surface, interaction energy between the tip and the sample is schematically presented in Figure 11. In fact, Figure 11 represents the interaction energy between two atoms. But ideally, the tip of AFM is terminated by a single atom, which the interaction between the AFM tip and those on the surface can be illustrated by Figure 11.

The interaction energy between AFM tip and atom on the surface has two components, one repulsive, indicating that the tip is very close to the surface and one attractive, indicating that the tip is not too close to the surface. Typically, in an AFM imaging, interactions like capillarity interactions, chemical bonding, electrostatic interactions etc could be excluded except the Van der Waals interactions, which corresponds to the minimum level of interaction energy in Figure 11. It is exactly the region where AFM tip could detect the interaction energy changes, for example, from repulsive to attractive. According to the strength of these interaction energies, there will be a deflection of the AFM cantilever and this deflection is in agreement with the Hooke's law. The deflection of the cantilever is measured using a laser spot reflected from the top surface of the

cantilever into an array of photodiode, the "movement" of this laser spot plus the computational simulation will restore the topology of the sample surface.

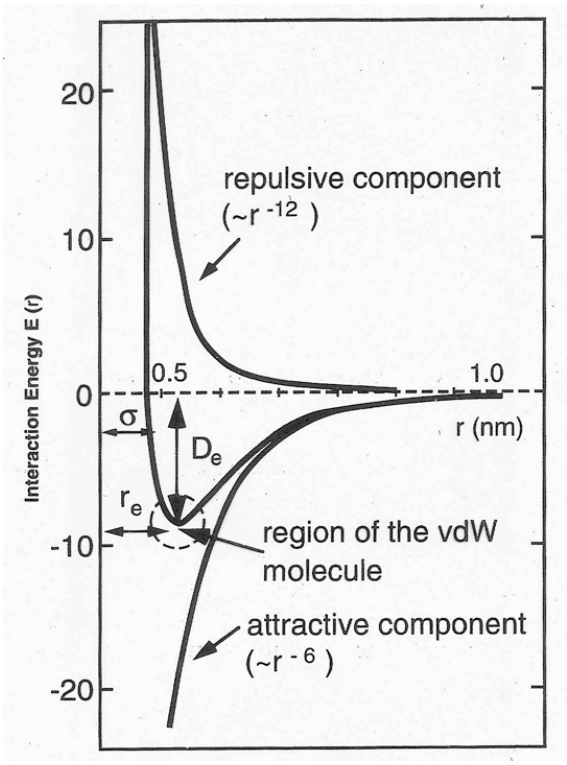

Figure 11: Presentation of surface/AFM tip interaction energy variation as a function of their distance

An attention should be paid here for data acquisition. Two types of data can be recorded during the scan, either the force variation can be recorded by immobilizing sample and moving the tip at a constant height or the 3D movement of the piezoelectric element can be recorded by maintaining the same force during the scan. Both type will lead to the same topology for same sample, but if the tip is scanned at a constant height, there is a risk that the tip may collide with the surface if the sample roughness is too important, leading to damage the tip. Hence, in most case, a feedback mechanism is used to adjust the tip-sample distance in order to maintain a constant force between the tip and the sample.

The sample is mounted on a piezoelectric tube and can be moved in the z direction for maintaining the constant force, and the x and y directions for scanning the sample.

II.2.3.2. AFM Imaging

The AFM can be operated in different imaging modes, such as static (also called contact) mode or dynamic (tapping) mode.

The first developed imaging mode is static (contact) mode. In this mode, the tip deflection is used as a feedback signal. Normally, a low stiffness cantilever is used in order to minimize the influence of acoustic noise. However, when the tip is approaching to the surface, the attractive forces may become quite strong and causing the tip to "snap-in" to the surface. Thus, the contact mode AFM is always done in contact with the sample where the overall force is repulsive, where comes from the name "contact mode". In this mode, the force between the tip and the surface is kept constant during scanning by maintaining a constant deflection. In this contact mode, interactions between AFM tip and the surface is repulsive, Figure 11, repulsive component.

In the dynamic mode (tapping mode), the cantilever is externally oscillated at or close to its fundamental resonance frequency or a harmonic. The oscillation amplitude, phase and resonance frequency are modified by tip-sample interaction forces. These changes in oscillation with respect to the external reference oscillation provide information about the samples characteristics. In this mode, interactions between AFM tip and the surface is attractive, Figure 11, attractive component.

Both frequency and amplitude can be modulated. In frequency modulation, changes in the oscillation frequency provide information about tip-sample interactions. Frequency can be measured with very high sensitivity and thus the frequency modulation allows for the use of very stiff cantilevers. In amplitude modulation, changes in the oscillation amplitude and/or phase provide the feedback signal for imaging, in this amplitude modulation, changes in the phase of oscillation can be used to discriminate between different types of materials on the surface because this change reflect directly the interaction intensity between the materials and the tip. Moreover, in ambient condition, most samples develop a liquid meniscus layer on the surface, which may stick the tip to the surface during the scan for a short-range forces investigation, the dynamic imaging mode has bypassed this problem very well but the resolution is better in contact mode.

During my research, the dynamic (tapping) imaging mode was employed and details of this imaging mode will be discussed in the next section.

II.2.3.3. Tapping mode

Tapping mode is a key advance in AFM. This potent technique allows high resolution topographic imaging of sample surfaces that are easily damaged, loosely hold to their substrate or difficult to image by other AFM techniques. Tapping mode overcomes problems associated with friction, adhesion, electrostatic forces, and other difficulties because, during the tapping mode measurement, the tip is alternately in contact with the surface. This intermittent contact with surface provides high resolution and avoids dragging the tip across the surface during the scan.

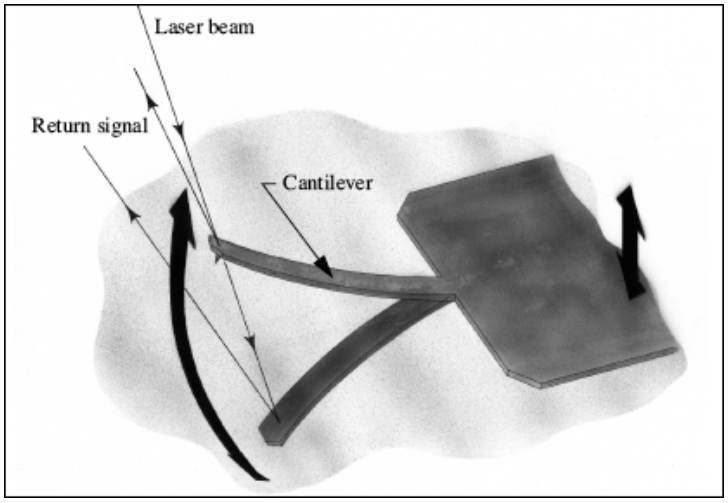

Figure 12: Schematic representation of the cantilever in air in tapping mode[6a]

In tapping mode, the cantilever is driven to oscillate up and down at near its resonance frequency by a small piezoelectric element mounted in the AFM tip holder (Figure 12). This vertical excitation of cantilever causes the tip to bounce up and down. As the cantilever bounces vertically, the reflected laser beam is deflected in a regular pattern over the photodiode array, generating a sinusoidal electronic signal. The signal is converted to a root mean square (RMS) amplitude value.

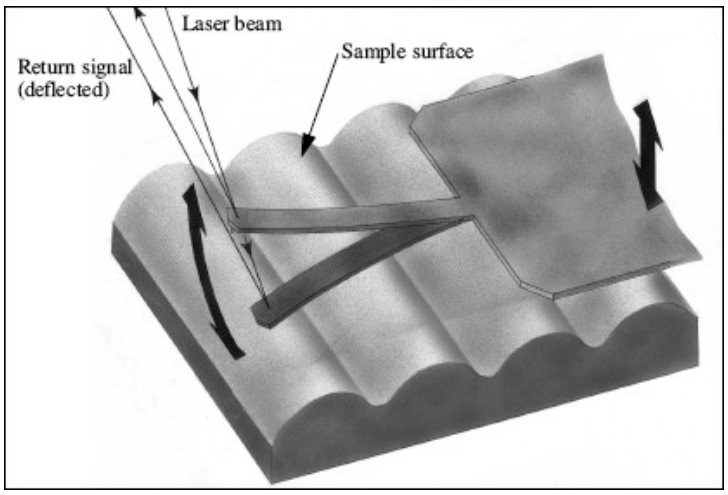

Figure 13: Schematic representation of the cantilever on sample surface in tapping mode. Deflection of the cantilever and return signal are exaggerated[6a]

Figure 13 represents the same cantilever at the sample surface. Although the piezoelectric element continues to excite the cantilever with the same energy, the tip is deflected in its encounter with the surface. The reflected laser beam ("return signal") reveals information about the vertical height of the sample surface and some characteristics of the sample material itself. These material characteristics may include elasticity ("hardness"), magnetic and/or electric forces present.

During tapping mode operation, the cantilever oscillation amplitude is maintained constant by a feedback loop. Selection of the optimum oscillation frequency is software-assisted and the force on the sample is automatically set and maintained at the lowest possible level. When the tip passes over a bump in the surface, the cantilever has less room to oscillate and the amplitude of oscillation decreases. Conversely, when the tip passes over a depression, the cantilever has more room to oscillate and the amplitude increases (approaching the maximum free air amplitude). The amplitude of this oscillation is greater than 10nm, typically 100 to 200nm. An electronic servo uses the piezoelectric actuator to control the height of the cantilever above the sample. The servo adjusts the height to maintain a set cantilever oscillation amplitude as the cantilever is scanned over the sample. A Tapping AFM image is therefore produced by imaging the force of the oscillating contacts of the tip with the sample surface.

When the tip contacts the surface, the high frequency (50k - 500k Hz) makes the surfaces stiff (viscoelastic), and the tip-sample adhesion forces are greatly reduced. Tapping Mode inherently prevents the tip from sticking to the surface and causing damage during

scanning. Also, the surface material is not pulled sideways by shear forces since the applied force is always vertical. Another advantage of the Tapping Mode technique is its large, linear operating range. This makes the vertical feedback system highly stable, allowing routine reproducible sample measurements.

In this imaging mode, the variation in amplitude oscillation gives directly surface topology information of the sample while the phase oscillation variation reflects to the chemical contrast of the sample surface.

II.2.3.4. Advantages and limits of AFM measurements

The AFM has several advantages over the scanning electron microscope (SEM). Unlike the electron microscope, which provides a two-dimensional projection or a two-dimensional image of a sample, the AFM provides a true three-dimensional surface profile. Additionally, samples viewed by AFM do not require any special treatments (such as metal/carbon coatings) that would irreversibly change or damage the sample. While an electron microscope needs an expensive vacuum environment for proper operation, most AFM modes can work perfectly well in ambient air or even a liquid environment. This makes it possible to study biological macromolecules and even living organisms.

A disadvantage of AFM compared with the scanning electron microscope (SEM) is the image size. The SEM can image an area on the order of millimeters by millimeters with a depth of field on the order of millimeters. The AFM can only image a maximum height on the order of micrometers and a maximum scanning area of around 150 by 150 micrometers.

Another inconvenience is that an incorrect choice of tip for the required resolution can lead to image artifacts. Traditionally the AFM could not scan images as fast as an SEM, requiring several minutes for a typical scan, while a SEM is capable of scanning at near real-time (although at relatively low quality) after the chamber is evacuated. The relatively slow rate of scanning during AFM imaging often leads to thermal drift in the image, making the AFM microscope less suited for measuring accurate distances between artifacts on the image. Even though, The AFM is a major investigation instrument during my research for visualizing the surface topology.

All Atomic Force Microscopic measurements were performed on MULTIMODE AFM supplied by Veeco USA with a controller Nanoscope IIIa (formerly called Digital Instruments.) For surface topology studies, AFM was operating in tapping mode with a non-coated Silicon cantilever (Veeco, model TAP150, typical frequency is about 68-132 kHz).

II.2.4. A simple mechanical wear test with rubbing machine

A rubbing machine was used for mechanical resistance tests on films at room temperature. This rubbing machine was built by the atelier mechanic department of L'Institut Charles Sadron[8]. The working pressure of this rubbing machine is 2 bars. The principle of the rubbing machine consists of brushing the sample surface, which is held by a pneumatic vacuum pump (Figure 14). The brushing cycles are automated and controlled by an electropneumatic way. This rubbing machine is not a quantitative apparatus, so there are no exact values for applied force, but for each rubbing, the applied force is kept constant, which means, for all rubbing test, the operating conditions are the same.

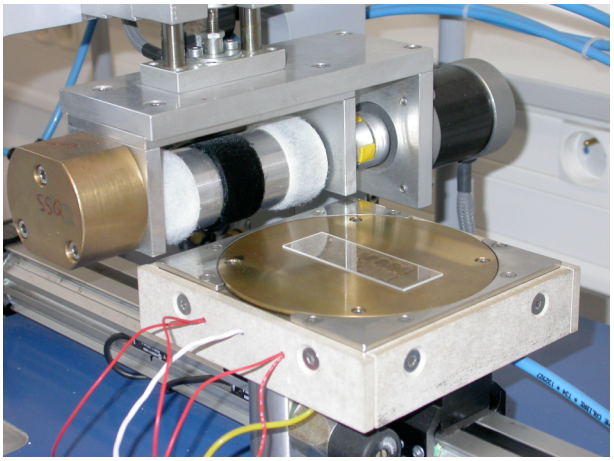

Figure 14: the Rubbing machine

II.2.5. Neutron reflectometry

This part is adapted from the reference 9.

Neutron reflectometry is a technique for measuring the inner structure of thin films, this technique is very similar to X-ray reflectometry or ellipsometry. Briefly, this technique involves shinning a highly collimated neutron beam onto a flat sample surface and measuring the coefficient of reflected radiation intensity as a function of scattering angle

or neutron wavelength. The reflectivity profile curve provides detailed information about the structure of the surface, including the thickness, density and roughness of any thin films layered on the substrate (single layer or a multilayer).

Compared to other reflectometry technique, neutron reflectometry has several specialties. The first specialty is that the neutron interacts directly with atoms nucleus, other than electronic cloud in a X-ray reflectometry measurement. This neutron-nucleus interaction is a short-distance interaction and can be presented by a Fermi punctual pseudo-potential function. This interaction depends not only on the nature of an element in the periodic table but also on the nature of various isotopes of the same element. For example, if all hydrogen atoms in a molecule have been replaced by deuterium atoms, there will be a significant modification in term of refractive index, which can be easily measured by a neutron beam, but the physical property of this molecule is not changed.

The second specialty is that the neutron has a spin ±1/2, making an interaction with atoms having magnetic moment possible. This specialty permits the measurement of the magnetic moment distribution in a thin film, even though this specialty is not employed in my research.

The last important specialty of neutron reflectometry is that neutrons have a very low absorption by investigated materials (except for Li, B, Ga etc). This low absorption is normally negligible, making a measured refractive index without imaginary part, as explained in Ellipsometry section by Kramers-Kronig relations.

What's more, the energy of incident neutron beam is quite small, making this technique non destructive, which is very important in biology or thin film measurement.

II.2.5.1. Principle of the neutrons reflectometry

In this section, the magnetic moment of neutrons and absorption by investigated materials are negligible.

II.2.5.1.1. Interaction neutron-nucleus and calculation of refractive index for neutrons

A neutrons beam arrives on a surface with an incident angle θ and reflected by the same angle θ (Figure 15), there are also some neutrons penetrating in the materials as a transmitted wave. This surface is separated by the interface between the vacuum or air (reflection index n=1) and the material with a reflection index n.

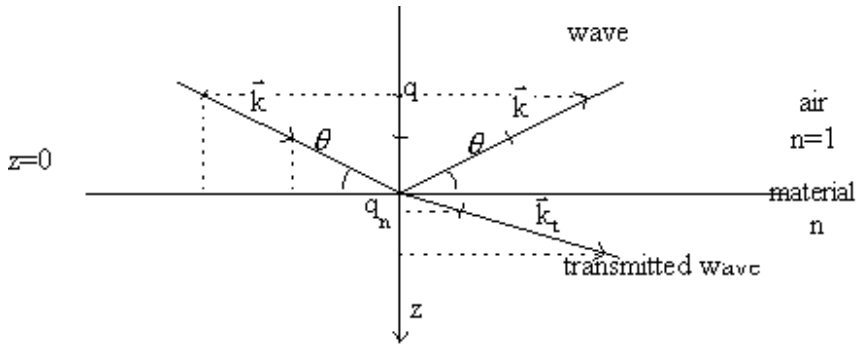

Figure 15: Schematic representation of the reflection of a neutron beam on a flat surface

In vacuum or in air, the wave vector k of a single incident neutron with a wavelength λ can be described by equation 19:

$$k = \frac{2\pi}{\lambda} \qquad \textbf{Equation 19}$$

The energy of this neutron is given by equation 20:

$$E = \frac{\hbar^2}{2m} k \qquad \textbf{Equation 20}$$

where $\hbar$ is the reduced Plank constant and m is the weight of the neutron.

In the material with refractive index n, the neutron interacts with the atom nucleus, this interaction can be described by a Fermi pseudo-potential V(r) by considering that neutron interacts punctually and independently with a single atom, given by equation 21:

$$V(r) = b\left(\frac{2\pi\hbar^2}{m}\right)\delta(r) \qquad \textbf{Equation 21}$$

where δ(r) is a Dirac function and b is the neutron coherent scattering length, which describes the interaction between neutron and atom nucleus. This neutron coherent scattering length is composed by a real part and an imaginary part. For all following sections, the imaginary part of coherent scattering length is negligible because of the low absorption of neutrons by materials.

In the vacuum or in air, the wave function of a neutron can be described by the Schrödinger equation:

$$\frac{\hbar^2}{2m}\Delta\Psi(r) + \left[E - V(r)\right]\Psi(r) = 0 \qquad \textbf{Equation 22}$$

In z direction, where reflection takes place, the potential function V(r) depends only on z, the Schrödinger equation can be re-written:

$$\frac{\hbar^2}{2m}\frac{d^2\Psi_z}{dz^2}+\left[E_z-V_z\right]\Psi_z=0 \qquad \textbf{Equation 23}$$

The potential V_z in the film can be calculated from the integration of Fermi pseudo-potential:

$$V_z=\frac{1}{V}\int_v V(r)dr=\frac{2\pi\hbar^2}{m}Nb \qquad \textbf{Equation 24}$$

where N is the number of atoms per volume unit and the product Nb is called the neutron coherent scattering length density.

The interaction neutron-nucleus and energy exchange take place only in the materials with the refractive index n when the neutron penetrate into the materials, causing an elastic diffusion. The energy conservation at z=0 permits to express the wave vector of neutron in the middle materials k_n as a function of k and v_z in equation 25:

$$E=\frac{\hbar^2k^2}{2m}=\frac{\hbar^2k_n^2}{2m}+V_z \qquad \textbf{Equation 25}$$

From Equation 24 and 25, Equation 26 can be obtained:

$$k_n^2=k^2-4\pi Nb \qquad \textbf{Equation 26}$$

If the material is homogeneous, the reflection index can be expressed by the ration of wave vector in the middle of materials and in vacuum or air:

$$n^2=\frac{k_n^2}{k^2}=1-\frac{\lambda^2}{\pi}Nb \qquad \textbf{Equation 27}$$

At the interface between the air and a medium of indices n, Descartes' law can be written: $\cos\theta=n\cos\theta_n$, the total reflection occurs if $\theta\le\theta_c$, where θ_c (the critical angle) is reflection angle and $\theta_n=0$.

When n>1, there is no total reflection, meaning that $\cos\theta_c = n$, while when n is close to 1, n can be developed by:

$$n \approx 1 - \frac{\lambda^2}{2\pi} Nb \qquad \textbf{Equation 28}$$

and we can get

$$1 - (\sin\theta_c)^2 = 1 - \frac{\lambda^2}{\pi} Nb \qquad \textbf{Equation 29}$$

which leads to equation 30:

$$\sin\theta_c = \sqrt{\frac{Nb}{\pi}\lambda} \qquad \textbf{Equation 30}$$

II.2.5.1.2. Reflection on a stratified film with reflection index n

The projection of wave vector on z direction, perpendicular to the surface, is defined as q, $q = \frac{2\pi}{\lambda}\sin\theta$, see Figure 15.

If the film is stratified, which means the film is composed by many layers units, the propagation of wave in layer p and layer p+1 can be written as following:

$$\Psi_z(z_p) = A_p \exp(iq_p z_p) + B_p \exp(-iq_p z_p)$$
$$\Psi_z(z_{p+1}) = A_{p+1} \exp(iq_{p+1} z_{p+1}) + B_{p+1} \exp(-iq_{p+1} z_{p+1})$$

Equation 31

where i^2=-1 and A_p, B_p are respectively the incoming and outgoing amplitudes in the layer p. We have also:

$$q_p^2 = q^2 - 4\pi Nb_p,\ q_{p+1}^2 = q^2 - 4\pi Nb_{p+1} \qquad \textbf{Equation 32}$$

By applying the continuity condition at the interface p/p+1, we get:

$$\Psi_z(z_p) = \Psi_z(z_{p+1}) = u(z_{p/p+1}),\ \Psi_z'(z_p) = \Psi_z'(z_{p+1}) = u'(z_{p/p+1}) \qquad \textbf{Equation 33}$$

the reflectivity at this interface is defined as the ratio between the reflected beam intensity and the incident beam intensity on layer p+1:

$$R = \frac{|B_p|^2}{|A_p|^2} = \left| \frac{1 - \dfrac{u'(z_{p/p+1})}{iq_p u(z_{p/p+1})}}{1 + \dfrac{u'(z_{p/p+1})}{iq_p u(z_{p/p+1})}} \right|^2$$ **Equation 34**

From equation 34, we calculate the reflectivity of the last interface, which is the layer in contact with the substrate. By repeating this calculation, the reflectivity at each interface in the thin film could be obtained, till the interface of outmost layer and air for example.

II.2.5.1.3 Ideal interface and the Fresnel reflectivity

If the layer p and p+1 are replaced by air and a substrate with reflection index n, this interface is perfect without any roughness as well. The reflectivity at this interface is called Fresnel reflectivity. In this case, $B_{p+1}=B_s=0$ because no reflectivity reaches at $z=\infty$. The Fresnel reflectivity can be written as:

$$R_F = \left|\frac{B}{A}\right|^2 = \left|\frac{q - q_s}{q + q_s}\right|^2 \text{ or } R_F = \left| \frac{1 - \left(1 - \left(\dfrac{q_c}{q}\right)^2\right)^{1/2}}{1 + \left(1 - \left(\dfrac{q_c}{q}\right)^2\right)^{1/2}} \right|^2$$ **Equation 35**

where q_c and q_s are from:

$$q_c^2 = 4\pi N b_s \text{ and } q_s^2 = q^2 - 4\pi N b_s = q^2 - q_c^2$$

Figure 16 represents a typical Fresnel reflectivity curve; the plateau corresponds to the total reflection.

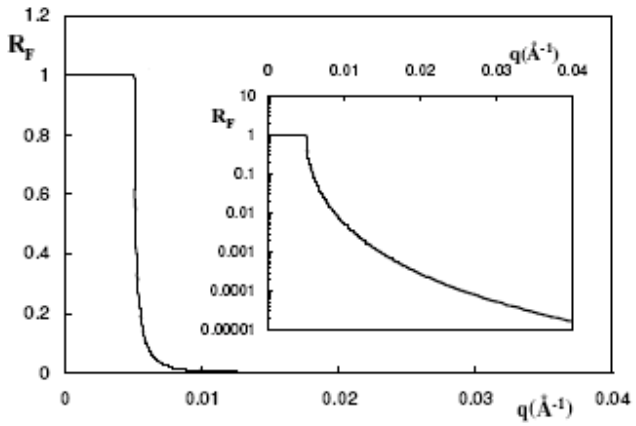

Figure 16: Presentation linear and semi-logarithmique representation of Fresnel reflectivity curve as a function of q (example interface air/silicium). Imgae extracted from reference 9

II.2.5.1.4. A homogeneous film on a substrate

In this last section, we will discuss the reflection on air/substrate interfacein the case of a homogeneous film on a substrate (Figure 17). In such a system, there are three medium: air with a reflection index n=1; the film with a reflection index n_1, a thickness d and a neutron coherent scattering length density Nb_1; the substrate with a reflection index n_s, a thickness D=∞ and a neutron coherent scattering length density Nb_s. The interface air/film is on position z=0 and the interface film/substrate is on position z=d.

When the incident neutron wave arrives at the air/film interface, the wave will be reflected first at z=0, then some neutrons penetrate into the film and are reflected again by the interface film/substrate at z=d. These two reflected wave will interfere between them. The interference will be constructive or destructive according to their path difference. As result, the reflectivity curve should present some interference fringes and the film thickness can be calculated from these fringes.

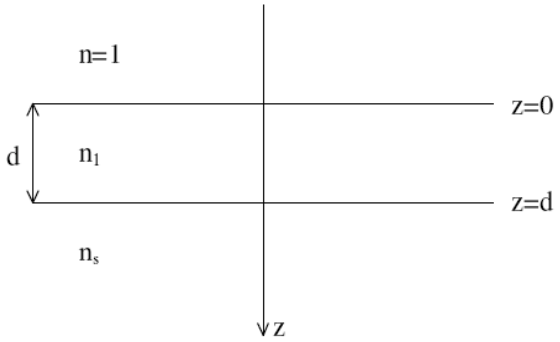

Figure 17: Schematic representation of a homogeneous film deposited on a substrate

After some modification, the reflectivity is re-written as:

$$R = \frac{\cos(2q_1 d)\left[1+\left(\frac{q_s}{q}\right)^2-\left(\frac{q_1}{q}\right)^2-\left(\frac{q_s}{q}\right)^2\right]+1-4\frac{q_s}{q}+\left(\frac{q_s}{q}\right)^2+\left(\frac{q_1}{q}\right)^2+\left(\frac{q_s}{q_1}\right)^2}{\cos(2q_1 d)\left[1+\left(\frac{q_s}{q}\right)^2-\left(\frac{q_1}{q}\right)^2-\left(\frac{q_s}{q}\right)^2\right]+1+4\frac{q_s}{q}+\left(\frac{q_s}{q}\right)^2+\left(\frac{q_1}{q}\right)^2+\left(\frac{q_s}{q_1}\right)^2} \qquad \textbf{Equation 36}$$

from this equation, we can clearly see the reflectivity R as a function of q presents some oscillation. The frequency of these oscillation is calculated from $2q_1d=m*2\pi$. The modified Bragg law at critical angle is presented by $2d\sqrt{\sin^2\theta_m-\sin^2\theta_c}=m\lambda$. These oscillations are called Kiessig Fringes[10] (Figure 18).

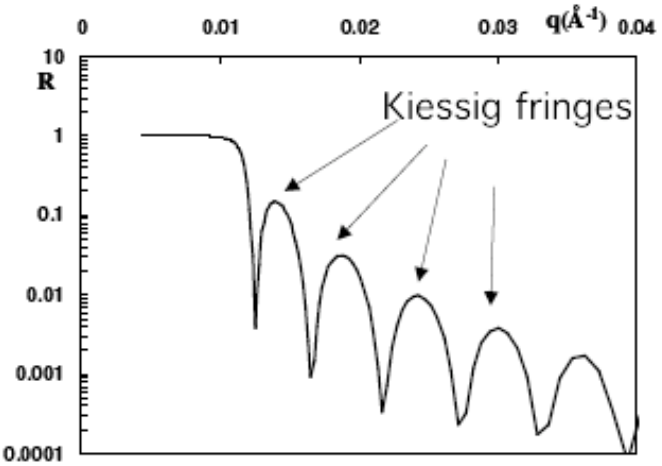

Figure 18: Schematic representation of reflectivity R as a function of q showing Kiessig fringes. Image extracted from reference 9

Until now, the surface or interface discussed in neutron reflectometry is surface/interface perfect, but in a real experiment, the sample will always have some defects, like surface roughness and molecule or polymer inter-diffusion in the film. These defects will modify slightly the shape of the reflectivity curve, as result, an adjustment is needed by fitting the experimental data.

II.2.5.2. Advantages of neutron reflectometry measurement

Neutron reflectometry operates similarly as other reflectivity techniques, in particular optical reflectometry or X-ray reflectometry, by using the same principle. This technique offers some advantages in a few significant ways.

Most important advantage is the interaction neutron-nucleus, that makes this technique more sensitive for measuring some elements, especially some lighter element, like hydrogen, carbon, nitrogen, oxygen etc. This sensitivity to isotopes will enhance greatly the contrast for the measurement.

Moreover, neutrons are highly penetrating but non-perturbing, which give a great flexibility in sample environment and permit the use of delicate samples like biological specimens. On the contrary, the X-ray exposes damage for certain samples and laser light will modify the physical property of certain samples (photo-resist as well). Also, optical reflectometry may include ambiguity due to the optical anisotropy, which can be resolved by neutron reflectometry.

II.2.5.3. The EROS G3 *bis* neutron reflectometry at the Laboratoire Léon Brillouin, Saclay FRANCE

II.2.5.3.1. Variable angle versus time of flight measurement

According to equation 31, the reflectivity is recorded as a function of wave vector q during a neutron reflectometry experiment. There are two different methods for measuring the reflectivity as a function of wave vector (Figure 19).

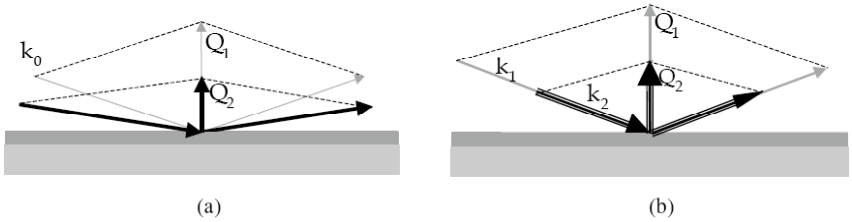

Figure 19: Principle of the neutron reflectivity measurement (A) θ, 2θ: variation of θ with a fixed neutron wavelength λ (B) time of flight: variation of neutron wavelength λ with a fixed incident angle θ

The first method is the (θ, 2θ) method, which is also used in X-ray reflectometry (Figure 19A). First, a monochromatic neutron beam has been sent to the sample surface at a

shaving incident angle, and then, a step-by-step measurement of reflected beam intensity is performed by turning the sample at a small angle θ and the detector at an angle 2θ. Since the wave vector is a function of incident angle, $q = \frac{2\pi \sin\theta}{\lambda}$, the variation of θ corresponds to the variation of wave vector q. Thus, a variation R~f (q) can also obtained as well.

The second method called "time of flight" can be employed in neutron reflectometry for measuring the reflectivity by fixing the incident angle θ and varying the neutron wave length λ (Figure 19B). The neutron flying speed can be easily calculated by using the De Broglie relation $v = \frac{h}{m\lambda}$, where h is the Plank constant. By using a chopper, a polychromatic neutron impulsion is sent to the sample. At time t=0, the beam reaches the sample surface at a shaving incident angle. After a certain time t, the reflected neutrons are captured by the detector located far away from the chopper at a distance L. The respectively neutron wavelength can be calculated by using the equation $\lambda = \frac{h}{mL}t$. The chopper is in rotation at a certain speed by ensuring that slow neutrons in the impulsion will be captured by the detector before rapid neutrons.

Before the measurement of the reflection coefficient, a preliminary measurement is necessary. An incident beam without reflection should be measured in order to know the energy dispersion of the incident beam. Then, the reflected beam intensity is divided by the incident beam for each wavelength in order to calculate the reflection coefficient.

This method is very practical for certain experiment, especially for air/liquid sample interface because the sample is stationary during the whole measurement and there's no need to turn around the sample as in the (θ, 2θ) method. Moreover, every reflectivity curves is measured at the same time.

Typically, the incident angle of neutron beam for this method is from 0.5° to 5°, corresponding a wave vector q varying from 0.005$Å^{-1}$to 0.3 $Å^{-1}$.

II.2.5.3.2 The EROS G3 *bis* spectrometer set up

EROS G3 *bis* neutron reflectometer at Laboratory Léon Brillouin in Saclay uses the time of filght technique for calculating the wave vector[9] (Figure 20).

Neutrons produced by Orphée reactor are firstly cooled by liquid hydrogen (T=20K) before they reach the neutron guide. At the exit of the neutron guide, a turning chopper with an adjustable window separates the neutrons beam, making sure that the slow neutrons enter into a vacuum collimator before the rapid neutrons. The incident neutron beam reaches the sample at a shaving incident angle θ, then is reflected by the sample/air or sample/vacuum interface. Typically, the maximum incident angle is up to 5°, corresponding to a q from 0.004 to 0.1Å^{-1}. The reflected neutrons beam are captured by a ^{3}He detector. The minimal measured reflectivity is in the order of 10^{-6}, the vertical position of the detector can be adjusted according to the incident angle θ.

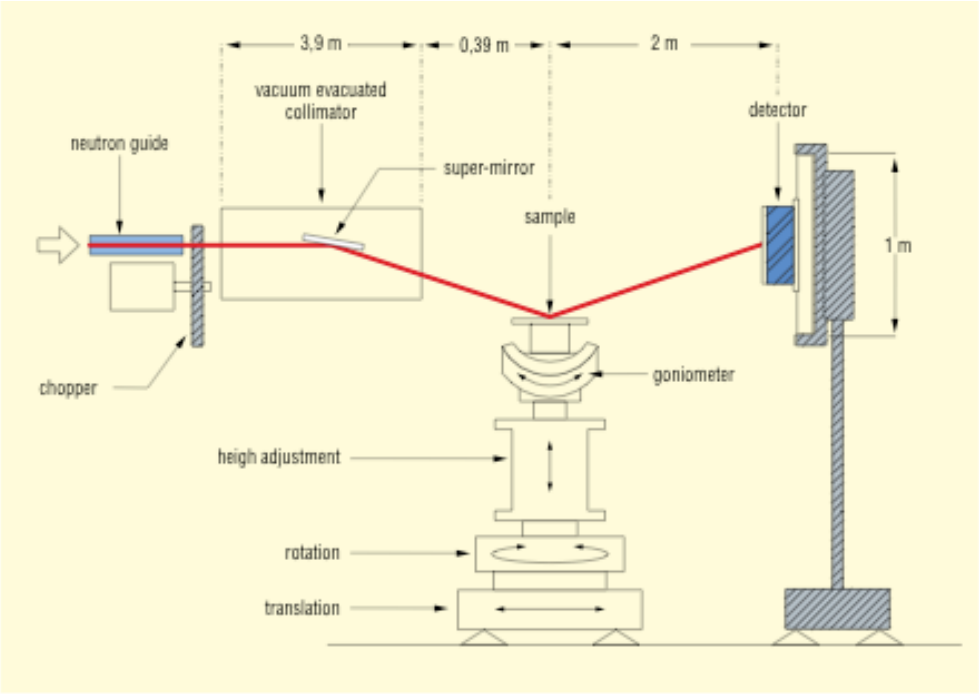

Figure 20: Schematic representation of EROS G3 *bis* spectrometer at laboratoire Léon Brillouin in Saclay

In our polyelectrolyte mutilayer structure analysis, the data were collected at a fixed angle of 0.93° with a neutron white beam covering wavelengths from 2.5 Å to 25 Å with a dl/l of 0.025. We used collimation slits of 2 mm and 1 mm, which leads to a δθ of 0.04° (δθ/θ ~ 0.045). The final accessible Q-range was 0.008-0.081 Å^{-1}. A standard treatment of raw data was applied to obtain reflectivity curves in absolute scale.

After experimental data acquisition, all data has been treated by using a classic algorithms in order to establish the main parameters for a structural model as described for example by Parratt[11] or Russell[12].

All datasets were analyzed using the Motofit software package[13], which uses the Abeles matrix formalism[14]. More specifically, we have used a classic box model in which each layer i (slab) is characterized by three variables: a scattering length density (SLDi), a thickness (Di) and a surface roughness (σi).

Bibliography*

*: All references cited in this thesis have their independent citation style in the corresponding journals

[1] X.P. Sun, S.J. Dong, E.K. Wang, *Materials Chemistry and Physics*, 2006, 96, 29.

[2] A. Izquierdo, S. Ono, J.C. Voegel, P. Schaaf, G. Decher*, Langmuir,* **2005***,* 21*,* 7558.

[3] (a) Kramers-Kronig Relations in Optical materials Research, Series: Springer Series in Optical Sciences, Vol. 110 V. Lucarini, J.J. Saarinen, K.E. Peiponen, E.M. Vartiainen, **2005**, Edit. Springer.

(b) Ellipsométrie: Théorie, F. Bernoux, J.P. Piel, B. Castellon, J.H. Lecat, P. Boher, J.L. Stehle, R6490, **2003**, Edit. Techniques de l'Ingénieur.

[4] The manual guide of Multiskop Ellipsometry

[5] R.M.A. Azzam, A.R.M. Zaghloul, N.M. Bashara, *J. Optic. Soc. Am.* **1975**, 65, 252.

[6] (a) MultiMode SPM Instruction Manual, Version 4.31ce, Digital Instruments Veeco Metrology Group, **1997**

(b) http://en.wikipedia.org/wiki/atomic_force_microscopy

[7] G. Binnig, H. Rohrer "Scanning tunneling microscopy" IBM Journal of Research and Development **1986**, 30,4 reprinted 44,½ Jan/Mar, **2000**.

[8] M. Brinkman, S. Pratontep, C. Chaumont, J.C. Wittmann; *Macromolecules*, **2007**, 40, 9420.

[9] (a) F. Ott, F. Cousin, A. Menelle, *J. Alloys Compd*. **2004,** 382, 29.

(b) the lecture of F. Cousin "La Réflectivité de Neutrons", Laboratoire Léon Brillouin, CEA Saclay, France

[10] H. Kiessig, *Ann. Phys. Leipzig,* **1931**, 10,769.

[11] L. Parratt, *Phys*. *Rev*. **1954**, 95, 359.

[12] T.P. Russell, *Mat.Sci.Rep*., **1990**, 5, 171.

[13] A. Nelson, *J*. *Appl*. *Crystallogr*. **2006**, 39, 273.

[14] F. Abeles, *Ann. Phys*. **1950**, 5, 596.

Chapter III Results and Discussions

III.1. Construction and characterization of spray-assembled polyelectrolyte films

III.1.1. Investigation of the layer structure of sprayed $(PSS/PAH)_n$ film by neutron reflectometry

III.1.1.1. Introduction to spray-assembled polyelectrolyte films

Introduced in the first chapter, two different mechanisms, the linear growth and the super-linear growth, for a LbL polyelectrolyte multilayer growth were characterized. In the present manuscript, studies were carried out only on linear growing films where no free polymer chain diffusion in the whole deposited film was observed. The system $(PSS/PAH)_n$ was chosen for an internal structural comparison between dipped and sprayed films. The choice of this $(PSS/PAH)_n$ system is motivated by the fact that such film is one of the most studied polyelectrolyte multilayer during the past ten years. A thorough structure and growth mechanism study has been performed for $(PSS/PAH)_n$ film prepared by dipping.

In a polyelectrolyte multilayer build-up procedure, the construction driving force is the electrostatic interactions. The formation of a single layer is performed by adsorption of polymer chains by diffusion from the solution to the substrate surface. The diffusion time is typically 15 to 60 minutes for the adsorption of a dipped single layer depending on the nature of the components.

Since 2000, a new preparation method of polyelectrolyte multilayer has been introduced[1,2]. The polymer solution was sprayed onto the surface for a film construction instead of dipping the surface into the polymer solution. The advantage of this method is that only small amounts of liquids are needed to coat even a large surface and that the deposition time was enormously reduced by a factor of about 50 to 150 times compared to the dipping method.

Meanwhile, the deposition method plays an important role in the final film characteristics. For example, an ellipsometry and a X-Ray reflectometry analysis have revealed that a dipped $(PSS/PAH)_n$ film is thicker than a sprayed film[2]. However, the surface roughness of dipped film is slightly higher (around 1.5nm) than a sprayed film (less than 1.0nm) as confirmed by a X-Ray reflectometry and a AFM analysis.

A neutron reflectometry study for dipped $(PSS/PAH)_n$ film has demonstrated that such a film has a stratified internal structure with inter-diffused layers instead of a truly layer-by-layer structure[3,4] like Italian lasagnes (Figure 1). In Figure 1, it shows clearly that both polycation (in blue) and polyanion (in red) are not isolated, it always exists a slight polymer chains inter-diffusion between two adjacent layers.

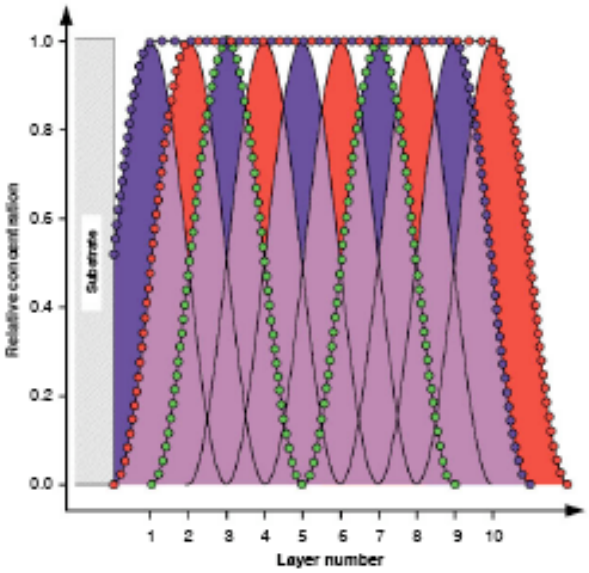

Figure 1: Schematic representation of a polyelectrolyte multilayer composed of 10 inter-diffused layers

One of frequently asked questions for a sprayed film is why there is a difference in film thickness as well as surface roughness for a dipped and a sprayed film having the same architecture? What are the structural changes induced by the preparation method?

When a liquid is sprayed onto the surface, a strong shear force will cause the fusion of liquid droplets to the liquid film on the surface. And this shear force seems to be responsible for the adsorption acceleration. During film construction, will shear forces remove some materials from the surface and lead to a film thickness diminution? As a consequence, will this thickness diminution correspond to a loss of stratified structure for sprayed polyelectrolyte multilayer? To our best knowledge, no similar studies were reported in order to verify if a sprayed polyelectrolyte multilayer keeps the stratified structure as observed for dipped films.

To answer these questions, a neutron reflectometry study was carried out on sprayed $(PSS/PAH)_n$ films to investigate the internal structure of such films. In addition, the

influence of the molecular weight of polymers on film structure and roughness was studied.

III.1.1.2. Chemical compounds and preparation methods

III.1.1.2.1. Polymers and solutions for spray experiments

All films have been deposited onto Silicon Wafers except for UV-Visible analysis where films were deposited on quartz slides. Before the deposition of each $(PSS/PAH)_n$ film, a precursor layer of PEI was firstly deposited on the substrate surface in order to improve the surface adhesion.

All polymers, PEI ($\overline{M_w}$ =25,000g/mol), PSS ($\overline{M_w}$ =70,000g/mol) and PAH ($\overline{M_w}$=70,000g/mol) were purchased from Sigma-Aldrich and were used as received.

For the study on molecular weight influence in film construction, PSS and PAH were purchased from Polymer Standard Service (Mainz, Germany) and were used as received. Therefore, three PSS and two PAH were employed:

- PSS $\overline{M_w}$=6,000 g/mol (PSS6k)
- PSS $\overline{M_w}$=15,000 g/mol (PSS15k)
- PSS $\overline{M_w}$=70,000 g/mol (PSS70k)
- PAH $\overline{M_w}$=15,000 g/mol (PAH15k)
- PAH $\overline{M_w}$=70,000 g/mol (PAH70k)

All polymers were dissolved in a 0.5M NaCl solution with a concentration of 3mM (in monomer concentration) except for PEI, which was dissolved in Milli-Q water. Roth manual sprayers called “Air Boy” were used for film construction. With this kind of sprayer, only liquid is sprayed onto the surface.

III.1.1.2.2. Film construction by spraying

The spray instrument set up and protocol are indicated in Figure 2.

The substrate was oriented vertically and the spray distance was fixed around 10 to 15 cm. The fluorescence image (Figure 2A) shows that the center of the spray spot is quite homogeneous although some inhomogeneity exists outside of the spray spot.

In a $(PSS/PAH)_n$ films construction, a PSS solution was sprayed on the surface for 5 seconds (t_1), after 15 seconds of waiting (adsorption time) (t_2), a rinse solution (0.5M NaCl) was sprayed on the surface for 5 seconds (t_3) in order to remove the un-adsorbed materials, after 15 seconds of waiting (t_4), the same procedure was repeated for PAH.

The total spray time for a single (PSS/PAH) layer pair is: $(t_1+ t_2+ t_3+ t_4)\times2= 80$ seconds. This spray time protocol was used during the whole work except for certain specified experiments.

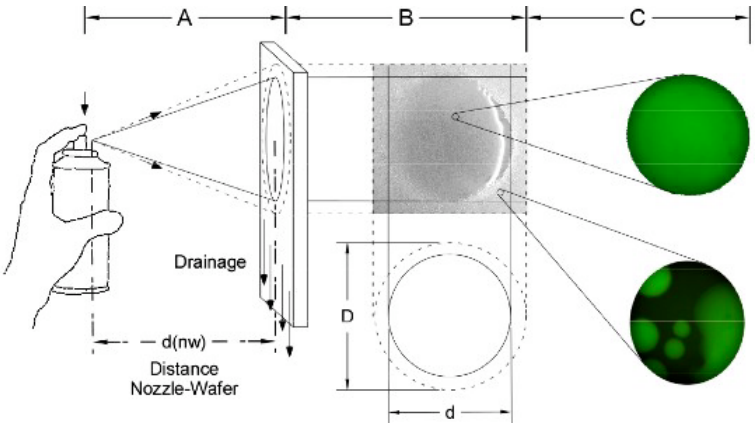

A: Spray instrument set up

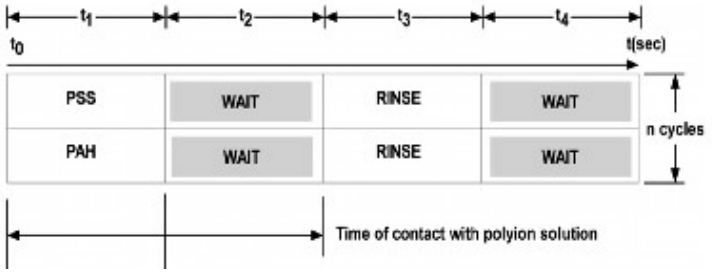

B: Spray time protocol

Figure 2: Schematic representation of the spray instrument set up (A) and the used spray time protocol (B)

In order to compare $(PSS/PAH)_n$ films prepared by spraying and dipping, some dipped films with same polymers concentrations and same architecture were prepared . The preparation protocol for dipped films were the following:

The PEI covered substrate was firstly dipped within a PSS solution for 25 minutes (t_1), then after three times 1 minute (t_2) rinse by a 0.5M NaCl solution, the substrate was dipped within a PAH solution for 25 minutes (t_3), finally, the substrate was rinsed three times (1 minute each) (t_4) with 0.5M NaCl solution.

The total dipping time for a single (PSS/PAH) layer pair is: $(t_1+ 3\times t_2+ t_3+ 3\times t_4) = 56$ minutes (3360 seconds). After the preparation, all $(PSS/PAH)_n$ films were dried under a nitrogen flow.

III.1.1.2.3. Characterization techniques for sprayed films

Different techniques were used for the characterization of sprayed $(PSS/PAH)_n$ films:

- ♣ Ellipsometry
- ♣ UV-Visible spectroscopy
- ♣ Atomic Force Microscopy (AFM)
- ♣ Neutron Reflectometry

Description of each technique is given in Chapter II

III.1.1.3. Discussion of experimental data concerning sprayed polyelectrolyte films

III.1.1.3.1. Influence of Molecular Weight on the spray-assembly

The construction of $(PSS/PAH)_n$ films with different molecular weight was performed. Three PSS and two PAH correspond to six different combinations:

- (PSS6k/PAH15k)
- (PSS15k/PAH15k)
- (PSS70k/PAH15k)
- (PSS6k/PAH70k)
- (PSS15k/PAH70k)
- (PSS70k/PAH70k)

If not specified, polymer concentrations in monomer repeat unit were: C(PEI)=C(PSS)=C(PAH)=3mM.

Ten layer pairs of (PSS/PAH) films were built up and the film thickness was measured by ellipsometry. Figure shows that each polymer couple has a linear film growth with a small error bars (less than 1 nm). However, these six polymer couples indicate three different (PSS/PAH) single layer pair increment (Table 1):

Polymer Couples	Single Layer Pair Increment (nm)
(PSS6k/PAH15k) (PSS15k/PAH15k)	~ 2.0
(PSS70k/PAH15k) (PSS6k/PAH70k) (PSS15k/PAH70k)	~ 2.3
(PSS70k/PAH70k)	~ 2.5

Table 1: (PSS/PAH) single layer pair increment as a function of polymer molecular weight

When there is at least one long polymer chain in the film, the single layer pair increment is 15% ~ 25% thicker than the film containing only short polymer chains. The maximum single layer pair increment appears when both PSS and PAH are long chain polymer. Thus, thicker films were obtained with polymers having the higher molecular weight.

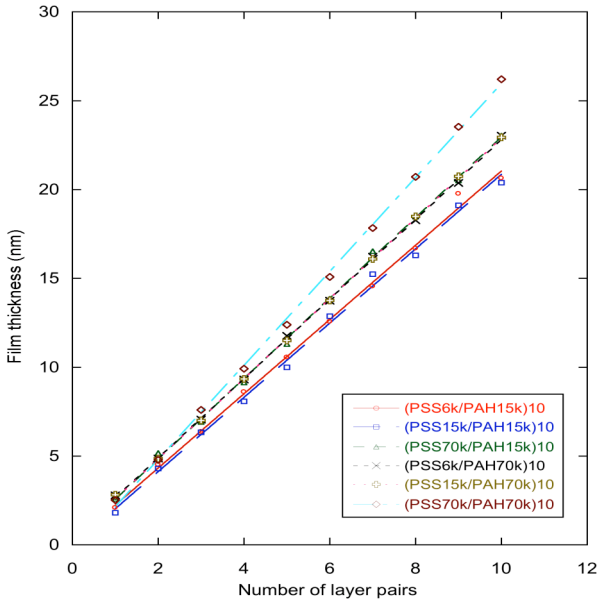

Figure 3: Build-up of $(PSS/PAH)_n$ film with polymer having different molecular weights measured by ellipsometry

With the whole molecular weight range, sprayed films are thinner than dipped films[5]. In sprayed films, film increment increase as function of molecular weight. As a consequence, the maximum film increment was obtained, which is around 2.5 nm for $(PSS70k/PAH70k)_n$ polymer couple at present preparation conditions. The single layer increment of this (PSS70k/PAH70k) polymer couple represents 80% of corresponding film prepared by dipping[5].

III.1.1.3.2. Film thickness and surface roughness characterization of films prepared by spraying

If not specified, all $(PSS/PAH)_n$ films mentioned in this manuscript refer to the $(PSS70k/PAH70k)_n$ film.

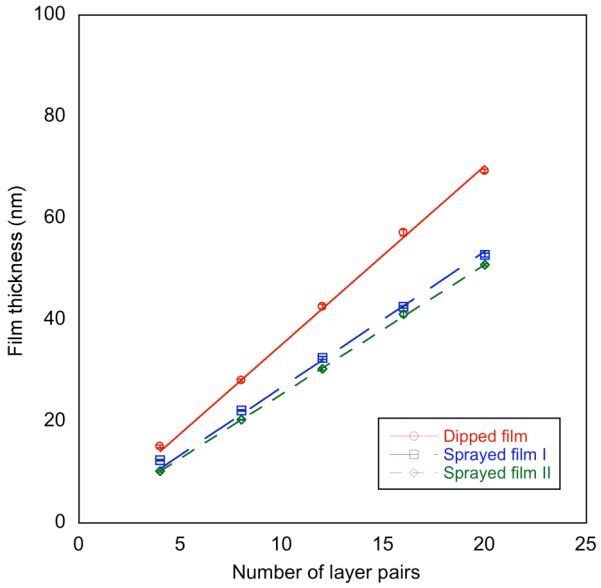

Figure 4: Variation of $(PSS/PAH)_n$ film thickness during build-up by dipping and spraying measured by ellipsometry

In order to compare with the dipped $(PSS/PAH)_{20}$ films, $(PSS/PAH)_{20}$ films were prepared by spraying (Figure). Both dipped and sprayed films have an excellent linear film growth. The single layer pair for dipped film is around 3nm against 2.5nm for sprayed film. Moreover, this sprayed films single layer pair increment is highly reproducible.

The $(PSS/PAH)_n$ films build up was monitored by UV-Visible spectroscopy (Figure 5) as well. The absorption peak at around 225 nm corresponds to the absorption of PSS aromatic ring. As the number of layer pair increases, the intensity of this peak increases

as well. By plotting the intensity of the adsorption peak at 225 nm as a function of the number of layer pairs, a linear film growth is obtained, as already observed by ellipsometry.

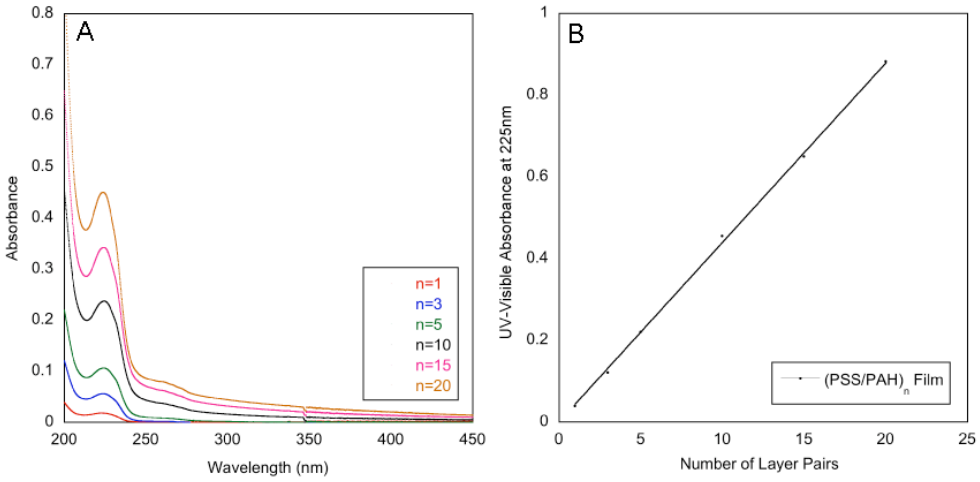

Figure 5: Build-up of a sprayed $(PSS/PAH)_{20}$ film monitored by UV-Visible spectroscopy (A) and the corresponding film growth monitored observed at 225 nm (B)

Surface morphology of $(PSS/PAH)_n$ films was analyzed by AFM (Figure 6). One $(PSS/PAH)_{20}$ film and one $(PSS/PAH)_{62}$ film were analyzed. AFM images (tapping mode, height images) indicate that the surface is quite homogeneous, without obvious aggregates on the surface. The surface roughness analysis for $(PSS/PAH)_{20}$ film indicates a RMS (Root Mean Square) roughness 0.8±0.1nm. This value is very similar to the results reported in the literature for sprayed $(PSS/PAH)_n$ film, typically less than 1.0nm[2]. While the surface roughness for dipped $(PSS/PAH)_n$ film is typically around 2-3nm[5]. Even for a thick sprayed (PSS/PAH) film, like a $(PSS/PAH)_{62}$ film, the surface roughness is always less then 1nm (1.0nm respectively)[5].

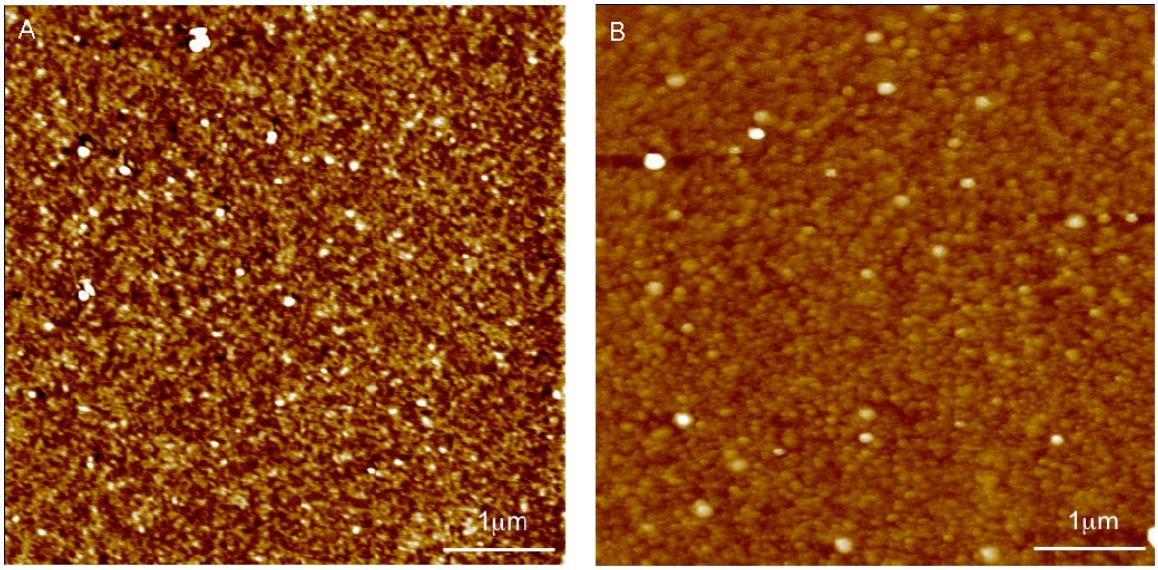

Figure 6: Height images of sprayed films, $(PSS/PAH)_{20}$ (A) and $(PSS/PAH)_{62}$ (B) by tapping mode AFM

These ellipsometry and AFM analysis confirmed that a sprayed $(PSS/PAH)_n$ film is thinner and smoother than a dipped $(PSS/PAH)_n$ film. In order to verify if a stratified structure still exists in a sprayed $(PSS/PAH)_n$ film, a neutron reflectometry analysis was necessary.

III.1.1.3.3. Investigation of the layer structure of sprayed $(PSS/PAH)_n$ film by neutron reflectometry

In collaboration with the laboratory Léon Brillouin in Saclay, France, a preliminary analysis of $(PSS/PAH)_n$ film internal structure was carried out in the beginning of 2007. One dipped and one sprayed sample with same architecture $[(PSS_{h7}/PAH)_4/(PSS_{d7}/PAH)]_8/(PSS_{h7}/PAH)_4$ were analyzed by neutron reflectometry (Figure 7).

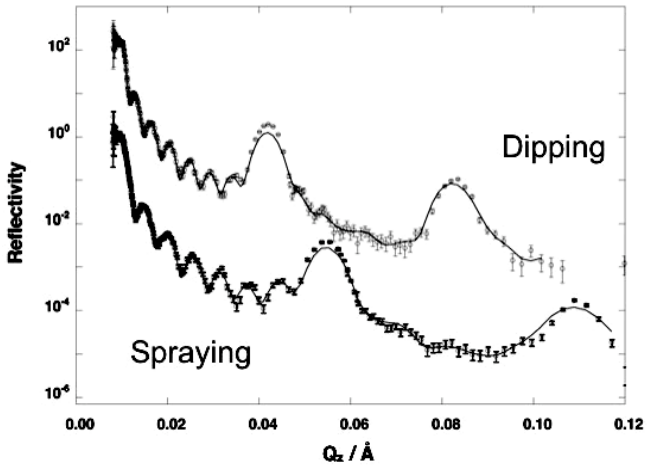

Figure 7: Neutron reflectometry curves of dipped and sprayed $[(PSS_{h7}/PAH)_4/(PSS_{d7}/PAH)]_8/(PSS_{h7}/PAH)_4$ films

The spectrum clearly shows that the sprayed $(PSS/PAH)_n$ film has two Bragg peaks as well as the dipped film. These Bragg peaks correspond to a stratified like structure. Moreover, the difference in position of Bragg peaks in sprayed and dipped films shows that a sprayed film is thinner than a dipped film. Is the thickness difference due to the preparation method? At present instrument resolution, no further information could be obtained. More experiments with an improved neutron resolution were necessary in order to figure out why a sprayed film has a thin film thickness then a dipped film.

In order to carry out a full investigation of sprayed $(PSS/PAH)_n$ film internal structure, more samples with different architectures have been prepared. Before the neutrons reflectometry test, each samples film thickness and corresponding reflection index were carefully measured by ellipsometer "Multiskop". The single layer pair increment measured by ellipsometry was around 2.3 nm to 2.6 nm and the corresponding reflection index was around 1.56 to 1.57 according to different architectures. Every sample was analyzed by neutron reflectometry, but only the first treated results are presented here.

First of all, two reference samples, a $(PSS_{h7}/PAH)_{10}$ sample with a minimum deuteration, and a $(PSS_{d7}/PAH)_{10}$ sample with a maximum deuteration, where all hydronated PSS have been replaced by deuterated PSS, were analyzed (Figure 8). Some reference parameters, such as film thickness of single (PSS_{h7}/PAH), (PSS_{d7}/PAH) layer pairs, respectively surface roughness and scattering length density were obtained. A model was then built-up from these reference parameters. Without

any additional adjustment, this model matches perfectly with the experimental results of two additional samples with more complicated architectures. Complete description of the neutron reflectometry experiments and analysis of $(PSS/PAH)_n$ sprayed films internal structure are described in details in the following paper published in C. R. Chimie in 2009[6].

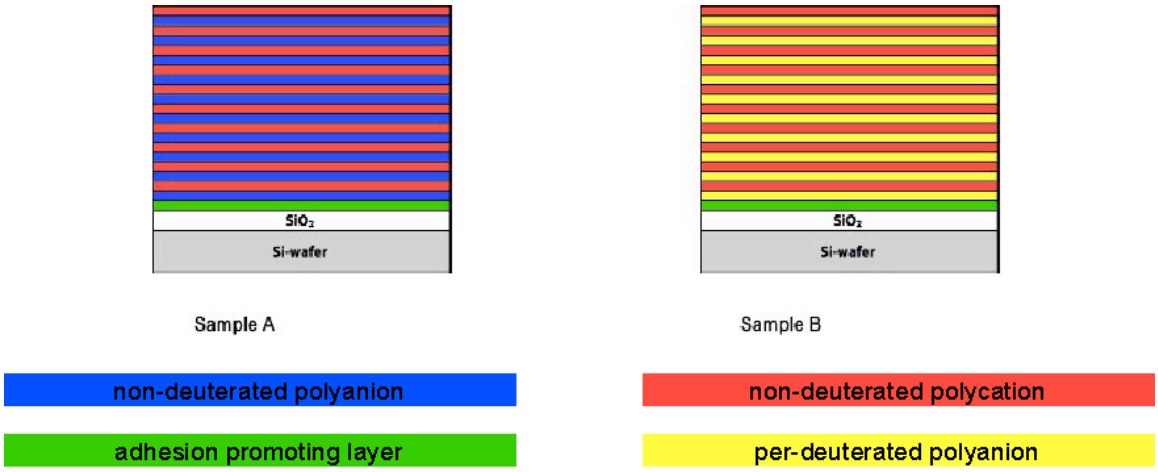

Figure 8: Schematic representation of hydronayed $(PSS_{h7}/PAH)_{10}$ film (sample A) and deuterated $(PSS_{d7}/PAH)_{10}$ film (sample B)

Available online at www.sciencedirect.com
ScienceDirect
C. R. Chimie 12 (2009) 225–234
COMPTES RENDUS CHIMIE
http://france.elsevier.com/direct/CRAS2C/

Full paper / Mémoire

Are sprayed LbL-films stratified? A first assessment of the nanostructure of spray-assembled multilayers by neutron reflectometry

Olivier Félix [a], Zhiqiang Zheng [a], Fabrice Cousin [b], Gero Decher [a,c,*]

[a] C.N.R.S., Institut Charles Sadron, 23, rue du Loess, 67034 Strasbourg Cedex 2, France
[b] Laboratoire Léon Brillouin, C.E.A Saclay, 91191 Gif-sur-Yvette Cedex, France
[c] Université Louis Pasteur, Faculté de Chimie, 1, rue Blaise Pascal, 67008 Strasbourg, France

Received 17 April 2008; accepted after revision 24 September 2008

In memory of Pierre-Gilles de Gennes who, through his many interests, among them polymers, interfaces and neutron scattering, contributed exceptionally to establish the field of soft condensed matter.

Available online 14 November 2008

Abstract

We describe first neutron reflectometry experiments on spray-assembled polyelectrolyte multilayer films containing regularly spaced layers of perdeuterated poly(styrene sulfonate). From samples containing either only non-deuterated layers or containing a maximum of deuterated layers we obtain all model parameters (thicknesses, scattering length densities and roughnesses) required for calculating the reflectivities of multilayer films with a regular superlattice structure. For two different superlattice films we show that we obtain an excellent match between experimental data and calculated reflectivities without any free fit parameter. Our data clearly demonstrate that spray-assembled polyelectrolyte multilayers are indeed stratified although some structural parameters differ enormously from films prepared by classic dipping. Our present experiments confirm a substantial difference in thickness and suggest a reduced interfacial roughness in spray-assembled films. ***To cite this article: O. Félix et al., C. R. Chimie 12 (2009).***

Résumé

Nous décrivons les premières expériences de réflectométrie de neutrons sur des films multicouches de polyélectrolytes assemblés par pulvérisation contenant des couches régulièrement espacées de poly(styrène sulfonate) perdeutéré. A partir d'échantillons contenant soit seulement des couches non-deutérées soit un maximum de couches deutérées, nous avons obtenu tous les paramètres modèles (épaisseurs, densités de longueur de diffusion et rugosités) nécessaires pour le calcul de la réflectivité des films multicouches avec une structure super-maille régulière. Pour deux films de super-maille différente, nous avons montré que l'on peut obtenir une excellente concordance entre les données expérimentales et les réflectivités calculées sans aucun paramètre d'ajustement libre. Nos données montrent clairement que les multicouches de polyélectrolytes assemblées par pulvérisation sont effectivement stratifiées même si certains paramètres diffèrent énormément des films préparés par trempage. Nos expériences

* Corresponding author.
E-mail address: decher@ics.u-strasbg.fr (G. Decher).

1631-0748/$ - see front matter © 2008 Published by Elsevier Masson SAS on behalf of Académie des sciences.
doi:10.1016/j.crci.2008.09.009

confirment une différence substantielle en épaisseur et suggèrent une rugosité interfaciale réduite dans les films assemblés par pulvérisation. ***Pour citer cet article : O. Félix et al., C. R. Chimie 12 (2009).***

Keywords: Polyelectrolyte multilayers; Neutron reflectometry; Superlattice film; Polymer; Interface; Spray-deposition; Nanofabrication

Mots-clés : Multicouches de polyélectrolytes ; Réflectométrie des neutrons ; Film super-maille ; Polymère ; interface ; Dépôt par pulvérisation ; Nanofabrication

1. Introduction

The spray-deposition of polyelectrolyte multilayers [1–11] has recently been gaining interest as an alternative to the well established assembly of such films by "dipping" (see for example : [8,12–21]).

In our earlier article [2] we have pointed out that one of the most interesting aspects of spray-deposition lies in the fact that spray-assembly can enormously accelerate the deposition time. Today we have cases in which the multilayer assembly of certain materials can be accelerated by a factor of up to 500. However, in the same article we have also pointed out that layer-by-layer assembled films prepared by "dipping" or by "spraying" may show considerable differences with respect to their properties. Most importantly it was noted that films with the same number of layers prepared from the same solutions by "dipping" or "spraying" differ in thickness, for films composed of the sodium salt of poly(styrene sulfonate) (PSS) and poly(allyl amine hydrochloride) (PAH) we noticed that spray-assembled films only had a thickness of about 70–75% of that observed for classic deposition by "dipping". Investigations by atomic force microscopy (AFM) revealed that both kinds of films also differ with respect to surface roughness. These structural differences, whose origin is far from being understood, demanded to investigate if spray deposited films also possess a stratified structure that was observed earlier by us by neutron reflectometry [22] for the case of multilayer films assembled by dipping. These first experiments also led to a structural model of polyelectrolyte multilayer films, that explained that a stratified albeit "fuzzy" structure is consistent with the often observed charge stoichiometry between polyanions and polycations [14]. Subsequent investigations of polyelectrolyte multilayers by neutron reflectometry revealed many more structural details of such films, including for example water or ion content [23–40].

Here we report on the first semi-quantitative analysis of neutron reflectometry experiments which we carried out on polyelectrolyted multilayers composed of PSS and PAH that were spray assembled in various superlattice architectures by selective positioning of perdeuterated layers of PSS in selected layers. We have used classic algorithms for establishing the main parameters for a structural model as described for example by Parratt [41] or Russell [42]. Our data sets were analyzed using the Motofit software package [43] which uses the Abeles matrix formalism [44]. More specifically, we have used a classic box model in which each layer i (slab) is characterised by three variables: a scattering length density (SLD_i), a thickness (D_i) and a surface roughness (σ_i). Since we investigate superlattice structures with a complex layer sequence, we had to devise a strategy to minimize the number of parameters for any manual or numerical curve fitting in order to arrive at a small number of physically meaningful structural data.

The chemical structures of the polymers are depicted in Scheme 1.

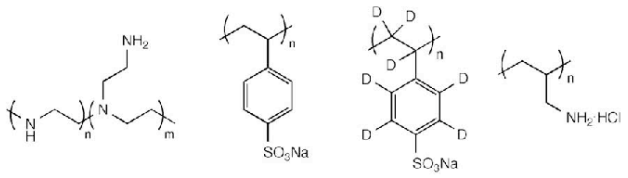

Scheme 1. Chemical structures of the polymers used for film fabrication.

2. Materials and methods

2.1. Polyelectrolyte solutions

Poly(sodium 4-styrenesulfonate) (PSS_{h7}, $\overline{M_w} = 70,000$ g/mol, Lot PI06005MU), poly(allylamine hydrochloride) (PAH, $\overline{M_w} = 70,000$ g/mol, Lot 05212MO-083) and branched poly(ethyleneimine) (PEI, $\overline{M_w} = 25,000$ g/mol, Lot 09620EA-193) were purchased from Aldrich (Lyon, France). Deuterated poly(sodium 4-styrenesulfonate) (PSS_{d7}, $\overline{M_w} = 80,800$ g/mol, Lot pssd8181105na) was purchased from Polymer Standards Service GmbH (Mainz, Germany).

All solutions were prepared using ultrapure water (Milli-Q system, Millipore) with a resistivity of at least 18.2 MΩ cm.

Polyelectrolyte solutions were always freshly prepared by direct dissolution of the respective adequate amounts to yield solutions with final concentrations of PEI of 1 mg/mL, PSS_{h7} and PSS_{d7} of 0.6 mg/mL and PAH of 0.27 mg/mL. Each polyelectrolyte, except PEI, was dissolved in Milli-Q water containing 0.5 M sodium chloride (NaCl, Reagent Plus, ≥99.5%, Batch#: 096K0076 was purchased from Sigma). PEI itself was dissolved in pure Milli-Q water. All final polyelectrolyte concentrations correspond to about 3×10^{-3} monomol/L in which monomol corresponds to moles of the respective monomer repeat unit. Here, we have ignored the molecular weight difference between PSS_{h7} and PSS_{d7}.

2.2. Film substrate

Silicon wafers with an orientation (100) and a thickness of 0.5 mm were purchased from Wafernet Inc. (San Jose, USA) They were then cut to a size of about 45 mm × 20 mm for polyelectrolyte film deposition.

Before the film deposition, all silicon wafers were cleaned by immersing firstly in a mixed solution of methanol and hydrochloric acid (1:1, v/v) for 30 min and then stored in a concentrated sulfuric acid solution for at least an overnight. All wafers were extensively rinsed in Milli-Q water after cleaning and used within a few hours for the deposition of multilayer films.

2.3. Ellipsometry

Measurement of the film thickness was carried out with a Multiskop instrument (Optrel GbR, Kleinmachnow, Germany) operating at a laser wavelength of 632.8 nm and a constant angle of 70°. For each substrate studied, several points were measured to obtain the average value for the film thickness.

2.4. Film buildup

All polyelectrolyte multilayer films were assembled after the deposition of a PEI precursor layer. The cleaned Si-wafers were dipped into a PEI solution for 5 min, rinsed in Milli-Q water and dried under a nitrogen flux prior to deposition by spraying or dipping.

The spray-deposition was carried out by using manual spray cans as described before [2]. Different spray cans were used for the PSS_{h7}, PSS_{d7}, PAH and the rinsing solution (a 0.5 M aqueous solution of NaCl), respectively. The spray conditions were as follows: polymer solution spraying time $t_1 = 5$ s, contact time $t_2 = 15$ s, rinsing time $t_3 = 5$ s, waiting time $t_4 = 15$ s. The deposition time for a single layer pair corresponds accordingly to $(t_1 + t_2 + t_3 + t_4) \times 2 = 80$ s.

The film deposition by dipping was carried out by immersing the substrate for 20 min in the polyelectrolyte solution followed by three rinsing steps of 100 s, 100 s, and 120 s.

2.5. Neutron reflectivity measurements

Specular neutron reflectivity experiments were carried out on the time-of-flight reflectometer EROS (LLB, CEA Saclay, Gif-sur-Yvette, France) [45]. The data were collected at a fixed angle of 0.93° with a neutron white beam covering wavelengths from 2.5 Å to 25 Å with a $\delta\lambda/\lambda$ of 0.025. We used collimation slits of 2 mm and 1 mm, which leads to a $\delta\theta$ of 0.004° ($\delta\theta/\theta \sim 0.045$). The final accessible Q-range was 0.008–0.081 $Å^{-1}$. A standard treatment of raw data was applied to obtain reflectivity curves in absolute scale.

3. Results and discussion

In a first series, we fabricated the following six film architectures for characterisation by neutron reflectometry. Fig. 1 represents the general film architecture of all samples as summarized in detail in Table 1.

All multilayer films were deposited on Si-wafers with a size of 45 mm × 20 mm × 0.5 mm, for technical reasons the dimensions of the multilayer films were 40 mm × 20 mm. The wafers were cleaned as previously reported and then immediately coated with a single layer of non-deuterated poly(ethyleneimine) (PEI).

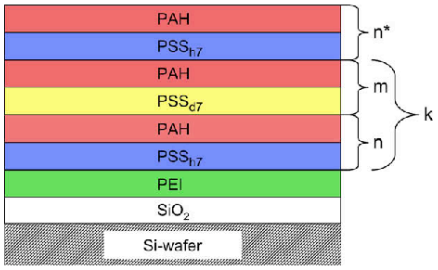

Fig. 1. Graphic representation of the layer architecture of the different multilayer samples.

For obtaining the base parameters for all samples we need to identify the thickness, the roughness and the SLDs for a single layer pair (PSS/PAH) either deuterated or non-deuterated. One of the problems of doing so arises from the fact that we require a layer of PEI on top of the SiO_2 surface, the direct adsorption of PAH on SiO_2 leads only to a very thin layer of PAH. For the preparation conditions used in the work presented here we have an ellipsometrically determined average thickness of this PEI layer of 11.5 Å which we feed directly into the model for calculating reflectivities. Another problem arises from the experimental scatter of data from different samples, which basically requires us to fit many data sets in parallel refining certain parameters by using data from several different data sets at the same time. While global fitting is one of the advantages of the MotoFit package, we wanted to avoid using an automated global fitting procedure for the first test experiments. We have therefore approached a true global fitting by manually adjusting parameters by small fractions and then applying the model to different data sets until we got good agreement of a single model with as many data sets as possible. This is the reason why we prefer to report below the values e.g. for thicknesses with a precision of 0.1 Å, while the resolution of the EROS beamline is only on the Å scale. We feel that this is justified since those values represent a "manual global average" over several data sets. A "manual" approach is only reasonable for a few data sets, in the future we are planning to extend our work by automatically fitting a large number of different data sets in parallel. In the discussion below we avoid going into the details of the "manual fitting", we prefer to elaborate how well a simple "manual approach" already works.

3.1. Sample A

A film composed of 10 layer pairs (or 20 layers) of PSS_{h7} and PAH (film architecture $Si/SiO_2/PEI/(PSS_{h7}/PAH)_{10}$). This is the reference film for all non-deuterated slabs in all film architectures.

This sample was used to verify that the scattering length density of the silicon wafer (SLD-Si) could be set to its regular value of 2.07×10^{-6} Å^{-2}, which was kept constant for all samples. The SLD of the surface layer of oxide (SLD-SiO_2) was set to 3.15×10^{-6} Å^{-2}, the surface roughness of the Si/SiO_2 and SiO_2/air interfaces (σ-Si/SiO_2) and (σ-SiO_2/air) was set to their common value of 4 Å and the thickness of the oxide layer (D-SiO_2) was determined to be 12.5 Å, all of these values were then kept constant for all further samples. Using these values as basic parameters, the scattering length density (SLD-nd) of the non-deuterated polymer film was determined to be 1.11×10^{-6} Å^{-2}. As total thickness (D-nd) for the polyelectrolyte film we obtained 265.7 Å, 11.5 Å of which we attributed to the PEI layer leaving 254.2 Å for the $(PSS_{h7}/PAH)_{10}$ part of the film. Finally the surface roughness (σ-nd) of a polyelectrolyte film containing no deuterated material was set to 13 Å. A free fit of this parameter typically resulted in slightly higher values, but a slight overestimation of roughness

Table 1
Multilayer architecture and preparation conditions of the 6 samples investigated by neutron reflectometry.

sample	layer sequence	$n = n^*$	m	k	total number of layer pairs	ellipsometric film thickness/Å		deposition by
						total	per layer pair	
A	$Si/SiO_2/PEI/(PSS_{h7}/PAH)_{10}$	0	10	0	10	247.5 ± 0.7	24.8	spraying
B	$Si/SiO_2/PEI/(PSS_{d7}/PAH)_{10}$	0	10	0	10	254.8 ± 3.0	25.5	spraying
C	$Si/SiO_2/PEI/[(PSS_{h7}/PAH)_3/(PSS_{d7}/PAH)_1]_6/(PSS_{h7}/PAH)_3$	3	1	6	27	639.1 ± 1.9	23.7	spraying
D	$Si/SiO_2/PEI/[(PSS_{h7}/PAH)_5/(PSS_{d7}/PAH)_1]_6/(PSS_{h7}/PAH)_5$	5	1	6	41	988.1 ± 12.3	24.1	spraying
E	$Si/SiO_2/PEI/[(PSS_{h7}/PAH)_4/(PSS_{d7}/PAH)_1]_8/(PSS_{h7}/PAH)_4$	4	1	8	44	1050.9 ± 2.6	23.9	spraying
F	$Si/SiO_2/PEI/[(PSS_{h7}/PAH)_4/(PSS_{d7}/PAH)_1]_8/(PSS_{h7}/PAH)_4$	4	1	8	44	1388.6 ± 7.6	31.6	dipping

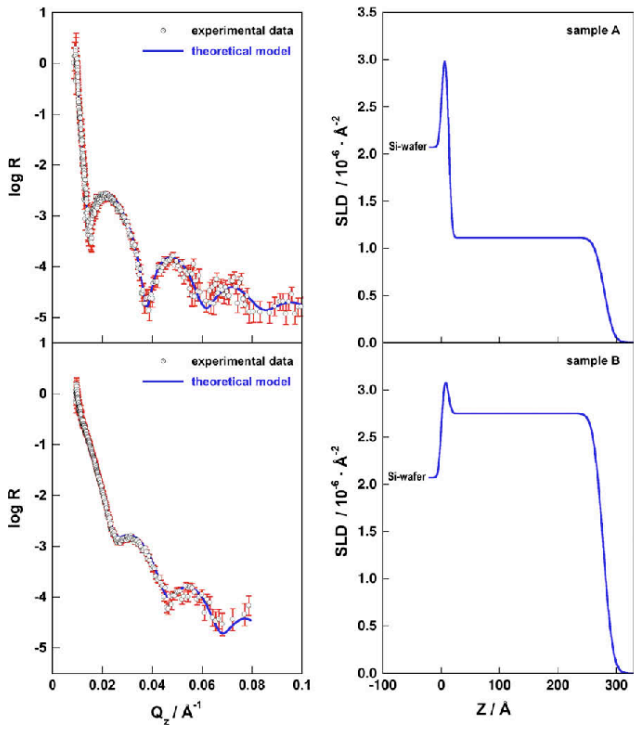

Fig. 2. On the left we depict the experimental reflectivity data of samples A (top) and B (bottom), the error bars for each data point are shown in red. The blue lines represent the calculated reflectivities of the box model as discussed in the text and summarized in Table 2. On the right we show the scattering length density profiles corresponding to the calculated reflectivities on the left (For interpretation of the references to colour in this figure legend, the reader is referred to the web version of this article).

values is common when using numerical fitting routines. The roughness of the PEI layer was set to a value of 9 Å because it is in direct contact with the inorganic surface and typically slightly thinner than the subsequent polyelectrolyte layers. The SLD for the PEI layer was assumed to be identical to the average density of sample A (1.11×10^{-6} Å^{-2}), all these values were then kept constant for all samples, the sole exception is discussed below.

3.2. Sample B

A film composed of 10 layer pairs of PSS_{d7} and PAH (film architecture $Si/SiO_2/PEI/(PSS_{d7}/PAH)_{10}$). This is the reference film for all deuterated slabs in all film architectures.

This film was used only for the determination of the scattering length density (SLD-d), the thickness (D-d) and the roughness (σ-d) of a polyelectrolyte film with a maximum of deuteration. The parameters (SLD-Si), (SLD-SiO_2), (D-SiO_2), (σ-Si/SiO_2) and (σ-SiO_2/film), were kept identical to the values in sample A. The total thickness of the deuterated film was determined to be 264.6 Å, leaving 253.1 Å for the $(PSS_{d7}/PAH)_{10}$ part of the film by considering a thickness of the PEI layer of 11.5 Å as in sample A. The roughness of the PEI layer and the roughness of the film/air interface were set to 9 Å and 13 Å respectively, the same values as in sample A.

Table 2
Model parameters used for calculating the theoretical reflectivities of samples A–F.

A. Parameters kept constant in all samples

layer/slab	D/Å	SLD/10^{-6} Å^{-2}	σ/Å
Si	∞	2.07	4.0
SiO_2	12.5	3.15	4.0
PEI	11.5	1.11/2.75[a]	9.0

B. Adjusted or variable parameters in all samples

sample	number of multilayer repeat units	non-deuterated slabs				deuterated slabs			
		SLD [10^{-6} Å^{-2}]	number of layer pairs	thickness [Å]	roughness [Å]	SLD [10^{-6} Å^{-2}]	number of layer pairs	thickness [Å]	roughness [Å]
A	–	1.11	10	254.2	13.0	–	–	–	–
B	–	–	–	–	–	2.75	10	253.1	13.0
C	6	1.11	3	76.1	13.0	2.75	1	25.4	13.0
D	6	1.11	5	126.8	13.0	2.75	1	25.4	13.0
E	8	1.11	4	104.8	13.0	2.75	1	26.2	13.0
F	8	1.11	4	138.5	18.0	2.75	1	34.6	18.0

[a] See text for details.

Since the thicknesses of the deuterated and non-deuterated films cannot be distinguished within the experimental error we can now define the average thickness value for a $(PSS/PAH)_1$ layer pair to be 25.4 Å which is the average of D-d and D-nd divided by 10. This value is the base value for all model calculations when we compute the thickness of a deuterated $(PSS_{d7}/PAH)_m$ slab or a non-deuterated $(PSS_{h7}/PAH)_n$ slab in any film architecture.

Please note that we have to use different SLD values for the PEI layers in samples A and B. When trying to introduce a layer of PEI as in all other samples (D-PEI = 11.5 Å, SLD-PEI = 1.11×10^{-6} Å^{-2} and σ-PEI = 9 Å), a fit of SLD-PEI always approached the same value as the density of the deuterated film (SLD-d), which was determined to be 2.75×10^{-6} Å^{-2}. If the SLD of PEI was kept at 1.11×10^{-6} Å^{-2} and the thickness of the PEI layer was numerically fitted, it always approached 0 Å. In fact, this should have been expected since adjacent polyelectrolyte layers strongly overlap [14], a detail which also shows up in the interfacial roughnesses of deuterated and non-deuterated layers of 13 Å. In sample B it is therefore impossible to use an independent PEI slab with a SLD of 1.11×10^{-6} Å^{-2} as in all other films, since in sample B the density of the PEI layer cannot be distinguished from the density of the rest of the deuterated film (SLD = 2.75×10^{-6} Å^{-2}).

Fig. 2 depicts on the left the experimental reflectivity data with the corresponding error bars and the calculated reflectivities (R) for the reference samples A and B using the model parameters as described above and summarized in Table 2. The SLD-profiles corresponding to the calculated reflectivities are shown on the right.

3.3. Samples C and D

Samples C and D are superlattice films containing deuterated and non-deuterated slabs with the following general architecture $Si/SiO_2/PEI/[(PSS_{h7}/PAH)_n/(PSS_{d7}/PAH)_1]_6/(PSS_{h7}/PAH)_{n^*}$.

In sample C n and n^* have a value of 3 and in sample D n and n^* have a value of 5. Sample C corresponds therefore to a film composed of a total of 27 layer pairs of PSS and PAH in which 6 deuterated layers of PSS_{d7} are distributed with an equidistant spacing within the whole film (film architecture $Si/SiO_2/PEI/[(PSS_{h7}/PAH)_3/(PSS_{d7}/PAH)_1]_6/(PSS_{h7}/PAH)_3$). Using the base value for a single layer pair of 25.4 Å yields thickness values for the $(PSS_{h7}/PAH)_3$ slabs of 76.1 Å while the $(PSS_{d7}/PAH)_1$ slabs have a thickness of 25.4 Å. Sample D ($n = n^* = 5$) then corresponds to a film composed of a total of 41 layer pairs of PSS and PAH, again with 6 deuterated layers of PSS_{d7} distributed with an equidistant spacing throughout the whole film (film architecture $Si/SiO_2/PEI/[(PSS_{h7}/PAH)_5/(PSS_{d7}/PAH)_1]_6/(PSS_{h7}/PAH)_5$). Using the base value for a single layer pair of 25.4 Å yields thickness values for the $(PSS_{h7}/PAH)_5$ slabs of 126.8 Å while the $(PSS_{d7}/PAH)_1$ slabs possess the same thickness as in sample C (25.4 Å).

Samples C and D can be regarded as control specimen for testing the quality of the parameters determined from samples A and B. Please note that we do not have any free parameters for calculating the model reflectivities because the thicknesses of the deuterated

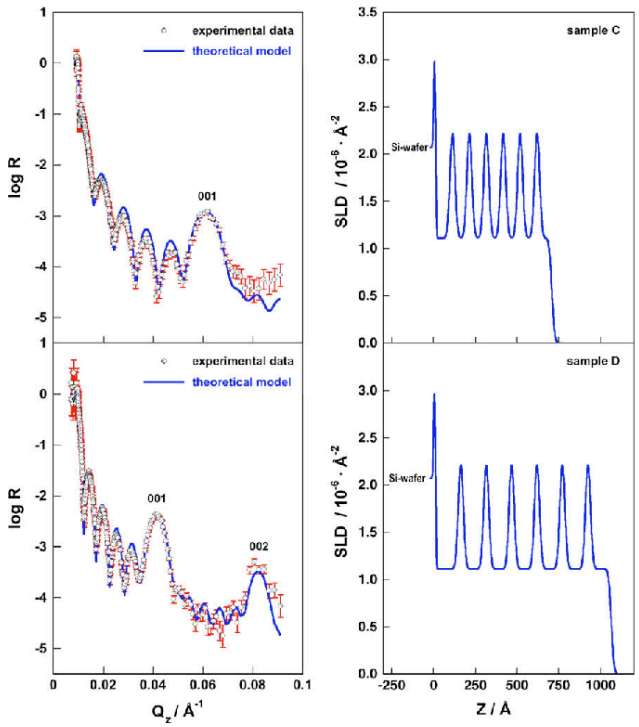

Fig. 3. On the left we depict the experimental reflectivity data of samples C (top) and D (bottom), the error bars for each data point are shown in red. The blue lines represent the calculated reflectivities of the box model as discussed in the text and summarized in Table 2. On the right we show the scattering length density profiles corresponding to the calculated reflectivities on the left (For interpretation of the references to colour in this figure legend, the reader is referred to the web version of this article).

and non-deuterated slabs are simply calculated from the corresponding number of base repeat units (PSS/PAH)$_1$ with a thickness of 25.4 Å. We used a multilayer model with 6 identical repeat units to simulate the experimental data, that is to say that all deuterated slabs in samples C and D were set to a SLD-d of 2.75×10^{-6} Å^{-2} and all non-deuterated slabs were set to a SLD-nd of 1.11×10^{-6} Å^{-2}.

Fig. 3 depicts on the left the experimental reflectivity data with the corresponding error bars and the calculated reflectivities (R) for the reference samples C and D using the model parameters as described above and summarized in Table 2. The SLD-profiles corresponding to the calculated reflectivities are shown on the right.

This excellent agreement between experimental data and a theoretical model without free parameters shows that the model is generally valid for spray-assembled polyelectrolyte multilayers of PSS and PAH in different superlattice architectures if prepared at identical conditions.

3.4. Samples E and F

Samples E and F are superlattice films containing deuterated and non-deuterated slabs with the same general architecture Si/SiO_2/PEI/[(PSS_{h7}/PAH)$_4$/(PSS_{d7}/PAH)$_1$]$_8$/(PSS_{h7}/PAH)$_4$. However, the samples were prepared by different deposition methods, sample E was fabricated by spraying and sample F was constructed by dipping. An important difference in comparison with samples A–D is that samples E and F were prepared from different solutions and about 6 months earlier than samples A–D.

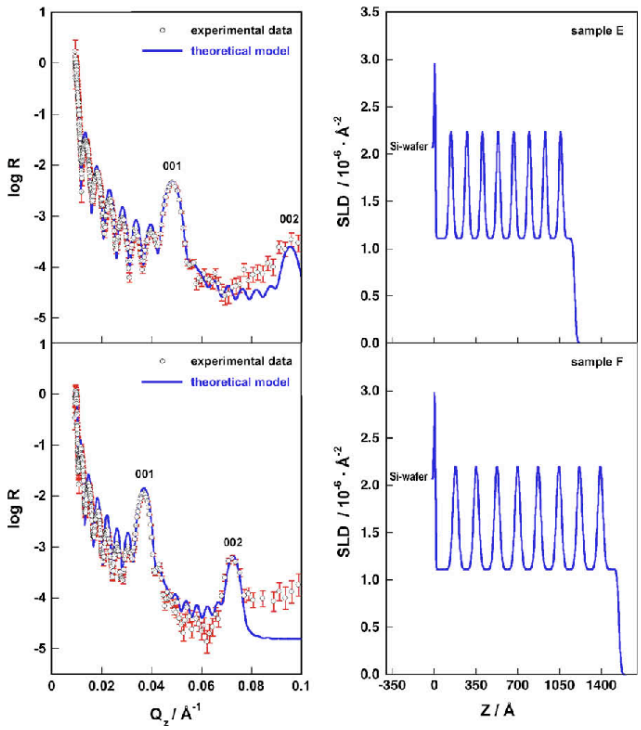

Fig. 4. On the left we depict the experimental reflectivity data of samples E (top) and F (bottom), the error bars for each data point are shown in red. The blue lines represent the calculated reflectivities of the box model as discussed in the text and summarized in Table 2. On the right we show the scattering length density profiles corresponding to the calculated reflectivities on the left (For interpretation of the references to colour in this figure legend, the reader is referred to the web version of this article).

Due to the fact that sample E was prepared at slightly different conditions than samples A–D, it was necessary to re-fit the thickness of the base repeat unit $(PSS/PAH)_1$ for sample E. It turns out that the thickness of the base repeat unit of sample E is 26.2 Å, which is 0.85 Å or 3.3% thicker than the thickness of the base repeat unit of samples A–D (25.4 Å). All other parameters of the multilayer model were kept identical to the values used for samples C and D. Fig. 4 shows that the experimental data and the calculated reflectivities are in excellent agreement after fitting only a single parameter (the thickness of the base repeat unit).

Sample F was prepared by dipping and we already know from previous experiments [2] that films prepared by dipping and by spraying differ considerably in thickness. The ellipsometrically determined thicknesses of samples E and F were 1050.9 ± 2.6 Å and 1388.5 ± 7.6 Å, thus the dipped sample is 1.321 times thicker than the sample prepared by spraying from the same solutions. This value is in perfect agreement with the previously reported differences between spraying and dipping. The value for the base repeat unit of sample E was therefore multiplied by 1.321 to yield the value of the base repeat unit of sample F of 34.6 Å. However, there was still a large discrepancy between the experimental data and the calculated reflectivities at this stage of structural refinement. Of course, it is always possible to give up a strict model and to fit additional parameters in order to obtain a better

agreement with the data. However, the only physical parameter for which we can justify a change is the roughness of the interface between the deuterated and non-deuterated slabs and the roughness of the film air interface. All these values were set to 18 Å, a value that yielded the best match for the intensities of the 001 and 002 peaks for the superlattice repeat unit. A slightly increased roughness for dipped films with respect to sprayed films was already observed before [2] and is also reflected in the standard deviations of the ellipsometrically determined thicknesses of samples E and F. The experimental data and the calculated reflectivities at this stage of structural refinement are presented in Fig. 4. The agreement between model and data is already quite good, however, the quality of the fit for sample F as expressed by the value of $\chi^2 = 30.4$ is not as good as the quality of the fit for sample E with a value of $\chi^2 = 14.5$. This indicates that there are even more subtle structural differences between polyelectrolyte multilayers that are assembled by spraying or by dipping. However, our current set of data does not allow us to refine further differences in a reasonable way. We are currently planning to investigate such structural details in the near future.

4. Summary and conclusions

Our first neutron reflectometry measurements on spray-assembled superlattice LbL-film architectures of deuterated and non-deuterated PSS and PAH clearly proof that such films are stratified. Depending on the distance between the deuterated layers, we observe one or two peaks (001 and 002) for the superlattice of the deuterated layers within our samples in the Q-range accessible with the EROS beamline at the Laboratoire Léon Brillouin. It is also very clear that spray-assembled films are about 30% thinner than films prepared by dipping. At the present state of structural refinement, we also have an indication for an increased surface roughness and increased interfacial roughnesses between deuterated and non-deuterated slabs in films prepared by dipping. However, our present set of data from samples prepared by dipping does not yet allow an exact determination of the SLD values for deuterated and non-deuterated slabs within films prepared by dipping.

The reflectivity data presented here and their structural refinement clearly show that subtle details in the architecture of polyelectrolyte multilayer films can be analyzed by neutron reflectometry. While the calculated reflectivities we present here do certainly not perfectly match the experimental data, they are in excellent agreement considering that these calculated reflectivities were obtained without any free parameter for samples C and D, and with only one free parameter for samples E and F. All results of the neutron reflectometry measurements are summarized in Table 2.

It will be very interesting to see in the future if even more subtle structural details can be picked up. At present, the spray-deposition of LbL-films is performed manually by using very simple pulverization cans which do not permit sufficient control over the spray process, especially with respect to pressure and delivered liquid volumes. A more precise control of the spray parameters is expected for future measurements with automated spray-deposition equipment with high quality nozzles.

However, the fact that spray-deposition does lead to stratified films and that such films are at least as smooth as films assembled by dipping — while the deposition times for spraying are reduced by at least a factor of 100 in comparison with dipping — makes spray-assembly an extremely attractive method for the fabrication of soft-matter thin films and devices. Spray-deposition allows for a more rapid deposition of multilayer films and apparently to a better control of the roughness, at least for the case of films composed of poly(styrene sulfonate) and poly(allylamine hydrochloride).

Acknowledgements

We acknowledge financial support from the Institut Universitaire de France (G. Decher), the Laboratoire Léon Brillouin, the Université Louis Pasteur, the C.N.R.S. and the French Ministère de l'Enseignement supérieur et de la Recherche (Z. Zheng). We appreciate the help of Dr. Andrew Nelson of ANSTO Australia in getting us started with his MotoFit package.

References

[1] J.B. Schlenoff, S.T. Dubas, T. Farhat, Langmuir 16 (2000) 9968.
[2] A. Izquierdo, S.S. Ono, J.C. Voegel, P. Schaaf, G. Decher, Langmuir 21 (2005) 7558.
[3] A. Michel, A. Izquierdo, G. Decher, J.C. Voegel, P. Schaaf, V. Ball, Langmuir 21 (2005) 7854.
[4] C.H. Porcel, A. Izquierdo, V. Ball, G. Decher, J.C. Voegel, P. Schaaf, Langmuir 21 (2005) 800.
[5] S.S. Ono, G. Decher, Nano Lett. 6 (2006) 592.
[6] C.H. Lu, I. Donch, M. Nolte, A. Fery, Chem. Mater. 18 (2006) 6204.
[7] C. Porcel, P. Lavalle, V. Ball, G. Decher, B. Senger, J.C. Voegel, P. Schaaf, Langmuir 22 (2006) 4376.
[8] K. Ariga, J.P. Hill, Q.M. Ji, Phys. Chem. Chem. Phys. 9 (2007) 2319.
[9] G. Francius, J. Hemmerle, J.C. Voegel, P. Schaaf, B. Senger, V. Ball, Langmuir 23 (2007) 2602.
[10] K.C. Krogman, N.S. Zacharia, S. Schroeder, P.T. Hammond, Langmuir 23 (2007) 3137.

[11] N. Laugel, J. Hemmerle, C. Porcel, J.C. Voegel, P. Schaaf, V. Ball, Langmuir 23 (2007) 3706.
[12] G. Decher, J.-D. Hong, J. Schmitt, Thin Solid Films 210/211 (1992) 831.
[13] G. Decher, in: J.-P. Sauvage, M.W. Hosseini (Eds.), Comprehensive Supramolecular Chemistry, Templating, Self-Assembly and Self-Organization, vol. 9, Pergamon Press, Oxford, 1996, p. 507.
[14] G. Decher, Science 277 (1997) 1232.
[15] G. Decher, M. Eckle, J. Schmitt, B. Struth, Curr. Opin. Colloid Interf. Sci. 3 (1998) 32.
[16] P. Bertrand, A. Jonas, A. Laschewsky, R. Legras, Macromol. Rapid Commun. 21 (2000) 319.
[17] P.T. Hammond, Curr. Opin. Colloid Interf. Sci. 4 (2000) 430.
[18] G. Decher, J.B. Schlenoff (Eds.), Multilayer Thin Films: Sequential Assembly of Nanocomposite Materials, Wiley-VCH, Weinheim, 2002.
[19] Z.Y. Tang, Y. Wang, P. Podsiadlo, N.A. Kotov, Adv. Mater. 18 (2006) 3203.
[20] A.P.R. Johnston, C. Cortez, A.S. Angelatos, F. Caruso, Curr. Opin. Colloid Interf. Sci. 11 (2006) 203.
[21] N. Jessel, P. Lavalle, V. Ball, J. Ogier, B. Senger, C. Picart, P. Schaaf, J.-C. Voegel, G. Decher, in: Y. Gnanou, L. Leibler, K. Matyiaszewski (Eds.), Macromolecular Engineering, Elements of Macromolecular Structural Control, vol. 2, Wiley-VCH, Weinheim, 2007, p. 1249.
[22] J. Schmitt, T. Grünewald, K. Kjær, P. Pershan, G. Decher, M. Lösche, Macromolecules 26 (1993) 7058.
[23] D. Korneev, Y. Lvov, G. Decher, J. Schmitt, S. Yaradaikin, Physica B 213&214 (1995) 954.
[24] G.J. Kellog, A.M. Mayes, W.B. Stockton, M. Ferreira, M.F. Rubner, S.K. Satija, Langmuir 12 (1996) 5109.
[25] H.P. Hong, R. Steitz, S. Kirstein, D. Davidov, Adv. Mater. 10 (1998) 1104.
[26] M. Lösche, J. Schmitt, G. Decher, W.G. Bouwman, K. Kjaer, Macromolecules 31 (1998) 8893.
[27] M. Tarabia, H. Hong, D. Davidov, S. Kirstein, R. Steitz, R. Neumann, Y. Avny, J. Appl. Phys. 83 (1998) 725.
[28] S. Kirstein, H.P. Hong, P. Steitz, D. Davidov, Synth. Met. 102 (1999) 1067.
[29] A. Plech, T. Salditt, C. Munster, J. Peisl, J. Colloid Interf. Sci. 223 (2000) 74.
[30] R. Steitz, V. Leiner, R. Siebrecht, R. von Klitzing, Colloids Surf., A Physicochem. Eng. Asp. 163 (2000) 63.
[31] B. Struth, M. Eckle, G. Decher, R. Oeser, P. Simon, D.W. Schubert, J. Schmitt, Eur. Phys. J. E — Soft Matter 6 (2001) 351.
[32] R. Steitz, V. Leiner, K. Tauer, V. Khrenov, R. von Klitzing, Appl. Phys., A Solids Surf. 74 (2002) S519.
[33] R. Kugler, J. Schmitt, W. Knoll, Macromol. Chem. Phys. 203 (2002) 413.
[34] K. Glinel, M. Prevot, R. Krastev, G.B. Sukhorukov, A.M. Jonas, H. Möhwald, Langmuir 20 (2004) 4898.
[35] H. Ahrens, K. Buscher, D. Eck, S. Forster, C. Luap, G. Papastavrou, J. Schmitt, R. Steitz, C.A. Helm, Macromol. Symp. 211 (2004) 93.
[36] H.W. Jomaa, J.B. Schlenoff, Macromolecules 38 (2005) 8473.
[37] M. Gopinadhan, H. Ahrens, J.U. Gunther, R. Steitz, C.A. Helm, Macromolecules 38 (2005) 5228.
[38] O.M. Tanchak, K.G. Yager, H. Fritzsche, T. Harroun, J. Katsaras, C.J. Barrett, Langmuir 22 (2006) 5137.
[39] P.A. Ribeiro, R. Steitz, I.E. Lopis, H. Haas, N.C. Souza, O.N. Oliveira, M. Raposo, J. Nanosci. Nanotechnol. 6 (2006) 1396.
[40] M. Gopinadhan, O. Ivanova, H. Ahrens, J.U. Gunther, R. Steitz, C.A. Helm, J. Phys. Chem. B 111 (2007) 8426.
[41] L. Parratt, Phys. Rev. 95 (1954) 359.
[42] T.P. Russell, Mater. Sci. Rep. 5 (1990) 171.
[43] A. Nelson, J. Appl. Crystallogr. 39 (2006) 273.
[44] F. Abeles, Ann. Phys. 5 (1950) 596.
[45] F. Ott, F. Cousin, A. Menelle, J. Alloys Compd. 382 (2004) 29.

III.1.1.4. Conclusion

Sprayed $(PSS/PAH)_n$ films were prepared and characterized, the influence of the polymer molecular weight on film construction and the layer structure of the spray-assembled films.

All sprayed films had an excellent linear growth regime, ellipsometry and AFM analysis confirmed that sprayed films are thinner but smoother than dipped films. Molecular weight does not lead to a films build-up mechanism change but a variation in films increment. The use of high molecular weight in both polycation and polyanion leads to the formation of thicker films. For the same architecture, sprayed films are 30% thinner than dipped films prepared under same conditions. But surface roughness of sprayed films is less than 1nm, compared to 2-3nm in dipped films. A thick sprayed film, with a thickness around 150nm, has a surface roughness around 1nm.

Neutron reflectometry analysis in sprayed films internal structure confirmed that the existence of stratified structure in sprayed $(PSS/PAH)_n$ films, at least in preparation conditions described before. Sprayed $(PSS/PAH)_n$ films have a mean film increment of 2.5nm, while that of dipped $(PSS/PAH)_n$ films is 3.5nm. The mean surface roughness of sprayed $(PSS/PAH)_n$ films is 1.3nm, while that of dipped $(PSS/PAH)_n$ films is 1.8nm. However, the slight difference in numerical fitting quality of sprayed and dipped samples indicates that there are some subtle structural differences caused by different preparation method, especially in sample E and F.

With present results, it has been confirmed that film increment diminution and preparation differences do not change film's internal structure but, at present time, it is unable to explain which parameters cause this increment diminution and formation of a smooth film in spraying. More samples with other architectures were analyzed by neutron reflectometry as well, but data treatment and interpretation are not finished yet. Detailed structural investigation will probably reveal the subtle difference in polyelectrolyte multilayer structure caused by different preparation method.

III.1.2. Elaboration of "Simultaneous Spray assembly" system, (collaboration with BASF)

III.1.2.1. Introduction

Mentioned before, LbL surface functionalization is a synthesis like process. At each step, one component participates in film construction, different functionality could be successively incorporated in the film. Generally, LbL deposition is not a time consuming process and spray can reduce enormously the working time compared to dip process. But the simplification in surface functionalization is always desirable.

In 2005, Porcel et al. reported for the first time an improvement of the sprayed layer-by-layer technique identified as simultaneous spray[7]. Instead of spraying alternatively the polyanion and polycation solutions on the substrate surface, both solutions were sprayed simultaneously on the surface.

This improvement completely changed the traditional concept of the LbL technique. In a traditional LbL deposition, for example a layer of polyanion is first adsorbed on the surface and after a rinsing step a polycation layer is deposited. The formation of the film results in the repetition of these adsorption and rinsing steps. Thus, complex formation between the polyanion and the polycation occurs only on the surface and lead to multilayer structure as shown by neutron reflectrometry.

However, in the case of a simultaneous spray procedure, polyion complexation does not occur only on the surface but also during the flying trajectory. Depending on different parameters, such as droplets density, spraying distance, opening position of nozzles, some polyanion droplets and those of polycation may collide with each other. Then these collided and uncollided droplets will merge with the liquid layer on the surface for film formation. At present time, there is no information about the exact ratio of collided and uncollided droplets in film formation. But the predominant complex formation takes place at the interface and the collision of droplets can be neglected.

In the simultaneous spray process, film formation and film growth will depend mostly on the simultaneous spray time, reported by Porcel[7]. Of course, gas pressure, solution viscosity, distance nozzle/substrate, polymer concentration and use of rinse solution will influence the film formation as well, but the spray time remains as the key parameter in this procedure. Porcel[7] reported as well that in a simultaneous spray process, the

thickness of the film is a function of sprayed time. In her work[7], only one polymer couple provides the formation of homogeneous film.

As a consequence, one of challenges in simultaneous spray is to find the appropriate polymer couple, which is capable to form a relative homogeneous film on the surface at a certain spray time. In collaboration with BASF, a simultaneous study of two BASF polymers, poly(vinylamine) and poly(acrylic acid, sodium salt), was carried out. The objective of this collaborative study was to investigate the full potential of a simultaneous spraying and to find optimum conditions, such as polymer concentrations, spray time, spray distance etc, allowing the formation of homogeneous films.

III.1.2.2 Chemical compunds and preparation methods

III.1.2.2.1 Polymers and solutions for simultaneous spraying

Three poly(vinylamine) and two poly(acrylic acid, sodium salt) samples with different molecular weight were received from BASF. The molecular weight of these polymers are the following:

- poly(vinylamine) A: $\overline{M_w}$ <10,000 g/mol
- poly(vinylamine) B: $\overline{M_w}$ = 45,000 g/mol
- poly(vinylamine) C: $\overline{M_w}$ = 340,000 g/mol

- poly(acrylic acid, sodium salt) A: $\overline{M_w}$ = 2,500 g/mol
- poly(acrylic acid, sodium salt) B: $\overline{M_w}$ = 70,000 g/mol

All polymers were dissolved in Milli-Q water and used as received without further purification.

III.1.2.2.2. Characterization techniques for simultaneous sprayed films

Different techniques were used to characterize poly(vinylamine)/poly(acrylic acid, sodium salt) films prepared by simultaneous spray:

- ♣ Ellipsometry
- ♣ Atomic Force Microscopy (AFM)

These techniques are described in details in Chapter II.

III.1.2.3. Discussion of experimental data concerning simultaneous sprayed films

III.1.2.3.1. Alignment of spray nozzles and optimization of control parameters.

Poly(vinylamine) and poly(acrylic acid, sodium salt) were both dissolved in Milli-Q water, therefore, only three nozzles were used. These three nozzles were horizontally placed (Figure 9).

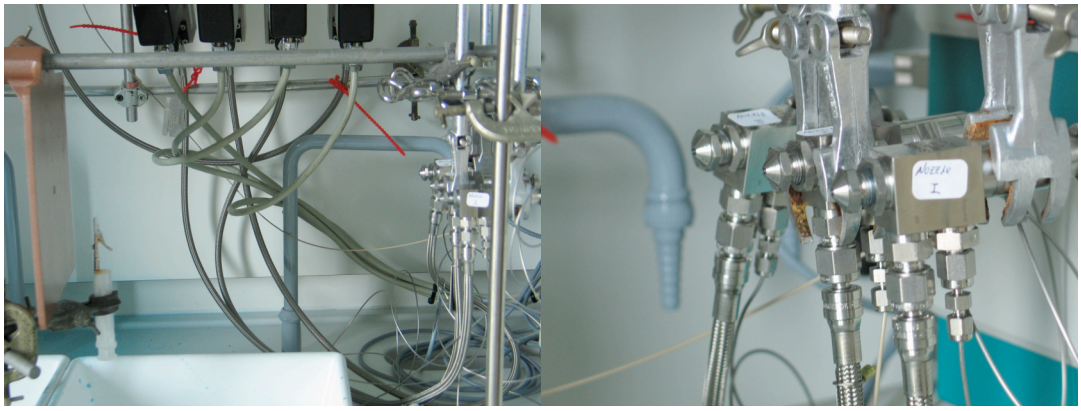

Figure 9: Nozzles alignment set-up (left), and enlargement of nozzles (right)

The first parameter to take care is the alignment of nozzles. Ideally, these nozzles should be on the same height position and the sprayed liquid cone should cover the same area. The alignment of nozzles was adjusted by using a blue colored liquid with Brilliant Blue R dye from Aldrich. This blue liquid was sprayed out from the nozzles one by one to an absorbent paper at a certain distance. The position of those three nozzles was carefully adjusted until the sprayed liquid from each nozzle covers almost the same area (Figure 10).

In Figure 10, a circle area was observed. In the center area, the color distribution is quite homogeneous, while in the edges of the circle area, similar with the manual spray set-up[2], some in-homogeneity was observed. Before every experiment, nozzle alignment was re-adjusted again and then their position was remained the same during the whole simultaneous spray experiment.

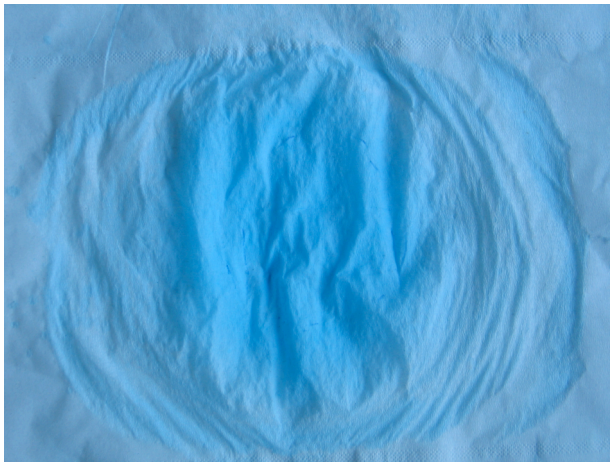

Figure 10: Approach used for spray nozzle alignment using a colored liquid

After nozzle alignment, some other parameters such as polymers concentration, sprayed time, sprayed distance, polymer flow rate, water flow rate and gas flow rate etc. should be tested before the simultaneous spray experiment. Polymer concentration was the first parameter to be investigated.

Before the simultaneous spray experiment, an optimum concentration should be found. Therefore, we used the manual spray process to carry out LbL deposition. The first concentration tested was 3mM. As firstly received polymers, a (poly(vinylamine)/poly(acrylic acid, sodium salt))$_{10}$ film was prepared, but unfortunately, there was no obvious film construction on Silicon wafer after spray deposition. After a random choice, a more concentrated solution (0.6M) was used. After the deposition of 6 sprayed layer pairs, a gel film was formed on the surface and the thickness of this film was around 75nm. By continuing the spray procedure, this film can be easily removed by liquid flow. This experiment indicated that a diluted solution is needed in order to construct a stable film on the surface. Then, two diluted polymer concentrations for both poly(vinylamine) and poly(acrylic acid, sodium salt) solutions, C=0.1M and C=0.3M were used.

With C=0.1M, a transparent (poly(vinylamine)/poly(acrylic acid, sodium salt))$_{10}$ film was formed after 10 sprayed layer pairs and the film thickness was around 40nm. This film was relatively homogeneous as shown by the film thickness measurement error given by ellipsometry (under 1.5nm).

With C=0.3M, a (poly(vinylamine)/poly(acrylic acid, sodium salt))$_5$ film with smaller and higher molecular weight were prepared. Film thickness was measured by ellipsometry after each layer pairs construction (Figure 11).

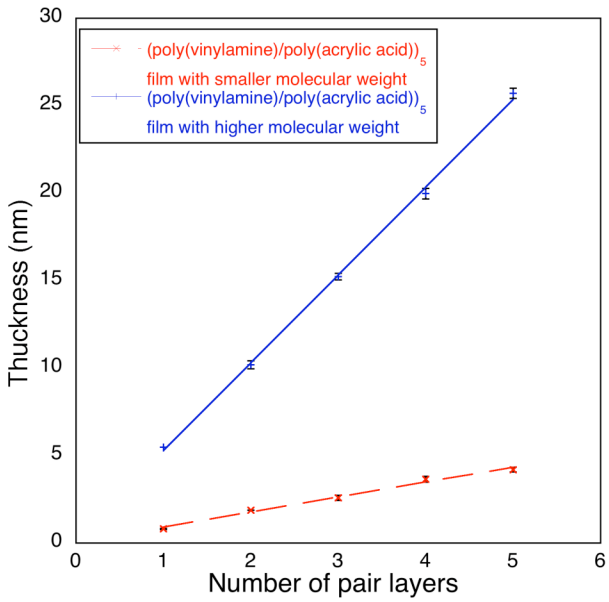

Figure 11: Variation of film thickness as a function of the number of layer pairs for (poly(vinylamine) /poly(acrylic acid, sodium salt))$_5$ film with smaller molecular weight (red line) and with higher molecular weight (blue line), measured by ellipsometry

Figure 11 shows that both manually sprayed (poly(vinylamine)/poly(acrylic acid, sodium salt))$_5$ film with smaller or higher molecular weight have an excellent linear growth. The film with higher molecular weight, blue line, has a thick single layer pair increment (5nm) than that of the film with smaller molecular weight, red line, (1nm). These results are very similar to (PSS/PAH)$_n$ films built-up by spraying with different molecular weight.

These preliminary results in polymer concentration indicate that, unlike the (PSS/PAH)$_n$ films construction, a much more concentrated solution for both poly(vinylamine) and poly(acrylic acid, sodium salt) is needed for film construction. Therefore, three concentrations, C=0.1M, 0.3M and 0.6M for both polymers, were chosen in simultaneous spray.

III.1.2.3.2. Simultaneous spray-assembly of (poly(vinylamine)/poly(acrylic acid, sodium salt)) films

The study on simultaneous spray by using poly(vinylamine) C and poly(acrylic acid, sodium salt) A, the two first received polymer from BASF was carried out.

By random choice, a small liquid flow rate for both polymer (0.5ml/min), a gas flow rate (8 dispensed volume/min) and a rinse water flow rate (5ml/min) in central nozzle at a spray distance equal to 20cm were chosen. With different spray time, a highly viscous gel film was formed on the surface as that observed in manual spray. This film can be easily removed from the substrate by water rinse after spray.

With the present parameters, heterogeneous films were formed on the substrate. In the following experiments, a higher gas flow was introduced in the liquid flow in order to form more homogeneous films by decreasing the size of the liquid droplets. Unfortunately, even at a higher gas flow rate (40 dispensed volumes/min), formed films were still highly viscous and could be easily removed from the substrate. After the removal of in-homogeneous films, there are transparent but highly heterogeneous films left on the substrate.

Then, a higher flow rate (5.0ml/ml) for polymer solutions was used in order to increase the homogeneity of transparent film left on the substrate after the remove of the viscous film. Two samples prepared under this experimental condition formed relative homogeneous films, measured by elliposmetry and BASF AFM analysis confirmed ellipsometry measurement (data not shown here). The optimum experimental conditions for the first (poly(vinylamine) C/poly(acrylic acid, sodium salt) A) simultaneous sprayed films were the following:

- Polymer concentration was 0.6M for both (poly(vinylamine) and poly(acrylic acid, sodium salt) solutions
- A spray distance of 20cm
- Polymer and water flow rates were 5.0ml/min
- Gas flow rate was 40.0 dispensed volumes/min
- Simultaneous spray pray time was 60 seconds
- With or without water rinse solution (central nozzle), homogeneity of the film did not change.

III.1.2.3.3. Influence of the molecular weight of the polymers on simultaneously sprayed films

In the previous paragraph, a highly viscous gel-like film formation other than transparent homogeneous film formation on the surface was observed. These results suggest that either the polymer solutions were too concentrated or that the molecular weight difference between poly(vinylamine) C (340,000) and poly(acrylic acid, sodium salt) A (2,500) did not allow the formation of a homogeneous film.

During following experiments, diluted polymer solutions were used and different poly(vinylamine)/poly(acrylic acid, sodium salt) polymer couples with different molecular weight were investigated. There are three poly(vinylamine)/poly(acrylic acid, sodium salt) couples according to their molecular weight:

- 1. (poly(vinylamine) C/poly(acrylic acid, sodium salt) B (340,000 g/mol and 70,000 g/mol respectively), molecular weight ratio ~5
- 2. (poly(vinylamine) B/poly(acrylic acid, sodium salt) B (45,000 g/mol and 70,000 g/mol respectively), molecular weight ratio ~1.6
- 3. (poly(vinylamine) A/poly(acrylic acid, sodium salt) A (<10,000 g/mol and 2,500 g/mol) molecular weight ratio ~4

These three couples were chosen in order to form polymer couples with similar molecular weights and to study the influence of molecular weight during film construction. Moreover polymer concentration was diluted from 0.6M to 0.3M, it was expected that a diluted polymer solutions could form only transparent film with out the viscous part.

For the first couple ((poly(vinylamine) C/poly(acrylic acid, sodium salt) B), the difference in molecular weight is almost 5 times. During the experiment, a gel-like film was always formed no matter adjustments in the liquid flow rate, gas flow rate, the spray distance or spray time. The only film formation was observed under the LbL deposition conditions for this polymer couple. A ((poly(vinylamine) C/poly(acrylic acid, sodium salt) B)$_5$ sample prepared by the simultaneous spray machine, but with LbL deposition, had a thickness around 24nm with a measurement error of 10%. Preparation conditions in ((poly(vinylamine) C/poly(acrylic acid, sodium salt) B)$_5$ film is the same with manual sprayed (PSS/PAH)$_n$ films, described before.

The two other polymer couples ((poly(vinylamine) B/poly(acrylic acid, sodium salt) B) and ((poly(vinylamine) A/poly(acrylic acid, sodium salt) A) were tested as well by

following the optimum experimental conditions used for ((poly(vinylamine) C/poly(acrylic acid, sodium salt) B) films tests. Very surprisingly, stable films were formed on the substrate surface. These films were not completely transparent or perfectly homogeneous neither and the formed films had a mixed structure of transparent film and gel particles. The homogeneity of the film depends on the ratio between transparent area size and gel particles area size. The smaller the gel particles area size is, the more homogeneous films is formed. Measured by ellipsometry, the thickness of ((poly(vinylamine) B/poly(acrylic acid, sodium salt) B) film varies from 2.5nm to 15nm by changing spraying time from 60 seconds to 300 seconds, without the use of central nozzle, rinse solution. Error bars measured by ellipsometry corresponds to 10% of film thickness.

The formation ((poly(vinylamine) B/poly(acrylic acid, sodium salt) B) film, having a similar molecular weight ratio (1.6), is more homogeneous than that of ((poly(vinylamine) A/poly(acrylic acid, sodium salt) A) film, having a bigger molecular weight ratio (around 4). This observation indicates that the molecular weight of polymer plays a key role in the simultaneous spray film construction process and strongly influence films formation. Moreover, the film thickness seems to be function of spraying time. Meanwhile, under present experimental conditions, the use of central water nozzle, in another word, the use of rinse solution during simultaneous spray changes the film thickness from 5nm (without) to 15nm (with) after 300seconds spray. The influence of rinse solution could be summarized that rinse water locally diluted polymers concentration, whereas film thickness depends strongly on polymers concentration.

Although it seems that films thickness variation is strongly influenced by spraying time. During the ((poly(vinylamine) B/poly(acrylic acid, sodium salt) B) film simultaneous spray, a long time spray (more than 600 seconds) will not increase film thickness but increase the size of gel particles area and eventually creates a viscous gel film. The formation of this viscous film is probably due to the growth and coalescence of gel like particles. This gel film covered surface becomes very inhomogeneous and it will be easily removed by rinse. If the sample is dried directly after spray without any rinse step, the dried gel film becomes completely heterogeneous and can not be measured by ellipsometry.

In following experiments, ((poly(vinylamine) B and poly(acrylic acid, sodium salt) B) were used for the construction of homogeneous films by simultaneous spraying because they have the most similar molecular weight.

III.1.2.3.4. Optimization of the spray-assembly of ((poly(vinylamine)/poly(acrylic acid, sodium salt)) films by simultaneous spraying

Based on optimum parameters used in ((poly(vinylamine) C/poly(acrylic acid, sodium salt) A) films construction, spraying parameters in ((poly(vinylamine) B/poly(acrylic acid, sodium salt) B) film construction were slightly adjusted:

- Polymer concentration was 0.3M for both poly(vinylamine) and poly(acrylic acid, sodium salt) solutions, because a homogeneous film was obtained in manual LbL spray at this concentration.
- A spray distance of 10cm, in order to have enough liquid on the surface
- Polymer and water flow rates were 6.0ml/min
- Gas flow rate was 40.0 dispensed volumes/min
- Without central nozzle (water rinse solution) in order to have a thick film

Under these conditions, a short sprayed time (less than 60 seconds) will lead to a partially transparent film with a few gel-liked particles on the surface, and a long sprayed time (more than 300 seconds) will lead to the viscous gel like film. With the following spraying times, a relative homogeneous film was obtained:

- 60 seconds water spray in order to wet the substrate, followed by
- 60 seconds (poly(vinylamine) spray in order to increase surface adhesion, followed by
- 60 seconds (poly(vinylamine) and poly(acrylic acid, sodium salt) simultaneous spray without central nozzle (water rinse solution), followed by
- 30 second additional adsorption time, followed by
- 60 seconds water rinse solution spray

After preparation, a transparent film with small gel-like particles was formed. The film thickness measured by ellipsometry was around 15.2±1.4nm.

In order to compare the film construction between simultaneous spray and LbL spray, a ((poly(vinylamine) B/poly(acrylic acid, sodium salt) B)$_5$ film was prepared by simultaneous spray machine with exactly the same conditions as for simultaneous spray. In this LbL spray process, the spray time is the same as in (PSS/PAH)$_n$ sprayed films construction. After films build-up, this LbL sprayed ((poly(vinylamine) B/poly(acrylic acid, sodium salt) B)$_5$ film had a mean thickness around 30.5±0.2nm.

Surface morphology of these simultaneous sprayed and LbL sprayed films were visualized by AFM (Figure 12).

Simultaneous sprayed ((poly(vinylamine) B/poly(acrylic acid, sodium salt) B) film and LbL sprayed ((poly(vinylamine) B/poly(acrylic acid, sodium salt) B)$_5$ film have a different surface morphology. LbL sprayed ((poly(vinylamine) B/poly(acrylic acid, sodium salt) B)$_5$ film shows a homogeneous morphology (Figure 12B) which is very similar to LbL sprayed (PSS/PAH)$_n$ films; while simultaneous sprayed ((poly(vinylamine) B/poly(acrylic acid, sodium salt) B) film surface morphology is less homogeneous. Figure 12A shows some bright areas, which corresponding to some islets on the surface with a Z scan range of 7nm. However, surface roughness of simultaneous sprayed ((poly(vinylamine) B/poly(acrylic acid, sodium salt) B) film and LbL sprayed ((poly(vinylamine) B/poly(acrylic acid, sodium salt) B)$_5$ film reveals a similarity. Simultaneous sprayed ((poly(vinylamine) B/poly(acrylic acid, sodium salt) B) film has a RMS value of 1.7±0.3nm and LbL sprayed ((poly(vinylamine) B/poly(acrylic acid, sodium salt) B)$_5$ film has a RMS value of 1.6±0.1nm.

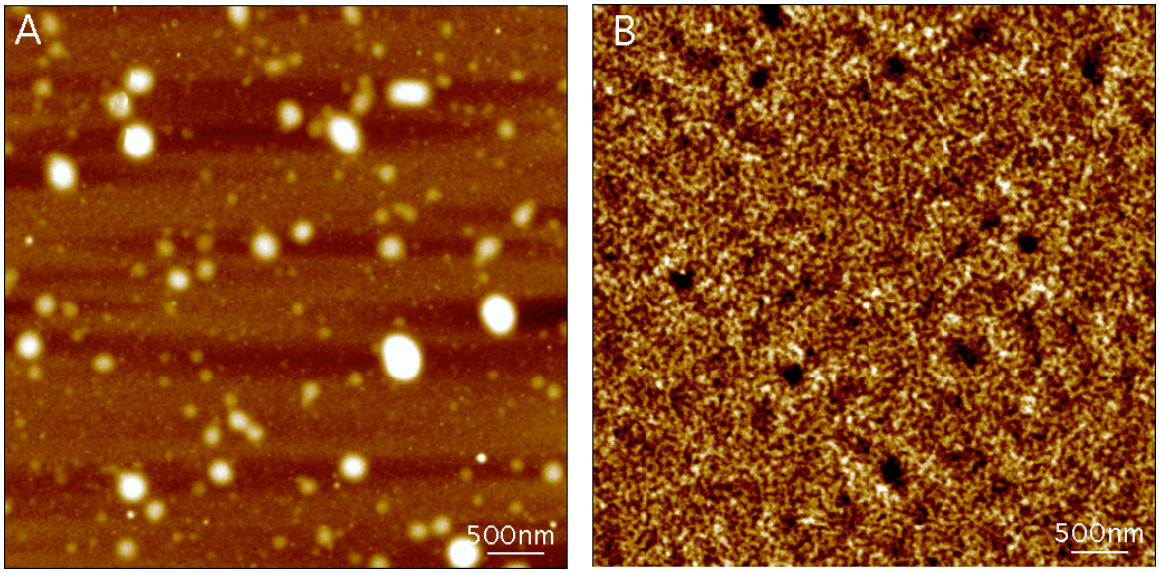

Figure 12: Height images of ((poly(vinylamine) B/poly(acrylic acid, sodium salt) B) film prepared by simultaneous spray (A) and ((poly(vinylamine) B/poly(acrylic acid, sodium salt) B)$_5$ film prepared by LbL (B) by tapping mode AFM

Films prepared by simultaneous spray are composed by transparent film and little gel-like particles. AFM analysis was carried out in the transparent area of the film.

During a simultaneous sprayed film construction, the complex of polyanion and polycation will form firstly some islets on the surface, then, the growth and coalescence of these islets will lead to the formation of a homogeneous film on the surface. In simultaneous sprayed ((poly(vinylamine) B/poly(acrylic acid, sodium salt) B) film, islets (bright spots) are probable polyions complex and under these islets, a quite homogeneous film was formed. From the image (Figure 12A) many small islets and some larger ones are observed. Larger islets probably come from the growth and the coalescence of small islets. If the continue growth of these larger islets will lead to the merge of all islets and the formation of a homogeneous film on the surface, with corresponding film thickness increase. Newly formed islets will be deposited on the surface for further homogeneous film construction.

III.1.2.4. Conclusion

In this ((poly(vinylamine)/poly(acrylic acid, sodium salt) simultaneous spray experiments, different parameters were studied in order to form homogeneous films on Silicon Wafers.

Studied parameters are polymer molecular weight, polymer concentration, spray distance, spray time, liquid (polymer and water) flow rate and gas flow rate. A similar polycation and polyanion molecular weight will easily lead to a transparent and relative homogeneous film formation on the substrate. A highly concentrated solution will form a undesirable viscous film and at present experiment conditions, a concentration of 0.3M for both polycation and polyanion is the optimum concentration in simultaneous sprayed film construction. At this concentration, a more or less homogeneous film could be obtained. Liquid flow rate and gas flow rate are also important parameters in film formation because they control polymers local concentration on the surface. Without the dilution from the central nozzle, and carried by a gentle gas flow, polymers flow will lead to a formation of a film even if the surface homogeneity is not yet perfect. An additional adsorption time between the spray step and the final rinse step will increase the film thickness as well.

III.2. Construction and characterization of functional LbL films containing gold nanoparticle

III.2.1. Introduction to functional LbL films with gold nanoparticle

One advantage of layer-by-layer technique is its capability to introduce not only polymers, but also other components like inorganic nanoparticle, proteins, DNA, micelles etc, in the film during construction. Moreover, the interactions used for film build-up is not limited to the electrostatic interactions, other interactions such as for example covalent bonds, hydrogen interactions, coordination bonds can also be used for film construction.

In this section, a polyelectrolyte/gold nanoparticle film was constructed by spray-assembly. Interactions between polyelectrolytes and gold nanoparticle were mainly electrostatic. Polymer/Gold nanoparticle thin films were and are still intensively studied for their unique properties in catalysis[8,9], nanoelectronics[10], optics[11] domains.

Schmitt et al. already reported the possibility to construct a polyelectrolytes/gold nanoparticle film by dipping[4]. The film structure was fully characterized by X-ray and neutron reflectometry. However, compared to the polymer adsorption time (normally 15-30 minutes), the adsorption of a single layer pair of gold nanoparticle takes 5 to 6 hours. For this adsorption time, the surface coverage by gold nanoparticle reaches only 30%[4]. This very long deposition time is the major constraint in nanoparticle incorporated thin film fabrication and its potential applications.

Another surface functionalization such as spin-coating could accelerate the deposition time of inorganic nanoparticle[12,13] and reduce the total working time. But the application of spin-coating in surface functionalization is limited by the fact that the size of employed substrate, normally in the order of several cm^2. Sping-coating does not allow a surface functionalization on a large surface, for example, at least more than 20 cm^2. On the contrary, the layer-by-layer spray process could combine advantages of LbL dip process and spin-coating process. Il allows a rapid surface functionalization on a large surface. Therefore, polyelectrolyte/gold nanoparticle thin films were prepared by spray and a full comparison between these sprayed colloid films and dipped colloid films[4] having the same architecture was performed.

First of all, the polyelectrolytes/gold nanoparticle films were prepared by spraying. The growth mechanism and the surface morphology of these films were investigated. A

strong plasmon interaction between two adjacent gold nanoparticle layers was observed in dipped colloid films[4]. These interactions were observed as well in colloid film prepared by spray. A study based on minimizing these plasmon interactions by increasing the distance between two adjacent gold nanoparticle layers was carried out. Finally, a thin colloid film containing a large number of gold nanoparticle layer separated by a minimum spacing distance was prepared and characterized. After a certain number of gold nanoparticle layer in the film, the film will undergo a color transition from a transparent to a violet color and finally to a metal-like golden color.

III.2.2. Chemical compounds and preparation methods

III.2.2.1. Preparation of the gold nanoparticle solutions

Synthesis of gold colloid solution is introduced in Chapter II. The colloid solution was ready for use after synthesis without any dilution or purification.

Measurements by transmission electronic microspcopy were performed in order to determine the mean diameter of gold nanoparticle. The mean diameter of gold nanoparticle was 13.6±0.2 nm. These gold nanoparticle were also characterized by UV-Visible spectroscopy (Figure 13).

Right after the synthesis, the UV-Visible absorption spectrum of freshly prepared gold nanoparticle solution indicates a strong absorption peak at around 550nm (Figure A). The size distribution of nanoparticle is homogeneous because there is no aggregates absorption peak at around 650-700 nm. The colloid solution was stored in dark environment at +4°C and used within one week. The colloid solution was very stable under the present storage condition. UV-Visible absorption spectrum of the same gold nanoparticle solution after a storage time of one month is shown in Figure B. No aggregates absorption peak at around 650-700 nm was observed by UV-Visible spectroscopy. The difference in absorption peak intensity is due to the different dilution ratio of these two colloid solutions.

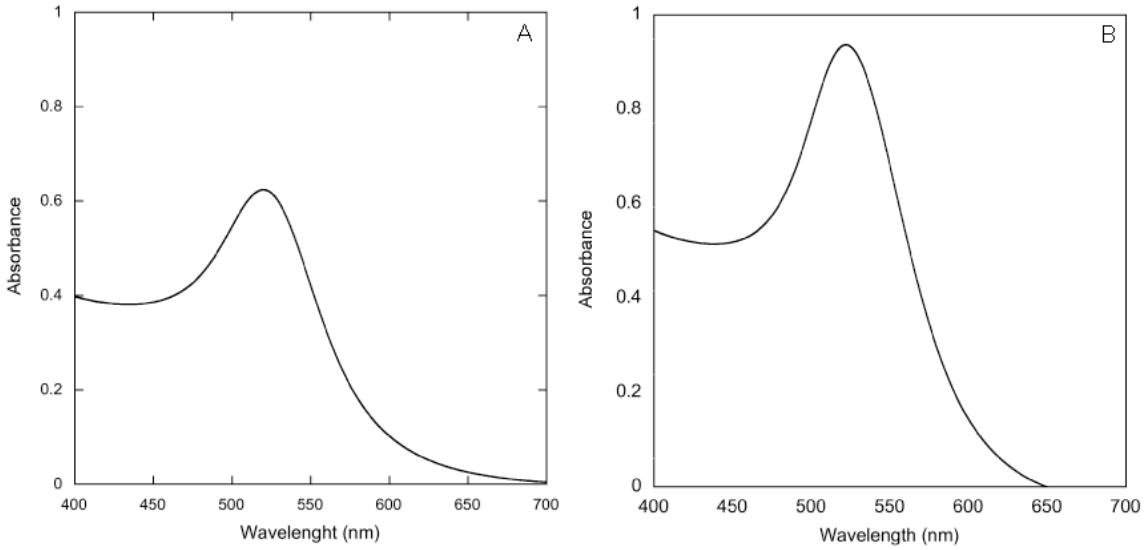

Figure 13: UV-Visible spectrum of a freshly prepared gold nanoparticle solution (A) and of a one month stored gold nanoparticle solution (B)

As gold nanoparticle were stabilized by citrate ions, they were negatively charged and were used as polyanion in colloid film construction.

III.2.2.2. Experimental conditions for polyelectrolyte/gold nanoparticle films construction

Polyelectrolyte/gold nanoparticle films were prepared by manual spray, same as that of $(PSS/PAH)_n$ films. All colloid films were sprayed on silicon wafers, except for UV-Visible analysis where colloid films were sprayed on quartz slides. All substrates were covered with a layer of PEI before films construction.

Polymer rinse was carried out with a 0.5 M NaCl solution and gold nanoparticle rinse was done with Milli-Q water.

A similar spray protocol of $(PSS/PAH)_n$ film preparation was used. A polymer was sprayed on the surface for 5 seconds (t_1), after 15 seconds adsorption time (t_2); the rinse solution was sprayed on the surface for 5 seconds (t_3) and a waiting time of 15 seconds (t_4). As result, the total spray time for a polymer layer is (t_1+ t_2+ t_3+ t_4)= 40 seconds.

A study, described later in the manuscript, will show that five nanoparticle spray cycles are necessary to get a similar surface coverage as a dipped film[4]. Gold nanoparticle solution was sprayed on the surface for 5 seconds (t'_1), after 15 seconds adsorption time

(t'_2); the rinse solution has been sprayed on the surface for 5 seconds (t'_3) and for a waiting time of 15 seconds (t'_4). The total procedure was repeated five times before the deposition of an additional polymer layer. The total spray time for a gold nanoparticle layer is $(t'_1 + t'_2 + t'_3 + t'_4) \times 5 = 200$ seconds.

As a consequence, the total spray time for a single layer pair of polymer/gold nanoparticle was 240 seconds. Compared to the reported dipping condition, the sprayed colloid film preparation has an acceleration of 75 times.

After the preparation, all samples were dried under a gentle nitrogen flow.

III.2.2.3. Characterization techniques for functional LbL films

Different techniques were used for the characterization of polymer/gold nanoparticle films:

- ♣ Ellipsometry
- ♣ UV-Visible spectroscopy
- ♣ Atomic Force Microscopy (AFM)

These techniques are described in details in Chapter II.

III.2.3. Discussion of experimental data concerning functional LbL films

III.2.3.1. Optimization of gold nanoparticle spraying condition in functional film construction

To be able to compare polymer/gold nanoparticle films prepared by dipping and spraying, it was necessary to determine how many nanoparticle spray cycles are necessary in order to have a similar surface coverage?

As a reference sample, a PEI covered quartz slide was dipped into a gold nanoparticle colloid solution for 6 hours as reported in literature[4]. After the dipping and the rinsing, the quartz sample was violet colored, which indicates the adsorption of gold nanoparticle onto it. Then, the sample was analyzed by UV-Visible spectroscopy (Figure 14). The maximum intensity of the gold nanoparticle deposited on the surface was 0.045 at 550-575nm.

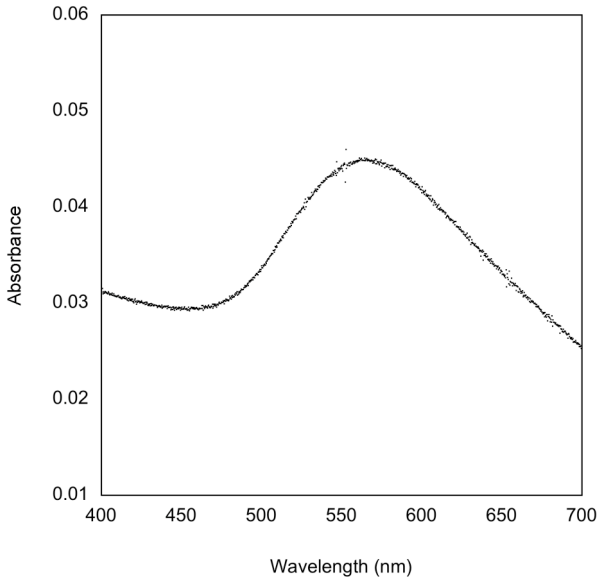

Figure 14: UV-Visible spectrum of a PEI/Au NP dipped sample

The Au NP absorption intensity of 0.045 observed for dipping was set to a reference value, the sprayed Au NP absorption should have the same or similar intensity. Gold nanoparticle were sprayed onto a new PEI covered quartz slide. After each spray cycle, the sample was analyzed by UV-Visible spectroscopy (Figure 15). After 5 spray cycles, gold nanoparticle absorption peak had an intensity of 0.050 which is close to the value obtained by dipping. In Figure 15, the absorption curve of Au NP after one spray cycle is not shown because the absorption intensity was not sensitive enough.

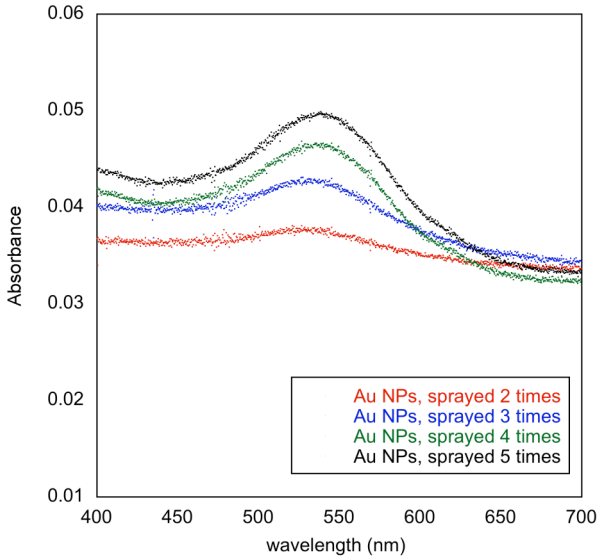

Figure 15: UV-Visible spectrum of a PEI/Au NP film observed after 2 to 5 spray cycles

It seems that a five nanoparticle spray cycles is the optimum parameter for getting the similar surface coverage as a dipped film in term of gold nanoparticle UV-Visible absorption.

In parallel, The surface morphology of dipped and sprayed Au NP samples were visualized by AFM (Figure 16) and the density of nanoparticle was calculated. In the literature[4], AFM of a dipped colloid film demonstrates that the surface was completely covered by gold nanoparticle but a X-ray reflectometry analysis revealed that the maximum surface coverage rate for such a film is around 30%. In order to determine if a five time sprayed colloid film has the "full" surface coverage, the AFM visualized was carried out.

Figure 16A represents a Au NP monolayer deposited on a PEI layer by dipping and Figure 16B represents a Au NP monolayer deposited on a PEI layer by spraying with five consecutive spraying cycles. At a first look, these two images are very similar, the PEI surface is totally covered by Au NP with comparable densities. These images are also similar to reported film prepared by dipping[4]. The density of Au NP on dipped layer (Figure 16A) and on sprayed layer with 5 spraying cycles (Figure 16B) is almost identical.

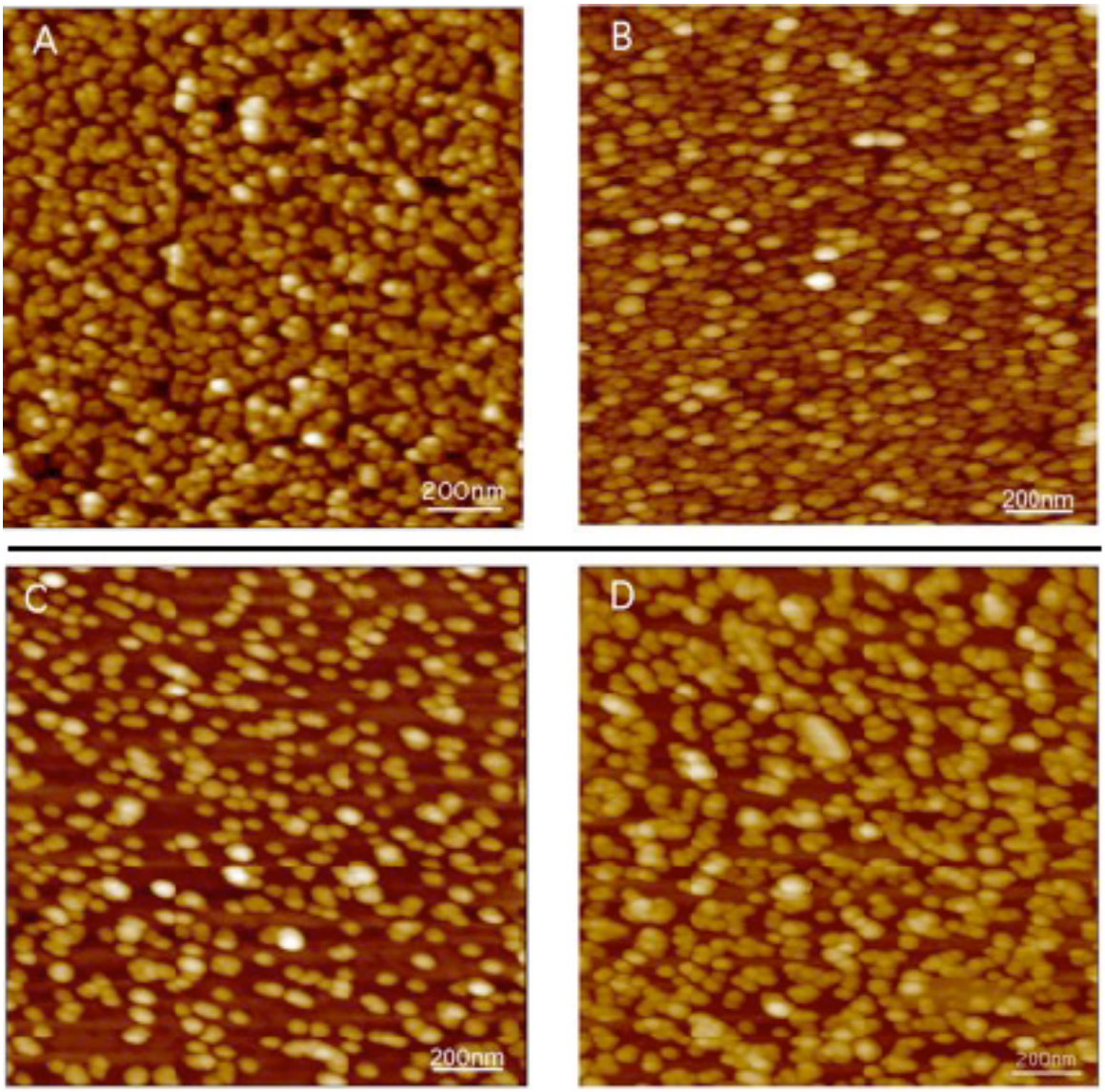

Figure 16: Analysis of the density of nanoparticles in differently prepared Au NP monolayers on PEI (A) Au NP assembled by dipping (B) Au NP assembled by spraying with five spraying cycles (C) Au NP assembled by spraying with one spraying cycles (D) Au NP assembled by spraying with three spraying cycles. Images are visualized by tapping mode AFM. All images are height images

However, AFM images (Figure 16C and D) of Au NP on sprayed layer with different spraying cycles are completely different with those of Au NP fully covered surface. Figure 16C represents a Au NP monolayer deposited on a PEI layer by spraying with one spraying cycle and Figure 16D represents a Au NP monolayer deposited on a PEI layer by spraying with three consecutive spraying cycles.

From these two images, surface is not completely covered by Au NP, uncovered PEI surface can be observed. But compare to Figure 16B, it clearly shows that the density of particle of Au NP monolayer prepared by spraying is a function of number of spraying

cycles. More Au NP were adsorbed on the surface, more the density of particle is important and more the monolayer is dense (Figure C to D to B).

Attention should be paid concerning the formation of the monolayer of Au NP. Figure 17A is a simplified scheme of the formation of (polyelectrolyte/Au NP)$_n$ film, when Au NP is adsorbed on the polyelectrolyte layer, instead of forming a perfect smooth layer (Figure 17A1), Au NP are confined to plane with a certain positional disorder (Figure 17A2), which is the origin of the Au NP layer's roughness. Figure 17B to E represent the adsorption of Au NP on polyelectrolyte surface and the formation of a monolayer. With the deposition of Au NP, polyelectrolyte surface will be progressively covered by Au NP with the increase of particle density (Figure 17B to D). However, in a monolayer formation process, some nanoparticle can be adsorbed onto others (Figure 17E and Figure 16B), which is probably due to the invisibility of polyelectrolyte chains by AFM. The schema Figure 17E is a "real" Au NP monolayer, but Figure 17A is used for the presentation of such film construction.

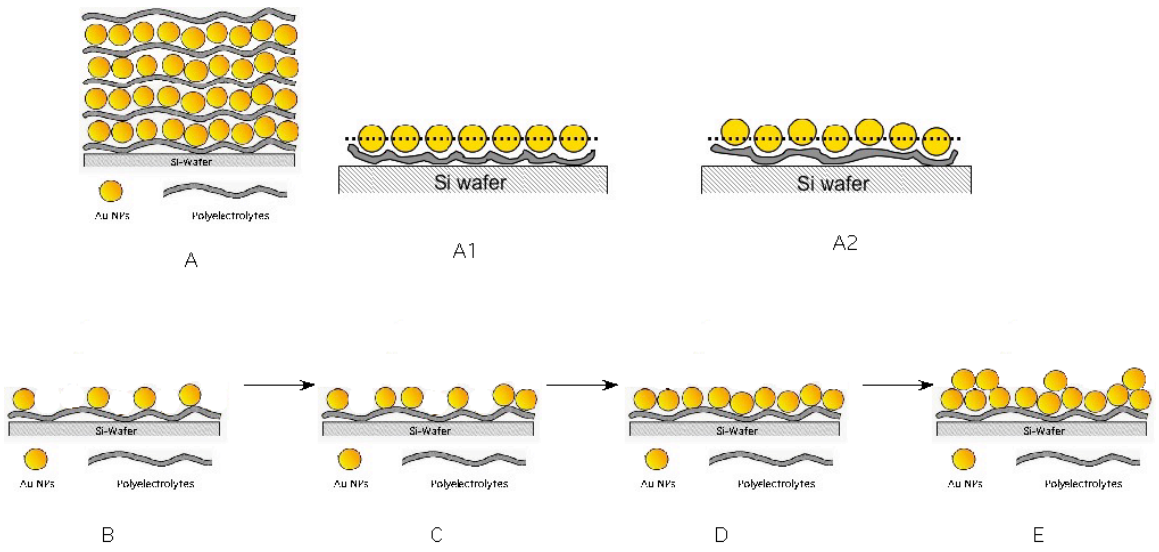

Figure 17: Schematic representation of (A) a simplified (polyelectrolyte/gold nanoparticle)$_n$ film and (B to E) the formation of a Au NP monolayer

Five spray cycles were fixed as the optimum number of spray cycles in a polymer/gold nanoparticle film construction, at least for the present preparation conditions. This procedure was applied in all following experiments concerning the gold nanoparticle film.

III.2.3.2. (Polymer/gold nanoparticle)$_n$ films construction and surface morphology investigation

A (PAH/Au NP)$_n$ film was built-up by spray. The PAH was chosen as polycation and the concentration of PAH was kept at the same value (3mM) as in (PSS/PAH)$_n$ film construction. The (PAH/Au NP)$_n$ film was deposited by spray on a PEI-covered substrate and in order to have the gold nanoparticle as the outmost layer, one layer of PSS was deposited on PEI. The concentration of PSS was identical to PAH concentration. The general architecture of this colloid film was Si/PEI/PSS/(PAH/Au NP)$_n$, shortly called (PAH/Au NP)$_n$ film. In this system, there is no interlayer diffusion of Au NP in PAH layers because Au NP were separated by only one PAH layer with a thickness less than 1.5nm, (according to neutron reflectometry measurement). This value is much less than Au NP mean size, 13.6nm in diameter, which avoids any particles interdiffusion. And leads to a linear film growth mechanism.

A (PAH/Au NP)$_5$ film was first constructed and film construction was monitored by ellipsometry (Table 2, Figure 18A) and UV-Visible (Figure 18B and C).

Film architecture	Film thickness (nm)
(PAH/Au)$_1$	14.1±0.2
(PAH/Au)$_2$	24.4±0.3
(PAH/Au)$_3$	32.8±0.3
(PAH/Au)$_4$	40.4±1.0
(PAH/Au)$_5$	44.8±0.9

Table 2: Build-up of (PAH/Au NP)$_n$ films monitored by ellipsometry

Film thickness and UV-Visible absorption were measured after each layer pair construction. Both ellipsometry and UV-Visible data indicate a linear film growth for (PAH/Au NP)$_5$ films, which corresponds to the growth mechanism reported for the dipped films having the same architecture[4].

One precision for ellipsometry measurement should be point out. In a film containing gold nanoparticle, the thickness measured by ellipsometry is not the true thickness of the film. This lack of precision is due to the Kramers-Kronig effect linked to the optical absorption of gold nanoparticle at laser wavelength of 632.8nm. But for these experiments, the true thickness of the films was not an important value, it was sufficient

to determine the relative growth increments without applying the Kramers-Kronig correction.

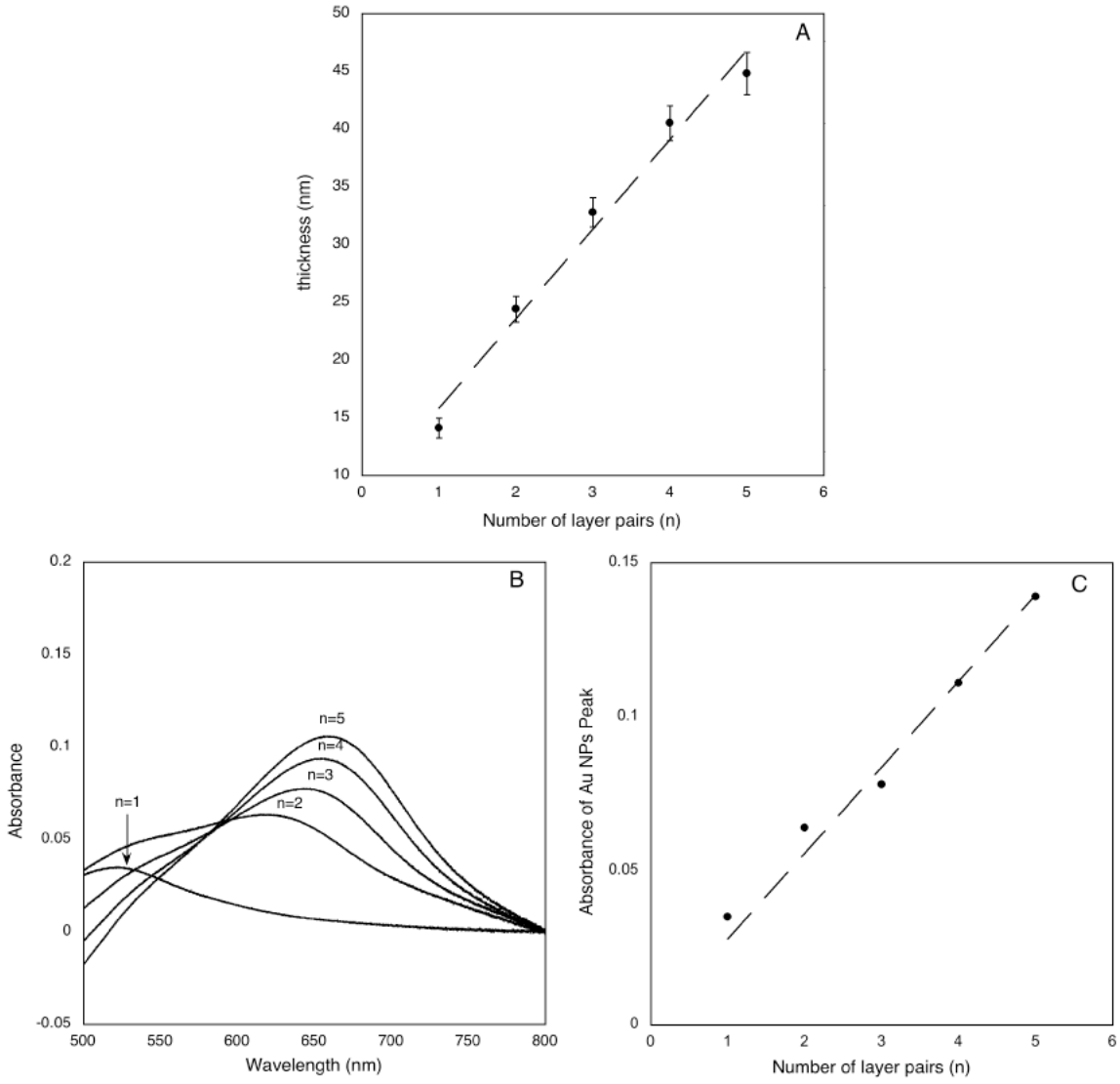

Figure 18: Growth of $(PAH/Au\ NP)_n$ film measured by ellipsometry (A) and UV-Visible spectroscopy (C). (B) corresponds to the UV-Visible absorption of $(PAH/Au\ NP)_n$ films containing as a function of the number of Au NP within the film

The UV-Visible absorption spectrum (Figure 18B) shows that the first gold nanoparticle layer deposited onto the surface leads to an absorption peak at around 520-550nm corresponding to the plasmon absorption of "individual" gold nanoparticle, as already shown for Au NP solution. By adding more gold nanoparticle layers onto the surface, the absorption peak shifts 640 ~ 680nm. This red shift is due to the strong plasmon

interactions between two adjacent gold nanoparticle layers. Details of the plasmon interactions between gold nanoparticle layers will be discussed in section III.2.3.3

An AFM analysis was carried out as well in order to visualize the surface morphology (Figure 19). AFM surface morphology visualization on $(PAH/Au\ NP)_5$ films indicates the formation of a dense Au NP layer. The surface is fully covered by nanoparticle. This image, corresponding to the film with 5 Au NP layers, is very similar to Figure 16B, where a monolayer of Au NP was visualized. However, surface roughness analysis gives a RMS value of 4.8±0.4nm for Figure 19 and a RMS value of 1.8±0.2nm for Figure 16B. This increase in RMS value indicates that the increase of Au NP layer in the film lead to a increase of film surface roughness.

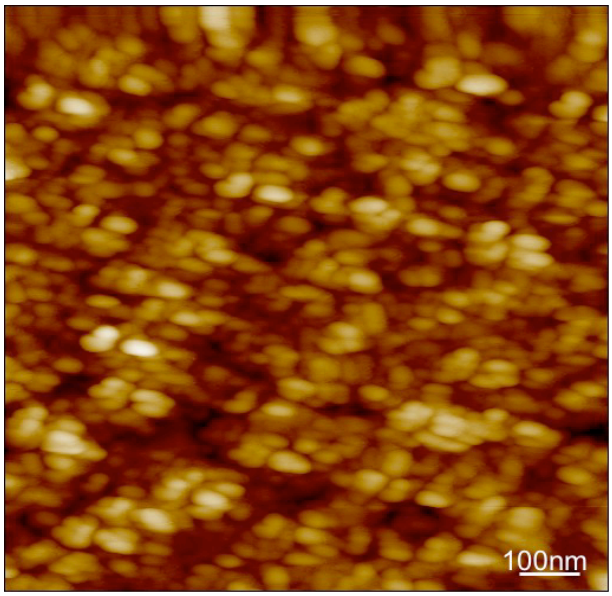

Figure 19: Height image surface morphology visualization of $(PAH/Au)_5$ sprayed film by tapping mode AFM. RMS=4.8±0.4nm

III.2.3.3. Investigation of interparticle distance in (polymer/gold nanoparticle)$_n$ films by measuring the bathochromic shift of the plasmon band

As reported in dipped (polymer/gold nanoparticle)$_n$ films[4], strong plasmon interactions exist when the spacing distance between two adjacent gold nanoparticle layers is not large enough, for example, less than 10nm in dipped films. These interactions can be progressively extinguished by increasing the spacing distance.

In order to verify if the plasmon interactions can be controlled by changing film architecture in sprayed films, as reported in dipped films[4]. Some new film architectures were prepared, the general architecture of these films is Si/PEI/$[(PSS/PAH)_m/(Au\ NP/PAH)]_n$. The number n corresponds to the number of Au NP layer in the film, Each Au NP layer in the film is separated by a spacer layer $(PSS/PAH)_m$, the thickness of this spacer layer is determined by the value of m. In a simplest case, where m=0, each Au NP layer is separated by a PAH layer, which corresponds to films architecture studied in previous section. Films with different values of m varying from 1 to 5 were investigated in order to if the plasmon interactions can be controlled by changing the thickness of spacer layer.

From the general architecture of film Si/PEI/$[(PSS/PAH)_m/(Au\ NP/PAH)]_n$, five detailed architectures were prepared and characterized:

$[(PSS/PAH)_1/(Au\ NP/PAH)]_4$, m=1, n=4
$[(PSS/PAH)_2/(Au\ NP/PAH)]_4$, m=2, n=4
$[(PSS/PAH)_3/(Au\ NP/PAH)]_4$, m=3, n=4
$[(PSS/PAH)_4/(Au\ NP/PAH)]_4$, m=4, n=4
$[(PSS/PAH)_5/(Au\ NP/PAH)]_4$, m=5, n=4

In these five architectures, with different n value, the thickness difference between each film is the thickness of the (PSS/PAH) layer, determined by the m value. The film construction was characterized by ellipsometry and UV-Visible spectroscopy (Figure 20).

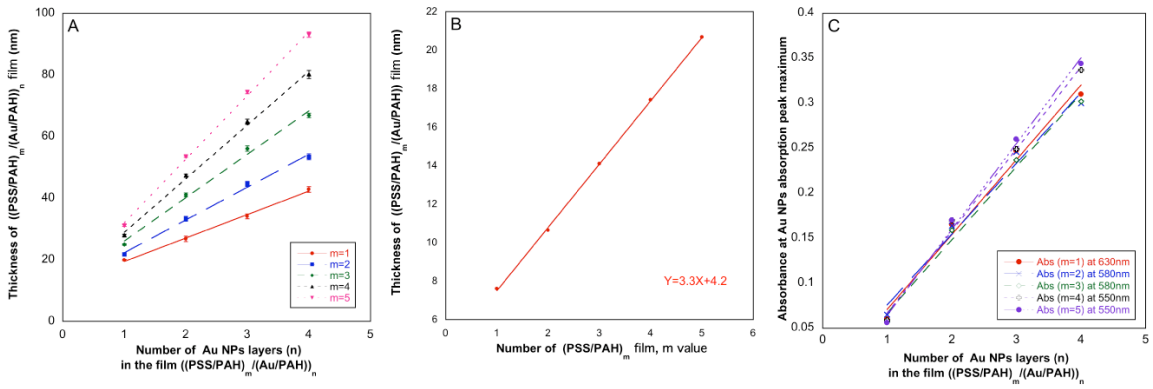

Figure 20: Construction of Si/PEI/$[(PSS/PAH)_m/(Au\ NP/PAH)]_n$ colloid films monitored by ellipsometry (A) variation of /$[(PSS/PAH)_m$ film thickness as function of m value (B) and UV-Visible spectroscopy (C)

During film construction, film thickness was measured by ellipsometry and UV-visible spectroscopy after the deposition of each repeat unit $(PSS/PAH)_m/(Au/NP)$. UV-Visible absorption of gold nanoparticle was observed between 550 nm – 650 nm according to different m value.

Both ellipsometry and UV-Visible data show for all architectures a linear film growth with small error bars as a function of number of Au NP in the film n (Figure 20A and C). From Figure 20A, it is possible to calculate the thickness of (PSS/PAH) spacer layer. Details are described as following.

First of all, all slopes of Figure 20A were collected, which corresponds to the thickness of $[(PSS/PAH)_m/(Au\ NP/PAH)]$ film. Then, these $[(PSS/PAH)_m/(Au\ NP/PAH)]$ films thickness was plotted again as a function of the number of (PSS/PAH) layer in the film, the m value (Figure 20B). From this figure, the slope corresponds to the increment of (PSS/PAH) layer pair in the film. After a linear fitting by KaleidaGraph 4.0, the increment of (PSS/PAH) layer pair in the film is 3.3nm. This value is slightly different with the value measured by neutron reflectometry, even $(PSS/PAH)_n$ films were prepared exactly with same conditions. I would like to assume that this slight difference in (PSS/PAH) layer pair increment is due to the lack of Kramers-Kronig correction during ellipsometry measurement. The ellipsometer PLASMOS SD2300 has not any correlation function for compensation of Kramers-Kronig effect.

The (PSS/PAH) layer pair increment in this experimental section was set to be 3.3nm. As a consequence, the thickness of spacing layer in $Si/PEI/[(PSS/PAH)_m/(Au\ NP/PAH)]_n$ film is 3.3, 6.6, 9.9, 13.2 and 16.5nm respectively for the variation of m value from 1 to 5.

Recently, we had the opportunity to test a spectroscopic ellipsometer (SenPro, Sentech Instruments Gmbh, Germany) with a wavelength range from 370 to 1050nm. Using this instrument, the Kramers-Kronig effect can be taken into account by reflection index calculation and a real colloid film thickness can be obtained. A $(PAH/Au\ NP)_{20}$ sprayed sample was measured and a total film thickness of 230-240nm was obtained. Thus, the single layer pair increment for (PAH/Au NP) is between 12 to 13 nm. While in previous ellipsometry measurement with PLASMOS SD2300, the thickness of sprayed $(PAH/Au\ NP)_{20}$ film was about 180nm. This calculation indicates that the Kramerss-Kronig correction represents nearly 30% of film thickness.

Independently, in UV-Visible measurement of $[(PSS/PAH)_m/(Au\ NP/PAH)]_n$ film (Figure 20C), the variation of absorbance of Au NP was set to be a function of number of Au NP layer in the film, the n value. Initially, spectra with different m value were expected to be overlapped. Because for a fixed n value, no matter the variation of m value, the number of Au NP layers in the film is the same. Figure 20C shows a very good overlapped spectra for all m value, except for n=4, where spectra are slightly separated.

This slight disagreement with the expectation could probably be explained by the bathochromic shift of the surface plasmon band, which will be discussed in next section (Figure 21).

The plasmon interactions between two adjacent sprayed gold nanoparticle layers were characterized by UV-Visible sprectroscopy (Figure 21).

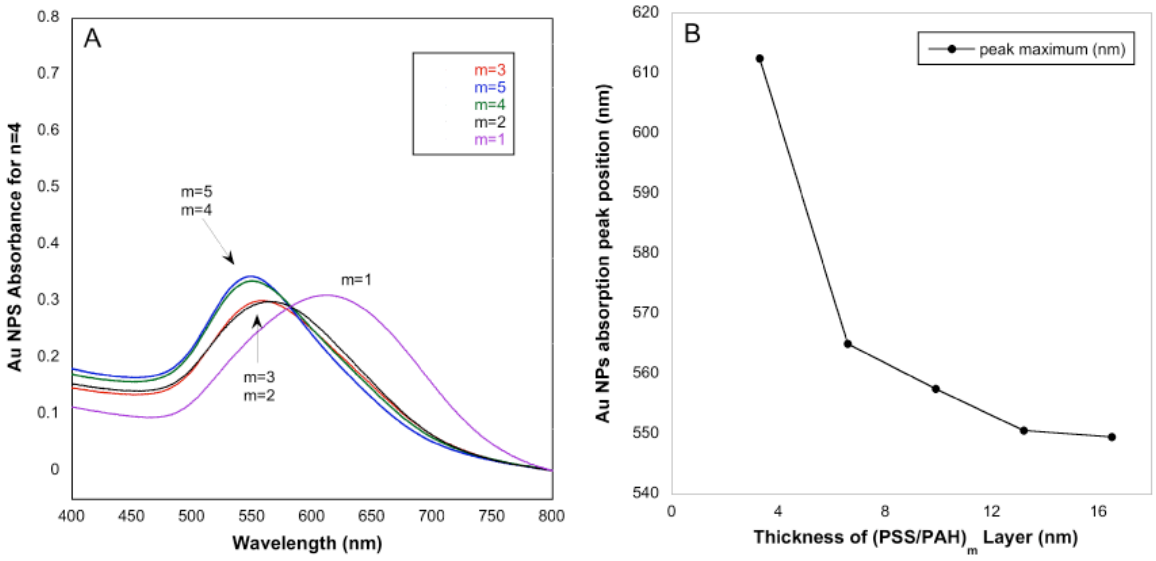

Figure 21: (A) UV-visible spectrum of $[(PSS/PAH)_m/(Au/PAH)]_4$ with m from 1 to 4. (B) Plot of maximum adsorption as a function of spacing polyelectrolyte layer thickness

When two adjacent gold nanoparticle layers have a small spacing distance, m=1, the adsorption peak has a red shift to λ_{max}=630nm and the peak is quite large compared to other four peaks (Figure A). These observations correspond to a strong plasmon interactions. These interactions come from the possibility of the free electron cloud of gold nanoparticle to overpass the polycation layer and "communicate" between themselves.

By increasing progressively the spacing distance between two adjacent gold nanoparticle layer from 3.3nm to 13nm or more (Figure 21B), the maximum absorption peak of gold nanoparticle shifts back to 550nm, corresponding to the absorption of a single layer pair of (PAH/Au NP) (Figure 14). Moreover, the peak width decreases by increasing the spacing distance m.

As conclusion, the plasmon interaction between two adjacent gold nanoparticle layers can be minimized for a spacing distance of 13nm or more. And this result is in agreement with the expected distance value for plasmon coupling.

After construction and characterization of films containing Au NP by ellipsometry and UV-Visible. Films surface morphology were visualized by AFM (Figure 22). Three samples were chosen, sample A (Figure 22A) corresponds to the architecture $[(PSS/PAH)_1/(Au\ NP/PAH)]_1$, sample (Figure 22B) corresponds to the architecture $[(PSS/PAH)_1/(Au\ NP/PAH)]_4$ and sample C (Figure 22C) corresponds to the architecture $[(PSS/PAH)_4/(Au\ NP/PAH)]_4$. The difference of these three samples is that only one Au NP layer in sample A but 4 Au NP layers in sample B and C. However, between sample B and C, the difference is the $(PSS/PAH)_m$ spacer layer, in sample B, there is only 1 (PSS/PAH) layer pair while in sample C, there are 4 (PSS/PAH) layer pairs.

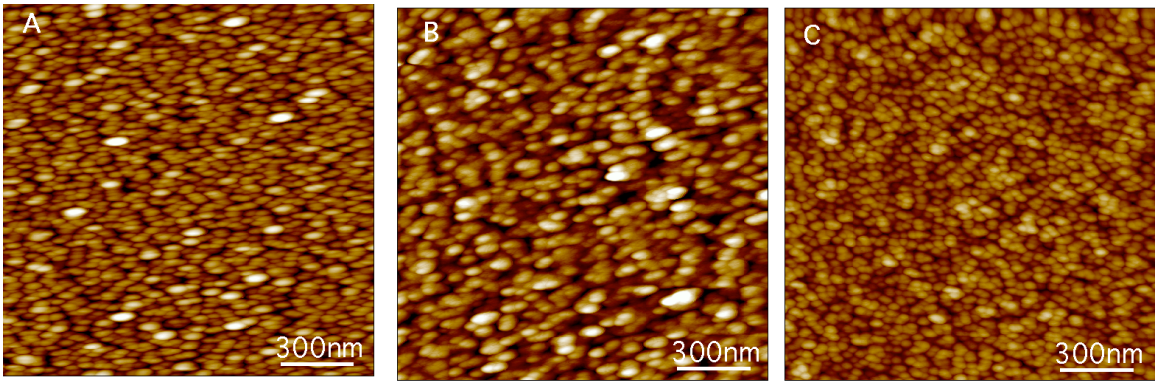

$[(PSS/PAH)_1/(Au\ NPs/PAH)]_1$ $[(PSS/PAH)_1/(Au\ NPs/PAH)]_4$ $[(PSS/PAH)_4/(Au\ NPs/PAH)]_4$

Figure 22: Qualitative comparison of the smoothing effect of polyelectrolyte layers (A) $[(PSS/PAH)_1/(Au\ NP/PAH)]_1$ film, RMS=1.7±0.2 (B) $[(PSS/PAH)_1/(Au\ NP/PAH)]_4$ film, RMS=5.8±1.0 and (c) $[(PSS/PAH)_4/(Au\ NP/PAH)]_4$ film. RMS=3.6±0.4. Height images visualized by tapping mode AFM

Film architecture	Surface roughness (RMS) nm
$(Au\ NP/PAH)_1$	1.8±0.2
$(Au\ NP/PAH)_5$	4.8±0.4
$[(PSS/PAH)_1/(Au\ NP/PAH)]_1$	1.7±0.2
$[(PSS/PAH)_1/(Au\ NP/PAH)]_4$	5.8±1.0
$[(PSS/PAH)_4/(Au\ NP/PAH)]_4$	3.6±0.4

Table 3: Surface roughness (RMS value) of polyelectrolyte/Au NP films with different architectures

Surface roughness of these three samples were measured and values were compared with that of $(Au\ NP/PAH)_1$ of Figure 16B and that of $(Au\ NP/PAH)_5$ of Figure 19. Detailed values are summarized in Table 3.

$[(PSS/PAH)_m/(Au\ NP/PAH)]_n$ films surface roughness analysis confirms the result in $(Au\ NP/PAH)_n$ films surface roughness analysis. If there is more Au NP layers in the film, the surface roughness will be more important. For example, in $[(PSS/PAH)_m/(Au\ NP/PAH)]_n$ films, when the number of Au NP layers increase from 1 layer to 4 layers, the surface roughness increases almost 350%. However, with the same number of Au NP layers in the film, for example $[(PSS/PAH)_1/(Au\ NP/PAH)]_4$ film and $[(PSS/PAH)_4/(Au\ NP/PAH)]_4$ film, the increase of the thickness of (PSS/PAH) spacer layers will reduce film surface roughness about 40%. This surface roughness reduction could probably be explained by the smoothing effect of polyelectrolyte layers. After the deposition of a Au NP layer, $(PSS/PAH)_n$ polyelectrolyte layer was deposited onto Au NP layer before next Au NP layer deposition. More thicker this polyelectrolyte layer, more smoother the film surface. The thickness increase of $(PSS/PAH)_n$ layer maybe partially compensated the surface roughness increase caused by the increase of number of Au NP layers in the film.

The combined results from Ellipsometry, UV-Visible spectroscopy and AFM demonstrated clearly that the spray deposition can be used to prepare linear growing $(polyelectrolyte/gold\ Nanoparticle)_n$ films in a quick way as compared to the dipped films, at least in the case of Au NP, PAH and PSS system. The plasmon interactions between two adjacent Au NP layers could be minimized by increasing the spacing distance between them. Films surface roughness increases as function of the number of Au NP layers, but can be reduced by a smoothing effect of polyelectrolyte layers between two adjacent Au NP layers.

III.2.3.4. Toward “metallic” films construction

The spray-assembly of functional LbL film containing Au NP can greatly reduce Au NP adsorption time from several hours to several minutes, which makes a surface coating with a large number of Au NP layers and fabrication of metallic films possible.

$(Au\ NP/PAH)_n$ films with 20 Au NP layers prepared by dipping, with 40 and 50 Au NP layers prepared by spraying were characterized AFM after preparation.

The surface roughness of the dipped dipped $(PAH/Au\ NP)_{20}$ film and sprayed $(PAH/Au\ NP)_{40}$ film were analyzed by AFM (Figure 23).

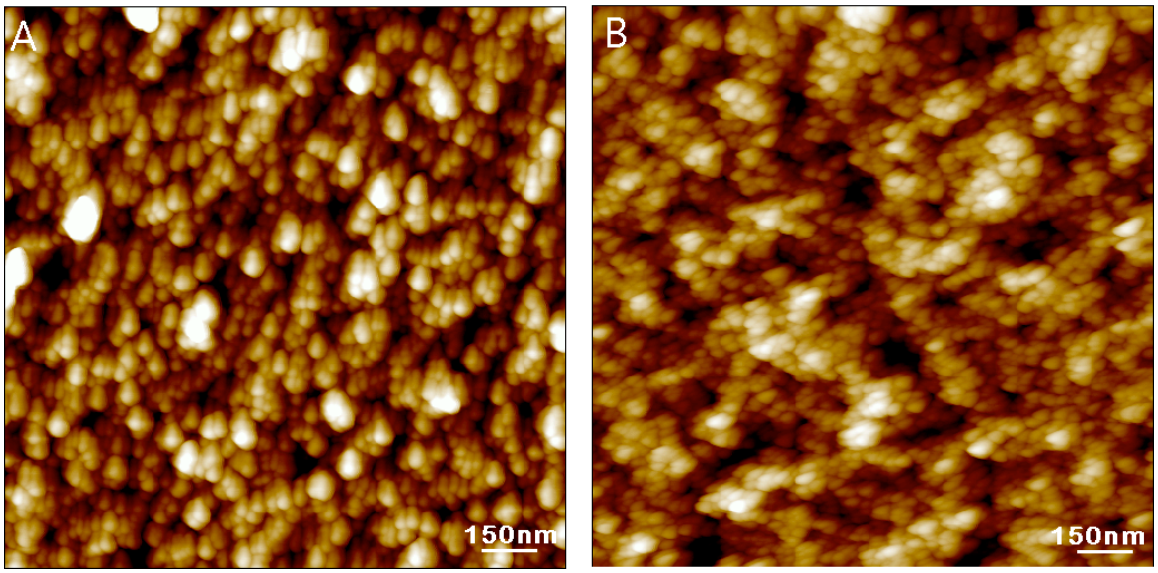

Figure 23: Surface morphology image of (A) $(PAH/Au\ NP)_{20}$ film prepared by dipping, RMS=8.5±1.2nm and (B) $(PAH/Au\ NP)_{40}$ film prepared by spraying, RMS=7.9±1.0nm. Tapping mode AFM, height images

Figure 23 shows that both dipped and sprayed films have a compact and dense Au NP layer on the surface. Surface roughness analysis revealed a RMS value of 8.5±1.2nm for dipped sample and a RMS value of 7.9±1.0nm for sprayed sample. This surface roughness analysis confirms results in Table 3. Surface roughness increases as a function of number of Au NP layers. More Au NP layers without "smoothing" polyelectrolyte layers lead to an increase of surface roughness with increasing thickness. Films surface roughness is a superposing roughness of several Au NP layers. Besides, surface roughness in dipped and sprayed $(Au\ NP/PAH)_n$ films may coincidentally corresponds to the fact that sprayed film is smoother than dipped films, even this result is found in polyelectrolyte films[2].

Figure 17E shows the formation of a Au NP monolayer on a polyelectrolyte surface. If a large number of Au NP are deposited on the surface without the "smoothing" layers. With the superposition of each Au NP layer's surface roughness (Figure 17A2 and E), the film will probably have a "mountain-valley" like structure demonstrated in Figure 24. In this structure, the maximum height and the minimum height of Au NP in the same layer could be Δh.

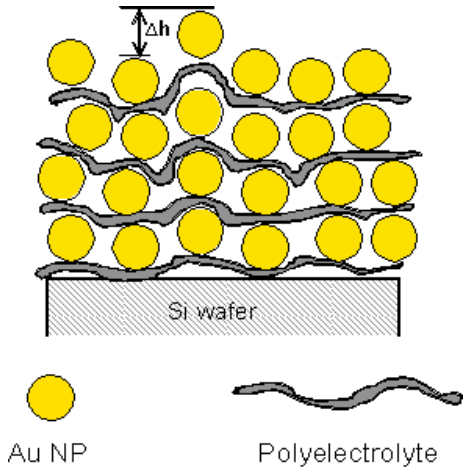

Figure 24: simplified schematic presentation of "mountain-valley" like polyelectrolyte/Au NP film

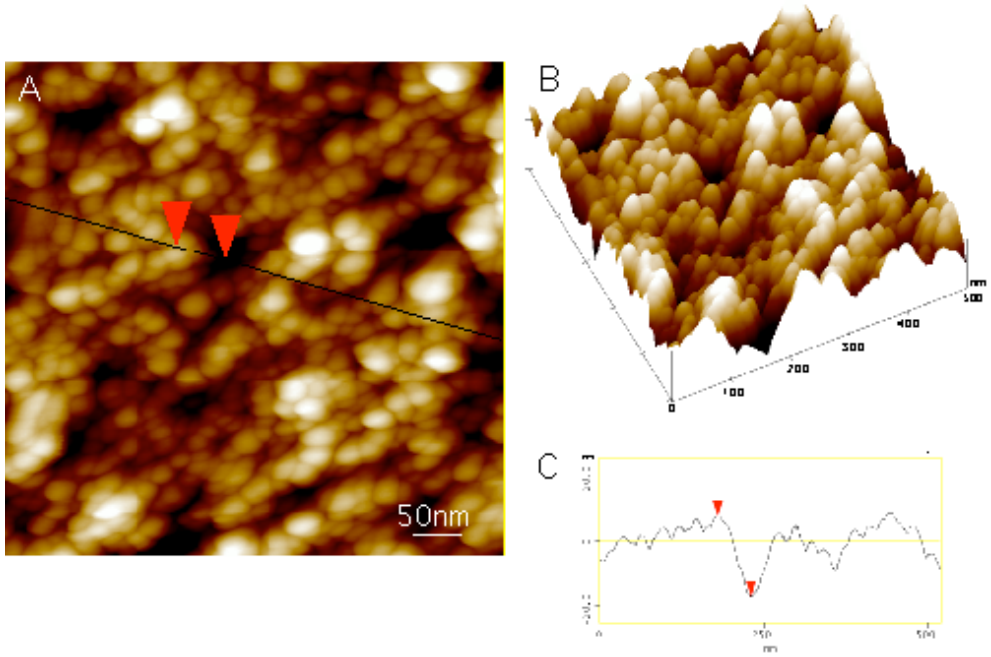

Figure 25: Surface morphology image of sprayed $(Au\ NP/PAH)_{50}$ film (A) 2D image with section analysis (B) 3D image of (A) and (C) spectrum of the section analysis of (A)

From Figure 23, we can already observe this "mountain-valley" like structure of Au NP layer. An AFM surface morphology visualization of a sprayed $(Au\ NP/PAH)_{50}$ film at a smaller scanning size compared to Figure 23 was carried out (Figure 25).

From Figure 25, the "mountain like" structure of Au NP layer can be clearly observed, other than Figure 16B, Au NP layer in Figure 26 is less dense. Dark parts of Figure 26 corresponds probably the valley area. Section analysis gives a vertical distance of 51nm

between red markers in Figure 25A. This distance maybe correspond to the height difference between Au NP at maximum height and those at minimum height in a same layer, which probably corresponds to the distance Δh illustrated Figure 25.

More over, after preparation, all three samples (dipped $(PAH/Au\ NP)_{20}$ film, sprayed $(PAH/Au\ NP)_{40}$ film and sprayed $(PAH/Au\ NP)_{50}$ film) had a metallic film formation on the surface and these film are highly reflective (Figure 26). Scratches on sample B and C are due to the sample holding tweezers.

Figure 26: Optical micrograph of (A) dipped $(PAH/Au\ NP)_{20}$ film, (B) sprayed $(PAH/Au\ NP)_{40}$ film and (C) sprayed $(PAH/Au\ NP)_{50}$ film

By simple optical inspection, all samples show excellent surface homogeneity. However, the preparation time for sample A is 3 weeks, with corresponding 6hours Au NP adsorption time, while the preparation time for both sample B and C is less than 1 days, by following the spraying condition in III.2.2.2

III.2.4. Conclusion

The preparation of functional LbL films containing Au NP by spraying was developed and optimized in this work. Compared to similar dipped films, sprayed films can reduce nearly 100times of Au NP adsorption time. Same as dipped films, sprayed $(PAH/Au\ NP)_n$ films have a linear growth mechanism as dipped films, and formed Au NP layers have a dense structure.

With this great reduction of Au NP adsorption time, it is possible to construct a functional LbL film containing a large number of Au NP layers. Sprayed films with at least 40 Au NP layers were constructed. After preparation, these films have a homogeneous metallic golden color.

Au NP containing functional LbL films surface roughness is more important than polyelectrolyte LbL films. This surface roughness increases as a function of number of Au NP layers in the film. But insertion of a polyelectrolyte "smoothing" layer into two Au NP layer could probably reduce the roughness increase.

Moreover, the surface plasmon interaction between two adjacent Au NP layers can be controlled by changing the thickness of polyelectrolyte spacing layers between Au NP layers, as reported in dipped functional film containing Au NP[4]. A spacing layer thickness of 13nm or more can efficiently avoid the bathochromic shift of Au NP surface plasmon band.

However, This Au NP surface plasmon band shift results is not in perfect agreement with the model of NP adsorption on polyelectrolyte film, recently reported by Kolasinska[14].

In their work, they found out that freshly prepared $(PSS/PAH)_n$ films are softer than post-treated $(PSS/PAH)_n$ films. And if nanoparticle is deposited on soft polyelectrolyte film, instead of forming a dense NP layer, they will diffuse into the film by forming an interfacial mixture, Figure 27. A dense NP layer will only be formed on the rigid polyelectrolyte film, for example post-treated $(PSS/PAH)_n$ film (Figure 27).

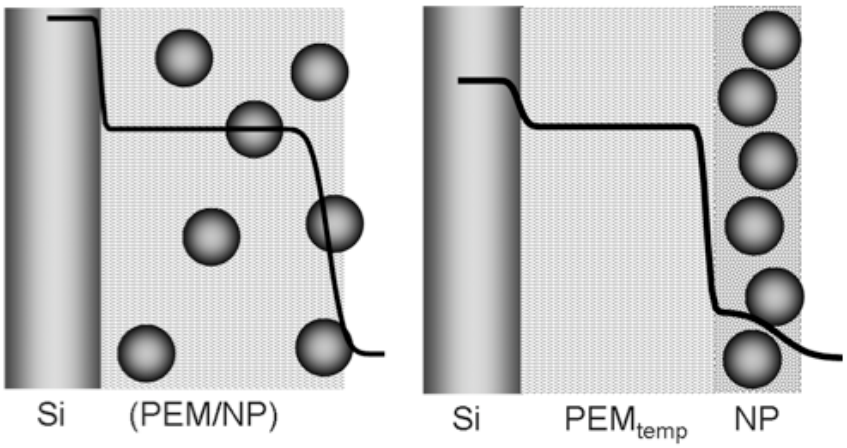

Figure 27: Model for explaining experimental data of neutron reflectometry about the adsorption of NP on soft, freshly prepared polyelectrolyte film (left) and on rigid, post-treated polyelectrolyte film (right). Black line in both image are the measured neutron reflectometry SLD profiles. Image extracted from reference 14

If their model is correct, NP diffuse into polyelectrolyte layers, Au NP surface plasmon band shift can not be controlled by simply changing the thickness of $(PSS/PAH)_n$ spacer layers. In my present work, it is found out that a 13nm or more thick spacing layer could

efficiently avoid Au NP bathochromic shift. But if Au NP diffused into $(PSS/PAH)_n$ layer, there will no Au NP absorption peak shift from 630nm to 550nm (Figure 21). Of course, I would likely assume that this results disagreement is maybe due to different film preparation methods as well as the chemical nature of used nanoparticle.

III.3. Improving of the mechanical resistance of functional LbL films

III.3.1. Mechanical properties of LbL films

The potential applications of a device depend on its chemical and physical stability. Several groups have working on colloid films containing gold nanoparticle for their applications in catalysis[9], nanoelectronic[10] and optic[11]. As a noble metal, gold nanoparticle has an excellent chemical stability and physical stability. Particularly, the mechanical properties of colloid films have been studied[15]. Some gold nanoparticle films with ultra strong mechanical properties have been prepared and fully investigated[15]. In my work, I am particularly interested in mechanical resistance of functional LbL films discussed previously.

First of all, the mechanical resistance of dipped and sprayed colloid films were tested by using a simple rubbing machine described in Chapter II. Without protective layers, after few rubbing cycles, nearly the whole $(Au\ NP/PAH)_n$ film was removed from the substrate. The mechanical resistance of dipped films is even worse then sprayed films. Therefore, a protective film was necessary for potential applications of these colloid films.

$(PSS/PAH)_n$ films were chosen as the first candidate for film protection because such films are so easy to prepare. The colloid films protected with $(PSS/PAH)_n$ layers had a slight improvement in mechanical resistance. In collaboration with Shahid QUERESHI, a visiting student in our team, who worked on the elaboration of robust LbL assembled films by using covalent bonding, such films were tested as protective layers for $(Au\ NP/PAH)_n$ film.

A branched poly(ethyleneimin) (PEI) as amino-component and poly(o-cresylglycidyl ether)-co-formaldehyde also known as Cresol Novolac Epoxy Resin (CNER) were chosen. Because these compounds provide the fastest access to mechanically sable LbL-films (thesis S. Quereshi)

After the epoxy film construction on top of $(Au\ NP/PAH)_n$ films, the mechanical resistance of these films were tested.. The mechanical resistance test of these films revealed a great improvement, which is function of the epoxy film thickness.

III.3.2. Chemical compounds and preparation methods

III.3.2.1. Polymer solutions for covalently linked LbL films

Poly[(o-cresyl glycidyl ether)-co-formaldehyde] (CNER, $\overline{M_n}$ = 1270 g/mol) was purchased from Sigma Aldrich (Cat 408034, batch # 06527MI) (Lyon, France).

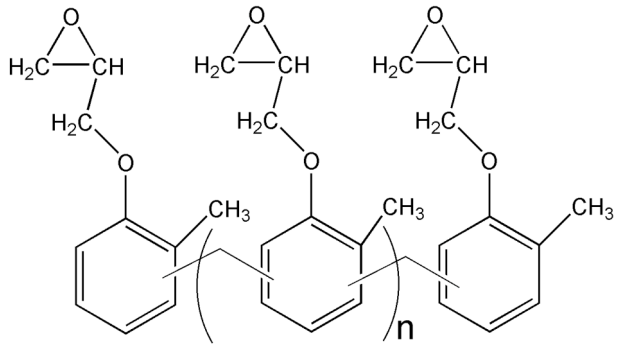

Figure 28: Chemical structure of CNER, Poly[(o-cresyl glycidyl ether)-co-formaldehyde], n≈3

Poly(sodium 4-styrenesulfonate), (PSS, $\overline{M_w}$ = 70000 g/mol,), Poly-(allylamin hydrochlorid), (PAH, $\overline{M_w}$= 70000g/mol) and branched Poly(ethylenimin), (PEI, $\overline{M_w}$= 25000g/mol) were purchased from Aldrich (Lyon, France).

CNER solutions were prepared by dissolution in Acetone (99.5%, from Sigma-Aldrich), while PSS, PAH and PEI solutions were prepared by using Milli-Q water. Polyelectrolyte solutions were always freshly prepared by direct dissolution of the respective polymer in adequate amounts. Thus, solutions of PEI at 1mg/mL, PSS at 0.6 mg/mL, and PAH at 0.27 mg/mL were prepared, respectively. Each polyelectrolyte, except PEI, was dissolved in 0.5M sodium chloride (NaCl, Reagent Plus, ≥99.5%, from Sigma), whereas PEI was dissolved in pure Milli-Q water. All final polyelectrolyte concentrations correspond to about 3×10^{-3} monomol/L (in which monomol corresponds to moles of the respective monomer repeat unit). These concentrations were kept constant during the whole study.

III.3.2.2. The rubbing machine: A simple test for mechanical abrasion of LbL films

As a major investigation instrument in LbL films mechanical resistance property study, the rubbing machine was often used. Besides, other techniques used in this section were:

- ♣ Ellipsometry
- ♣ Atomic Force Microscopy (AFM)

These techniques are described in details in Chapter II.

III.3.3. Discussion of experimental data concerning the improvement of mechanical resistance

III.3.3.1. Mechanical resistance test of dipped and sprayed films containing Au NP

First of all, a dipped and a sprayed colloid films with the same architecture Si/PEI/PSS/(PAH/Au NP)$_5$/PAH were prepared and characterized. After the preparation, the film thickness was measured by ellipsometry. The dipped film had a thickness of around 60nm while the sprayed film thickness was around 41nm. This difference is probably due to the fact that a long Au NP adsorption time was employed in dipped films construction, which corresponds to more Au NP adsorption on the surface.
After film construction, the mechanical resistance of dipped and sprayed Si/PEI/PSS/(PAH/Au NP)$_5$/PAH colloid film has been tested by rubbing machine. Thus, film thicknesses were measured as a function of rubbing cycles.

Number of rubbing cycles	Dipped film thickness (nm)	Sprayed film thickness (nm)
0	59.8±0.1	41.2±0.4
1	6.4±1.3	36.4±0.5
5	3.3±0.8	8.8±2.4
15	1.8±0.3	5.0±1.0

Table 4: Film thickness of dipped and sprayed Si/PEI/PSS/(PAH/Au NP)$_5$/PAH colloid film after rubbing tests

Before the rubbing test, both dipped and sprayed films had a small thickness error, as typically observed for homogeneous films. After the rubbing test, the dipped and sprayed film thickness shows a great difference. After only one rubbing cycle, the dipped film had

lost nearly 90% in film thickness while sprayed film lost only 10%. However, after 5 rubbing cycles, the sprayed film lost 80% in film thickness. After 15 rubbing cycles, dipped colloid film had probably only the PEI layer on the substrate while sprayed film had sill 10% of film left. The results indicate a slightly higher mechanical resistance for sprayed films compared to dipped ones.

This weak mechanical resistance of such colloid films is maybe due to the weak interactions between PAH and Au NP. In these colloid films, spherical gold nanoparticle are connected with PAH polymer chains via negatively charged citrate. However, The Au NP is surrounded by citrate, which is only weakly bounded to the gold. By applying a strong shear force during the rubbing test, this connection between Au NP layer and PAH layer will be destroyed and the film will be removed and lead to a film thickness decrease. However, with the same architecture, the reason why dipped colloid films had weaker mechanical resistance than sprayed colloid films is still unknown. But apparently, sprayed films is robust than dipped films, for this reason, investigation on sprayed colloid films was focused on in order to have stronger mechanical resistance film.

The surface morphology of sprayed Si/PEI/PSS/(PAH/Au NP)$_5$/PAH colloid film before and after rubbing test was visualized by AFM (Figure 29).

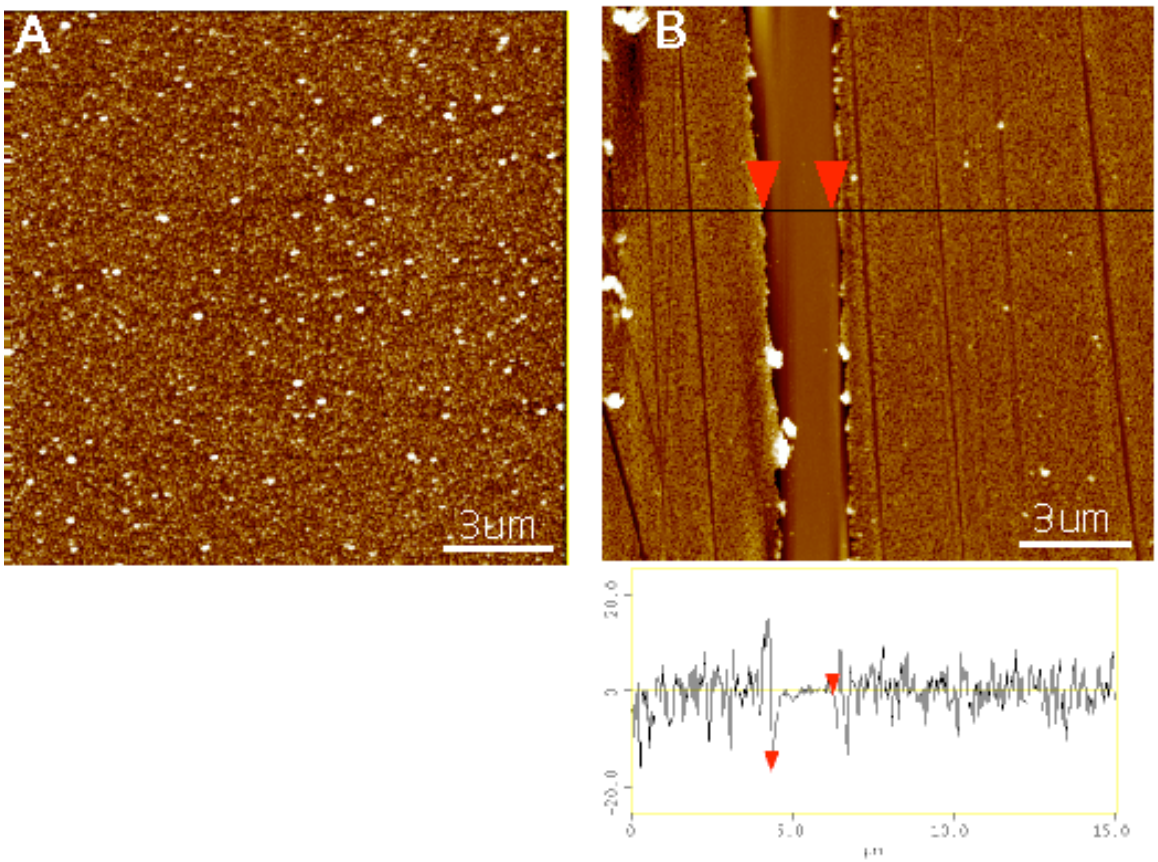

Figure 29: Morphology image of sprayed Si/PEI/PSS/(PAH/Au NP)$_5$/PAH colloid film before the rubbing test, RMS=6.7±0.5nm (A) and after 1 rubbing cycle, RMS=5.2±0.3nm (B), by tapping mode AFM. Both are height images

Figure 29 shows a great difference for a sprayed colloid film before and after rubbing test. Before the rubbing test (Figure 29A), the colloid film surface morphology is quite homogeneous with a roughness (RMS) of 6.7±0.5nm at a scanning size of 15μm. After 1 rubbing cycle (Figure 29B), the film was broken under shearing force. Section analysis indicates a vertical distance of 16.1nm and a horizontal distance of 1.9μm for the trench on the surface. The vertical distance of the trench represents already ~40% of the initial thickness of the colloid film. Moreover, the surface roughness analysis in Figure 29B reveals a surface roughness (RMS) of 5.2±0.3nm. During the rubbing test, the colloid film surface was progressively eroded by forming a trench. However, the slight decrease of surface roughness of rubbed film is probably due to the palette-knife effect, which may make film more and more smooth.

III.3.3.2. Mechanical resistance test of functional films protected by weak LbL films

From the previous mechanical resistance analysis results of un-protected Au NP colloid films, we can clearly see that these films have a very weak mechanical resistance: dipped films are worse than sprayed films. A protection film is absolutely necessary in order to increase the mechanical resistance of gold nanoparticle film. $(PSS/PAH)_n$ films were chosen as first candidate for film protection because $(PSS/PAH)_n$ films and gold nanoparticle films could be prepared by the same assembly technique, the spraying.

First of all, a $(PSS/PAH)_3$ film and a $(PSS/PAH)_6$ film were sprayed on a $Si/PEI/PSS/(PAH/Au\ NP)_5/PAH$ colloid film. After deposition, the architecture of the protected film is $Si/PEI/PSS/(PAH/Au\ NP)_5/PAH/(PSS/PAH)_n$ where n=3 or 6. Film construction was monitored by ellipsometry.

After the deposition of $(PSS/PAH)_n$, the equivalent (PSS/PAH) layer pair increment is 0.8nm for $(PSS/PAH)_3$ film and 1.3nm for $(PSS/PAH)_6$ film. These values are smaller than those measured by neutrons reflectometry for sprayed (PSS/PAH) film (2.5nm) because the surface of Au NP layer is less smooth than silica surface. When polymers were deposited on a Au NP layer, some polymer chains will subside into Au NP cavity area, which corresponds to the decrease of film increment.

Thickness of film without (PSS/PAH) cover layer (nm)	Thickness of film without (PSS/PAH) cover layer (nm)
50.8±1.1	51.5±1.3
Thickness of film with 3 (PSS/PAH) cover layers (nm)	Thickness of film with 6 (PSS/PAH) cover layers (nm)
53.2±0.7	59.3±1.5
Equivalent thickness of cover layer (nm)	Equivalent thickness of cover layer (nm)
~2.4	~7.8

Table 5: Ellipsometry measurement of $Si/PEI/PSS/(PAH/Au\ NP)_5/PAH/(PSS/PAH)_n$ film thickness with n=3 and n=6

Then, the mechanical resistance of colloid films protected by $(PSS/PAH)_n$ was tested. Films thickness was measured as a function of the number of rubbing cycles (Table 6).

Number of rubbing cycles	$(PSS/PAH)_3$ protected colloid film thickness (nm)	$(PSS/PAH)_6$ protected colloid film thickness (nm)
0	53.2±0.7	59.3±1.5
1	48.6±1.2	56.5±0.8
5	27.8±3.7	44.9±3.5
10	21.2±3.5	37.6±4.8
15	11.1±7.7	25.1±9.3
25	5.1±4.7	11.6±8.0

Table 6: Thickness variation of Si/PEI/PSS/(PAH/Au $NP)_5$/PAH/$(PSS/PAH)_3$ film and Si/PEI/PSS/(PAH/Au $NP)_5$/PAH/$(PSS/PAH)_6$ film measured by ellipsometry after rubbing tests

Compared to results obtained for un-protected colloid films (Table 4), there is an obvious improvement of the mechanical resistance by adding $(PSS/PAH)_n$ film as protection layer. Colloid film with 3 (PSS/PAH) protection layer lost 60% in thickness after 10 rubbing cycles while that with 6 (PSS/PAH) protection layer lost 40% in thickness after same number of rubbing cycles. One precision should be point out that all samples were tested and measured right after preparation without any post-treatment. $(PSS/PAH)_n$ films have a slight protection effect but this effect is not satisfied enough. $(PSS/PAH)_n$ top layer can resist no more than 10 rubbing cycles. After then, the whole film is broken and most of the film is removed with corresponding decrease of film thickness. In order to visualize the surface morphology changes of $(PSS/PAH)_n$ protected colloid films before and after rubbing test, an AFM analysis was carried out.

Figure 30 is the surface morphology of Au NP film protected by 3 (PSS/PAH) top layers before (Figure 30A) and after (Figure 30B to D) different rubbing cycles. Before rubbing cycles, film has a very homogeneous overview. After 5 rubbing cycles (Figure 30B), where film lost 50% in thickness, shear force have formed many trenches on the surface and one big trench is formed as well in the middle of the image. In and around this trench, removed materials are aggregated, (bright areas in the image).

After 15 rubbing cycles (Figure 30C), there is a dramatic morphology change. Most of film is removed from the surface, only some film residue is left. In a zoomed image (Figure 30D), the rest of the film could be clearly observed in the upper center of the image. Section analysis indicates that the height of the remaining film varies from 4nm to

15nm. Except for the brightest spot in Figure 30D, it has a height of 176nm, meaning that the film tears up and then material piles up during the rubbing test.

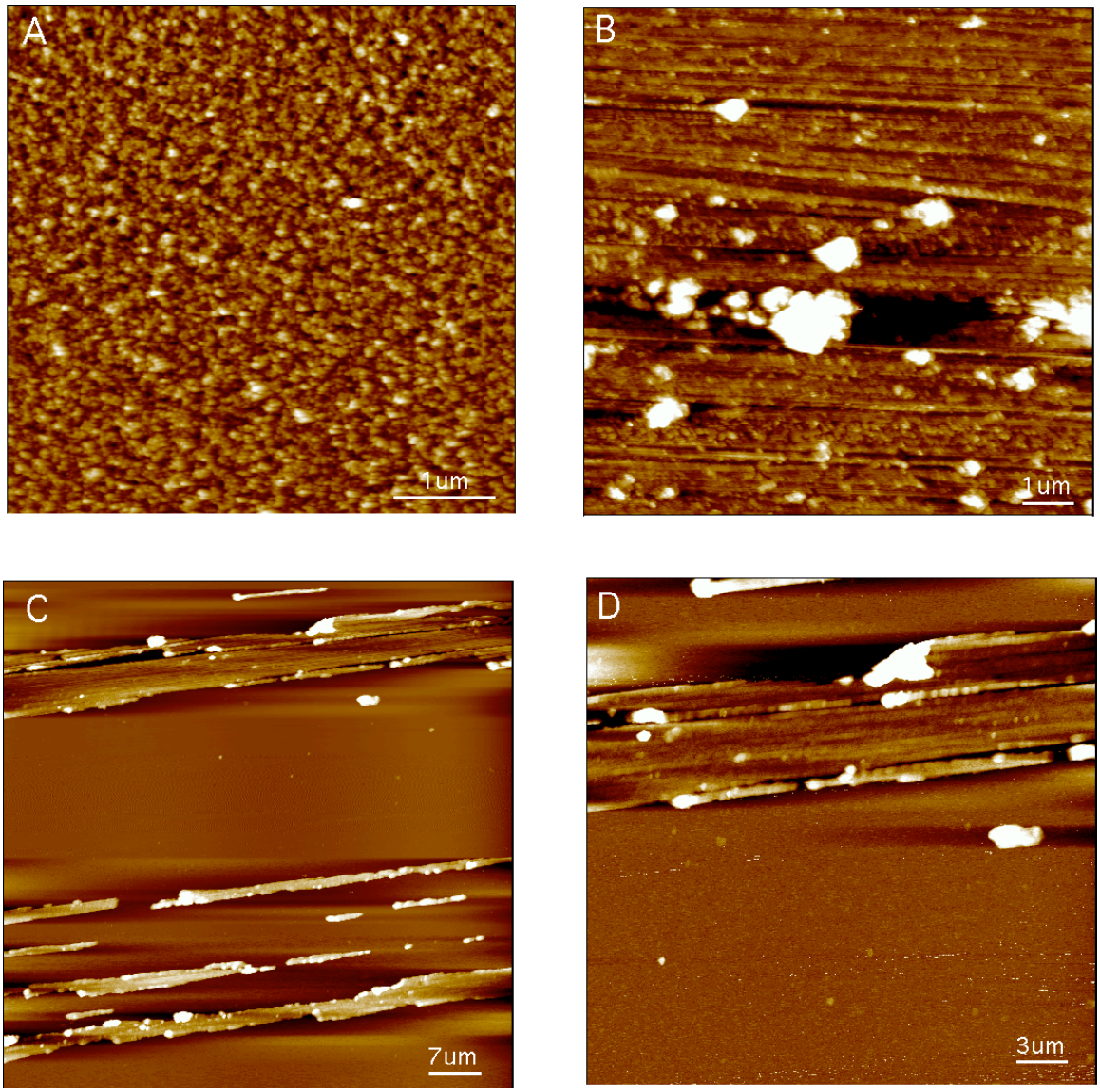

Figure 30: Surface morphology images of $(PAH/Au\ NP)_5/PAH/(PSS/PAH)_3$ film (A) before rubbing test (B) after 5 rubbing cycles (C) after 15 rubbing cycles (D) zoom of image C by tapping mode AFM. All images are height image

However, Au NP film protected by 6 (PSS/PAH) top layer shows a different surface morphology after 15 rubbing cycles test (Figure 31) than that with 3 (PSS/PAH) top layer. Before the rubbing test, the film is homogeneous, similar to Figure 30A. But after 15 rubbing cycles, surface morphology of $(PSS/PAH)_6$ film protected Au NP films is better than $(PSS/PAH)_3$ film protected colloid film. Most of the film is still attached on the surface and some trenches are formed. Two big trenches are also formed, one in the

upper part of the image and another one in the bottom part of the image. Removed material aggregates could be observed in the trench at the bottom part of the image.

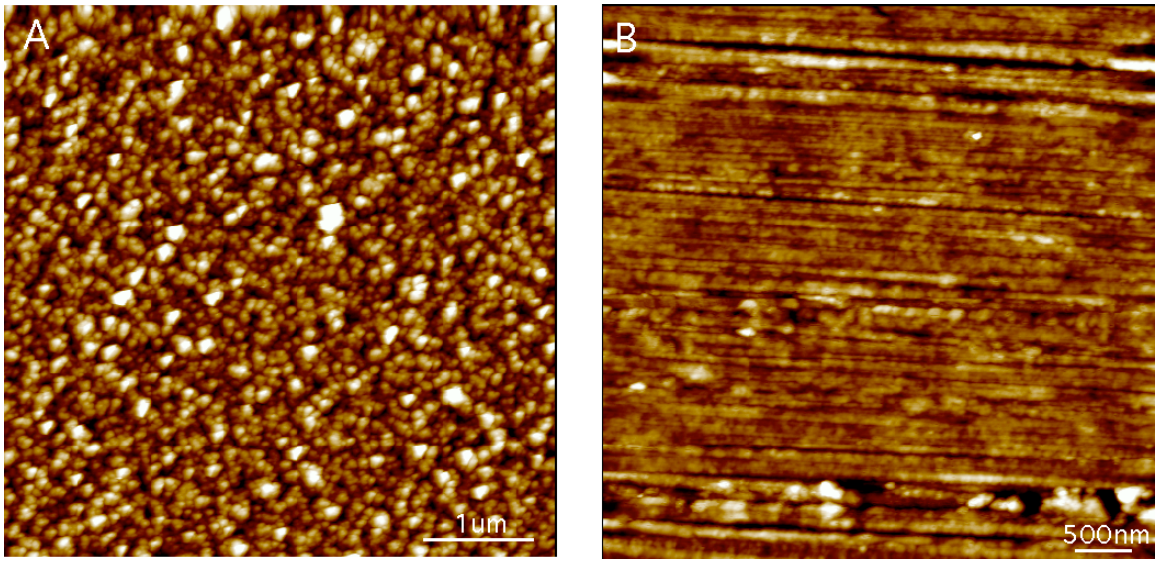

Figure 31: Surface morphology images of (PAH/Au NP)$_5$/PAH/(PSS/PAH)$_6$ film (A) before and (B) after 15 rubbing cycles by tapping mode AFM. Both images are height images

These mechanical resistance tests on (PSS/PAH)$_n$ film protected Au NP films clearly show that the protection effect is a function of top layers thickness. Under the shear forces during the test, some small trenches are formed on the surface. While rubbing cycles continue, these trenches are enlarged and the depth of these trenches increase with rubbing cycles until they bypass the thickness of protection film. Then film will be removed from the surface. However, the (PSS/PAH)$_n$ film protection effect is not really good for further applications of colloid films. In order to improve the mechanical resistance of this (PSS/PAH)$_n$ film protected colloid film, some treatments have been performed to (PSS/PAH)$_n$ film in order to increase its mechanical resistance for a better protection of gold nanoparticle films.

III.3.3.2.2. (PSS/PAH)$_n$ film mechanical resistance tailoring

In previous section, all mechanical resistance tests were carried out on freshly prepared (PSS/PAH)$_n$ films. However, these freshly prepared samples were not robust enough for a gold nanoparticle films protection. Some post treatments were performed to (PSS/PAH)$_n$ film in order to increase the (PSS/PAH)$_n$ films resistance. First of all, an old (PSS/PAH)$_{20}$ film stored for 9 months at ambient temperature was chosen randomly. After a manual mechanical resistance test with an abrasive paper, this sample demonstrated a strong

mechanical resistance. This result probably indicates that a time aging process could increase the $(PSS/PAH)_n$ film mechanical resistance. The mechanical resistance of some freshly prepared and different time aged $(PSS/PAH)_n$ films was tested by rubbing machine.

First of all, the mechanical resistance of a $(PSS/PAH)_3$ sprayed sample, a $(PSS/PAH)_6$ sprayed sample and a $(PSS/PAH)_{10}$ sprayed sample were tested right after film preparation (Figure 32).

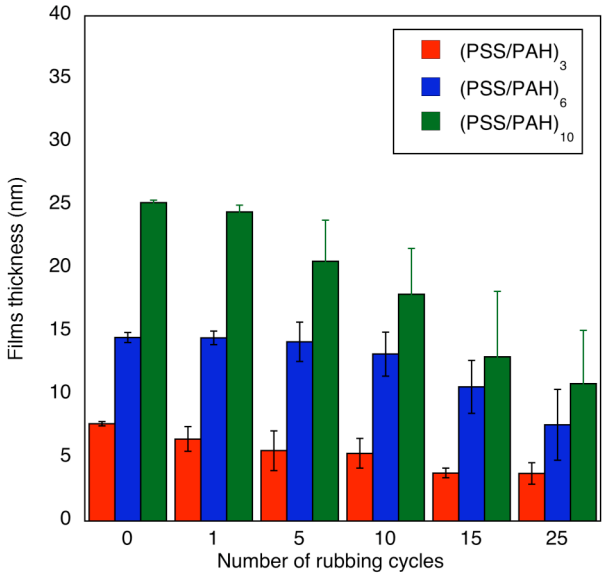

Figure 32: Freshly prepared $(PSS/PAH)_n$ films thickness variation as a function of number of rubbing cycles

Figure 32 shows that several rubbing cycles are needed in order to induce measurable damage. After 1 rubbing cycles, there is no obvious film thickness change for all samples. By increasing the number of rubbing cycles, $(PSS/PAH)_n$ films show different damage as function of the number of layer pairs n (Figure 32, Table 7). Moreover, surface roughness of $(PSS/PAH)_n$ films increases with the number of rubbing cycles as indicated by the increase of error bars in Figure 32.

After 15 cycles, $(PSS/PAH)_n$ film has lost at least 50% of the initial film thickness. After 25 rubbing cycles, film are totally removed, except for $(PSS/PAH)_{10}$ film. Meanwhile, the film thickness error bar measured by ellipsometry increases significantly with the increase of the number of rubbing cycles, representing 10 to 30% of film thickness after 5 rubbing cycles. This increase corresponds to an increase of samples surface roughness.

Number of rubbing cycles	$(PSS/PAH)_3$ film lose percentage	$(PSS/PAH)_6$ film lose percentage	$(PSS/PAH)_{10}$ film lose percentage
5	48%	23%	18%
15	79%	57%	48%
25	90%	80%	57%

Table 7: Percentage of $(PSS/PAH)_n$ film lose as a function of the number of rubbing cycles

The surface morphology of $(PSS/PAH)_6$ film was analyzed by AFM (Figure 33).

Figure 33 shows that after 15 rubbing cycles, $(PSS/PAH)_6$ film was torn up by the shear forces. There is one big trench in the middle of the image and one smaller one in the upper part of the image. Surface roughness measurement gave a RMS value of 3.1±0.8nm. Bright parts in the image are probably removed materials aggregates on the surface. Section analysis of the image shows a horizontal distance of 1.31nm and a vertical distance, corresponding to the depth of this trench, of 17.28nm. This depth corresponds to the total $(PSS/PAH)_6$ film thickness, meaning that film in the trench was totally removed.

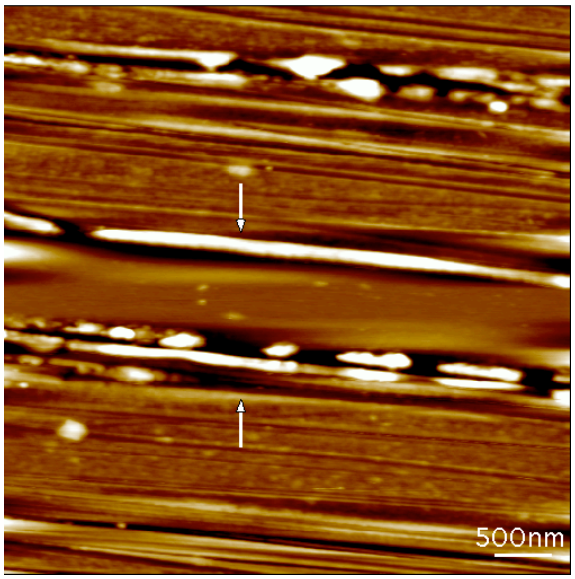

Figure 33: Surface morphology image of freshly prepared $(PSS/PAH)_6$ film after 15 rubbing cycles (height image) by tapping mode AFM

Comparison between freshly prepared and aged $(PSS/PAH)_n$ showed a significant difference in film mechanical resistance. It seems that polymer chains could rearrange after preparation and during storage period and this rearrangement is maybe the origin of mechanical resistance improvement. If some treatments could accelerate this

rearrangement, the mechanical resistance of the film can increase as well. First of all, the effect of time aging and molecular weight on mechanical resistance of $(PSS/PAH)_n$ films was studied.

III.3.3.2.2.1. Time aging effect and molecular weight effect in $(PSS/PAH)_n$ films mechanical resistance tailoring

A sprayed $(PSS70k/PAH70k)_{10}$ film was prepared. After preparation, this sample was stored under ambient condition at room temperature for one week. Then, the mechanical resistance of this one week aged sample was tested. Table 8 shows the film thickness variation of an one week aged film and of a one freshly prepared film of $(PSS70k/PAH70k)_{10}$ during the rubbing tests.

Results indicate that the mechanical resistance of the one week aged sample is slightly higher than the freshly prepared sample. However, by taking into account the ellipsometry measurement error range, this improvement could be negligible, because after rubbing test, film thickness range of freshly prepared films and one week aged films is overlapped. Compare to the excellent mechanical resistance of a 9 months aged sample, no mechanical resistance improvement caused by 1 week aged sample could probably be explained by the fact that the rearrangement of polymers may take a long time, days even years.

Number of rubbing cycles	Freshly prepared $(PSS/PAH)_{10}$ film thickness (nm)	Film thickness loss percentage (%)	One week aged $(PSS/PAH)_{10}$ film thickness (nm)	Film thickness loss percentage (%)
0	25.2±0.2	0	25.5±0.2	0
5	20.6±3.3	~18	23.5±3.8	~16
15	13.0±5.2	~48	18.5±5.4	~34
25	10.9±4.2	~56	17.1±4.2	~39

Table 8: Freshly prepared and one week aged $(PSS/PAH)_{10}$ film thickness variation and thickness loss percentage as function of number of rubbing cycles

Till now, PSS and PAH polymers had the same molecular weight (70,000g/mol). The investigation of the influence of molecular weight on mechanical resistance of $(PSS/PAH)_n$ films was carried out.

$(PSS/PAH)_{10}$ films with different molecular weight were prepared, mechanical resistance of these films right after preparation and after 1 week aging was tested (Figure 34).

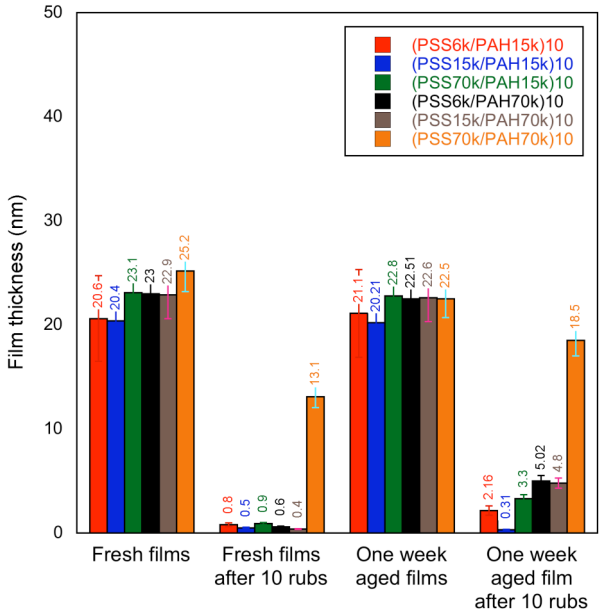

Figure 34: Influence of molecular weight and time aging on the mechanical resistance of $(PSS/PAH)_n$ films monitored by ellipsometry

Unfortunately, use of smaller molecular weight polymers does not increase the mechanical resistance of films. This weak mechanical resistance of films with smaller molecular weight can probably be explained by the entanglement between polymer chains and by numbers of anchoring points between polymer chains and the surface. Long chain polymers have more entanglement points between them as well as anchoring points with the surface than short chain polymers. During a rubbing test, films with long chain polymer are more robust than those with short chain polymers, because the shear force can not completely break all entanglement and anchoring points of long chain polymers.

In the following tests, PSS and PAH with a molecular weight of 70,000g/mol were used all the time.

III.3.3.2.2.2. Vacuum dry effect in $(PSS/PAH)_n$ films mechanical resistance tailoring

As no significant improvement of mechanical resistance was observed with aged films or by varying the molecular weight of polymers, we investigated the effect of drying. The difference between a freshly prepared and a time aged sample could be due to the percentage of water molecules within the film. After film preparation, even if the film was dried by nitrogen flow, some water molecules are still present into the matrix of the polymer films. During storage, some of these water molecules can evaporate.

In a rubbing test, these water molecules may play a role as lubricant causing a weak resistance of the film. If some treatments could accelerate the evaporation of these water molecules, the film should be more robust. As a consequence, the effect of vacuum on mechanical resistance improvement was studied.

After preparation, all samples were stored under vacuum condition (0.3mbar) during different time before the rubbing tests. Three sprayed $(PSS/PAH)_6$ films were prepared. After preparation, they were stored under vacuum condition, respectively, during 1h, 24h and one week. Film thickness was measured right after preparation, after vacuum storage and after the different rubbing cycles (Table 9, Figure 35).

Results show that the storage of $(PSS/PAH)_6$ film under vacuum for 24h leads to the best mechanical resistance. A shorter (1h) or a longer (1 week) drying time under vacuum is less efficient. At present, the precise role of water molecules in film reorganization is not clear.

Film thickness (nm)	$(PSS/PAH)_6$ film, 1h vacuum	$(PSS/PAH)_6$ film, 24h vacuum	$(PSS/PAH)_6$ film, 1 week vacuum
Initial	16.1±0.3	16.4±0.2	16.6±0.2
After vacuum	15.6±0.4	16.2±0.2	16.3±0.4
After 5 rubbing cycles	12.7±4.7	13.6±2.6	10.4±5.6
After 15 rubbing cycles	5.5±4.1	11.4± 2.5	4.0±3.3
After 25 rubbing cycles	2.2±1.1	8.2±4.4	1.9±0.9

Table 9: Film thickness variation of $(PSS/PAH)_6$ films after preparation, different vacuum storage time and different rubbing cycles

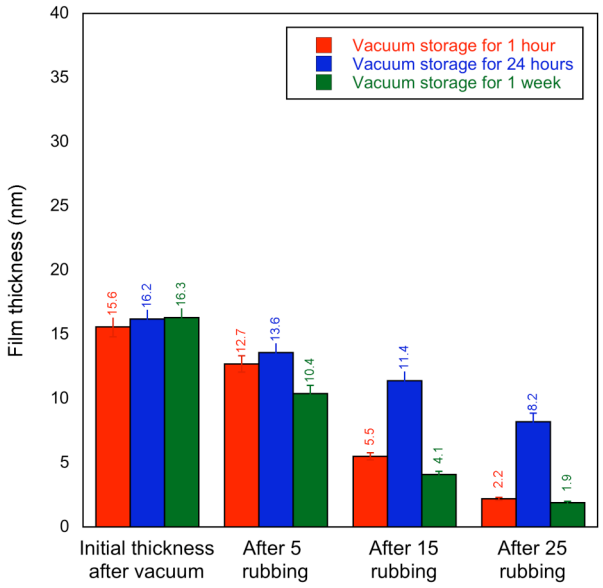

Figure 35: Variation of $(PSS/PAH)_6$ film thickness as a function of vacuum treatment and various rubbing cycles measured by ellipsometry

The 1 week vacuum dried sample shows a weak mechanical resistance as well. One possible reason is that all water molecules are evaporated, which leads to the formation of a easily broken brittle film. On the contrary, the weak mechanical resistance of 1 hour vacuum dried sample could be due to the inefficient water evaporation in the film. At present time, a vacuum drying time of 24 hours seems to be the appropriate time to reach

an adequate quantity of water molecules in the film matrix in order to get the best mechanical resistance.

This study shows that a certain percentage of water molecules within the film may play a crucial role in the mechanical resistance of such $(PSS/PAH)_n$ films. Above and below this percentage range, the mechanical properties of the film decrease significantly, which may explain the weak mechanical resistance of 1h vacuum sample and the deterioration of mechanical resistance of 1 week vacuum sample.

These results on $(PSS/PAH)_n$ film mechanical resistance demonstrates that weak LbL films have a weak mechanical resistance, which explains the slight protection effect to functional LbL films containing Au NP.

III.3.3.3. Can functional films be protected by tough LbL top layers?

∗ In collaboration with Shahid QUERESHI, a visiting student in our team, who worked on the elaboration of robust LbL assembled films by using covalent bonding, such films were tested as protective layers for $(Au\ NP/PAH)_n$ film.

III.3.3.3.1. Choice for tough LbL materials: epoxy glue for assembling tough layers

First of all, the construction of $(PEI/CNER)_n$ films at different polymer concentrations and at different deposition times was studied in order to find optimum experimental conditions. As the CNER was dissolved in organic solvent (acetone), the spray deposition was not used for film deposition. Therefore, $(PEI/CNER)_n$ films were deposited by dipping.

For all $(PEI/CNER)_n$ multilayer films, the pre-cleaned substrate (Silicon wafer or Quartz slide) was firstly dipped in a PEI solution for a certain time t_1, followed by 2 minutes (t_2) subsequent rinsing with Milli-Q water in three different baths. After drying, the substrate was dried with a nitrogen stream. The substrate covered with a PEI monolayer was then dipped in the epoxy resin solution prepared in acetone. The dipping time (t_3) for epoxy solution was kept the same as for the PEI solution (t_1=t_3). Finally, the substrate was rinsed in pure acetone for 2 minutes (t_4) in three different baths. All the dipping and rinsing solutions had a volume of approximately 15 ml.

Consecutive rinsing in three different solvent baths ensured the removal of weakly adsorbed material and reduced cross-contamination of the solutions in comparison with

rinsing in a single bath. After drying the film under a stream of pure nitrogen gas, ellipsometry measurements were carried out to determine the thickness of the multilayer. Typically, for the multilayer architectures $(PEI/CNER)_n$, the total number of deposited layer pairs "n" was between 4 and 12. The outermost layer was always an epoxy layer. For a single layer pair, the total deposition time is $t = t_1 + t_2 + t_3 + t_4$.

Concentrations (C) of epoxy and of PEI solutions were the same, C(PEI)=C(CNER). Typically, 6 concentrations, 1, 10, 20, 40, 80 and 100 mg/ml for both PEI and epoxy solutions, were used for the build-up of PEI/Epoxy multilayer. In addition, the effect of deposition time for PEI and epoxy solutions was studied. Five different dipping time, $t_1 = t_3 = 25$, 50, 120, 180 and 240 minutes, were chosen. However, for all concentrations and for all dipping times, the rinsing time was kept the same i-e three rinse cycles of 2 minutes each ($t_2=t_4$). After the deposition of each layer pair, the film thickness was measured by ellipsometry.

Figure 37 and Table 10 show a linear build-up for $(PEI/CNER)_n$ film at different concentrations. In this $(PEI/CNER)_n$ film construction experiment, the concentration of PEI and CNER solutions were the same and the dipping time for each polymer layer was 50 minutes. The choice of this dipping time will be explained in the next section.

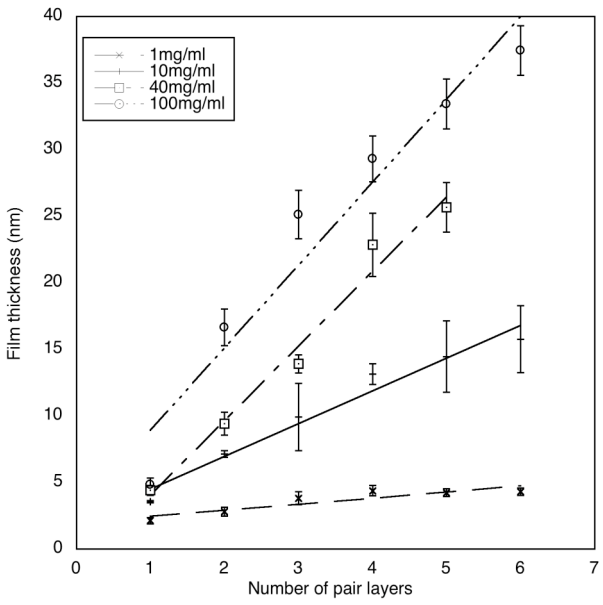

Figure 36: Thickness variation of $(PEI/CNER)_n$ films for different polymers concentrations as a function of the number of layer pairs

Concentration of Polymers (mg/ml)	Single layer pair increment (nm)
1	0.5
10	2.5
40	5.6
100	6.2

Table 10: Single layer pair increment for $(PEI/CNER)_n$ film build-up at different polymer concentration, calculated from the values of Figure 37

The film thickness of $(PEI/CNER)_n$ increases linearly as a function of number of layer pairs deposited on the surface. The single layer pair increment increases by increasing the polymer concentration in the solution from 0.45nm for 1mg/ml polymer solutions to 6.22nm for 100mg/ml polymer solutions. This linear growth of $(PEI/CNER)_n$ films was also confirmed by UV/visible spectroscopy experiments. Figure 39 shows the linear increase of absorption at 200 nm as a function of the number of deposited layer pairs at different polymer concentrations. The absorption at around 200nm corresponds to the phenol group of CNER.

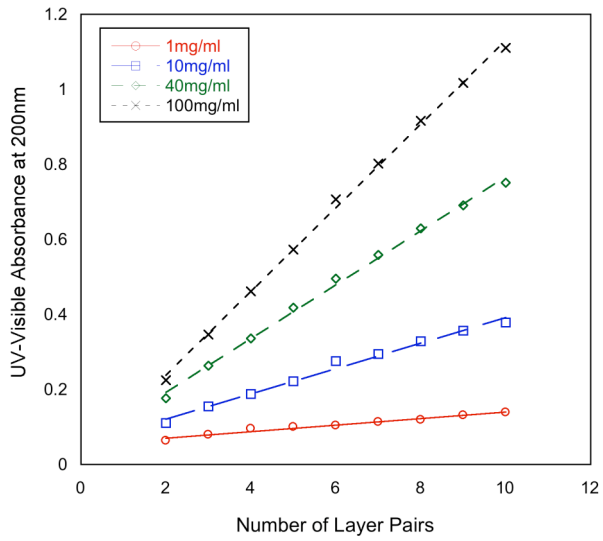

Figure 37: UV/Visible absorption of $(PEI/CNER)_n$ films at 200nm and at different concentrations as a function of the number of layer pairs

Beside the influence of polymer concentrations in film construction, the effect of dipping time was also studied for $(PEI/CNER)_n$ films (Figure 40). Results show that there's an interesting correlation between the average growth per layer pair and their concentration.

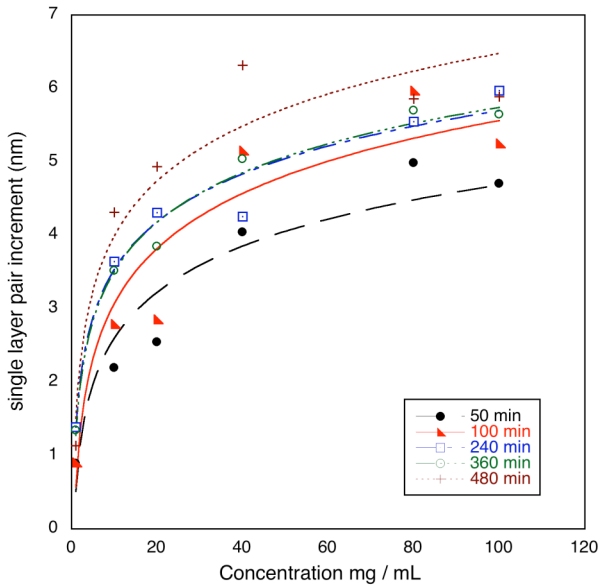

Figure 38: Variation of the single layer pair increment of $(PEI/CNER)_n$ films at different adsorption times as a function of polymer concentrations measured by ellipsometry

The variation of single layer pair increment of $(PEI/CNER)_n$ film as a function of polymer concentration and dipping time was studied. Time values indicated in Figure 38 correspond to the dipping time used for each polymer single layer. The layer pair increment was calculated as following. First of all, a matrix of polymer concentration and polymer adsorption time was built, corresponding concentrations were 1, 10, 20, 40, 80, 100mg/ml and corresponding adsorption time were 50, 100, 240, 360, 480 min per layer. This matrix means that 30 series of $(PEI/CNER)_n$ films with corresponding polymer concentrations and adsorption times were constructed. Films thickness was measured by ellipsometry after construction and every single layer pair increment was calculated. The variation of the increment as a function of polymers concentration at different adsorption time was presented in Figure 38.

When the concentrations of PEI and CNER were increased from 1 mg/ml to 40mg/ml, there is a significant film increment increase of 300% to 400% for all tested dipping time. For concentration higher than 40mg/ml, this increment increase slowed down to only 20%~25% for all dipping times, which means that further increase in concentration does not increase film thickness as well.

Based on theses results, an optimum concentration of 40mg/ml was chose because further increase in concentration does not lead to a dramatic change in films increment and an optimum dipping time of 50 minutes for a single layer deposition was chose as well, and this choice is based on the fact that a films increment variation has similar behavior at different adsorption time. In terms of working time gain, 50 minutes for a single layer deposition was used in all following experiments.

III.3.3.3.2. Mechanical resistance tests for tough LbL top layers protected functional films

After the construction of $(PEI/CNER)_n$ films, their mechanical resistance were studied by rubbing machine. Surface morphology and thickness variation of $(PEI/CNER)_n$ films before and after rubbing tests were characterized by AFM and ellipsometry respectively.

A $(PEI/CNER)_9$ film was chosen for mechanical resistance tests. This sample had a good mechanical resistance. Ellipsometry analysis showed that after film preparation, film thickness was 51.2±1.3nm. And after a 60 consecutive rubbing cycles, 70% to 75% of the epoxy film was still attached to the substrate. Figure 41 shows the surface morphology of $(PEI/CNER)_9$ film observed by AFM before and after rubbing.

Before rubbing tests, CNER film has a homogeneous surface morphology (Figure 39A). After 60 consecutive rubbing cycles, only some trenches appeared on the surface (Figure 39B). Therefore, there is no dramatic surface morphology change before and after rubbing test. Surface roughness analysis indicates a slight RMS change from 2.9±0.2nm (Figure 39A) to 4.7±0.3nm (Figure 39B). Section analysis (Figure 39B and 39B1) indicates a vertical distance of 12.28nm between one of the trenches, corresponding to 45% of the initial thickness of the epoxy film. AFM analysis confirmed that most epoxy film is still attached on the substrate after rubbing tests and the good mechanical properties of epoxy component.

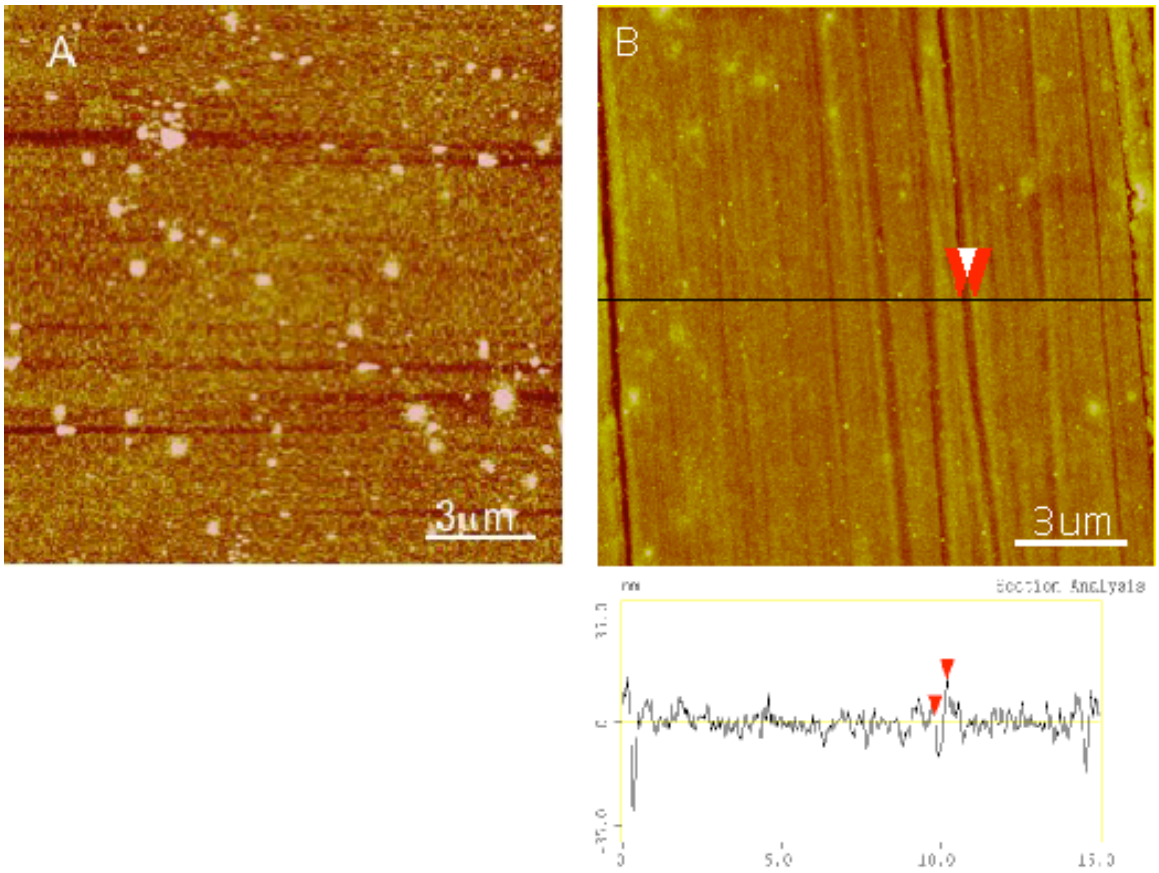

Figure 39: Surface morphology images of $(PEI/CNER)_9$ film before rubbing tests (A) and after 60 rubbing cycles(B). B1 shows a section analysis of (B) by tapping mode AFM. Both images are height images

These results suggest strongly that $(PEI/CNER)_n$ films could probably protect Au NP films. Therefore, we investigated the construction of gold nanoparticle films protected by a $(PEI/CNER)_n$ films and studied the mechanical properties of these films.

A $(PEI/CNER)_n$ film with different thicknesses were deposited on the top of Au NP film. Two different epoxy thicknesses were chosen, $(PEI/CNER)_3$ and $(PEI/CNER)_6$. The film buildup was measured by ellipsometry. Concentrations for both PEI and CNER solution were 40mg/ml and the dipping time for each polymer was 50 minutes.

The general architecture of this complex film is: Si/PEI/PSS/$(PAH/Au\ NP)_m$/(PAH/PSS)/$(PEI/CNER)_n$, briefly $(Au\ NP/PAH)_m$/$(PEI/CNER)_n$.

Table 11 shows the thickness of (Au NP/PAH)$_m$/(PEI/CNER)$_n$ films during construction.

Film architecture	Film thickness (nm)	
	(PAH/Au)$_5$/(PEI/CNER)$_3$	(PAH/Au)$_5$/(PEI/CNER)$_6$
(PAH/Au)$_5$/(PEI/CNER)$_1$	44.0	45.7
(PAH/Au)$_5$/(PEI/CNER)$_2$	46.1	45.4
(PAH/Au)$_5$/(PEI/CNER)$_3$	48.7	47.6
(PAH/Au)$_5$/(PEI/CNER)$_4$	-	48.5
(PAH/Au)$_5$/(PEI/CNER)$_5$	-	52.8
(PAH/Au)$_5$/(PEI/CNER)$_6$	-	55.5

Table 11: Thickness measurements of (PAH/Au)$_5$/(PEI/CNER)$_3$ and (PAH/Au)$_5$/(PEI/CNER)$_6$ films during the build-up by ellipsometry

Attention should be paid here for the irregularity of this complex film growth. The average film thickness for a single (PEI/CNER) layer is around 5nm for C=40mg/ml and t_1=t_3=50minutes as shown in the previous section. However, in the presence of the gold colloid film, the average film thickness for a single (PEI/ER) layer decrease to 2 or 3 nm. This phenomena is probably induced by the passage from an aqueous environment needed for the construction of the colloid film and for the deposition of PEI layers to an organic solvent environment for the deposition of CNER layers.

After film construction, the mechanical resistance of these two films was tested. The two architectures mentioned above were coded as following:
[PEI/PSS/(PAH/Au)$_5$/PAH/PSS]/[PEI/CNER]$_3$ coded as (PAH/Au)$_5$/(PEI/CNER)$_6$
[PEI/PSS/(PAH/Au)$_5$/PAH/PSS]/[PEI/CNER]$_6$ coded as (PAH/Au)$_5$/(PEI/CNER)$_3$

As the thickness of colloid film was kept constant for both architectures, the mechanical resistance of the films should only depend on the thickness of epoxy film. Surface morphology were analyzed by AFM before and after rubbing test while film thickness changes were measured by ellipsometry after washing the rubbed film with acetone, the objective of this additional rinse step is to remove film residues attached on the surface in order to avoid ellipsometry measurement imprecision.

Rubbing cycles	Film thickness (nm)	
	$(PAH/Au)_5/(PEI/CNER)_6$	$(PAH/Au)_5/(PEI/CNER)_3$
0	55.5	48.7
1	55.0	47.6
5	54.7	38.5
15	55.2	28.8
25	54.6	17.8

Table 12: Thickness measurements of $(PAH/Au)_5/(PEI/CNER)_3$ and $(PAH/Au)_5/(PEI/CNER)_6$ as a function of the number of rubbing cycles

Table 12 shows the variation of film thickness of epoxy film protected colloid film after different rubbing cycles. Compared to the colloid film without protection (Table 4), data indicate clearly that the presence of an epoxy film significantly improves the mechanical resistance of the colloid film. However, the mechanical robustness is related to the thickness of the epoxy film. After 25 rubbing cycles, the thickness of $(PAH/Au)_5/(PEI/CNER)_6$ film does not change significantly (98% of the film was left) while the thickness of $(PAH/Au)_5/(PEI/CNER)_3$ film decreases considerably (only 36% was left on the surface). To confirm these results, films were investigated by AFM (Figure 40).

Figure 40 shows a significant improvement of the mechanical resistance of epoxy protected films as a function of epoxy film thickness. There is a big difference between $(PAH/Au)_5/(PEI/CNER)_3$ film (Figure 40A) and $(PAH/Au)_5/(PEI/CNER)_6$ film (Figure 40B). The $(PAH/Au)_5/(PEI/CNER)_3$ film was completely torn up after 5 rubbing cycles. The dark part on the AFM images (Figure 40A) is probably the PEI layer or the silicon substrate. AFM surface roughness analysis indicates a RMS of 3.4±0.6nm for $(PAH/Au)_5/(PEI/CNER)_3$ film before the rubbing test, which is very similar to the RMS (2.9nm, Figure 40A) of $(PEI/CNER)_9$ film. After 5 rubbing cycles, AFM section analysis gives a surface roughness RMS of 10.7nm (Figure 40A) and a vertical distance of 50.7nm (Figure 40A-1) corresponding to the height of the initial film (Table 12).

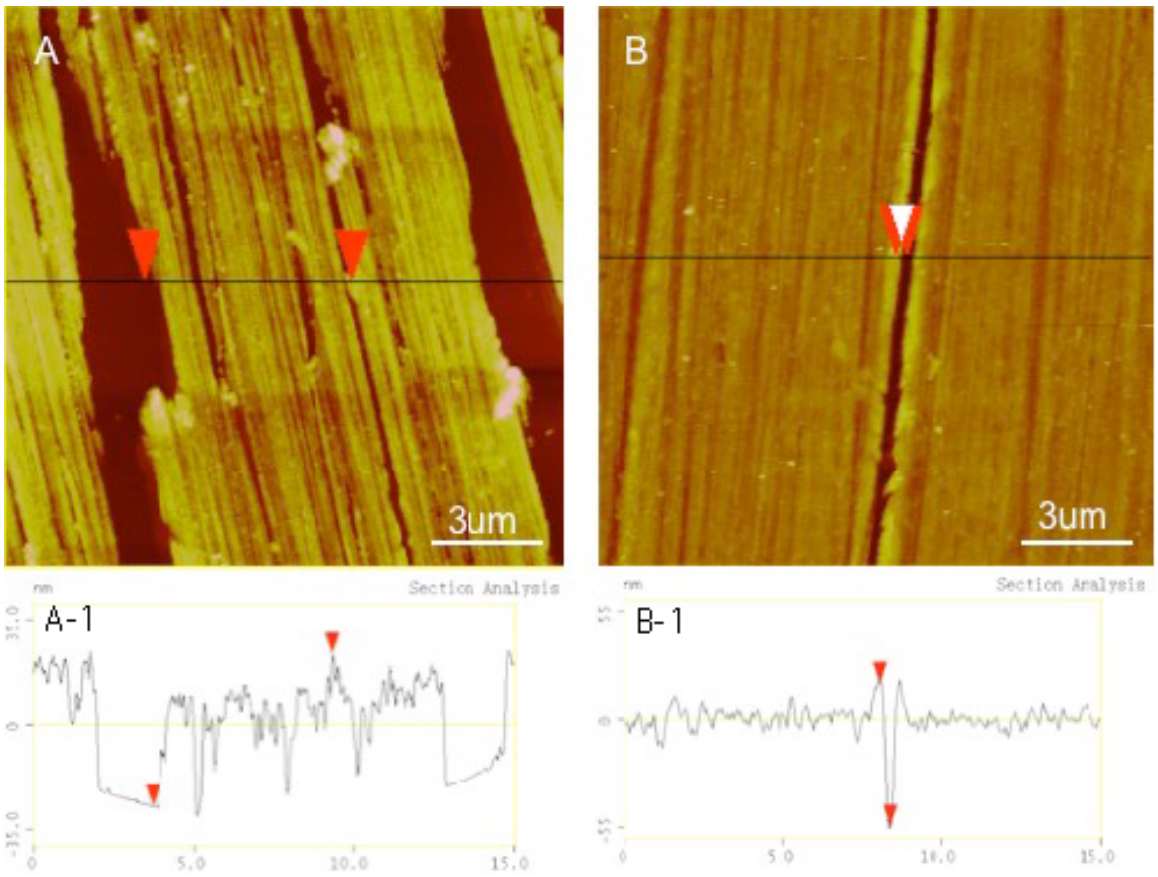

Figure 40: Surface morphology images of epoxy protected Au NP films after rubbing tests. (A) $(PAH/Au)_5/(PEI/CNER)_3$ film, film after 5 rubbing cycles and (B) $(PAH/Au)_5/(PEI/CNER)_6$ film, after 25 rub cycles by tapping mode AFM. All images are height images

For $(PAH/Au)_5/(PEI/CNER)_6$ film, there are some small trenches and a big one on the surface (Figure 40B) like the (PEI/CNER) film after 60 rubbing cycles (Figure 40B). The friction force probably induced an enlarged trenches (Figure 40B) with a surface roughness RMS rising from 4.7±0.3nm (Figure 39B) to 24.7nm, the roughness of the trench, measured by AFM section analysis. The trench with red markers has a vertical distance of 55.45nm (Figure 40B), which corresponds to the thickness of $(PAH/Au)_5/(PEI/CNER)_6$ film. Except this trench, most of film still sticks on the substrate, which means that a 10nm or more $(PEI/CNER)_n$ film could efficiently protect Au NP film.

Both ellipsometry and AFM analysis have confirmed that the deposition of an epoxy layer over a Au NP film can improve significantly the mechanical resistance of the whole film. However, this improvement is dependent of the epoxy film thickness. In our present study, we showed that a $(PEI/CNER)_6$ film was good enough for an optimum protection.

After 25 rubbing cycles, 98% film is still on the surface compared to 36% for $(PEI/CNER)_3$ film and to 12% for non protected film after 15 rubbing cycles. Therefore, the thickness of $(PEI/CNER)_6$ film, which is around 10nm, is the minimum thickness to an efficient protection of colloid film, at least at present experimental conditions.

III.3.3.3.3. Conclusion

In this section, we have showed that multilayer can be fabricated by the adsorption of polymers (PEI and CNER) through covalent linkages at ambient conditions. A linear growth of the film was observed by ellipsometry and UV-visible spectroscopy. Study on the influence of polymer concentration and dipping time on film construction allowed to get optimum deposition conditions. During mechanical resistance tests, the epoxy film demonstrates an excellent resistance due to the covalent cross-linking between different layers. Finally, this epoxy films could be used as an efficient protection of the gold nanoparticle films. The colloid film protected by an external epoxy film showed a great mechanical robustness increasing with the number of epoxy layer. In our work, a $(PEI/CNER)_6$ film provides an adequate protection for the underlying weak gold nanoparticle film.

Bibliography*

*: All references cited in this thesis have their independent citation style in the corresponding journals

[1] J.B. Schlenoff, S.T. Dubas, T. Farhat, *Langmuir* **2000**, *16*, 9968.
[2] A. Izquierdo, S.S. Ono, J.C. Voegel, P. Schaaf, G. Decher, *Langmuir,* **2005**, 21, 7558.
[3] G. Decher,. *Science* **1997**, *277*, 1232.
[4] J. Schmitt, G. Decher, W.J. Dressick, S.L. Brandow, R.E. Geer, R. Shashidhar, J.M. Calvert. *Advanced Materials* **1997**, *9*, 61.
[5] J. Schmitt, T. Grünewald, G. Decher, P.S. Pershan, K. Kjaer, M. Lösche, *Macromolecules,* **1993**, 26, 7058
[6] O. Félix , Z. Zheng, F. Cousin, G. Decher, *Comptes. Rendus. Chimie*, **2009**, 12 (1-2) 225.
[7] C.H. Porcel, A. Izquierdo, V. Ball, G. Decher, J.C. Voegel, P. Schaaf. *Langmuir,* **2005**, *21*, 800.
[8] C.J. Zhong, M.M. Maye, *Advanced Materials,* **2001**, *13*, 1507.
[9] E. Katz, I. Willner, *Angewandte Chemie-International Edition,* **2004**, *43*, 6042.
[10] A.N. Shipway, M. Lahav, I. Willner, *Advanced Materials,* **2000**, *12*, 993.
[11] S.F. Cheng, L.K. Chau, *Analytical Chemistry,* **2003**, *75*, 16.
[12] C.Y. Jiang, S. Markutsya, V.V. Tsukruk, *Advanced Materials,* **2004**, *16*, 157.
[13] S.G. Kim, N. Hagura, F. Iskandar, A. Yabuki, K. Okuyama, *Thin Solid Films,* **2008**, *516*, 8721.
[14] M. Kolasinska, T. Gutberlet, R. Krastev, *Langmuir,* **2009**, *25*, 10292.
[15] C. Lu, H. Möhwald, A. Fery, *J. Phys. Chem. C,* **2007**, 111, 10082.

Conclusion and perspectives

During my graduate research, I have explored how far one can push layer-by-layer spray assembly. All experiments including pure polyelectrolyte multilayer and polyelectrolyte/gold nanoparticle hybrid multilayer were prepared by classic layer-by-layer spray assembly process. Only a few samples were prepared by dipping for use as reference.

I. Layer structure study of sprayed $(PSS/PAH)_n$ films

In the first part of my work, the layer structure of sprayed polyelectrolyte multilayer was investigated by neutron reflectometry. A well characterized polyelectrolyte multilayer system, poly(styrene sulfonate)/poly(allylamine hydrochloride), (PSS/PAH), was chosen for this structural study.

With an acceleration of 25-150 times as compared to the dipping method, the spraying method is a high-speed process. But the resulting films differ from films prepared by dipping. The explanation of why sprayed films are thinner than dipped film is not completely clear at present time. But there is evidence that local shear effect maybe involved. If this would be the case, such effect could potentially be destructive with respect to layer architecture and interpenetration. A layer structure study by scattering reflectometry method was necessary and carried out by neutron reflectometry.

Several sprayed samples with different film architectures and as comparison periodic position of deuterated layers as well as one dipped sample were analyzed. Scattering length densities, film thicknesses per layer and interfacial roughnesses were obtained from samples with a minimum and a maximum deutration. A mean film increment of a sprayed $(PSS/PAH)_1$ film, deposited from solutions of 0.5M NaCl, is around 2.54nm, which is around 20% thinner than dipped films and surface roughness is less than 1.0nm.

These values were then applied without any corrections to superlattice films with different spaced deuterated layers to obtain theoretical. It turned out that all models agreed well with all film architectures without any adjustable parameters. More over, both sprayed and dipped samples maintained this structure even after a 6 months storage at ambient conditions. Other films architectures were measured by neutron reflectometry and their analysis is in progress. These additional results are expected to improve the precision of the results already obtained.

II. Toward a simpler film forming process: simultaneous spraying

Simultaneous spray deposition is even more interesting than alternating spray deposition. However, there were only two successful experiments reported from our team and many attempts to find more systems failed. In collaboration with BASF, we set up a spraying device, which allows to control precisely parameters such as liquid flow (HPLC pumps) and air flow, which control droplet size and density in the spray jet and the speed of the droplets. With this device, we could even achieve the spray deposition of (PSS/PAH) films as system, which had previously failed in any attempt for simultaneous spray deposition.

A more detailed study was carried out with the polymers, poly(vinylamin) and poly(acrylic acid), for which a series of molecular weight is available.

In agreement with the classic rules for polymer complex formation, if polyions have a large difference in their molecular weight, only weakly attached, highly heterogeneous gel-like and easily removable films were obtained. Polyions with similar molecular weight permit the deposition of stable films. Besides, polymer concentration is also a most important parameter in simultaneous sprayed films. In contrast to alternate spraying of LbL films, in which the optimum polymer concentrations are relatively low, about 3mM, simultaneous spraying of the same compound requires higher polymer concentration, up to 0.6M.

With the nozzles that were used for all spray experiments, the best results of the formation of stable and homogeneous films on the surface were obtained at a liquid flow rate of about 6ml/min and a high gas flow rate at about 40 dispensed volume/min for spraying time of one minute for ((poly(vinylamine)/poly(acrylic acid, sodium salt)) polymer couple, with similar molecular weight. In addition, an additional 30 seconds contact time, between spraying and rinsing steps is indispensable for forming homogeneous films after 60seconds of spraying. The film thickness of such film is about 15nm, 2.5 times *thicker* than ((poly(vinylamine)/poly(acrylic acid, sodium salt))$_5$ LbL-films, with similiar molecular weight, prepared by alternate spraying under same preparation conditions.

The surface morphology of this simultaneously sprayed film was analyzed by AFM and compared to manually sprayed films (Figure). The surface roughness of simultaneous

sprayed film is about 1.7nm as compared to that of LbL sprayed films, which is about 1.1nm.

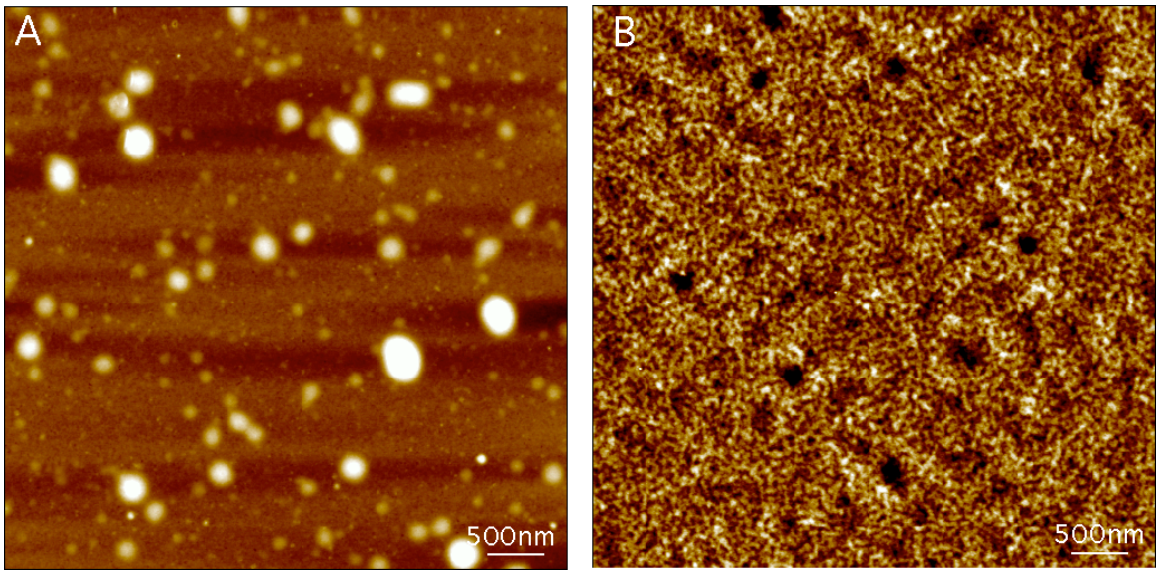

Figure 1: Height images of (Lup 5095/Sok 70) film prepared by simultaneous spray (A) and $(\text{Lup 5095/Sok 70})_5$ film prepared by LbL (B) by tapping mode AFM

However, there is a different morphology for simultaneously sprayed and alternating sprayed films. Even after optimization, in alternating sprayed film (Figure 1B), the film surface is more homogeneous, while in simultaneous sprayed films (Figure 1A), some islets (bright dots) were observed. These islets are probably polymer complex and during the simultaneous deposition, the growth and the coalescence of these islets will lead to the formation of a uniform film on the surface.

We conclude that spray deposition leads to films with excellent quality and even very good quality in the case of simultaneous spraying. In addition to classic parameters for controlling film deposition, such a concentration, ionic strength, temperature, pH, adsorption time etc…, there are several additional parameters that control the spray cone itself, like liquid flow, air flow, nozzle type, spray distance etc. A complete study of all these parameters will be necessary to further film construction by alternating and simultaneous spraying. A second generation device that will allow to control these parameters, even better than the "RoboSpray" device developed with BASF, is presently under construction.

III. Construction of Polyelectrolyte/Au NP films

Having established a solid control for the spray deposition of polymers, it was interesting to investigate the spray deposition of functional films containing nanoparticle.

Similar to films prepared by dipping, sprayed films show linear film growth (3 A and B). Figure 3A is the proof that the (PSS/PAH) pairs do lead to an increase of the film thickness. Figure 3B is proof that the structure of the individual Au NP layers does not change much when changing n of $(PSS/PAH)_n$. Figure 3A and 3B together and further supported by Figure 4, are proof that the spray deposition of Au NPs lead to multilayer films in which the particles are confined to plane with a certain positional disorder in direction of the layer normal, Figure 2. When Au NPs are adsorbed on the polyelectrolyte layer by forming a Au NP monolayer, instead of forming a perfect smooth monolayer without any positional disorder (Figure 2A), Au NP will form a monolayer with certain positional disorder, Figure 2B. This positional disorder, "roughness" of the Au NP layer, is further investigated by AFM.

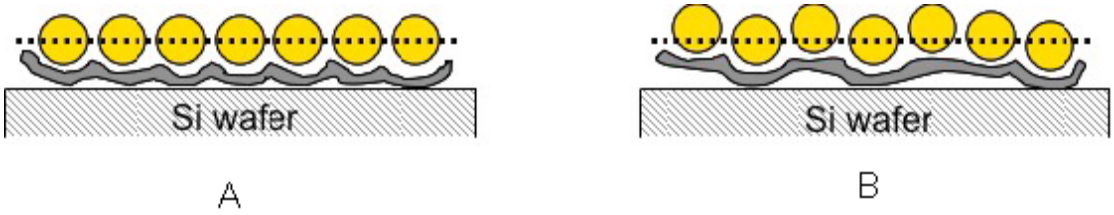

Figure 2: Formation of a Au NP monolayer on the polyelectrolyte layer (A) without Au NP positional disorder (B) with Au NP positional disorder

The strong plasmon interactions between gold nanoparticle and of course also between layers of nanoparticle allows to use Au NPs for probing the local structure of the film and to determine if the spray deposition of NPs also lead to a penetration into the multilayer below, which was already observed in the case of protein multilayers by dipping[1] or recently for magnetic particles by neutron reflectometry[2].

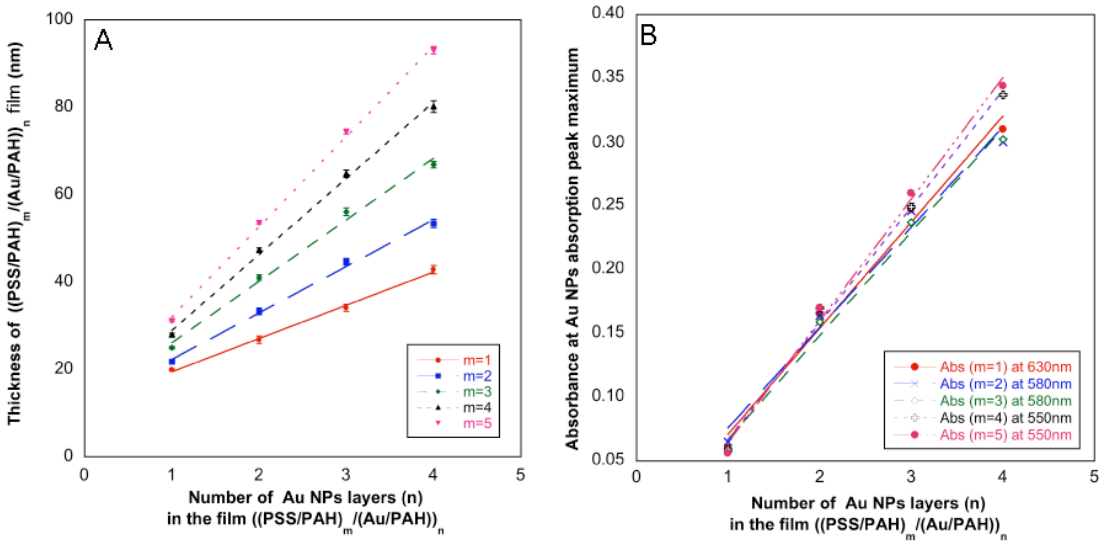

Figure 3: Constructions of Si/PEI/$[(PSS/PAH)_m/(Au\ NP/PAH)]_n$ colloid films monitored by ellipsometry (A) and UV-Visible spectroscopy (B)

The interaction of gold nanoparticle leads to a displacement of the plasmon band (bathochromic shift) of several tens of nanometers as a function of their distance (4A).

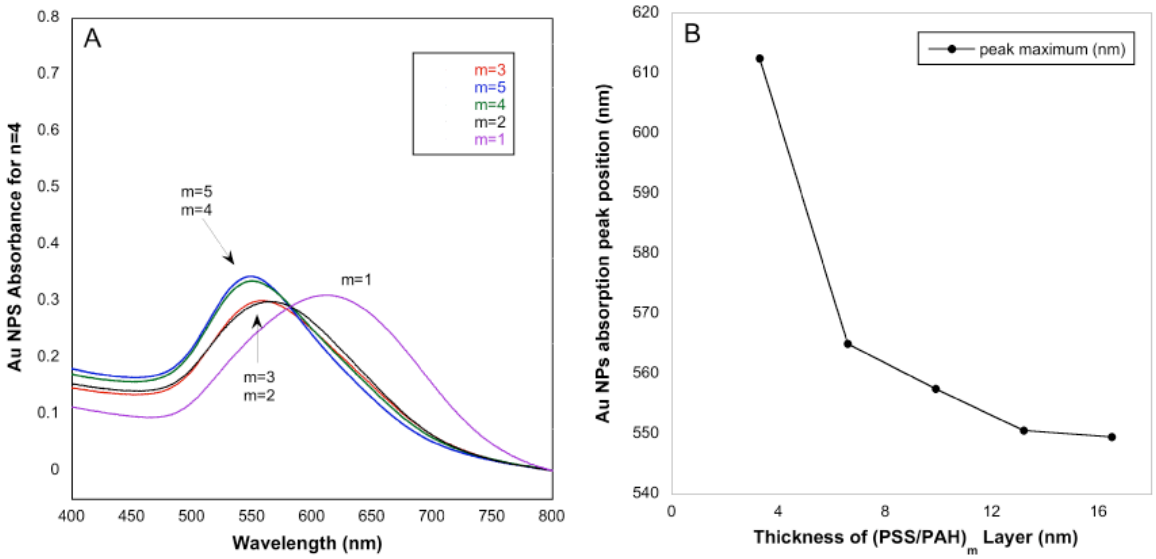

Figure 4: (A) UV-visible spectrum of $[(PSS/PAH)_m/(Au\ NP/PAH)]_4$ with m from 1 to 4. (B) Plot of maximum adsorption as a function of spacing polyelectrolyte layer thickness

However, the plasmon interaction between two adjacent gold nanoparticle layers could also be progressively extinguished by increasing the spacing distance between them (4B). For example, when two adjacent Au NPs are separated by a 13nm or more (PSS/PAH)

layer, the inter-layer plasmon interaction can not be observed any more by UV-Visible spectroscopy.

With spray-assembly, it is possible to construct Au NPs film with a large number of Au NP layers. A film with 50 Au NPs layers was prepared. AFM analysis (Figure 5) revealed this positional disorder of Au NPs in the same layer, which comes from the superposition of each Au NP layers roughness (Figure 2B). Figure 5B is a 3D surface morphology image of $(Au\ NP/PAH)_{50}$ film, which demonstrates clearly the "mountain-valley" like structure of Au NPs. Figure 5C shows that the positional disorder of Au NPs can be 51nm for Au NPs in the same layer.

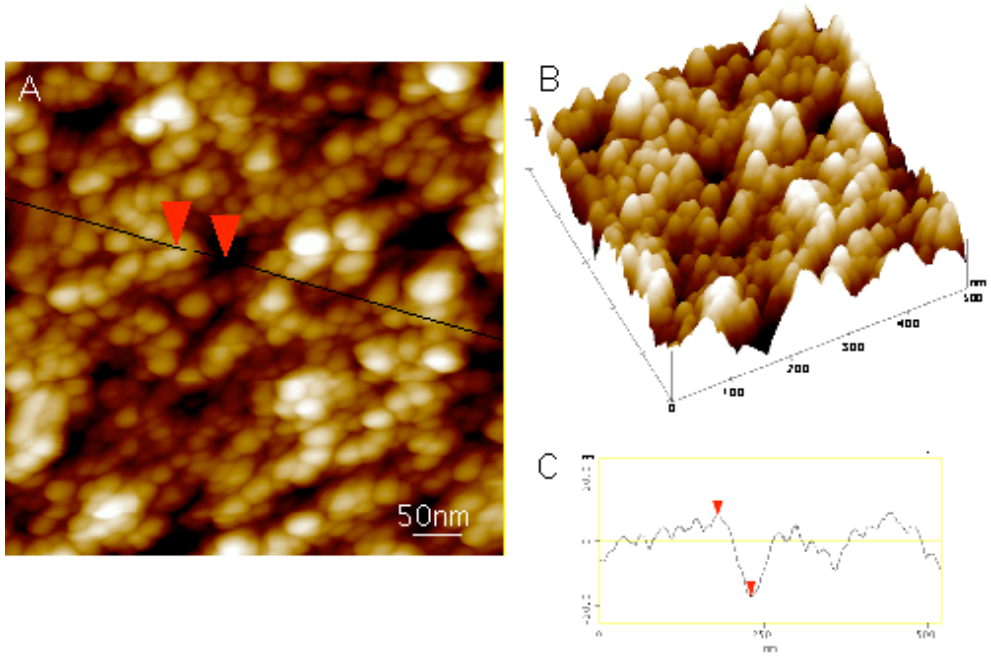

Figure 5: Surface morphology image of sprayed $(Au\ NP/PAH)_{50}$ film (A) 2D image with section analysis (B) 3D image of (A) and (C) spectrum of the section analysis of (A)

With the increase of Au NPs deposition numbers, all films are highly colored with a metallic golden coloration (Figure 6, scratch is due to the sample holding tweezers), and by simple optical inspection, all samples show excellent surface homogeneity

Figure 617: sprayed $(PAH/Au\ NPs)_{50}$ film

IV. Protective LbL-layers for mechanically weak functional multilayer

Some of the Au NPs films are mechanically very weak and are easily wiped off from the substrate under shear force. For example, in a rubbing test, after a few rubbing cycles, a $(PAH/Au\ NP)_5$ film was totally removed from the substrate. Any application of soft functional films would thus greatly benefit from protective layers. Therefore, a covalent polyelectrolyte multilayer, epoxy/polyamine film, were tested as protection film. The chemical structure of used epoxy is presented in Figure 7.

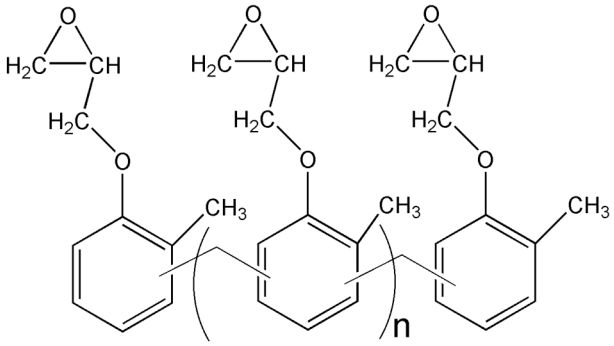

Figure 7: Chemical structure of CNER, Poly((o-cresyl glycidyl ether)-co-formaldehyde), n≈3

The choice of optimum polymer concentrations and adsorption time has been performed before the test of epoxy/polyamine films protection effect. A linear growth regime has been observed under all preparation conditions. When optimum conditions were obtained, PEI/CNER films mechanical resistance were tested before the assembly with

Au NPs based hybrid films. As expected, the PEI/CNER films are very robust and resistant to shearing force.

As expected, PEI/CNER films have an obvious protection effect to Au NPs hybrid films (Figure 8). This protection effect is a function of the PEI/CNER film thickness. In the optimized case, a protective film below the critical thickness of about 10nm is not sufficient stable to 5 rubbing cycles (Figure 8A). A film with a thickness of 10nm or more gives good protection against wear, even after 25 rubbing cycles. Only single trench is observed by AFM, Figure 8B.

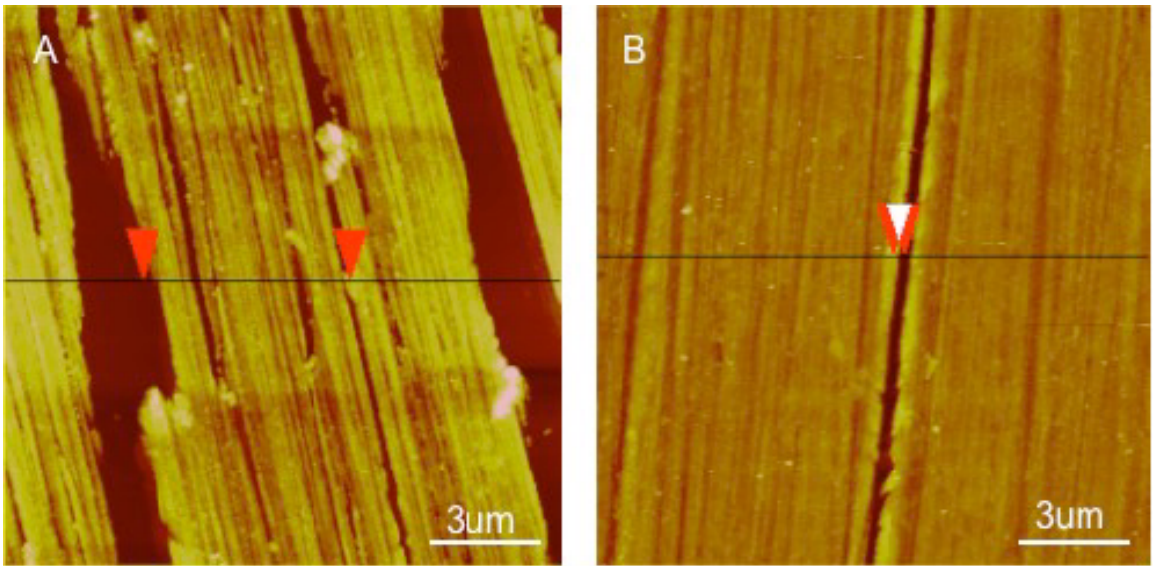

Figure 8: Surface morphology images of epoxy protected Au NP films after rubbing tests. (A) $(PAH/Au)_5/(PEI/CNER)_3$ film, film after 5 rubbing cycles and (B) $(PAH/Au)_5/(PEI/CNER)_6$ film, after 25 rub cycles by tapping mode AFM. All images are height images

The results presented here act as a proof of concept. Further optimiwation of the protective layers will probably be required for specific applications.

Bibliography*

*: All references cited in this thesis have their independent citation style in the corresponding journals

[1] D.S. Salloum, J.B. Schlenoff, *Biomacromolecules,* **2004**, *5*, 1089.
[2] M. Kolasinska, T. Gutberlet, R. Krastev, *Langmuir,* **2009**, *25*, 10292.

Abstract

In this dissertation Layer-by-Layer (LbL) polyelectrolyte and polyelectrolyte/ nanoparticle films were prepared using a number of different methods and were closely characterized. Firstly spray-assembled polyelectrolyte films were studied using Neutron Reflectivity and the results confirmed that stratified layers are formed. Thus, spray assembly of LbL-films is rapid and leads to high quality films. In addition, we studied the assembly of polyelectrolyte films by simultaneous spraying in collaboration with BASF AG.

A second topic is the preparation of functional polyelectrolyte films using the example of spray-assembled lbL-films containing gold nanoparticles(Au NP). Compared to dip LbL deposition, spray assembly yielded Au NP multilayers in a fraction of the time. Additionally, it was found that with spray assembly the Au NP could be confined to individual horizontal strata without the need for additional treatment of the films as recently reported for a similar case[1]. It was also found that varying the sandwiched polymer layers controls the film's superposing roughness and thus the surface plasmon coupling between two adjacent Au NP layers.

Thirdly, we established that even weak LbL-films can be mechanically protected by robust epoxy multilayers if the robust coating exceeds ≈10 nm in thickness.

1. M. Kolasinska, T. Gutberlet, R. Krastev, *Langmuir,* **2009**, *25*, 10292

Key words: Polyelectrolyte, Multilayer Films, Spray Assembly, Neutron Reflectometry, Gold nanoparticle, Mechanical resistance

Résumé

Dans cette thèse, des films couche-par-couche de polyélectrolytes et polyélectrolytes/nanoparticules ont été préparés en utilisant différentes méthodes et ont été soigneusement caractérisés. En premier lieu, des films de polyélectrolytes assemblés par pulvérisation ont été étudiés par Réflectométrie des Neutrons et les résultats ont confirmés la formation de couches stratifiées. Ainsi, l'assemblage par pulvérisation de films LbL est rapide et conduit à des films de haute qualité. En plus, nous avons étudié l'assemblage de films de polyélectrolytes par pulvérisation simultanée en collaboration avec la BASF AG.

Le deuxième sujet a consisté en la préparation de films de polyélectrolytes fonctionnels en utilisant l'exemple des films LbL assemblés par pulvérisation contenant des nanoparticules d'or (Au NP). Comparé au dépôt LbL par trempage, l'assemblage par pulvérisation a fourni des multicouches de Au NP en une fraction de temps. De plus, il a été montré qu'avec un assemblage par pulvérisation les Au NP ont pu être confinées dans des couches individuelles horizontales sans avoir besoin d'un traitement additionnel des films, comme cela a été reporté récemment pour un cas similaire[1]. Il a également été observé que les couches polymères sandwichs contrôlent la rugosité des films superposés et ainsi le couplage plasmon de surface entre deux couches adjacentes de Au NP.

Troisièmement, nous avons établi que même des films LbL faibles peuvent être protégés mécaniquement par des multicouches époxy robustes si le revêtement robuste dépasse ≈10 nm en épaisseur.

1. M. Kolasinska, T. Gutberlet, R. Krastev, *Langmuir,* **2009**, *25*, 10292

Mots clés: Polyélectrolyte, Films Multicouches, Assemblage par Pulvérisation, Réflectometrie des Neutrons, Nanoparticules d'or, Résistance Mécanique